Quantifying Uncertainty for In-situ Stress Estimates using Reservoir Geomechanical Pressuremeter

by

DongMing Zheng

A thesis submitted in partial fulfillment of the requirements for the degree of

Doctor of Philosophy

in

Geotechnical Engineering

Department of Civil and Environmental Engineering
University of Alberta

Abstract

Over the last two decades, several high-profile caprock performance issues, such as surface steam and fluid releases, have highlighted the importance of caprock integrity assessments and the critical role that robust determination of the initial in-situ stress tensor plays in these assessments. Traditionally, the minimum in-situ stress, which is a key component of the in-situ stress tensor, is determined from diagnostic fracture injection tests or minifrac tests. However, it is challenging to select the minimum stress from these tests. Consequently, recent research has pursued alternative techniques to help constrain the values of the in-situ stresses, resulting in the development of a reservoir geomechanical pressuremeter (RGP) that will allow for an integrated assessment of the in-situ reservoir rock compressibility and the direction and magnitude of maximum and minimum horizontal stresses. A conventional high-pressure pressuremeter was modified for deployment in a borehole using industry-standard wireline technology. RGP field tests were conducted at the Primrose Site project in 2016. Five intervals in three formations - Westgate, Joli Fou, and Clearwater - were tested with the deployment of the RGP tool. Interpretation and analysis of these data can provide vital information for the oil and gas industry, such as the shear modulus, undrained shear strength, and orientation and magnitude of anisotropic in-situ stresses.

The frequentist and Bayesian statistical methods proposed were first applied to the uncertainty quantification of in-situ horizontal stress using a self-bored pressuremeter (SBP). The statistical methods used in the SBP test were then used to analyze the RGP tests. Using raw data from the Primrose-Wolf Lake project , uncertainties were first identified, followed by data conversion and

corrections. Using the corrected RGP data, analytical and numerical models were coupled with optimization algorithms to find the best parameter estimates. To address the problem of non-unique solutions, uncertainty analyses were conducted using frequentist statistical assessment methods. With mean, standard deviations, and confidence intervals, uncertainties from parameter estimation were quantified, and non-uniqueness issues were addressed. Alternatively, Bayesian inference methods were adopted to evaluate in-situ horizontal stresses and material properties under a Bayesian statistical framework.

To account for the radial and azimuthal anisotropies of borehole material, the modified strain-hardening/softening model was implemented in the statistical analysis for RGP tests in deep geological formations. The advantages of this model over the Mohr-Coulomb and conventional strain-hardening/softening models were verified through the interpretation of triaxial compression tests, demonstrating superior prediction accuracy, validity, and applicability.

Compared with conventional pressuremeter interpretation methods, the proposed frequentist statistical inverse analysis methods can quantify the potential uncertainty and errors from ground properties and in-situ horizontal stress. In addition, the proposed Bayesian approach can continuously update one's beliefs with new data through an open system, which is superior to the frequentist statistical methods employed in pressuremeter studies. The statistical methodology described in this study can be extended to other engineering inverse analysis problems, such as the calibration of constitutive models and inverse analysis of in-situ stress fields for horizontal drilling, tunnelling, and hydraulic fracturing.

Preface

This thesis is an original work by Dongming Zheng. Some chapters of this thesis have been published:

Chapter 4 of this dissertation has been published in the Canadian Geotechnical Journal with my co-authors, Dr. Bo Zhang and Dr. Rick Chalaturnyk, in the Reservoir Geomechanics research group. I am responsible for establishing the methodology for the inverse analysis of pressuremeter tests and statistical assessments of the estimated parameters, coding with Matlab and FLAC, calculation, data analysis, and paper writing.

> Zheng, D., Zhang, B., and Chalaturnyk, R. 2021. Uncertainty quantification of in-situ horizontal stress with pressuremeter using a statistical inverse analysis method. Canadian Geotechnical Journal. https://doi.org/10.1139/cgj-2021-0004

Chapter 5 of this dissertation has been published in the Canadian Geotechnical Journal with my co-authors, Dr. Bo Zhang and Dr. Rick Chalaturnyk, in the Reservoir Geomechanics research group. I am responsible for Bayesian modelling programming, prior and posterior predictive checks, inference diagnosis, model comparison and manuscript writing.

> Zheng, D., Zhang, B., and Chalaturnyk, R. 2024 Quantifying uncertainty of in-situ horizontal stress and geotechnical parameters using a Bayesian inference approach for pressuremeter tests. Canadian Geotechnical Journal. Just-IN https://doi.org/10.1139/cgj-2023-0686

Chapter 6 of this dissertation has been published in GeoConvention 2023 with my co-authors, Dr. Nathan Deisman, Dr. Bo Zhang and Dr. Rick Chalaturnyk in the Reservoir Geomechanics research group. I am responsible for the parameter estimation and uncertainty quantification for the RGP tests in the Primrose-Wolf Lake field, including raw data conversion and corrections, code writing, data analysis, and paper writing.

> Zheng, D., Deisman, N., Zhang, B., and Chalaturnyk, R. 2023. Statistical inverse analysis of the RGP tests at Primrose-Wolf Lake oil sands field. GeoConvention 2023, Calgary, Canada.

Dedication

To my home country, China

To my dear parents, Shaoru Zheng and Xinqiu Zhang

To my beloved wife and daughter, Hongxian Li and Ruby Zheng

Acknowledgements

The author gratefully appreciates my supervisor, Professor Rick Chalaturnyk of the University of Alberta. His distinguished research vision, plentiful knowledge, and sincere support encouraged me to achieve academic success. In addition, the author is deeply indebted to Dr. Nathan Deisman and Dr. Gonzalo Zambrano-Narvaez, P. Eng. of the Reservoir Geomechanics Research Group, for valuable suggestions and guidance.

My gratitude goes to the RG^2 team for accomplishing the pressuremeter in-situ tests in 2016. Mr. Peter Thomsen of Canadian Natural Resources Limited is deeply appreciated for providing suggestions and advice on this in-situ test program. I am also indebted to my peer PhD student, Lang Liu, for sharing knowledge, testing data, and research insights with me.

Dr. Bo Zhang is deeply appreciated for his time and effort in reviewing and editing this manuscript. I also appreciate Dr. Jeff Boisvert for his advice on Bayesian inference analysis.

I want to thank Abel Juncal, Colin Dreger, and Anton Bogrash at the University of Alberta for their help in my research. My final acknowledgements are to all the Reservoir Geomechanics Research Group members during my PhD study over the past nine years.

Table of Contents

List of Tables

List of Figures

List of Symbols

a	current cavity radius of instrument
a_0	initial radius of instrument
a_m	internal radius of the membrane at rest
a_{max}	maximum radius of instrument
Δa	change in radius of instrument
b	estimated parameters
b'	estimated optimal parameters
b_0	optimal parameters estimated
b_i	parameters to be estimated
b_m	external radius of the membrane at rest
c	cohesion
c′	drained cohesion
c_0	parameter in conformal mapping function
c_u	undrained shear strength
CI	confidence interval
COD	coefficient of determination
d	trial step in trust region
d_m	damage variable
D	pressuremeter instrument diameter
E	Young's modulus
E'	drained Young's modulus
E_0, E_i	Initial Young's modulus
E_m	expansion of the membrane
E_{50}	secant Young's modulus at 50% strength
F_i	*i*-th failure region
F_m	*m*-th failure region
G	shear modulus
G_0	initial shear modulus estimate

G_{50}	secant shear modulus at 50% strength
G_i	initial shear modulus
I	identity matrix
J	Jacobian matrix
K_0	ratio between the horizontal and vertical effective geostatic stresses
L	pressuremeter instrument length
m	number of failure regions
n	number of observed data
N	region of trust
N_s	number of samples in subset simulation
N_l	maximum number of simulation levels
$P(F_i)$	intermediate conditional failure probability
n – p	degrees of freedom
p	number of parameters
p_i	initial pressure exerted on soil
p_c	cavity pressure
p_0	cavity reference pressure
P	total pressuremeter pressure
P_F	probability of failure
P_i	measured pressure after mapping
P_{max}	maximum total pressuremeter pressure
$P(F_i)$	failure probability of an intermediate event
q	approximation of the objective function f(x)
R^2	coefficient of determination
$\hat{P}_i$	predicted pressure
$\hat{P}_i(b_i)$	predicted pressure, a nonlinear function of b_j
$\hat{R}$	Gelman-Rubin statistic
r_b	radius of EP boundary
S_u	undrained shear strength
S_{u0}	initial shear strength estimate

S_{uc}	softened/hardened undrained shear strength
SD	standard deviation
SD(b')	standard deviation of b_0
MSE	mean squared errors
SSE	sum-of-squared errors
SST	total sum of squares
s^2	calculated error variance
t_m	thickness of the stainless-steel sheath strips
t(1–a/2, n–p)	100(1 – a ⁄2)*th* percentile of t distribution with n – p degrees of freedom
u_r	radial displacement
u_θ	circumferential displacement
V	cavity volume
V_0	original cavity volume
ΔV	change in cavity volume
Y_i , y	observed data
Y	mean of observed data
$\hat{Y}_i$	predicted data
$\hat{Y}_i(b_i)$	a nonlinear function of b_i
y	dependent variable
x_0, y_0	offset of the ellipse center radial displacement
β	softening or hardening coefficient during unloading
β_c	softened/hardened variable for cohesion
β_m	parameter in conformal mapping function
α_s	y-intercept in a micrometre plot
β_s	sensitivity in a micrometre plot
β_{su}	softened/hardened variable for undrained shear strength
β_ϕ	softened/hardened variable for friction angle
β_ψ	softened/hardened variable for dilation angle
ε_s	standard deviation in a Bayesian linear regression model
ε_{random}	random errors

$\varepsilon_{systematic}$	systematic errors
ϵ_v	volumetric strain
γ	shear strain
γ_c	shear strain at cavity wall
γ_y	shear strain at onset of fully plastic behavior
c''_0	initial undamaged value for cohesion
ϕ''_0	initial undamaged value for friction angle
ψ''_0	initial undamaged value for dilation angle
c''	softened/hardened cohesion
ϕ''	softened/hardened friction angle
Ψ	slope of cell pressure against $log(\Delta V/V)$
ψ''	softened/hardened dilation angle
$\Delta e_1{}^{ps}, \Delta e_3{}^{ps}$	major and minor principal plastic shear strain increment
$\Delta e_m{}^{ps}$	volumetric plastic shear strain increment
Δe^{ps}	plastic shear strain increment
δ	increment of the estimated parameter
λ	non-negative damping factor identity matrix
υ	Poisson's ratio
σ	standard deviation of unknown parameters
σ_0	mean horizontal stress
σ_r	radial stress
σ_s	data noise in a Bayesian linear regression model
σ_θ	circumferential stress
σ_{h0}	initial in-situ horizontal stress
σ_{hmin} , σ_h	minimum in-situ horizontal stress
σ_{hmax} , σ_H	maximum in-situ horizontal stress
σ_v	in-situ vertical stress
σ_{hy}	yield stress
θ	unknown parameters
$\hat{\theta}$	parameters to be estimated

$\hat{l}$	log-likelihood function to be evaluated
μ	predicted data
τ	shear stress
$\tau_{r\theta}$	shear stress in polar coordinates system
φ	friction angle
φ	drained friction angle
Θ	parameter space

1.0 Introduction

1.1 Background knowledge

Alberta's oil sand has the third largest oil reserves in the world. As of 2016, Alberta's oil sands proven reserves were 165.4 billion barrels (bbl) and comprised the vast majority of the proven oil reserves in Canada. However, more than 80% of the reserves are deeper than 65 m, which is unsuitable for surface mining. As a result, thermal recovery processes such as steam-assisted gravity drainage (SAGD) have become mainstream in the Alberta oil sands areas. Steam injection pressure is one of the most important operating parameters for determining the success of SAGD (AER, 2014).

A maximum operating pressure (MOP) formula was developed by the Alberta Energy Regulator (AER – Directive 23, 2024) to ensure caprock integrity, primarily governed by tensile failure. However, to address the potential risk of caprock shear failure, geomechanical modelling is the tool identified to assess the complex factors contributing to potential caprock shear failure (AER – Directive 23, 2024). In the geomechanical model, in-situ stresses should be characterized over the region to be modelled. There are more than ten approaches available to measure in-situ horizontal stresses in the deep ground (Liu, 2015). Minifrac tests have been routinely used by the oil sand industry to measure the in-situ minimum horizontal stress. However, it is concluded that "most measurements provided data of low confidence and should be deemed inconclusive' (Yuan et al. 2013). In addition, the AER pointed out that the rock properties measured in the laboratory were not representative of larger-scale values incorporated in a geomechanical simulator because of the fissures and slickensides of clay shales. Alternatively, an in-situ technique, the reservoir geomechanical pressuremeter (RGP) tool, has been proposed as a method to potentially solve these challenges.

Since the introduction of the pressuremeter by Louis Menard in 1955, the in-situ pressuremeter testing approach has been developed and practiced in Europe and elsewhere, with considerable success over the past several decades. The characteristics of shallow ground, such as strength, in-situ horizontal stress, and permeability, can be derived from measurements of the pressure and the change in volume or radius of the expanding membrane. Because of inevitable sample disturbance, simple laboratory testing results may often be scattered and unreliable. The principal advantage of the pressuremeter is that the boundary conditions are usually well-defined and controlled. However, it has been found that the test results are sensitive to the ground properties, installation techniques, and test procedures. Consequently, it is necessary to quantify the uncertainty propagated from the soil or rock spatial variability, tool installation, measurement errors, and modelling.

Based on a 73 mm high-pressure dilatometer, RGP1 was developed by the Reservoir Geomechanics Research Group (RG^2) at the University of Alberta. RGP1 is a Menard-type (inserted in the pre-bored borehole) pressuremeter for deeper formations that allows for an integrated assessment of the in-situ reservoir rock compressibility, as well as the direction and magnitude of the maximum and minimum horizontal stresses. RGP1 can provide unique in-situ data for reservoir and caprock integrity assessments associated with thermal recovery operations in unconventional reservoirs.

In February 2016, an RGP1 field test was conducted by the University of Alberta at Primrose-Wolf Lake project near Bonnyville, Alberta. Five downhole tests (B0T1 to B0T5) were conducted in four test pockets over four separate tool deployments. Data retrieved from B0T2 are discarded because the test was deemed unsuccessful (RG^2, 2016). As a result, four RGP downhole tests were selected for this study. The RGP field test details, including the site location, geology and lithology, borehole information, and tool calibration, can be found in the research report (RG^2, 2016) and published literature (Liu et al., 2020).

1.2 Motivation

A preliminary interpretation of raw data from the RGP tests was based on the analytical solutions for cylindrical cavity expansion theory under the isotropic stress plane (Gibson and Anderson, 1961; Jefferies, 1988; Yu and Netherton, 2000). However, Bell and Gough (1981) pointed out that many oil wells in Alberta are noncircular, and the elongations are caused by large, unequal horizontal principal stresses. Therefore, an inversion study on RGP field tests provides solutions for RGP expansion and contraction under an anisotropic stress field in saturated, fractured soft rock formations. Consequently, the anisotropic stress field was examined in this study and eventually applied in a reservoir geomechanical model. Ground properties and in-situ parameters, such as rock formation stiffness, shear strength, and the magnitude and orientation of in-situ horizontal stresses, play a vital role in geomechanical modelling for predicting the MOP and potential risk of caprock shear failure. Using RGP testing data, analytical and numerical models were coupled with optimization algorithms in inverse analyses to find the best parameter estimates. A modified strain-hardening/softening model was proposed to simulate the clay shale response to applied pressure. Both frequentist and Bayesian statistical approaches were used in this study to quantify the uncertainties propagated from rock spatial variability, tool calibration, tool deployment, measurement errors, and modelling. Consequently, non-uniqueness problems are solved (or at least partially solved).

1.3 Scientific hypothesis

The scientific hypothesis underpinning this research is that it is possible to adequately constrain the uncertainty bounds for estimates of the magnitude and orientation of the minimum and maximum horizontal stresses from an RGP test.

1.4 Research objectives

The main objective of this research is to develop a platform for the statistical inverse analysis of pressuremeter and RGP tests using frequentist and Bayesian approaches, combined with analytical and numerical models. This approach seeks to reduce the degree of non-uniqueness in parameter estimation. The platform is implemented using Matlab and Python, effectively enabling the statistical inverse analysis of RGP tests in the Primrose-Wolf Lake project or any other future pressuremeter tests.

1.5 Workflow

For the initial stages of this research, the frequentist and Bayesian statistical methods are applied in the uncertainty quantification of in-situ horizontal stress with a self-bored pressuremeter (SBP). Following this, data obtained from field tests conducted with the RGP tool are converted and corrected using deterministic and Bayesian approaches. With corrected arm displacements, a deterministic solution is proposed for parameter estimation, that is, a computational model is coupled with an optimizer to find the best parameter estimate. To quantify the uncertainty from the parameter estimation, both frequentist and Bayesian statistical methods were implemented. After frequentist and Bayesian statistical assessments, the geotechnical properties and in-situ parameters were evaluated statistically.

1.6 Outline of the thesis

It should be noted that this study was partially prepared in a paper-based format. Chapters 4 and 5 have been published in the Canadian Geotechnical Journal, and Chapter 6 has been published in the conference proceedings of GeoConvention 2023. This dissertation comprises eight chapters and three appendices. A brief description of the contents of each chapter and the appendix are given below.

Chapter 1: Introduction: Project background, motivation, methodology, objectives, and outline of this thesis.

Chapter 2: Research background of pressuremeter analysis and interpretation

Chapter 3: Assessment of sources of uncertainty in RGP data: Data conversion, corrections, and uncertainty quantification of RGP testing data. Uncertainties are identified for the RGP test, followed by raw data analyses with both the deterministic and Bayesian methods.

Chapter 4: Uncertainty quantification of in-situ horizontal stress with a pressuremeter using a statistical inverse analysis method: A frequentist statistical inverse analysis method is proposed for the analysis of an SBP test. The in-situ horizontal stress and geotechnical parameters were estimated using local and global optimization algorithms. The problem of non-unique solutions is addressed in the uncertainty quantification of the estimated parameters.

Chapter 5: Bayesian approach for uncertainty quantification of in-situ horizontal stress and geotechnical parameters with a pressuremeter: Bayesian inference approaches are developed to conduct parameter estimation and Bayesian statistical assessment from posterior distributions. Given this new evidence, the posterior distributions can be updated using Bayesian inference.

Chapter 6: Statistical inverse analysis of RGP case study —The frequentist approach is applied in the real RGP test project. The in-situ horizontal stress and clay shale properties were estimated using analytical, semi-analytical, and numerical models. Statistical assessments quantify the parameter uncertainty with 95% confidence intervals or 95% credible intervals. The model fit was evaluated using the coefficient of determination, and its uncertainty was illustrated using prediction bands.

Chapter 7: Bayesian inverse analysis of RGP case study - The Bayesian approach is applied to the RGP test results at Primrose-Wolf Lake oil sands. The in-situ horizontal stress and clay shale properties were estimated using the analytical solution. Statistical assessments quantified parameter uncertainty with 95% credible intervals. The model fit was evaluated using the coefficient of determination, and its uncertainty was illustrated using prediction bands. With new evidence of Young's modulus E, the posterior distribution of Young's modulus E can be updated through Bayesian inference.

Chapter 8: Concluding remarks: Summary and conclusions of this research, limitations, and future work.

Appendix A: Verification of the modified strain-hardening/softening model through the interpretation of triaxial testing data: triaxial compression testing data were utilized to verify the advantages of the modified strain-hardening/softening model proposed in Chapter 6 over the Mohr-Coulomb and strain-hardening/softening models.

Appendix B: Optimization algorithms for inverse analysis and interpretation of SBP tests using conventional deterministic methods: the theories of three optimization algorithms discussed in Chapter 4 are briefly introduced in Appendix B. In addition, conventional methods are used to verify the effectiveness of the results from the inverse analysis. Data from triaxial tests are also deduced to constrain the range of estimated parameters.

Appendix C: Stiffness and strength of clay shale in the plastic zones: the variations of stiffness and shear strength of clay shale in the plastic zones at all stages during RGP testing studied in Chapter 6 were illustrated.

1.7 Extent and limitations

The case study in this thesis is limited to raw data from RGP tests in the Primrose-Wolf Lake project near Bonnyville, Alberta, in 2016. The conclusions were based on the results of the RGP field test conducted in 2016 and associated laboratory testing reports.

2.0 RESEARCH BACKGROUND OF PRESSUREMETER ANALYSIS AND INTERPRETATION

As this thesis is partially organized in a paper-based style, Chapters 4, 5, and 6 are self-contained studies and consequently, some repetition of literature reviews, figures, and equations between chapters exists. This chapter provides a general background review of the research topics related to this research, while the following chapters provide more detailed reviews for topics specifically covered in those chapters.

2.1 Introduction

Since Louis Menard introduced the pressuremeter in 1955, the in-situ testing instrument has established its reputation for estimating ground properties for foundation engineering and retaining structure designs (Clarke, 1995; Mair and Wood, 1987; Schnaid, 2009). Using the measured cell pressure and volume or radial displacements, the undrained shear strength, shear modulus, in-situ horizontal stress, and soil permeability can be deduced from the pressuremeter testing curves through graphical plotting or curve-fitting methods. Sections 2.2 to 2.5 briefly review the theoretical and numerical analyses of pressuremeter tests over the past decades. Section 2.6 proposes statistical assessment methods for uncertainty quantification of parameter estimates with a pressuremeter. Section 2.7 reiterates the problems existing in previous studies.

2.2 Literature review of the pressuremeter test

Based on cylindrical expansion theory, Gibson and Anderson (1961) proposed a theoretical relationship between the volume of the measuring cell and the applied radial pressure for the Menard Pressuremeter (MPM) test. Ideally, a borehole of radius a_0 is drilled in clay under the condition of radial plane strain. The undrained pressuremeter test assumes no volumetric deformation in the plastic annulus surrounding the borehole. Ladanyi (1972) extended Gibson and Anderson's method to determine the stress-strain curve using a conventional pressuremeter test. The average mobilized strength and corresponding shear strains between any two successive pressures can be obtained by applying the proposed equations to an actual pressuremeter curve. Consequently, the deduced undrained stress-strain curve can provide the post-peak softening behavior of sensitive clays. It was concluded that the loading rate in a conventional pressuremeter test may exceed the rate used in the undrained laboratory test, which probably contributes to the higher undrained strength values.

Houlsby and Withers (1988) carried out seven full displacement pressuremeter tests in clay using a cone pressuremeter consisting of a 43.7 mm diameter pressuremeter mounted above a prototype piezo friction cone. The Hencky strain, e.g. a logarithmic strain, was chosen for the mathematical analysis because of its ability to capture large strains. The values of the undrained shear strength, shear modulus, and horizontal stress were derived using expansion-contraction curves. It was concluded that the analytical solution fits the unloading curves obtained from the cone pressuremeter tests remarkably well. The conventional derivations mentioned above are generally based on the radial plane strain, elastic, perfectly plastic soils, and undrained conditions. By using the Hencky strain definition, Shuttle (2007) proved that the cavity contraction solution provided by Houlsby and Withers (1988) and Jefferies (1988) is identical if the higher-order terms are neglected in the expansion. In addition, it was demonstrated that the unloading portion of the pressuremeter curve can provide reliable estimates of the undrained shear strength, similar to high-quality triaxial tests.

Carter et al. (1986) presented closed-form solutions for the expansion of cylindrical and spherical cavities. Plane strain and isotropic elastic and perfectly plastic soil conditions are assumed in the derivation of the pressure-expansion relationship. Compared with the analysis by Hughes et al. (1977), elastic strains in the plastic region were considered in the evaluation. The closed-form solution is applicable to the interpretation of pressuremeter tests (small strain) and installation of driven piles in cohesive frictional soil (large strain).

However, the analysis of the SBP test is still based on a simple linear elastic-perfectly plastic clay model. A more sophisticated model is required to reconcile the actual elastic modulus with the actual ground. For the MPM tests, the solution can be invalid because of the restriction on a perfect self-boring borehole. However, a complete stress-strain relation can be derived from a simple graphical procedure only under undrained conditions (Palmer, 1972); there is no restriction on the other two assumptions, namely, small strain and elastic perfectly plastic surrounding soils. It was found that the stress difference $(\sigma_r - \sigma_\theta)$ was twice the slope of the graph of cell pressure Ψ against $log(\Delta V/V)$, where σ_r and σ_θ denote the radial and circumferential stresses, respectively; ΔV represents the change in cavity volume; V represents the cavity volume. To avoid possible erratic estimates of the stress difference $(\sigma_r - \sigma_\theta)$ due to the inevitable scatter between adjacent measurements, various mathematical functions obtained by fitting the full or partial pressuremeter data can yield smooth and differentiable curves (Baguelin et al., 1972; Prevost and Höeg, 1975).

Bolton and Whittle (1999) derived a solution for the undrained expansion tests based on a power-law function $\tau = \alpha\gamma^{\beta}$, where τ *and* γ denote the shear stress and shear strain, respectively, and the values of α *and* β can be obtained from unloading and reloading loops. The cavity pressure and shear strain relation can be derived as: $p_c = p_0 + c_u\left[\frac{1}{\beta} - ln\, ln\,(\gamma_y)\ + ln\, ln\,(\gamma_c)\right]$. When $\beta = 1$, the solution is identical to the solution proposed by Gibson and Anderson (1961). In addition, a complete expression for pore water generation during undrained cavity expansion is provided. Similarly, Denby and Clough (1980) included a hyperbolic stress-strain curve (Duncan and Chang, 1970) to account for the nonlinear characteristic behavior of soil. Data from 32 self-boring tests on the northern shore of San Francisco Bay were interpreted using the Duncan-Chang hyperbolic curve. The hyperbolic stress-strain model was also implemented in the analytical solution proposed by Ferreira (1992). For the undrained pressuremeter tests, the small strain (<15%) equation for the SBP test and the large strain equation for the full displacement pressuremeter test and pre-bored pressuremeter test were derived using Cauchy's strain and Green's strain, respectively. It was concluded that the unloading data and last points of the loading portion play a major role in the methodology to interpret undrained tests, and the early part of the loading curve is assumed to not represent the natural soil response. In addition, Ferreira advised that the expansion should reach a strain level sufficiently close to the limit pressure owing to the disturbance of the pressuremeter installation.

Zhou et al. (2015) proposed a semi-analytical solution for cylindrical cavity expansion in elastic-perfectly plastic soil under a biaxial in-situ stress field. The stress and elastic-plastic boundary around the cylindrical cavity were determined by conformal mapping and complex variable theory. This semi-analytical solution can reflect the elliptical effect around the cylindrical cavity expansion, providing a theoretical tool for pressuremeter analysis in an anisotropic in-situ stress field.

Yeung and Carter (1990) conducted a numerical study of pressuremeter tests in soft clays. A two-dimensional axisymmetric finite element model was used to investigate the effects of test depth, non-homogeneity, and relative stiffness. They concluded that the interpretation of pressuremeter tests using Gibson and Anderson's solution might overestimate the undrained shear strength by 18–36% higher than the true value at deep depths. Finite membrane length, L/D ratio, and testing depth were considered in the analyses. However, the above conclusion is based on analyzing a specific two-dimensional finite element model in a Tresca material.

Fahey and Carter (1993) performed finite element analyses to simulate the behaviour of pressuremeter tests in sand using a nonlinear elastic-plastic model. It was concluded that it is important to model the whole test rather than the unload-reload loops only.

Fawaz et al. (2002) conducted pressuremeter chamber tests in sand, and deduced the geotechnical parameters using the finite element method. They pointed out that the pressuremeter modulus derived from pressuremeter chamber tests should be divided by a coefficient of α between 1/3 and 1/4 to obtain the elastic modulus.

Yu et al. (2005) presented the results of a two-dimensional finite element method (FEM) simulating an SBP test in undrained clay with critical state soil models. The effects of geometry (L/D) and over-consolidation ratio (OCR) on soil strength are discussed. Instead of the conventional total stress analysis proposed by Gibson and Anderson (1961), an effective stress formulation was employed to consider the variation in soil strength and highly overconsolidated soil. This study indicated that the pressuremeter geometry and OCR have a significant effect on the overestimation of the undrained shear strength.

To understand the consolidation characteristics of soil, Fahey and Carter (1986) conducted the strain hold test (SHT) and pressure hold test (PHT), respectively. It demonstrated that the PHT may be a useful variant on the SHT. The values of coefficient of consolidation from the field SHT, the numerical modelling of PHT, and the back analysis of trial embankment behaviour agree well. Jang et al. (2003) numerically analyzed an SHT in an SBP test with an Abaqus model. With a modification method for soil permeability, the curve of the time factor T_{50} was newly proposed. Liu et al. (2017) proposed a method for interpreting the horizontal permeability from PHTs using a regression analysis approach.

Previous researchers have made valuable contributions to the development of interpretation and theoretical analysis of pressuremeter tests. However, most of these studies focused on the deduction of closed-form solutions or parameter estimation using a deterministic method. Sections 2.3 to 2.5 will briefly discuss the theoretical and numerical solutions to pressuremeter tests, which will also be utilized as computational models in this study.

2.3 Analytical solutions to a pressuremeter test

2.3.1 Analytical solution proposed by Gibson and Anderson (1961)

A pressuremeter test can be simulated using analytical, semi-analytical, and numerical models. With the assumption of a linear elastic-perfectly plastic Tresca material around the borehole wall, Gibson and Anderson (1961) proposed the formulation of an expansion curve for an idealized pressuremeter test in clay under undrained conditions. According to Gibson and Anderson, there are three stages in this formula:

Stage 1: The pressuremeter pressure P increases from zero to the initial in-situ horizontal stress σ_{h0}, $0 \leq P \leq \sigma_{h0}$:

$$\frac{\Delta V}{V_0} = \frac{P}{G} \tag{2.1}$$

where V_0 denotes the original volume of the soil cavity, ΔV represents the increase in volume, and G indicates the shear modulus.

Stage 2: The pressuremeter pressure increases from the original in-situ horizontal stress σ_{h0} to $\sigma_{h0} + S_u$, $\sigma_{h0} \leq P \leq \sigma_{h0} + S_u$:

$$\frac{\Delta V}{V_0} = \frac{P}{G} \tag{2.2}$$

where S_u denotes the shear strength. Yield occurs at the end of Stage 2.

<u>Stage 3</u>: Plastic yielding is initiated until the termination of expansion, the relationship between the pressure and the volumetric strain $\epsilon_v = \frac{\Delta V}{V_0}$ is given by:

$$P = \sigma_{h0} + S_u \left[1 + ln\left(\frac{G}{S_u}\right)\right] + S_u ln\left[\frac{\Delta V}{V} - \left(1 - \frac{\Delta V}{V}\right)\frac{\sigma_{h0}}{G}\right] \tag{2.3}$$

where P denotes total pressuremeter pressure; V denotes the current volume of soil or rock cavity. As $G \gg \sigma_{h0}$, $\frac{\sigma_{h0}}{G} = 0$, Equation 2.3 can be simplified as (Clarke, 1995; Mair and Wood, 1987; Yu, 2006):

$$P = \sigma_{h0} + S_u \left[1 + ln\left(\frac{G}{S_u}\right)\right] + S_u ln\frac{\Delta V}{V} \tag{2.4}$$

Equations 2.3 and 2.4 are applicable for the Menard pressuremeter (pre-bored pressuremeter) test in a borehole, where the in-situ stress is totally or partially relieved in a testing pocket with the assumption of small deformations. Unlike SBP, the Menard pressuremeter cell is usually smaller than the pocket at the start of testing. Therefore, if unloading causes the cavity to yield or collapse due to stress relief, no compensation can be made for the disturbance related to the pressuremeter installation (Mair and Wood, 1987).

2.3.2 The analytical solution proposed by Jefferies (1988)

Jefferies (1988) extended the solution proposed by Gibson and Anderson (1961) to the contraction phase of an SBP test. Because there is no in-situ horizontal stress relief in an SBP testing pocket, only two stages are presented in the expansion phase:

<u>Stage 1</u>: The pressuremeter pressure increases from the original in-situ horizontal stress σ_{h0} to $\sigma_{h0} + S_u$, $\sigma_{h0} \le P \le \sigma_{h0} + S_u$:

$$\frac{a - a_0}{a_0} = \frac{(P - \sigma_{h0})}{2G} \tag{2.5}$$

where a_0 denotes the initial radius of the instrument, a represents the current radius of the device. The left side of Equation 2.5 is the cavity strain ϵ_c, which is approximately one-half of the volumetric strain $\epsilon_v = \frac{\Delta V}{V_0}$ as shown in Equation 2.2. The yielding of the borehole wall first occurs at the end of Stage 1. The denotation of a in Equation 2.5 reflects the difference in measurements from volumetric change to radius displacement with the development of the pressuremeter device. Differential radial displacements can be recorded with individual caliper arms, from which the anisotropy of in-situ horizontal stresses can be identified.

Stage 2: Plastic yielding is initiated until the termination of expansion, $\sigma_{h0} + S_u \leq P \leq P_{max}$. The relationship between pressure and the ratio of the initial radius to the current radius $\frac{a_0}{a}$ is given by:

$$P = \sigma_{h0} + S_u \left[1 + ln\left(\frac{G}{S_u}\right)\right] + S_u ln\left[1 - \left(\frac{a_0}{a}\right)^2\right] \tag{2.6}$$

Stage 3: Following the termination of expansion, the elastic displacement in the contraction phase is induced by the principal stress rotation of 90°, during the third stage $P_{max} - 2S_u \leq P \leq P_{max}$:

$$\frac{a - a_{max}}{a_{max}} = \frac{(P - P_{max})}{2G} \tag{2.7}$$

where a_{max} denotes the maximum radius of the instrument at the termination of expansion.

Stage 4: Once the maximum internal pressure has been lowered by approximately twice the shear strength of the clay ($P \leq P_{max} - 2S_u$), the plastic displacement in Stage 3 is initiated until the plastic cavity collapses (Jefferies, 1988). The relationship between P and a reported by Jefferies is:

$$P = P_{max} - 2S_u - 2S_u ln\left[\left(\frac{a_{max}}{a} - \frac{a}{a_{max}}\right)\left(\frac{G}{2S_u}\right)\right] \tag{2.8}$$

where P_{max} the maximum pressuremeter pressure; a_{max} denotes the maximum radius of the instrument. To account for the strength softening or hardening effect during unloading in the SBP contraction phase, Jefferies (1988) introduced a simple fraction β_{su} of the loading strength:

$$S_{u_c} = \beta_{su} S_u \tag{2.9}$$

Then, the pressure that initiates plastic deformation during the contraction stage becomes $P = P_{max} - (1 + \beta_{su})S_u$, and Equation 2.8 should be rewritten as (Jefferies, 1989):

$$P = P_{max} - (1+\beta_{su})S_u - S_u ln\left\{\left[1-\left(\frac{a}{a_{max}}\right)^2\right]\left[\frac{G}{(1+\beta_{su})S_u}\right]\right\} - \beta_{su}S_u ln\left\{\left[\left(\frac{a_{max}}{a}\right)^2 - 1\right]\left[\frac{G}{(1+\beta_{su})S_u}\right]\right\} \quad (2.10)$$

where β_{su} denotes softening/hardening coefficient in unloading. Using the analytical solution proposed by Jefferies (1988), displacements measured in the field can be directly applied to the equations described above after calibration corrections.

The solutions proposed by Gibson and Anderson (1961) and Jefferies (1988) were deduced from the Tresca criterion under assumed undrained conditions. Thus, the soil was modelled as an isotropic, homogeneous, and perfectly elastic-plastic material. In addition, the effects of the overburden pressure on the soil response to pressuremeter expansion and contraction were not considered. Therefore, the idealization and oversimplification of the material properties and boundary conditions in these solutions can result in non-negligible discrepancies between the measured and predicted data. Furthermore, these solutions cannot simulate anisotropic in-situ stress fields. Thus, alternative approaches should be adopted to analyze RGP tests in deep formations.

2.4 The semi-analytical solution proposed by Zhou (2015)

Zhou et al. (2015) proposed a semi-analytical solution for cylindrical cavity expansion in elastic-perfectly plastic soil under a biaxial in-situ stress field. The stress and elastic-plastic boundary around the cylindrical cavity were determined by conformal mapping and complex variable theory. This semi-analytical solution can reflect the elliptical effect around the cylindrical cavity expansion, which provides a theoretical tool for pressuremeter analysis in an anisotropic in-situ stress field. The elastic-plastic (EP) boundary for cylindrical cavity expansion is an ellipse under a biaxial in-situ stress field described by Equations 2.11 to 2.13.

$$r_b(\theta_p) = \frac{c_0(1+\beta_m)}{\sqrt{1+\left[(1+\frac{\beta m}{1-\beta m})^2-1\right]\theta_p}} \quad (2.11)$$

$$c_0 = a \times e^{(\frac{1}{2s_u})(-\left\{[1+K_\sigma]\frac{\sigma_0}{2}\right\}+\sigma_a - s_u)} \quad (2.12)$$

$$\beta_m = \frac{(K_\sigma - 1)\sigma_0}{2s_u} \quad (2.13)$$

According to Cao et al. (2001), the stress in the plastic zone can be written as

$$\sigma_r = 2s_u ln\left(\frac{r_p}{a}\right) - \sigma_a \tag{2.14}$$

$$\sigma_\theta = 2s_u - \sigma_a \tag{2.15}$$

$$\tau_{r\theta} = 0 \tag{2.16}$$

The stress in the elastic zone can be described by two complex stress functions.

$$\sigma^e{}_x + \sigma^e{}_y = 4Re[\emptyset(\xi)] \tag{2.17}$$

$$\sigma^e{}_y - \sigma^e{}_x + 2i\tau^e_{xy} = 2\left[\frac{\overline{w(\xi)}}{w'(\xi)}\emptyset'(\xi) + \psi(\xi)\right] \tag{2.18}$$

The displacement in the plastic zone can be written as

$$u_r = B_0\frac{1}{r} + \sum_{n=1}^{\infty}\left\{A_n\, sin\,\left[\sqrt{4n^2-1}\, ln\, r\right] + B_n\, cos\left[\sqrt{4n^2-1}\; ln\, r\right] \times C_n cos2n\theta\right\} \tag{2.19}$$

$$u_\theta = -\sum_{n=1}^{\infty}\left\{A_n(sin\left[\sqrt{4n^2-1}\; ln\, r\right] + \sqrt{4n^2-1}cos\left[\sqrt{4n^2-1}\; ln\, r\right]) + B_n(cos\left[\sqrt{4n^2-1}\right.\right.$$
$$\left.\left. ln\, r\right] - \sqrt{4n^2-1}sin\left[\sqrt{4n^2-1}\; ln\, r\right])\right\} \times \frac{C_n sin2n\theta}{2n} \tag{2.20}$$

The distribution of predicted displacement in the elastic zone can be expressed

$$2G(u+iv) = \frac{c_0 s_u}{\xi} \tag{2.21}$$

The semi-analytical solution proposed by Zhou et al. (2015) can be used in a biaxial in-situ stress field. However, the solution cannot simulate pressure-hold test (PHT) or strain-hold test (SHT). Although a complete pressuremeter test usually consists of one or two PHTs (SHTs), there is a limitation to utilizing the solution in such cases. To overcome the limitations of analytical and semi-analytical solutions, a numerical model was proposed to simulate a pressuremeter test.

2.5 Numerical modelling of pressuremeter tests

In addition to the analytical and semi-analytical solutions discussed above, a numerical model using the Finite Element Method (FEM) or the Finite Difference Method (FDM) can be built to simulate pressuremeter tests in clay, sand, and rock (Yeung and Carter, 1990; Yu and Netherton, 2000). A properly built numerical model can address the sources of inaccuracy from oversimplified assumptions in analytical solutions regarding the geometry, boundary conditions, and constitutive model (Yu, 2006).

In Chapters 4, 5, and 6, FDM models are built to simulate an SBP test in clay and RGP tests in clay shale. FDM models vary from a simple axisymmetric model to a full two-dimensional model, depending on the requirements of accuracy and efficiency. To limit the amount of repetition in this chapter, the modelling details are provided at the beginning of Chapters 4, 5, and 6.

2.6 Statistical assessment methods for uncertainty quantification of the identified parameters with a pressuremeter

With the analytical, semi-analytical, and numerical models discussed above, one can determine the geotechnical design parameters using curve-fitting techniques (Arnold, 1981; Denby and Clough, 1980; Gibson and Anderson, 1961; Jefferies, 1988). However, Houlsby (1989) pointed out that non-unique solutions exist using the curve-fitting method through visual comparison only. However, even if the curve fit is achieved using an optimization algorithm (Ferreira, 1992; Gaone et al., 2019; Huang et al., 1986; Levasseur et al., 2008; Obrzud et al., 2009), the non-uniqueness can not be eliminated (Zheng et al., 2021). Alternatively, if a unique solution cannot be found, uncertainty quantification can be used to constrain the variability of the identified parameters. To quantify the uncertainties from soil or rock variability, measurement errors, and modelling methods, both frequentist and Bayesian statistical methods were adopted for the parameter estimation of the pressuremeter test in this study.

2.6.1 Frequentist statistical methods

To quantify the variability in parameter estimates, a statistical assessment can be performed under the frequentist framework. The random variables generated in the optimization process can reproduce potential parameter uncertainties. The evaluation of parameters and their uncertainties in the model prediction for an inverse analysis requires confidence intervals, as discussed by Bard (1974), Ledesma et al. (1996) and Knabe et al. (2012). According to Bard (1974), the reliability and correlation of parameter estimates can be evaluated using the covariance matrix. The $100(1-\alpha)\%$ confidence intervals for the identified parameters can be deduced using the standard deviation (SD) derived from the covariance matrix. The covariance matrix and confidence intervals derived from the frequentist statistical assessment were used to evaluate the variability of the predicted horizontal stress and ground properties.

Chapter 4 presents a published paper on uncertainty quantification of parameter estimation from pressuremeter tests using a frequentist statistical method.

2.6.2 Bayesian inference methods

More than 250 years have passed since Bayes' theorem was published in 1763. The posterior predictive distribution, which is the distribution of possible unobserved values conditional on the observed values, is determined by Bayes' rule, which is expressed as:

$$p(\theta|y) = \frac{p(y|\theta)p(\theta)}{p(y)} \tag{2.22}$$

$p(\theta|y)$ denotes posterior distribution; $p(y|\theta)$ denotes likelihood, which is the distribution of the observed data conditional on the parameters; $p(y)$ represents marginal likelihood or evidence; $p(\theta)$ represents prior distribution.

Unlike the frequentist approach, whose probability is based on trials, Bayesian inference compromises prior information and observed data to determine the posterior distribution of the observed data. Bayesian inference methods based on Bayes' theorem have gained increasing attention from the geotechnical community over the last few decades (Zhang and Liu, 1995; Yan et al., 1997; Wang et al., 2010; Wang and Cao, 2013; Juang et al., 2013; Bozorgzadeh et al., 2019).

With Bayesian inference methods, prior knowledge can be integrated by using project-specific in-situ testing data. Posterior distributions of uncertain parameters can be used to update the prior knowledge. This solution can overcome the issue of limited testing data in pressuremeter (or RGP) tests by including previous knowledge and data available in past projects and research. However, a simple linear function instead of a computational model has usually been implemented in previous studies (Bozorgzadeh et al., 2019; Cao and Wang, 2014; Feng et al., 2020; Wang and Cao, 2013; Yan et al., 1997; Zhang and Liu, 1995), which prevents the Bayesian inference methods from being widely applied in geotechnical engineering practice and research. Therefore, a simple linear function cannot properly simulate a pressuremeter or an RGP test. It is usually agreed that only a strictly deduced closed-form solution or a well-built numerical model can adequately simulate a pressuremeter or an RGP test (Gibson and Anderson, 1961; Jefferies, 1988; Liu, 2015; Yeung and Carter, 1990; Yu, 2006; Zheng et al., 2021; Zhou et al., 2015). Therefore, the critical step in this study was to effectively implement a closed-form solution or numerical model in the Bayesian framework. However, Bayesian inference is usually computationally expensive compared with traditional frequentist approaches. Therefore, accomplishing the Bayesian inference task in a computationally efficient manner is a challenge for geotechnical researchers and practitioners.

Chapter 5 presents the uncertainty quantification of the parameter estimation from pressuremeter tests using a Bayesian approach.

2.7 Observations from Literature Review

Based on the discussions above, non-unique solutions to parameter estimates exist in the inverse analysis of the pressuremeter (or RGP) test using a conventional deterministic method. The non-uniqueness problems are identified and solved (or at least partially solved) in Chapter 4 using frequentist statistical assessment methods for SBP tests in clay (Zheng et al., 2021).

Another challenge in the inverse analysis of the pressuremeter (RGP) test is dealing with new data. Traditionally, new data cannot be automatically integrated into previous frequentist statistical assessments, which usually rely on a single pressuremeter (or RGP) test. With the Bayesian inference approach, one's beliefs can be continuously updated with new data. In Chapter 5, the Bayesian inference method is utilized for the uncertainty quantification of the estimated parameters and the renewal of one's belief with new data. At present, most applications of Bayesian inference in geotechnical engineering are limited to coupling with simple linear functions. One of the innovative contributions of this research is the implementation of both analytical solutions and the numerical model to simulate the pressuremeter test in the Bayesian statistical framework, rather than a simple linear function presented by other researchers. The effects of different samplers on MCMC simulations were also examined.

Consequently, the Bayesian inference approach proposed in this study is an open estimation system.

Unlike conventional pressuremeter tests, an RGP tool is usually deployed at a deep depth in reservoir caprock formations. Consequently, sources of uncertainty in RGP data are assessed from tool calibration, rock spatial variability, tool deployment, measurement errors, data acquisition, and modelling. Chapter 3 presents the data conversion, corrections, and uncertainty quantification of the RGP testing data.

Although Chapters 4 and 5 demonstrate the applicability of the statistical inverse analysis methods in self-bored pressuremeter tests in shallow grounds, the effectiveness of the inverse analysis methods on RGP tests in deep geological formations needs to be verified. Thus, Chapters 6 and 7 introduce a case study to conduct the inverse analyses of an RGP test in the Primrose-Wolf Lake oil sands field using the frequentist approach discussed in Chapter 4 and the Bayesian approach in Chapter 5. In addition to the analytical and semi-analytical models, a modified strain-softening/hardening model was implemented in the numerical modelling to simulate the RGP test. The profile of the in-situ stresses shows a good match between the measured and predicted data using the numerical model, providing increasing confidence that the methods developed in this research can be successfully applied in RGP tests in deep geological formations.

To validate the proposed modified strain-hardening/softening model, a triaxial compression test is simulated in Appendix A through interpretation of the triaxial testing data. The results are compared with those obtained using the Mohr-Coulomb model and strain-hardening/softening model.

Finally, to simulate the RGP testing with a computational model, some ideal conditions need to be assumed:1) no tool rotation occurred during the RGP test; 2) the temperature maintained inside the testing trailer can ensure that the data sensors are in a consistent working condition; 3) the magnetic field does not influence the magnetic sensor of the RGP tool; 4) the borehole is assumed to be vertical and cross-sectional with a regular smooth shape, circle, or eclipse; 5) no major breakout and spalling, or drilling-induced fractures exist around the borehole wall; 6) continuum mechanics and small strain theory are assumed in the numerical models and single-phase fluid flow in the coupling process. The surrounding medium is treated as a poroelastic or poroplastic material in a coupled fluid mechanical model.

3.0 ASSESSMENT OF SOURCES OF UNCERTAINTY IN RGP DATA

The execution of a Reservoir Geomechanical Pressuremeter (RGP) test involves a multitude of steps ranging from the initial calibration of sensors and membranes to the acquisition of test data during field programs. It is important to understand the embodied uncertainties represented by each of these phases in order to quantify the uncertainty of in-situ stress estimates based on data collected during the RGP test. Consequently, this chapter provides a reasonably detailed assessment of the origin of uncertainties that arise during tool calibration, deployment and field testing, including inherent uncertainties resulting from data processing of raw data collected from the field tests. Calculating the confidence interval using a frequentist approach requires a large population of data from multiple tests, which would generally be considered impractical or prohibitively expensive in practice. Therefore, based on the uncertainty assessment described in this chapter, a Bayesian linear regression modelling approach is used to define lower and upper bound confidence intervals for an RGP test curve.

3.1 RGP components and testing procedures

The RGP testing system is composed of three components: (i) surface control and data acquisition; (ii) wireline and gas line deployment; and (iii) downhole pressure and temperature probe. The unmodified version of the RGP is a high-pressure dilatometer (HPD) manufactured by Cambridge In-situ Ltd (Cambridge In-situ Ltd., 2012). Compared to a conventional pressuremeter, the RGP system developed by RG^2 at the University of Alberta allows in-situ downhole pressuremeter testing at depths (e.g., up to 1000 m depths) beyond conventional geotechnical engineering practice. Figure 3.1 illustrates the layout of the RGP testing system devices. The testing procedure is shown in the flowchart in Figure 3.2 .

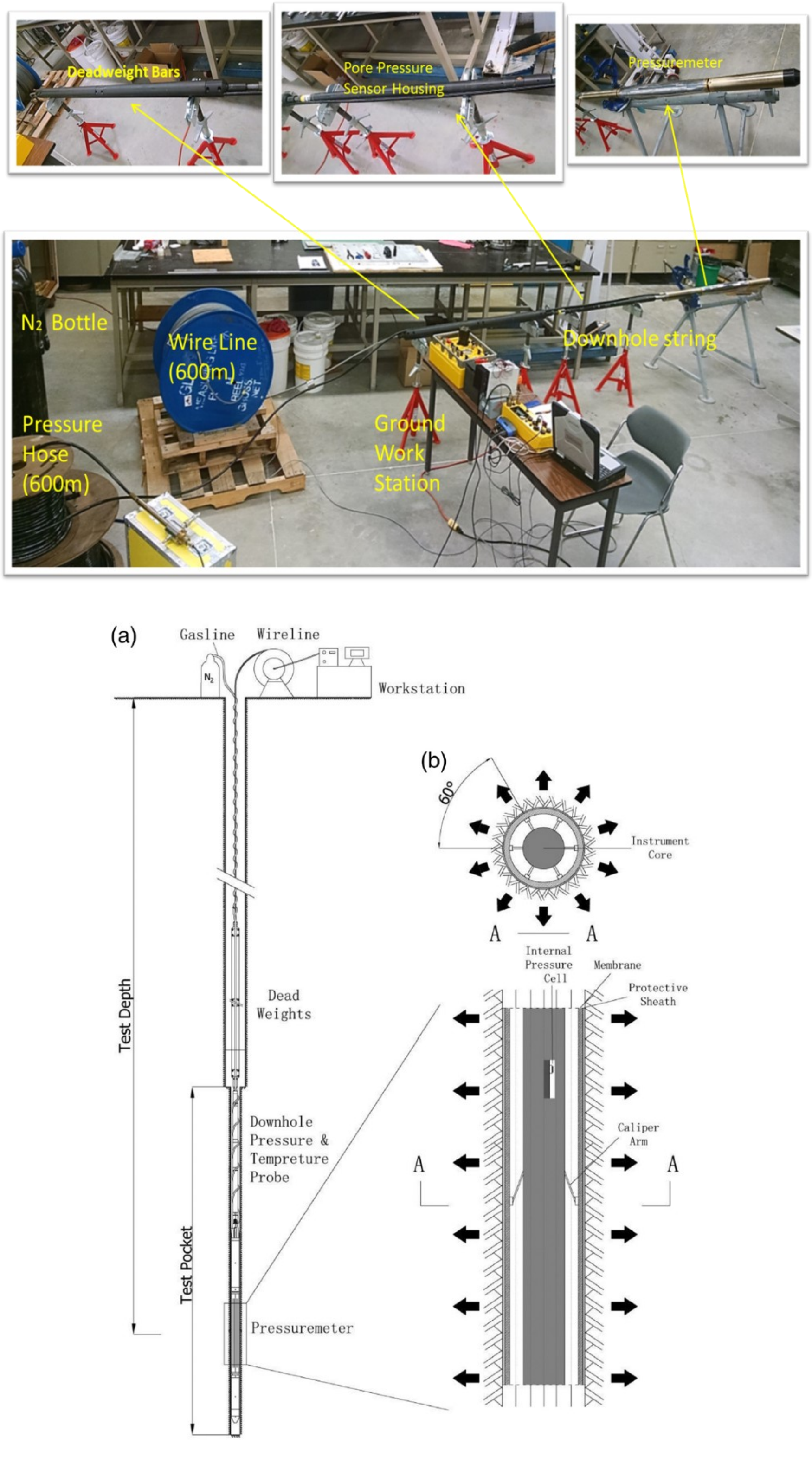

Figure 3.1 The layout of the RGP testing system devices (RG^2,2016; Liu et al., 2019)

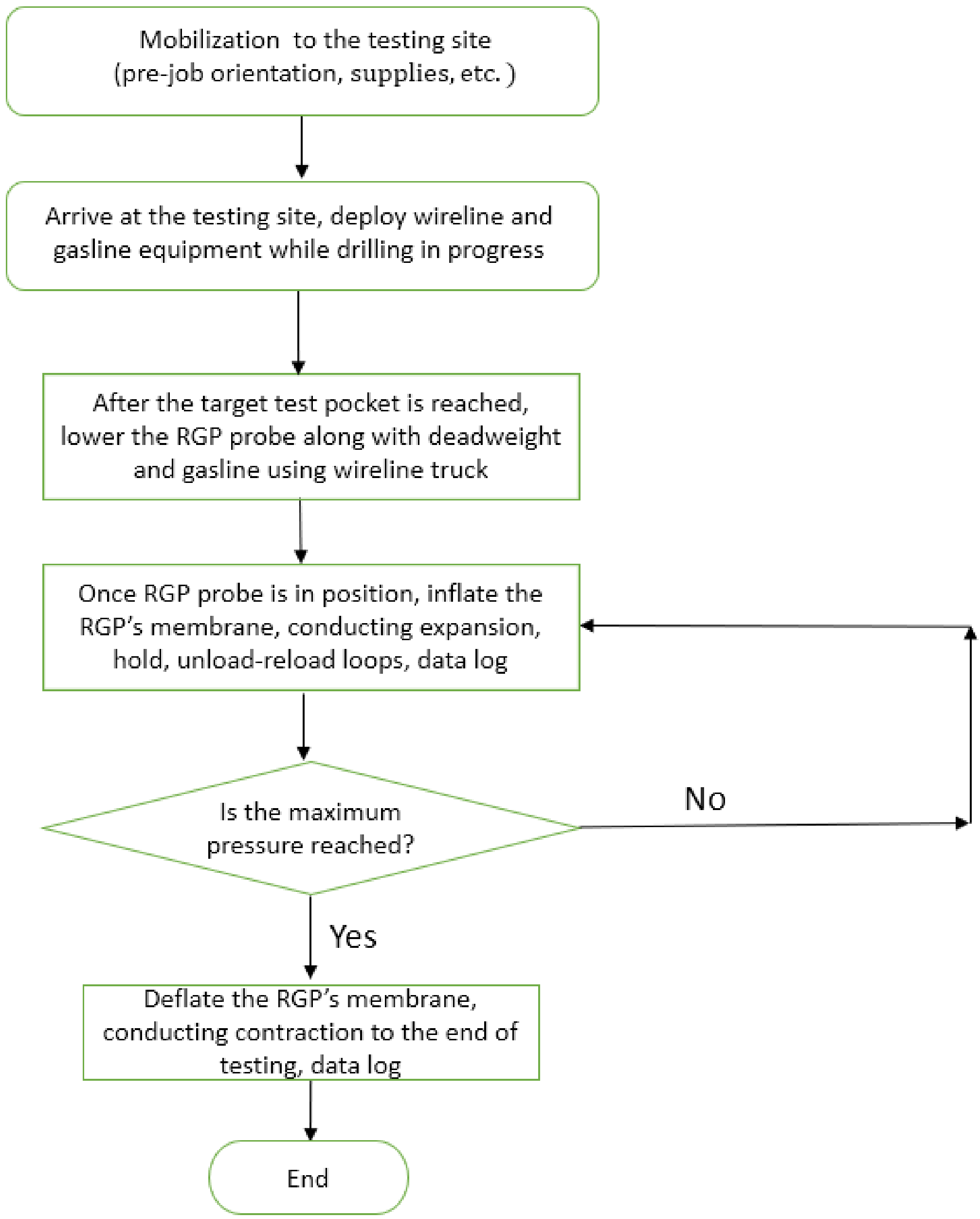

Figure 3.2 Flowchart for RGP testing process

3.2 Identification of uncertainties in the RGP test and inverse analysis

Uncertainties in an RGP test can originate from ground material spatial variability, tool calibration, tool deployment, measurement errors, and modelling. Errors existing in tool calibration, tool deployment, and measurement have two components, namely, random error and systematic error. Random errors are always present and are generally unavoidable but can be reduced by repeated measurements. Systematic errors are introduced by inaccuracies inherent to the system, such as errors in the calibration process, but can be identified and eliminated by following standardized procedures.

The primary sources of uncertainty in RGP tests are briefly discussed below.

1) **Displacement and pressure measuring transducers**: Pressure cell and strain arm transducers need to be calibrated periodically. The following measurements have been identified with experience gained from lab-based and field work with the RGP tool:
   a) <u>Random errors</u>:
      i) The non-linearity and hysteresis when using the sensitivity calibration to convert readings from volts to mm or kPa.
      ii) Zero and slope readings derived from calibration best fit line.
   b) <u>Systematic errors</u>:
      i) Air leakage in the injection line: unexpected pressure drop in the pressure line.
      ii) Imperfect calibration of a micrometre or pressure gauge: biased calibrated values for arm displacement and pressure measurement.
      iii) The switch of nitrogen bottles: unexpected pressure variations in the pressure line.
      iv) Leakage at the metering valve in the control box: an exact pressure can not be maintained.
      v) Non-centralization of the RGP at the pocket entry: distorted readings of displacement and pressure.

vi) Interference of the different environments between laboratory and field: it includes factors such as weather (precipitation, temperature, humidity) and the influence of magnetic fields, such as those from nearby metal objects.

Calibration on pressure cell and strain arm transducers is usually conducted in standard laboratory conditions. Therefore, on-site calibration should be performed considering temperature, humidity, and magnetic field variations different from the in-house laboratory environment. For instance, RGP testing in winter in Alberta may encounter extremely cold weather conditions. In such cases, errors can still be reduced to a minimal level by following proper procedures on-site (e.g., heated storage for the RGP tool and its auxiliary equipment, shortening the exposure to cold air, etc.).

2) **Membrane stiffness:** Membrane stiffness shall be subtracted from the raw pressuremeter curve in data calibration, which can be obtained by inflating the pressuremeter in free air. The expansion rate for membrane inflation in air is similar to that used in strain-controlled field tests (Schnaid, 2009). The following measurement errors during membrane inflation calibration have been identified:

a) Random errors:

i) Variation in membrane properties.

ii) The transducer slope and y-intercept on the pressure axis of the graph by inflating the pressuremeter in a steel cylinder.

b) Systematic errors:

i) Inflate the instrument in a tight steel cylinder

In practice, the membrane is usually inflated inside a thick-walled steel cylinder instead of free air due to safety concerns. In such a case, there could be not enough gap between the membrane and the steel wall. The stiffness of the membrane could be exaggerated. This calibration is crucial in soft clay.

3) **System compliance calibration:** Calibration of measuring system compliance will evaluate the control unit, line connection, and compression of the probe. During calibration, the probe is inflated inside a thick-walled steel cylinder, and pressure is raised in increments until the

maximum anticipated working pressure is reached. The change in the thickness of the membrane is also evaluated in this process. The slope of system compliance has an appreciable influence on the calibrated data for an inverse analysis and shear modulus as a result (Schnaid, 2009; Mair and Wood, 1987).

a) Random errors:
   i) Finding the best-fit slope through the loading/unloading loops.
   ii) Variation in membrane properties.
   iii) Axial movement of the membrane during expansion.
   iv) Effect of Chinese lantern strips, which are stainless steel shealths protecting the membrane from sharp edges.
   v) The eccentricity of the instrument due to the low friction between the membrane and the steel.

b) Systematic errors:
   i) Probe movement with respect to the cylinder.
   ii) Loading rate.

4) **Membrane thinning:** The membrane stretches during expansion, and the change in thickness is calculated with the assumption of a constant cross-section area.

a) Random errors:
   i) Variation in membrane thickness.
   ii) Variation of pressure applied to the membrane.

b) Systematic errors:
   i) The assumption of a circular cross-section during expansion.

5) Operator

The errors derived from observation can be mistakes in the collection of data, which are random or systematic. To eliminate systematic errors, an operator needs to be well-trained and consistent throughout the whole testing program. A detailed testing proposal shall be prepared and approved ahead of the field test. Observational errors may come from the operator/team member's fatigue on the night shift, so fatigue management should also be managed. To quantify these random errors, a deviation can be included in the statistical analysis.

6) On-site: Deployment of pressuremeter

The deployment of the pressuremeter probe is always challenging and needs teamwork with the drilling crew and downhole service operators. The deployment of the RGP tool requires four separate pieces of equipment: a drilling rig, an open-hole wireline truck, a power spooling unit, and an RGP control trailer. Several hundred meters of control line supplying nitrogen air should be handled carefully. The temperature inside the trailer should be maintained at the same temperature as it was calibrated to ensure the data sensors are in the same working conditions. Also, it was found that the magnetic sensor in the pressuremeter tool may be potentially influenced by a nearby metal objective, such as a wireline truck. Therefore, calibration of the compass inside the pressuremeter tool shall be completed before the arrival of other equipment or far away from the radius of influence.

7) On-site: Downhole testing

A full bottle of nitrogen should be used to maintain constant pressure. Unexpected pressure variations should be avoided due to the switch of nitrogen bottles during the test. To minimize the systematic errors in the expansion and unload-reload stages, continuous pressure supply by oil instead of nitrogen is suggested in the in-house RGP test. Rotating and twisting of the supply line shall be avoided while inflating the pressuremeter membrane, which could cause significant errors in the acquisition of data because the tool inclination and rotation is not considered in this research. The eccentricity due to tool movement should be considered in data correction.

8) Raw data analysis

Raw pressuremeter curves should be corrected according to the calibration procedures mentioned above. Corrections need to account for the fact that the pressure and strain arm displacements inside the membrane differ from the pressure and displacements on the borehole wall due to the expansion of the membrane. Ellipse fitting can be used in data corrections to find the best fit of the ellipse for individual arm displacements under each load increment.

9) Inverse analysis

In-situ horizontal stresses and the properties of borehole material can be derived from the inverse analysis of the RGP test. Both analytical and numerical models can be implemented in the inverse analysis to simulate the RGP testing. However, an oversimplified analytical model may cause significant errors in the inverse analysis. Conversely, a complicated numerical model may require unknown input parameters and significant computational effort. Instead of finding a unique 'true' value, statistical assessments on derived parameters can be used to quantify the estimation uncertainty.

For this research, both deterministic and Bayesian inference methods will be applied to quantify the uncertainties propagated from calibration, measurement and analysis errors described above. It is recognized that additional sources of uncertainty in RGP test interpretations can arise from issues associated with inclined boreholes, tool rotation, borehole disturbance, and material heterogeneity. These are beyond the scope of the current research but are recognized as important and identified as topics for future research.

3.3 Analysis of raw data using a deterministic approach

Raw data retrieved from the RGP test need to be converted to arm displacements and cell pressure, followed by data corrections with the instrument calibration data. According to the pressuremeter working instructions (Cambridge In-situ Ltd., 2012), strain arm gauges and pressure transducers, membrane stiffness and thinning, system compliance, and compass orientation shall be calibrated prior to conducting an RGP in-situ test. Then, calibration data can be used to correct the arm displacement and cell pressure.

3.3.1 Collection of raw data from RGP tests

Raw data for radial expansion of the membrane are obtained from electrical signals collected from strain gauges embedded in the six internal arms during an RGP test. The raw data are in units of volts, which can be converted into six independent arm displacements with readings of zero and slope through micrometre calibration. For the field data analyzed in this study, the first pocket of the RGP tests was drilled in the Westgate Formation, 259 m below the ground surface. In total, 557 separate recordings of electrical signals from six arm gauges were collected and are plotted in Figure 3.3. Similarly, the data for the RGP tests conducted in the Joli Fou and Clearwater Formations are illustrated in Figure 3.4 and Figure 3.5 , respectively.

The raw data illustrated in Figures 3.3, 3.4, and 3.5 cannot be directly used in the RGP interpretation and inverse analysis. Through the conversion by a linear regression model, cell pressure and arm displacements can be obtained for further data corrections and interpretation of the RGP tests.

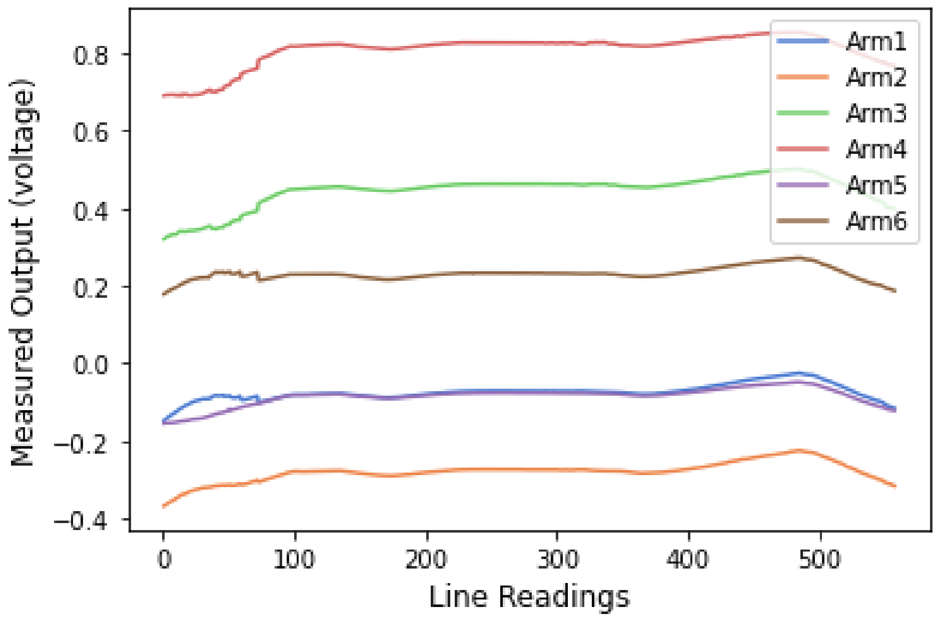

Figure 3.3 Signal output from the six arms for RGP testing in the Westgate Formation

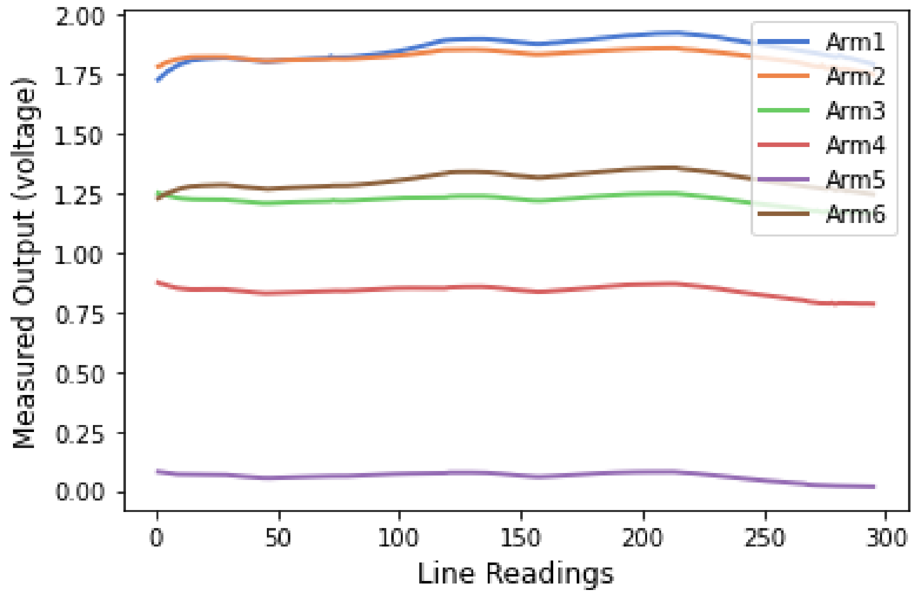

Figure 3.4 Signal output from the six arms for RGP testing in the Joli Fou Formation

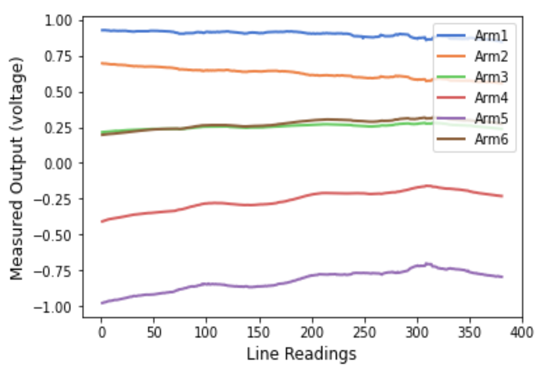

a)

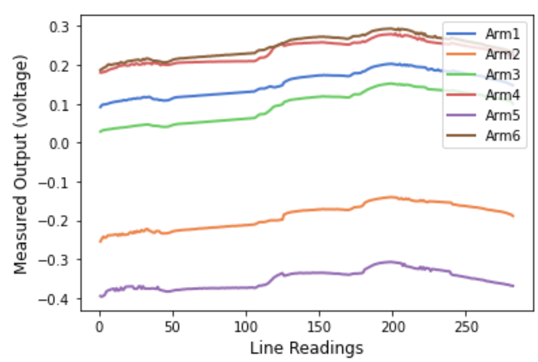

b)

Figure 3.5 Signal output from the six arms for RGP testing in the two tested intervals in the Clearwater Formation: a) Black Shale and b) Grey Shale.

3.3.2 Data conversion from signals to arm displacements and cell pressure

To find the relationship between the strain gauge output and arm displacement, a micrometre was mounted above each arm, and the readings of the voltage output from the strain gauge were recorded. With the data points from micrometre readings and voltage output, the zero and slope of the best fit straight line can be obtained from the least square linear regression model, which is:

$$y_i = b_s + m_s x_i \tag{3.1}$$

$$m_s = 1/\beta_s, \;\; b_s = \alpha_s/\beta_s$$

where α_s and β_s denote the zero (y-intercept) and slope (sensitivity) in a micrometre or pressure cell calibration plot, respectively; x_i represents the signal voltage output, and y_i represents the arm displacement or total cell pressure (TCP). The values of α_s and β_s for six arm strain gauges and two pressure cell transducers are listed in Table 3.1. Then, arm displacements and TCP can be calculated with the voltage outputs from strain gauges and pressure cell transducers using the least square linear regression model shown in Equation 3.1.

The uncorrected displacements of individual arms for RGP testing in the four geological formations, illustrated in Figures 3.6, 3.7, 3.8 and 3.9 need to be corrected for membrane stiffness and system compliance effects on arm displacements and cell pressures.

Table 3.1 The slope (sensitivity) and zero (y-intercept) of strain gauges and pressure transducers

Slope and zero	Arm 1	Arm 2	Arm 3	Arm 4	Arm 5	Arm 6	TPC A*	TPC B*
β_s (mV/mm or mV/MPa*)	273.5	288.9	286.6	276.5	241.7	273.5	98.3	116.3
α_s (mv)	-1465.2	-1898.9	-1786.6	-1718.9	-2341.8	-1629.6	60.6	-78.4

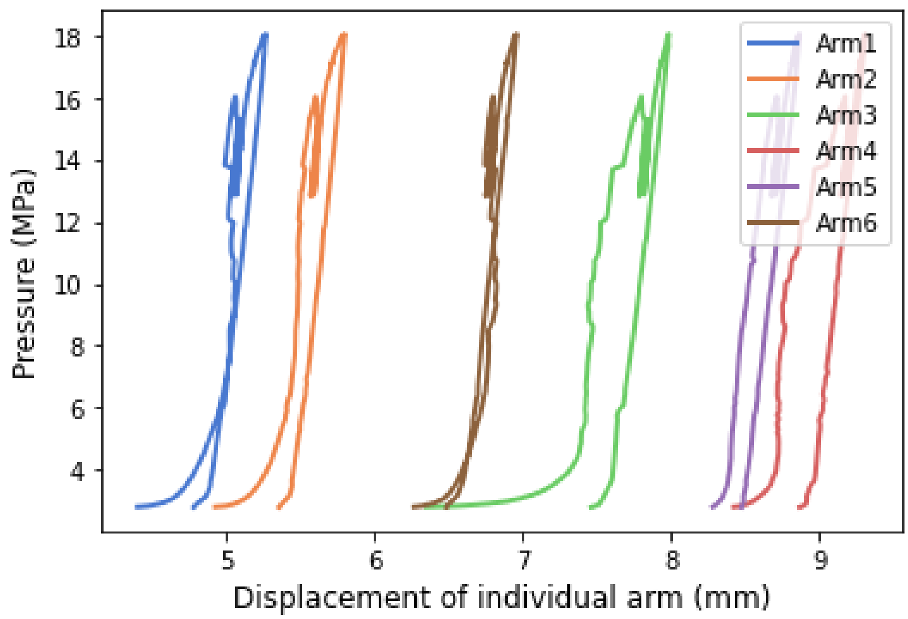

Figure 3.6 Uncorrected curves for RGP testing in the Westgate Formation

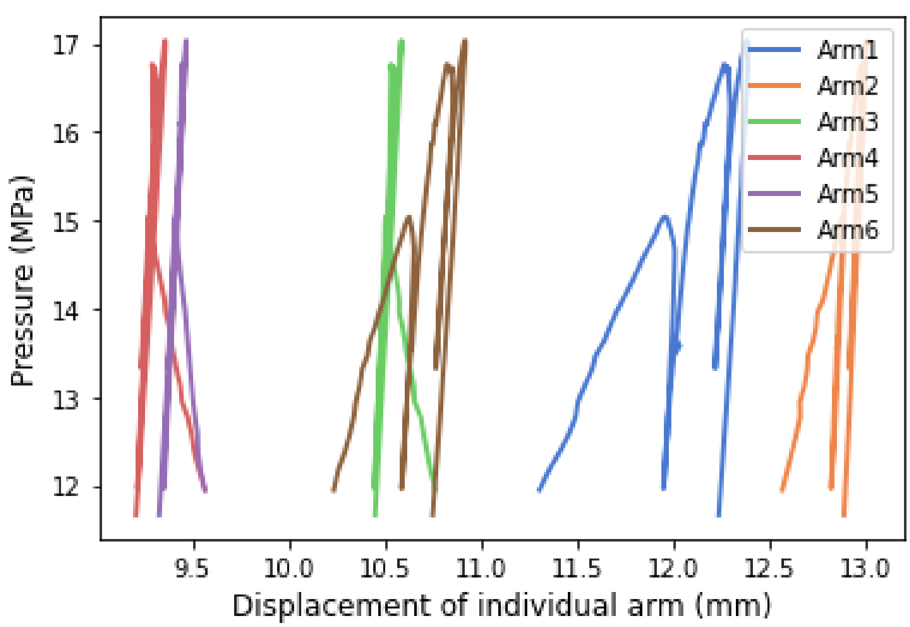

Figure 3.7 Uncorrected curves for RGP testing in the Joli Fou Formation

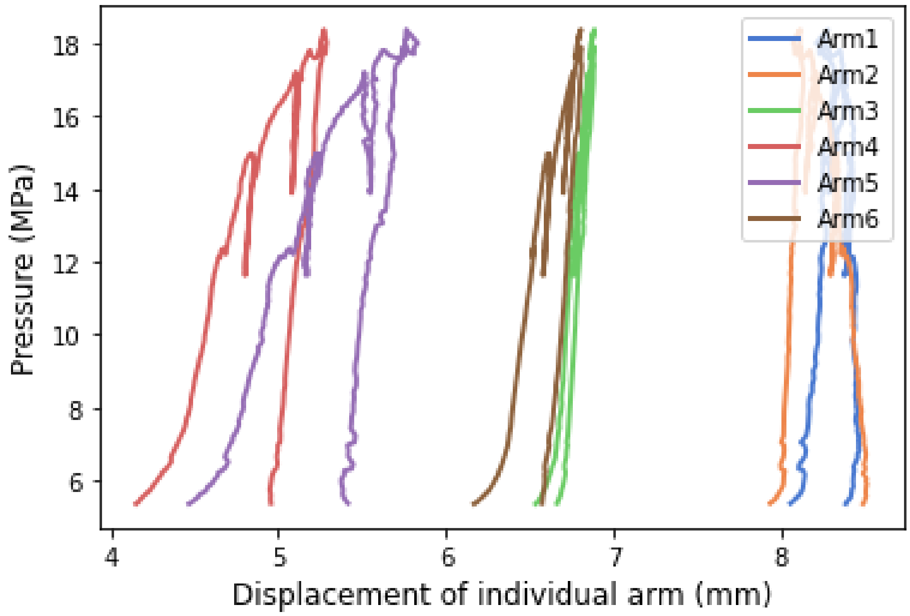

Figure 3.8 Uncorrected curves for RGP testing in the Clearwater black shale Formation

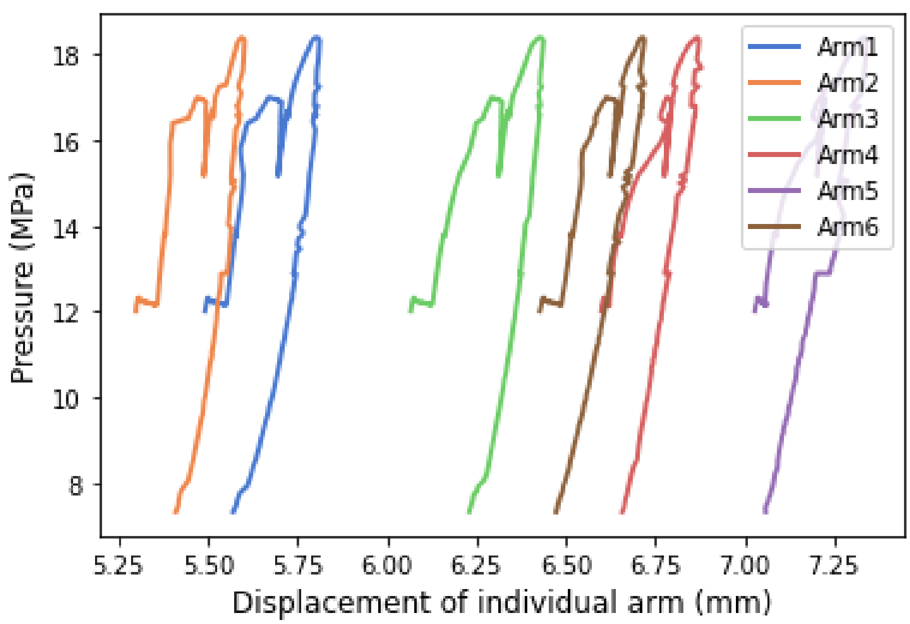

Figure 3.9 Uncorrected curves for RGP testing in the Clearwater grey shale Formation

3.4 RGP testing curves corrected to system compliance and membrane stiffness

The instrument will deform while the pressure is internally applied during a pressuremeter test (Cambridge In-situ Ltd., 2012). To obtain calibration data due to instrument deformation, the RGP probe was inflated in a steel cylinder. Figure 3.10 illustrates that the mean value of slope, derived from system compliance calibration (Liu, 2017), is 1.3 mm/GPa with an error margin of 0.4 mm/GPa.

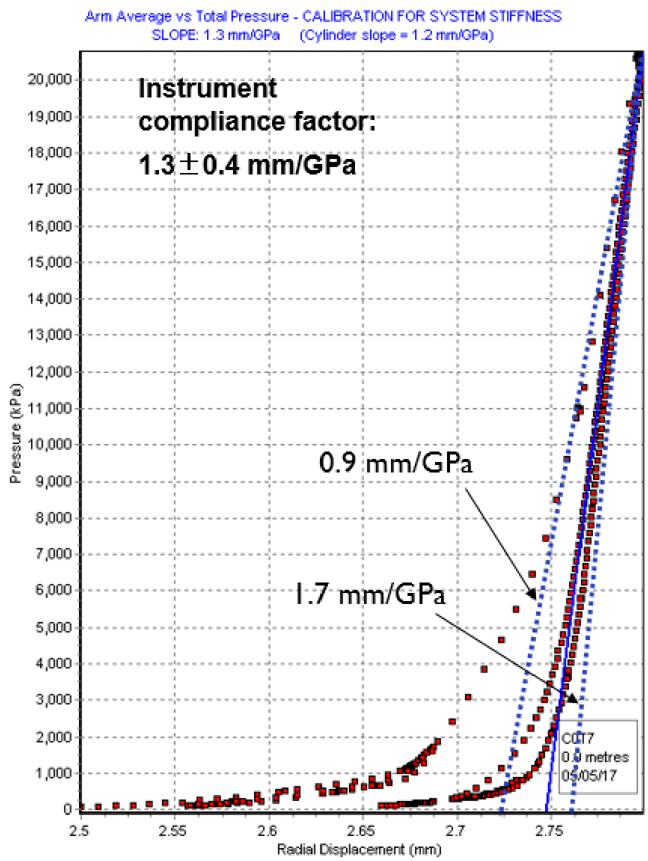

Figure 3.10 RGP system compliance calibration (Liu, 2017)

To obtain membrane correction information, the RGP instrument was pressurized inside a steel cylinder instead of “free air” for safety reasons. The steel cylinder fits closely at the ends of the membrane but allows a large expansion elsewhere (Cambridge In-situ Ltd., 2012). Figure 3.11 illustrates that the zero and slope corrected to membrane stiffness are 0.0352 MPa and 0.0322 MPa/mm (RG^2, 2016), respectively.

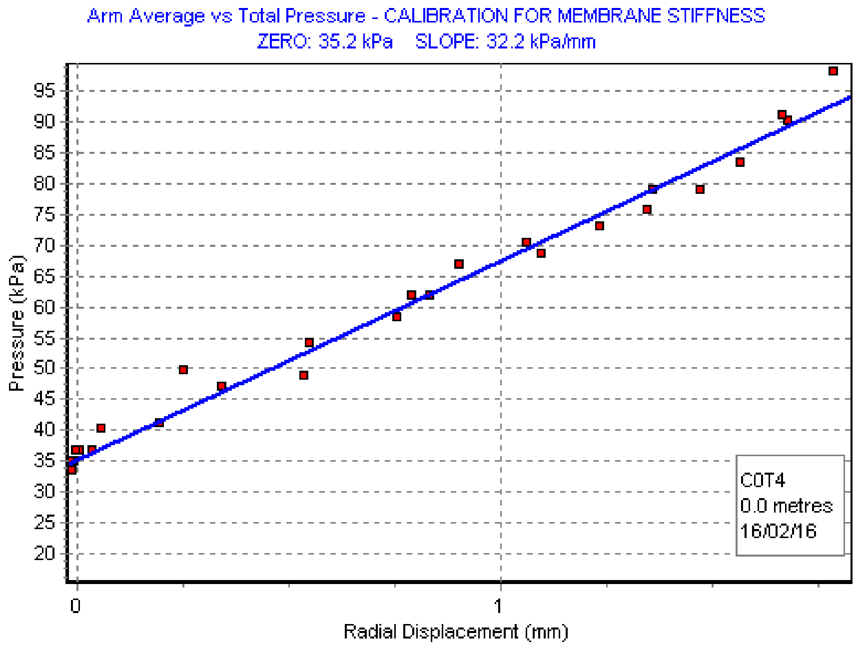

Figure 3.11 RGP membrane stiffness calibration (RG[2], 2016)

With these system compliance and membrane stiffness calibrations, the uncorrected RGP testing curves shown in Figure 3.6 to Figure 3.9, can be corrected and are shown in Figure 3.12 to Figure 3.15.

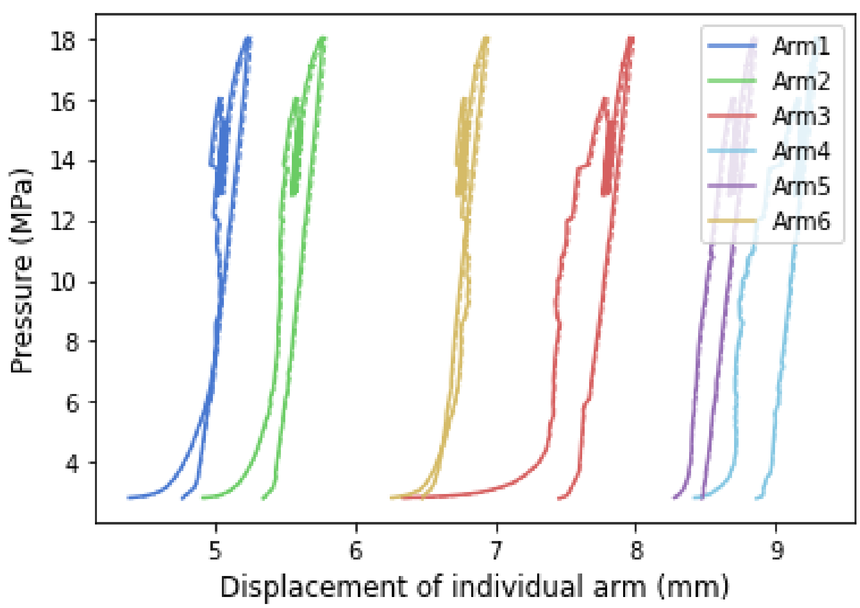

Figure 3.12 Curves corrected to system compliance and membrane stiffness for RGP testing in the

Westgate Formation. The dashed line is the uncorrected curve, and the solid line is the corrected curve.

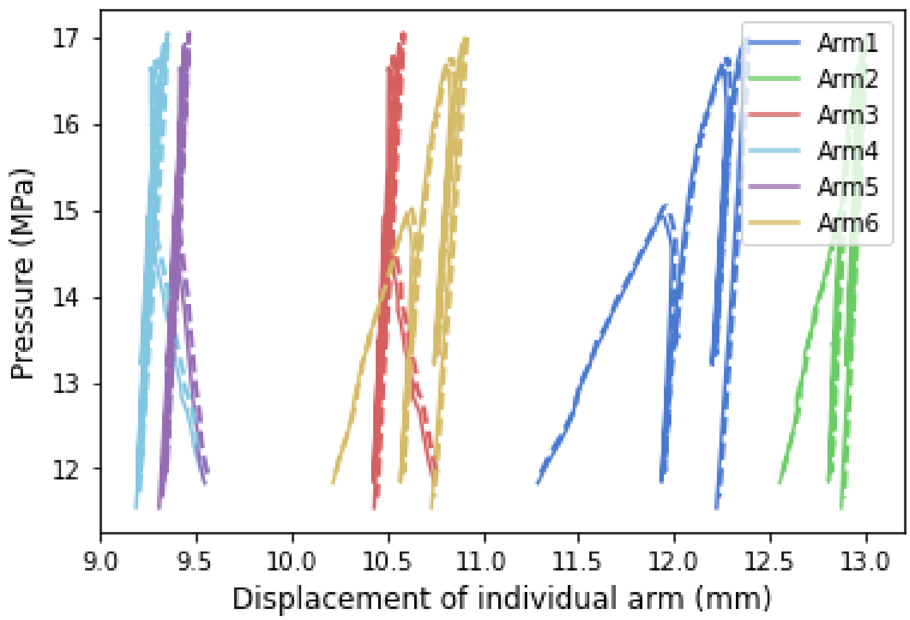

Figure 3.13 Curves corrected for system compliance and membrane stiffness for RGP testing in the Joli Fou Formation. The dashed line is the uncorrected curve, and the solid line is the corrected curve.

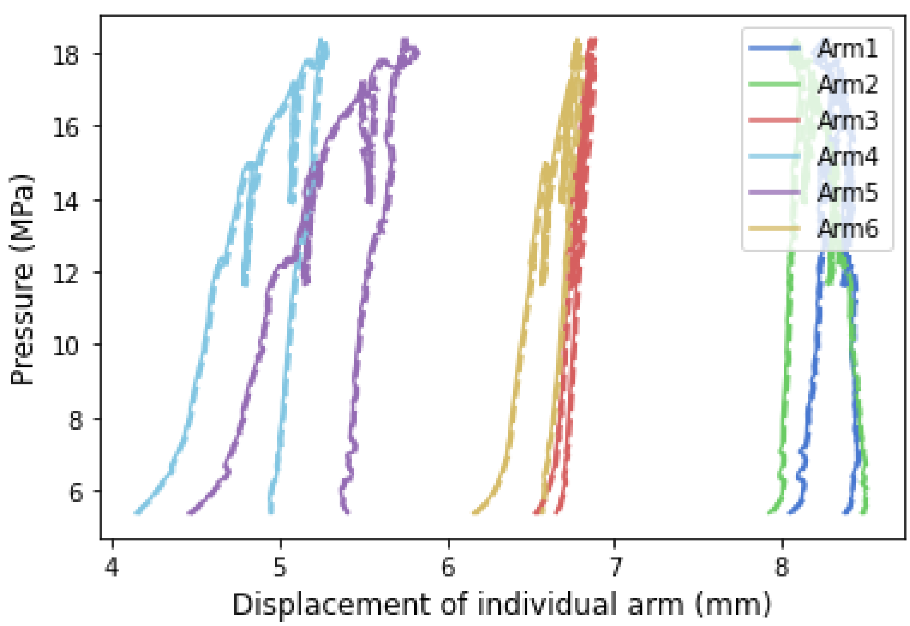

Figure 3.14 Curves corrected for system compliance and membrane stiffness for RGP testing in the Clearwater black shale Formation. The dashed line is the uncorrected curve, and the solid line is the corrected curve.

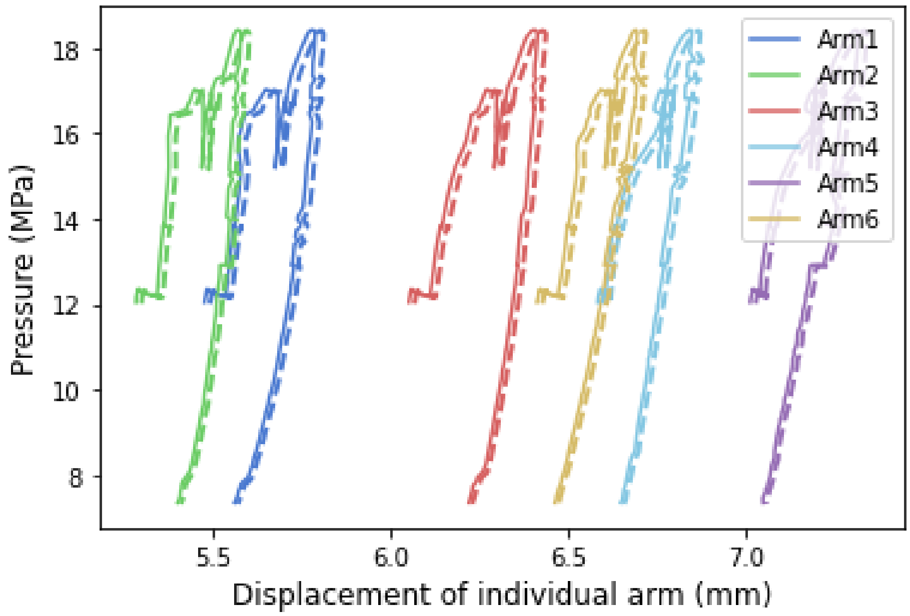

Figure 3.15 Curves corrected for system compliance and membrane stiffness for RGP testing in the Clearwater grey shale Formation. The dashed line is the uncorrected curve, and the solid line is the corrected curve.

It is noticed that the differences between corrected (solid) and uncorrected (dashed) lines are quite small but there is a notable shift from solid line to dashed line for the Clearwater grey shale. It may indicate the serverity of borehole disturbance due to the existence of weaker layers and bentonitic layers in Clearwater grey shale Formation (Zadeh, 2016).

Data correction to system compliance can substantially reduce estimation errors, especially when measuring the shear modulus of hard rocks (Cambridge In-situ Ltd., 2012). Additional corrections prior to formal pressuremeter interpretation are required to account for membrane thinning and tool eccentricity that may exist during the RGP measurement.

3.5 Arm displacement corrections to membrane thinning and ellipse fitting

As the thickness of the pressuremeter membrane changes while being stretched during a test, data correction to membrane thinning shall be further carried out. To consider membrane thinning, the calculation (Cambridge In-situ Ltd., 2012) is presented below:

$$E_m = \sqrt{[(b_m - t_m)^2 + d_m(2a_m + d_m)]} - (b_m - t_m) \tag{3.2}$$

where E_m denotes the actual expansion of the membrane; a_m denotes the internal radius of the membrane at rest; b_m denotes the external radius of the membrane at rest; d_m represents the measured movement of the strain arm; t_m represents the thickness of the stainless-steel sheath strips.

To calculate the arm displacements at any azimuth, the deformed shape of the borehole subjected to pressuremeter loading pressure can be fitted with an ellipse. Then, the arm displacements $0^\circ \sim 360^\circ$ can be easily obtained by subtraction of the previous ellipse from the present one corresponding to each loading increment. Schwerzmann et al. (2006) used general equations for circles and ellipses to fit eight positions of caliper arms. Figure 3.16 illustrates the schematic diagram of the expanded arms of an eccentric calliper inclinometer probe in a rotated elliptic borehole. Thus, the problem of eccentricity (refer to Figure 3.16) encountered in the corrected arm displacements can be solved with the ellipse fitting approach.

The equation of an ellipse in the polynomial form:

$$Ax^2 + Bxy + Cy^2 + Dx + Ey = 1 \tag{3.3}$$

With coordinates of the ellipse centre relative to the calliper arm centre:

$$x_0 = \frac{2CD - BE}{B^2 - 4AC}, y_0 = \frac{2AE - BD}{B^2 - 4AC} \tag{3.4}$$

$$tan2\alpha = \frac{B}{A - C} \tag{3.5}$$

and

$$a = \sqrt{\frac{2(1+F)}{A+C+\frac{B}{\sin(2\alpha)}}}, b = \sqrt{\frac{2(1+F)}{A+C-\frac{B}{\sin(2\alpha)}}} \tag{3.6}$$

where

$$F = Ax_0^2 + Bx_0y_0 + C \tag{3.7}$$

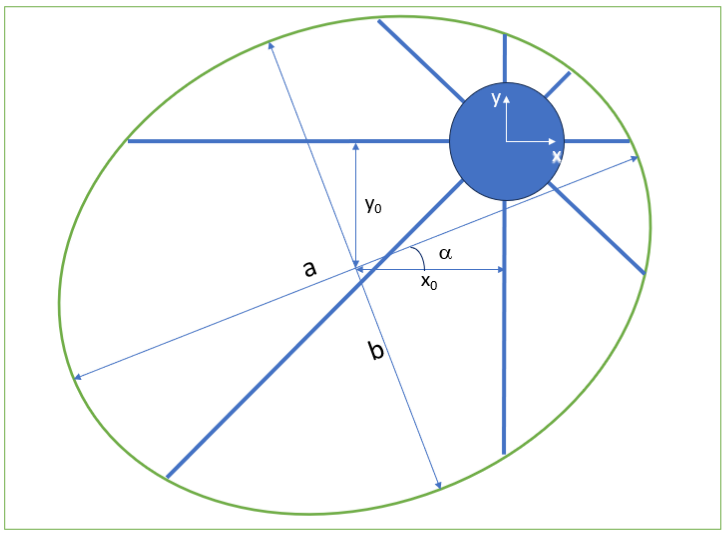

Figure 3.16 Schematic diagram of the expanded arms of the calliper inclinometer probe in an elliptical borehole (adapted from Schwerzmann et al., 2006)

Substituting the corrected arm displacements shown in Figure 3.12 to Figure 3.15 into Equations 3.3 to 3.7, a system of six linear equations for the five coefficients can be derived. To solve the overdetermined linear equations, Matlab and AutoCAD VBA codes are programmed to find the best-fit ellipse for six arm readings. However, the shape of the deformed borehole could be irregular. The assumption of an elliptical borehole may introduce additional errors.

Using the ellipse curve fit function, the deformed borehole radii can be plotted at any azimuth (refer to Figure 3.32 to Figure 3.35). This permits both the analytical and numerical models to use the deformed borehole radii in workflows to determine the best estimates of geotechnical properties and in-situ stresses. However, as described in Section 3.2, uncertainties propagated from tool calibration, deployment and data collection should be considered in data corrections. The analysis of raw data discussed in Section 3.3 is conducted with a deterministic approach, which cannot quantify the uncertainties in data corrections. Therefore, a Bayesian inference approach is adopted to address this issue.

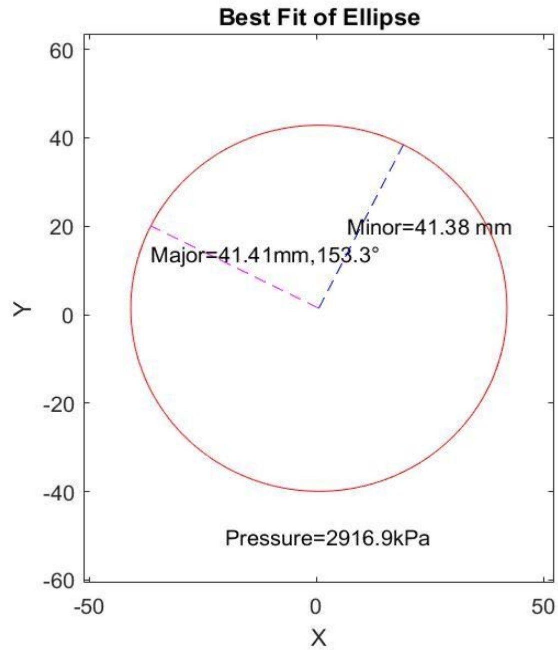

Figure 3.17 The best fit of ellipse with the corrected displacements of the six arms for Westgate Formation

3.6 Analysis of raw data using Bayesian inference methods

Sections 3.3 to 3.5 discuss the application of a deterministic approach in the data conversion and corrections for an RGP test. To account for the uncertainty owing to tool calibration, deployment disturbance and measurement errors, uncertainty quantification should be carried out under a statistical framework. Traditionally, frequentist approaches prevail in the geotechnical engineering community, but in recent years, Bayesian inference methods have been gaining momentum (Cao and Wang, 2014; Feng et al., 2020). Unlike the frequentist approaches, whose probability is based on many trials, Bayesian inference integrates prior knowledge and project-specific information (geological maps, previous test reports, and even personal judgment). The posterior predictive distribution, that is, the distribution of possible unobserved values conditional on the observed values, can be characterized under a Bayesian framework. Besides the deterministic method discussed above, the raw RGP data can also be converted and corrected using a Bayesian inference approach, as discussed in Chapter 5.

3.6.1 Bayesian linear regression modelling on micrometre calibration data

The raw calibration data plotted in Figure 3.3, Figure 3.4 and Figure 3.5 is used to convert sensor voltage measurements into arm displacements. The calibration conversion equation can be treated in a Bayesian statistical way by quantifying the uncertainty propagated from micrometre calibration. The variables, $\alpha_s \; and \; \beta_s$, shown in Figure 3.18 represent the y-intercept and slope of the calibration equation, respectively. The values of $\alpha_s = -1310.9 \; mV \; and \; \beta_s = 234.2 \; mm/mV$ can be treated as prior information. This information is used to carry out further statistical inference on the data points shown in Figure 3.18 with a Bayesian linear regression model. The Bayesian linear regression model can be expressed as:

$$y \sim N(\mu_s = b_s + m_s x, \sigma_s = \varepsilon_s) \tag{3.8}$$

$$m_s = 1/\beta_s, \;\; b_s = \alpha_s/\beta_s$$

where y denotes the arm displacements following a Gaussian distribution with mean $b_s + m_s x$, and standard deviation ε_s. The standard deviation introduced in Equation 3.8 provides a measure of the data noise σ_s while converting raw data into arm displacements.

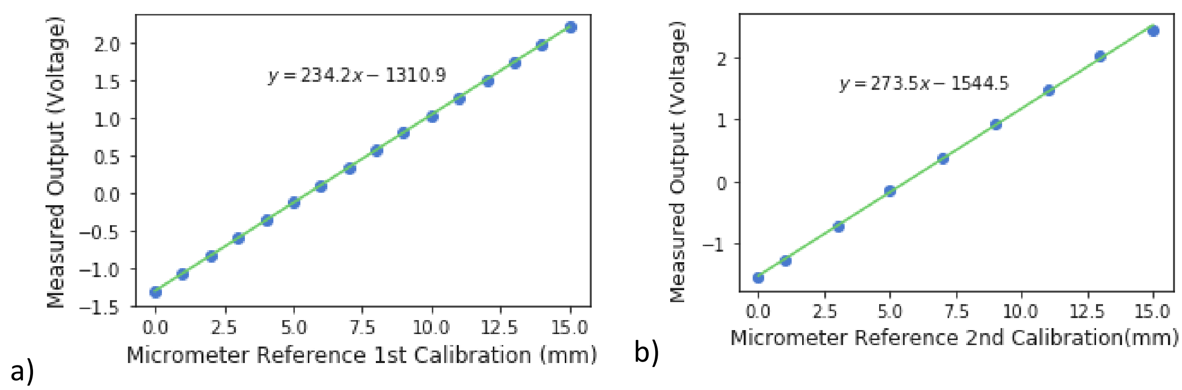

Figure 3.18 Linear regression of data points from a) first and b) second calibrations for Arm1

According to the working instructions (Cambridge In-situ Ltd., 2012), 0.5% of the sensor sensitivity is taken as an acceptable limit for hysteresis. Correspondingly, a standard deviation of 0.024 mm has been presumed as the random error limit in the measurement of arm deflection. For Arm1, about 50% of the random error limit, 0.012 mm, is used for the Bayesian inference.

There is no prior knowledge of the initial systematic error. For the current research, this has been conservatively estimated to be 0.002 mm or about 1/6 of the assigned random error. The standard deviation σ_s is the sum of random and systematic errors (Equation 3.9). The data points in Figure 3.18 (1st calibration) are used as evidence to update the standard deviation σ_s:

$$\sigma_s = \varepsilon_{random} + \varepsilon_{systematic} = 0.012 + 0.002 = 0.014\,mm \qquad (3.9)$$

It has been argued that prior knowledge of systematic error is very subjective (Gelman et al., 2014), but for this research, it is assumed that it doesn't violate the Bayesian theorem because the data points (evidence) from micrometre calibration will compromise the prior knowledge. The more the data points are, the weaker the prior knowledge will become.

Chapter 7 provides additional discussion on the application of the No-U-Turn (NUTS) sampling algorithm for random sampling in Monte Carlo Markov Chain (MCMC) simulation.

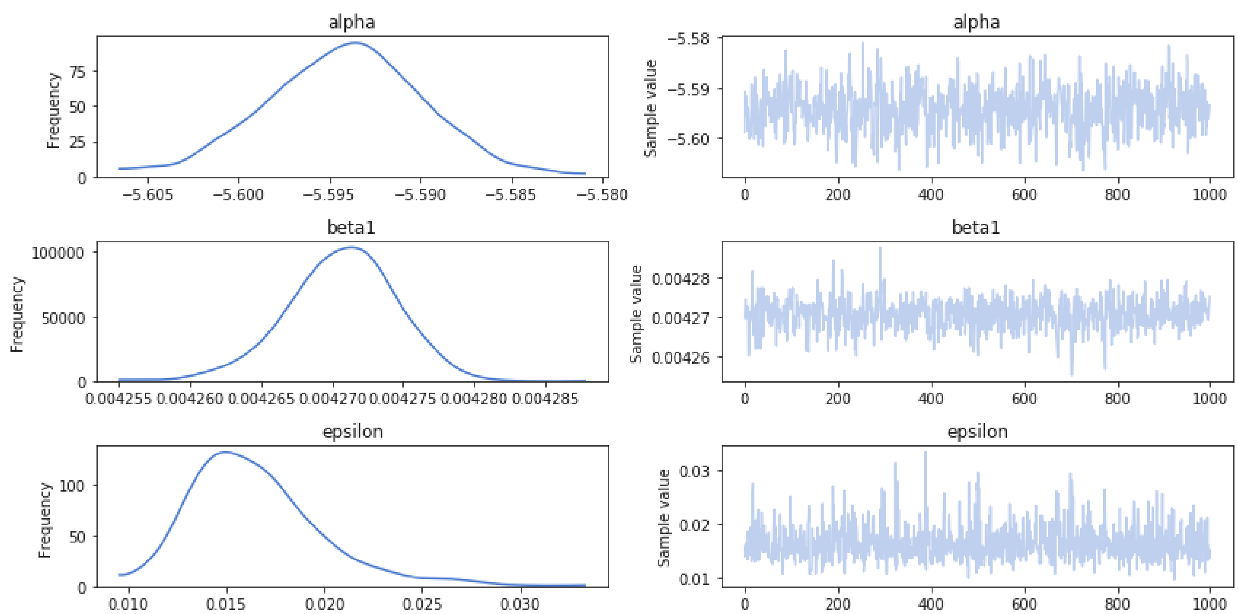

Figure 3.19 KDE (Kernel Density Estimation) and trace plots after Bayesian inference using the first calibration data of Arm1.

The results from the Bayesian inference on the first calibration data (evidence) are shown in Figure 3.19 and summarized in Table 3.2. Table 3.2 shows that the standard deviation of arm displacement is updated from 0.014 mm to 0.0165 mm (mean epsilon). Then, the updated standard deviation of 0.0165 mm is used as prior knowledge for the following Bayesian inference on the second calibration data points shown in Figure 3.18b.

Table 3.2 Posterior parameters after Bayesian inference using the first calibration data of Arm1

zero and slope	mean	sd	mc_error	hpd_2.5	hpd_97.5
b_s (mm)	-5.59	4.33e-03	1.62e-04	-5.60	-5.59
m_s (mm/mV)	4.27e-03	3.88e-06	1.52e-07	4.26e-03	4.28e-03
$epsilon$ (mm)	1.65e-02	3.33e-03	1.16e-04	1.06e-02	2.32e-02

Similarly, kernel density estimation (KDE) and trace plots from Bayesian linear regression on the second calibration data (evidence) are illustrated in Figure 3.20 and summarized in Table 3.3, respectively.

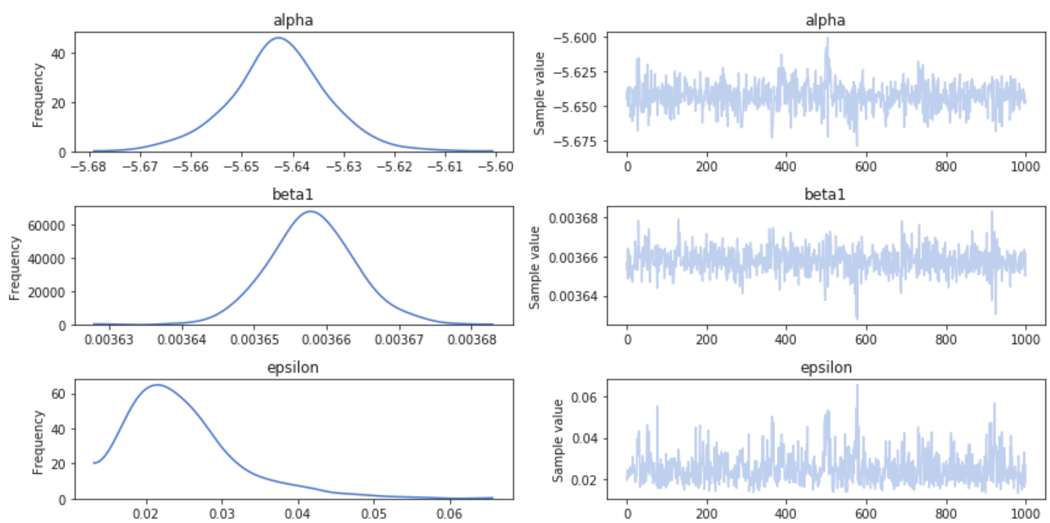

Figure 3.20 KDE and trace plots after Bayesian inference using the second calibration data of Arm1

Table 3.3 shows that the standard deviation of arm displacement is updated from 0.0165 mm to 0.0249 mm (mean epsilon), which can be used as the posterior knowledge for the raw data conversion using Equation 3.8.

With the Bayesian inference method introduced above, the standard deviations for other strain arms can be updated similarly. The standard deviations for Arms 1 to 6 after Bayesian inference using two calibration data are illustrated in Figure 3.21.

Table 3.3 Posterior parameters after Bayesian inference using the second calibration data of Arm1

zero and slope	mean	Std Dev.	mc_error	hpd_2.5	hpd_97.5
b_s (mm)	-5.64 (-5.59)	9.60e-03 (4.33e-03)	4.32e-04 (1.62e-04)	-5.66 (-5.60)	-5.62 (-5.59)
m_s (mm/mV)	3.66e-03 (4.27e-03)	6.16e-06 (3.88e-06)	2.51e-07 (1.52e-07)	3.65e-03 (4.26e-03)	3.67e-03 (4.28e-03)
$epsilon$ (mm)	2.49e-02 (1.65e-02)	7.27e-03 (3.33e-03)	3.65e-04 (1.16e-04)	1.39e-02 (1.06e-02)	4.04e-02 (2.32e-02)
(###): Numbers in parenthesis are the original posterior parameters from Table 3.2					

Note that the initial standard deviations for the six arms follow a uniform distribution due to a lack of prior information. After updating with first and second micrometre calibration data (the evidence), the posterior standard deviations tend to follow a Gaussian distribution. The standard deviations inferred from the second calibration are used to predict the arm displacements with the signals (raw data) collected from the RGP test.

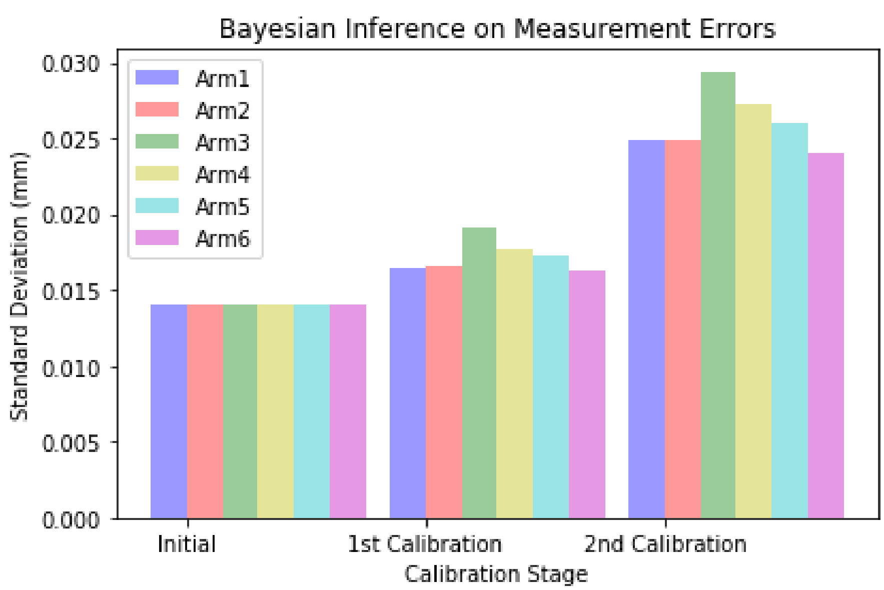

Figure 3.21 Bayesian inference on the standard deviations using micrometer calibration data

3.6.2 Bayesian linear regression modelling on the data from total pressure cell calibration

By inflating the pressuremeter inside a steel cylinder, readings on the transducer voltage output can be plotted in Figure 3.22. Similar to the strain arms, the sensitivity of the pressure measuring transducer can be determined by the best fit line through data points retrieved from the total pressure cell (TPC).

Similar to strain arms, the standard deviation $\sigma_s = 1.25\ kPa$ can be considered as a random error in the measurement of pressure. Also, there is no prior knowledge of the initial systematic error of the internal pressure transducer. A value of 0.75 kPa is assigned to the initial systematic error, which will be updated by the following two calibration tests.

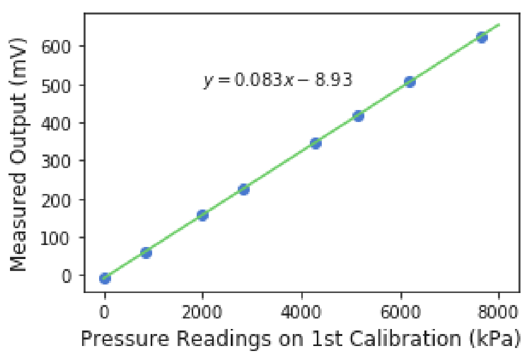

a)

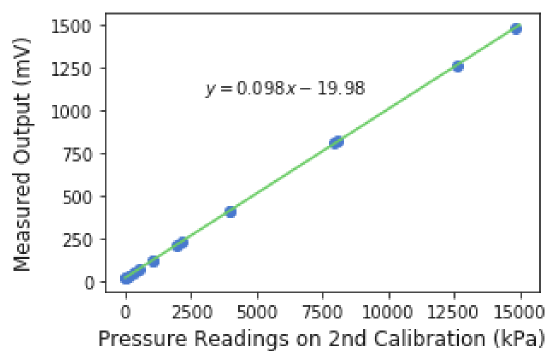

b)

Figure 3.22 Linear regression of data points from first (a) and second (b) total pressure cell calibrations

The standard deviation σ_s is formulated in Equation 3.10:

$$\sigma_s = \varepsilon_{random} + \varepsilon_{systematic} = 1.25 + 0.75 = 2.0\ kPa \tag{3.10}$$

Using the same procedure described in §3.6.1, the posterior standard deviations obtained from the Bayesian inference for the TPC are illustrated in Figure 3.23.

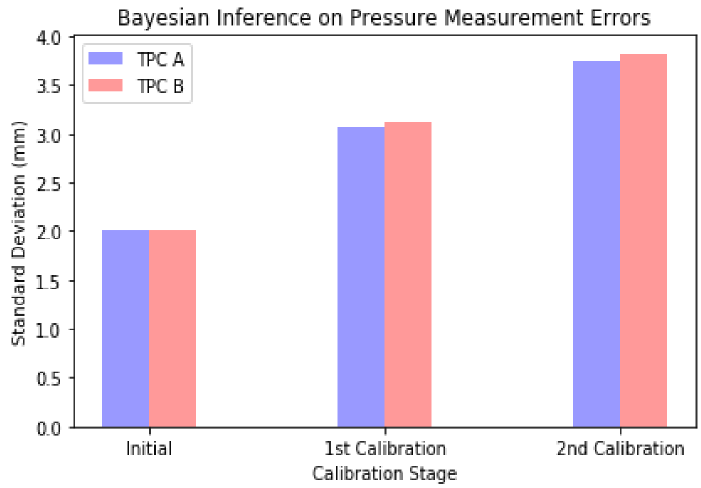

Figure 3.23 Bayesian inference on TPC calibration data

The posterior standard deviations in Figure 3.21 and Figure 3.23 are summarized in Table 3.4. The values of the second micrometre/pressure calibration will be used for further Bayesian analysis to account for uncertainty from membrane stiffness, system compliance and membrane thinning.

Table 3.4 Posterior standard deviations of strain arms and TPC after Bayesian inference

Standard Deviation σ_s	Arm1 (mm)	Arm2 (mm)	Arm3 (mm)	Arm4 (mm)	Arm5 (mm)	Arm6 (mm)	TPC A (kPa)	TPC B (kPa)
Initial	0.014	0.014	0.014	0.014	0.014	0.014	2.0	2.0
First micrometre/TPC calibration	0.017	0.017	0.019	0.018	0.017	0.016	3.06	3.12
Second micrometre/TPC calibration	0.025	0.025	0.029	0.027	0.026	0.024	3.74	3.82

3.6.3 Data conversion from signals to arm displacements and total pressure using Bayesian linear regression model

The raw data collected from RGP tests are the digital outputs from the strain gauge signals or pressure transducers. The displacements of the six arms predicted with the Bayesian linear regression model (Equation 3.8) are plotted in Figure 3.24 to Figure 3.27

The lower and upper bounds of 95% credible interval (CR) are represented by the solid lines and the mean displacement with the dashed line. The width of 95% CR defines the range of prediction uncertainty owing to the calibrations of micrometre and TPC, as well as measurement errors. The relatively narrow width of 95% CR shown in Figure 3.24 indicates fewer uncertainties for the RGP test in the Westgate Formation, whereas the broader width of 95% CR in Figure 3.27 implies more uncertainties exist in the RGP test in the Clearwater grey shale Formation. As the slope, zero (y-intercept), and standard deviation σ are all the same for the four testing pockets; different widths of 95% CR indicate that the Bayesian linear regression model used in the raw data conversion is data-driven.

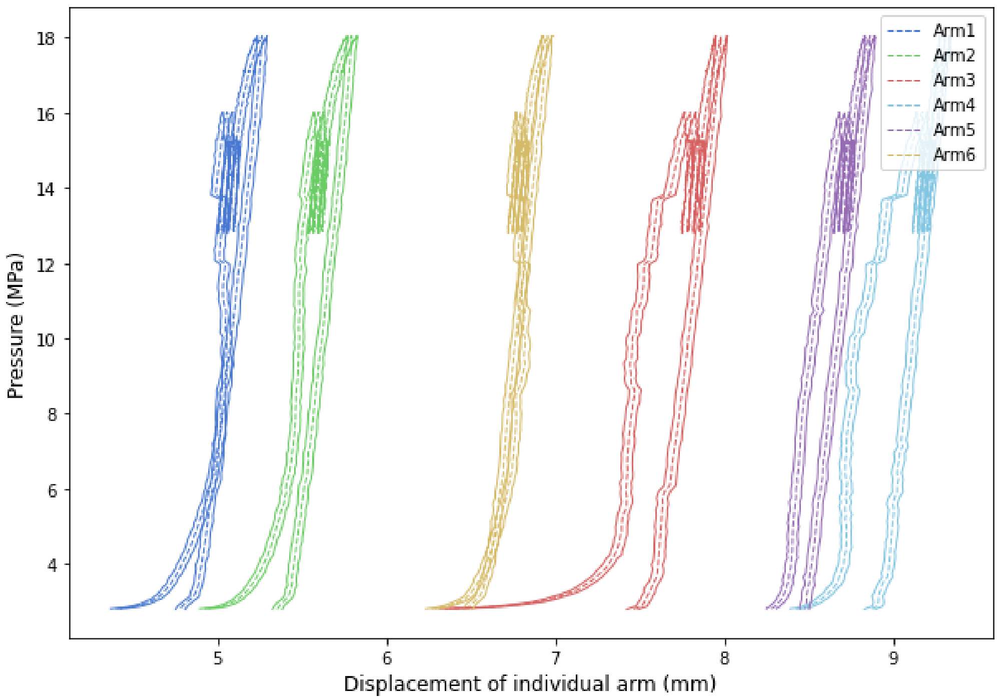

Figure 3.24 Uncorrected curves for RGP testing in Westgate using Bayesian linear regression model

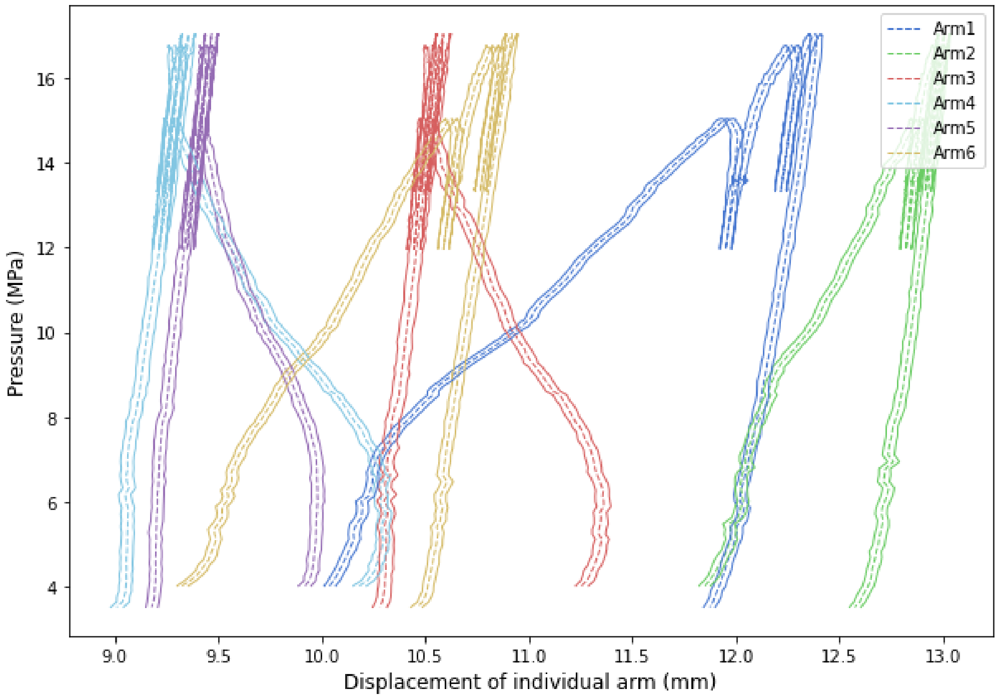

Figure 3.25 Uncorrected curves for RGP testing in Joli Fou using Bayesian linear regression model.

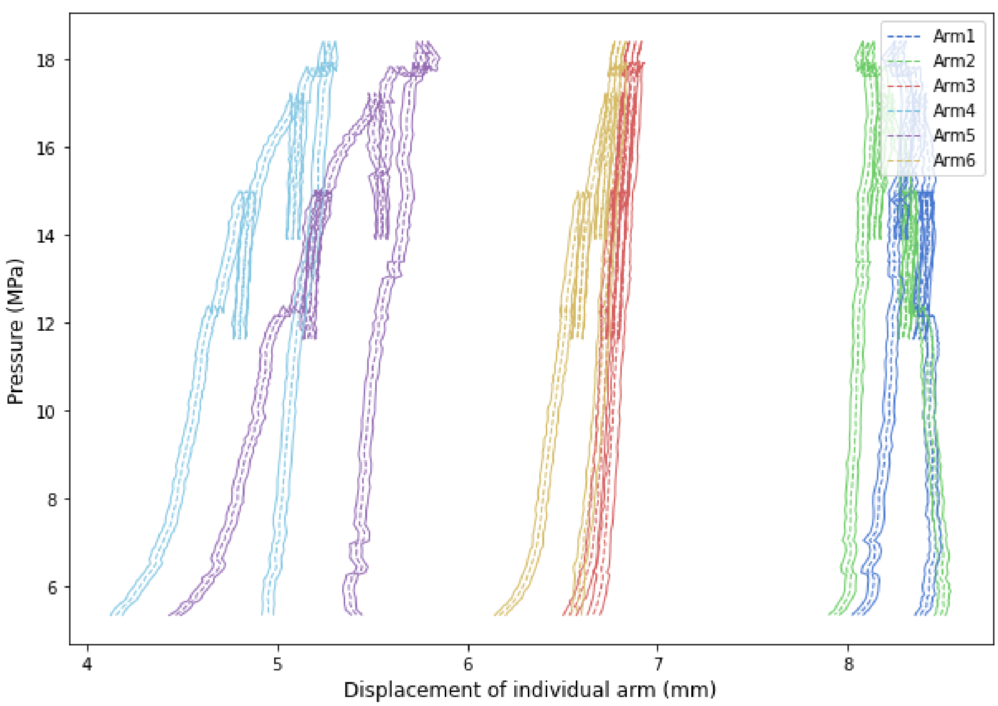

Figure 3.26 Uncorrected curves for RGP testing in Clearwater black using Bayesian linear regression model.

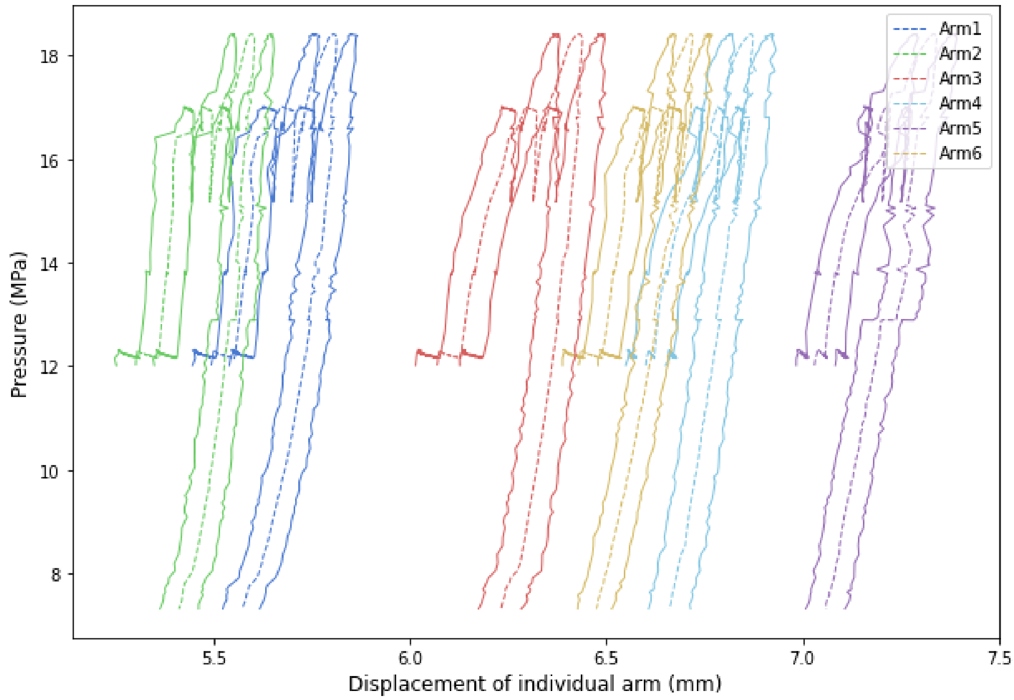

Figure 3.27 Uncorrected curves for RGP testing in Clearwater grey using Bayesian linear regression model.

3.7 RGP test curve corrected to system compliance and membrane stiffness

After converting the raw data from voltage to mm, the next step is to correct the arm displacements to the compliance of the measuring system and the measured pressure to membrane stiffness. The instrument compliance factor was determined to be 1.3 mm/GPa (Liu, 2017) by fitting the calibration data. The equivalent measurement errors are assumed to follow a Gaussian distribution $\sim N(0, 0.00225^2)$. The arm displacements before and after the correction are illustrated in Figure 3.28 to Figure 3.31.

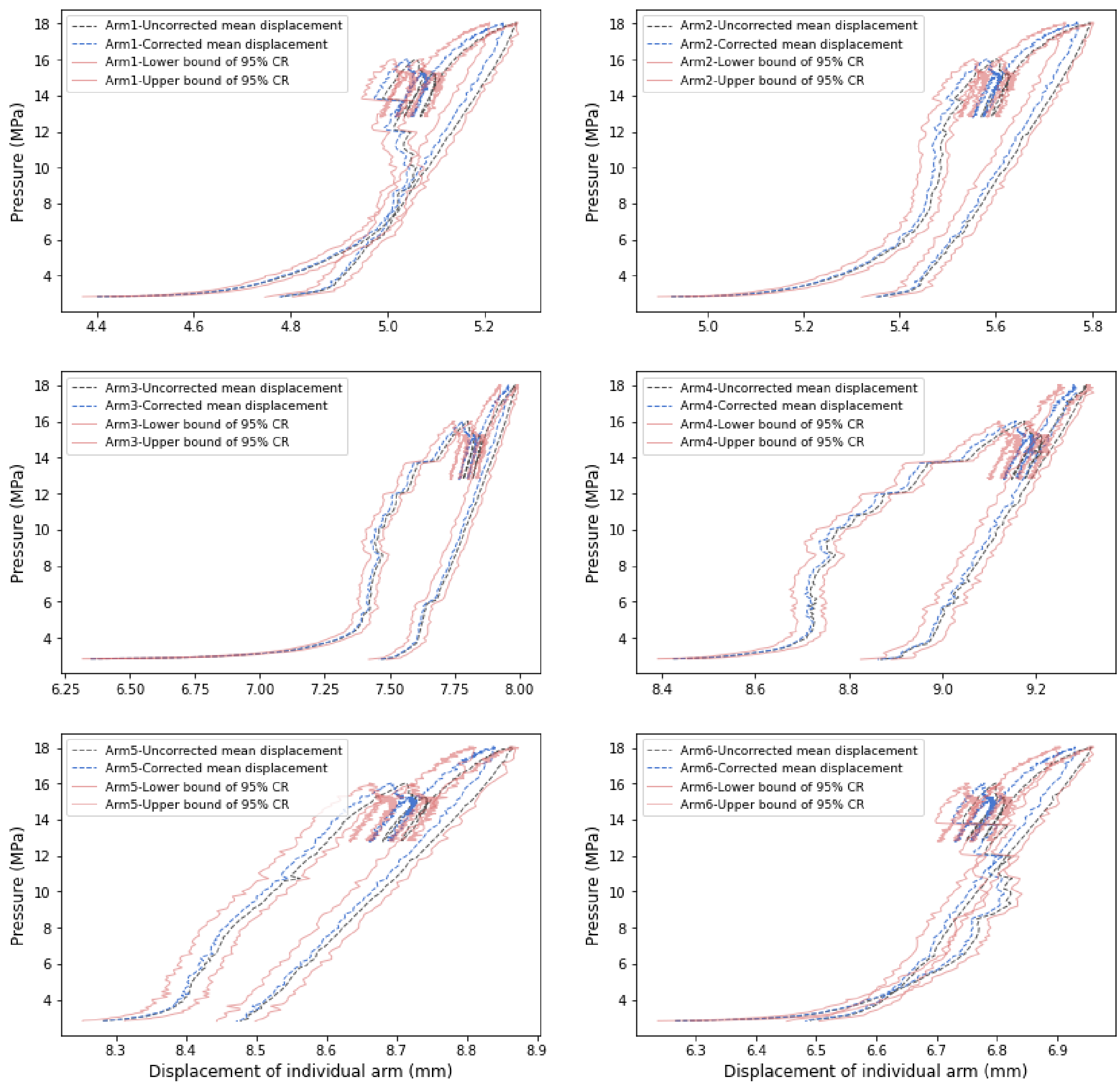

Figure 3.28 Curves corrected to system compliance and membrane stiffness for RGP testing in Westgate.

Compared to the uncorrected mean arm displacements, the corrected ones after system compliance are slightly reduced, which could cause significant errors when deriving the rock stiffness from the inverse analysis of the RGP test. In addition, the corrected curve looks more erratic than the uncorrected one because measurement errors are applied in the data correction. It indicates corrections to system compliance are necessary for clay shale formations.

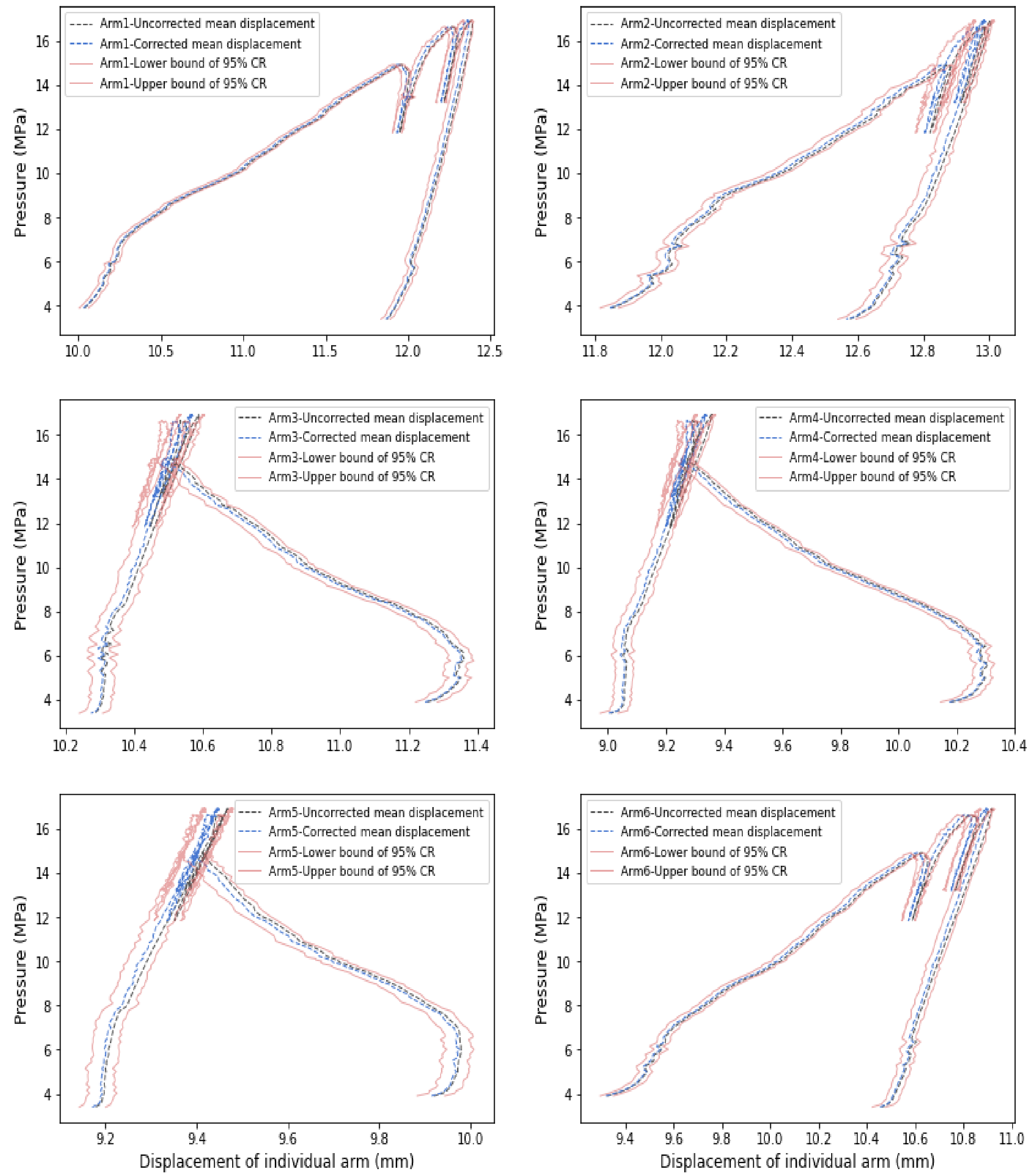

Figure 3.29 Curves corrected to system compliance and membrane stiffness for RGP testing in Joli Fou.

By examining Figure 3.30, displacements of Arm1 and Arm2 vary dramatically and fail to produce smooth testing curves. Figure 3.31 shows the greatest width of 95% CR among the four RGP tests, indicating the maximum uncertainty from tool measurement and data retrieval in the Clearwater grey shale testing pocket. Besides, at the same depth, the bandwidths of 95% CR derived from

Bayesian inference can differentiate the uncertainties between strain arms owing to the anisotropies of in-situ stresses and borehole material properties. For example, Arm4 and Arm5 in Figure 3.30 have much fewer uncertainties than Arm1 and Arm2. The same phenomenon can be observed in other testing pockets.

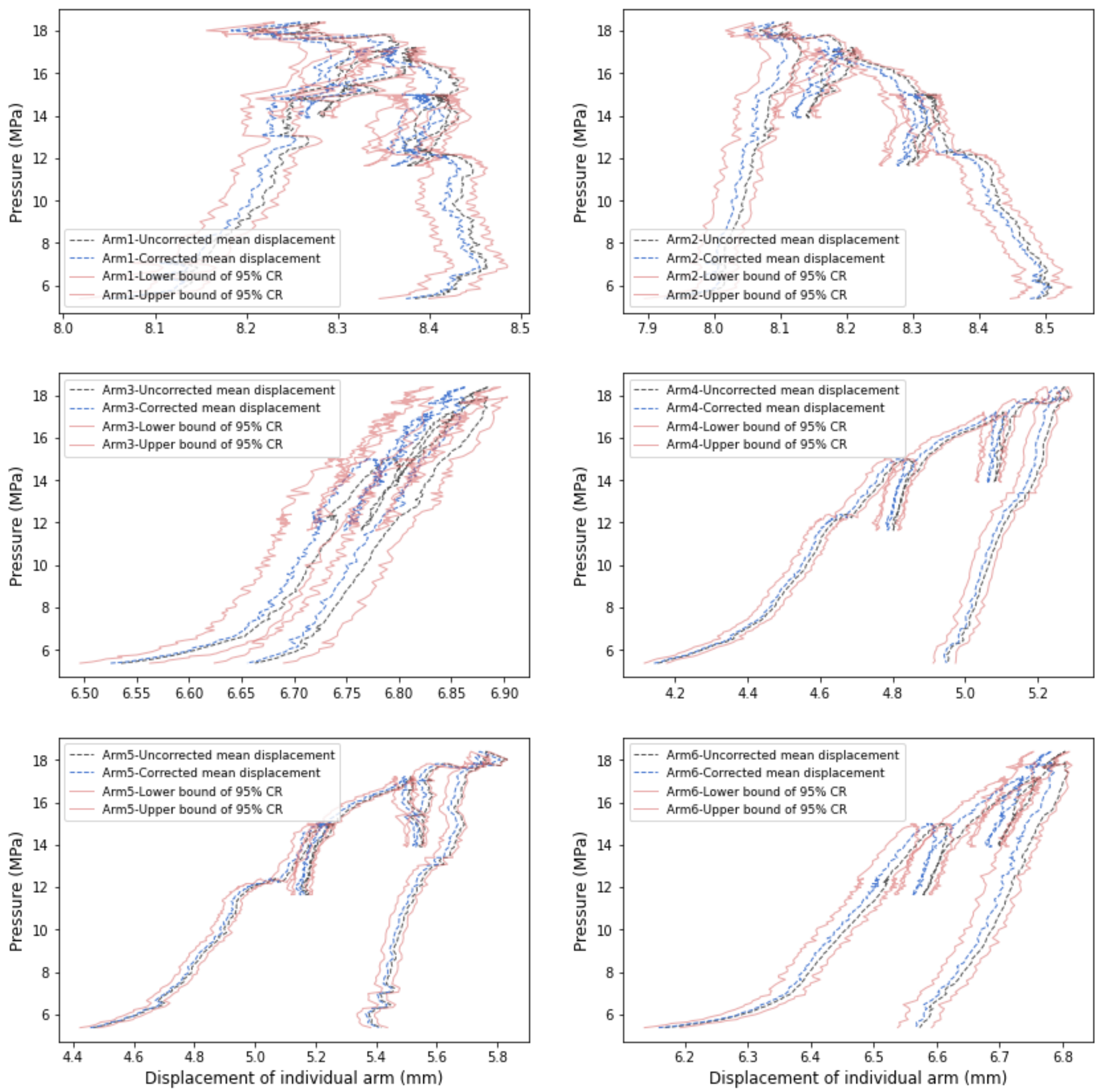

Figure 3.30 Curves corrected to system compliance and membrane stiffness for RGP testing in Clearwater black.

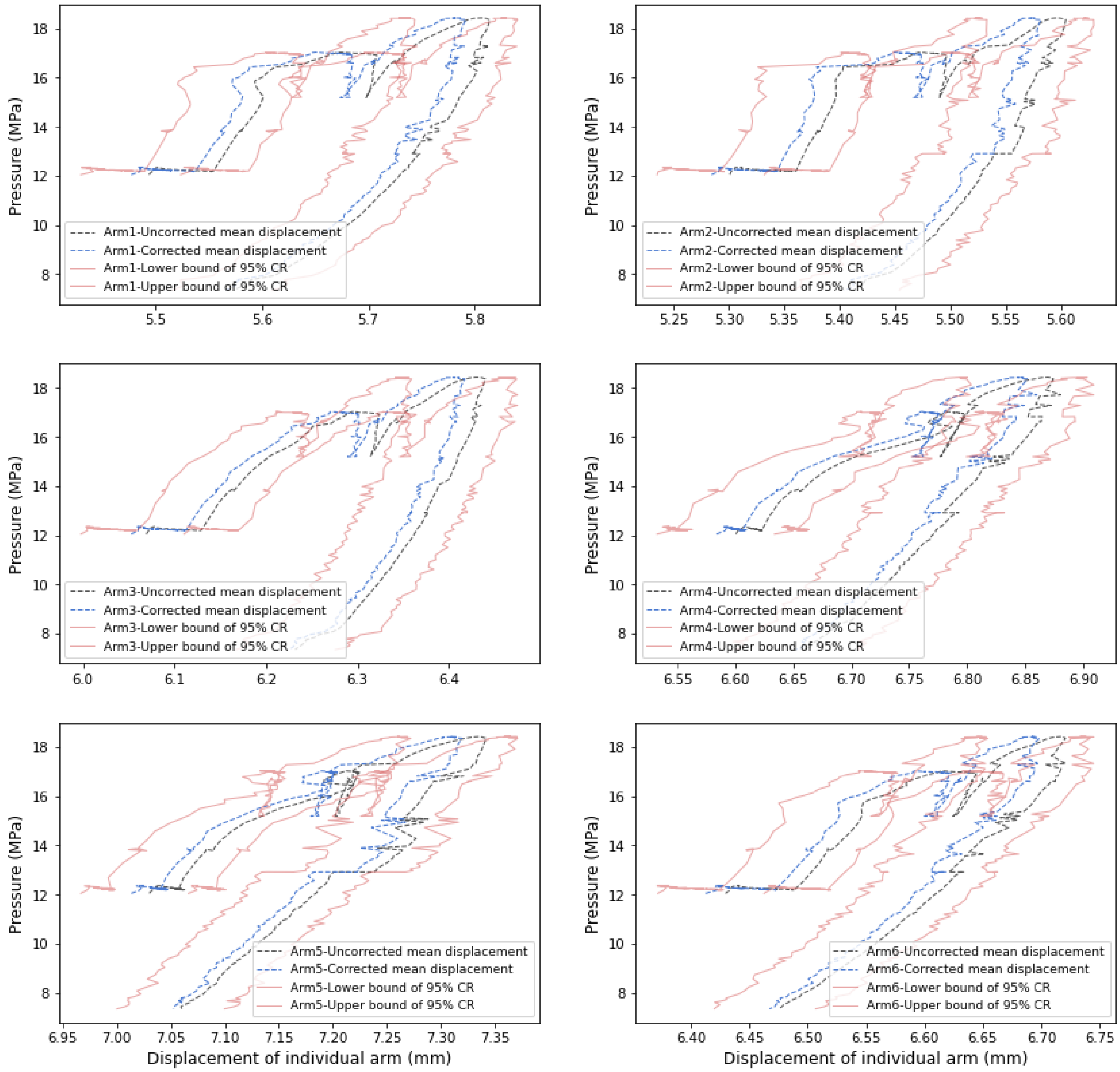

Figure 3.31 Curves corrected to system compliance and membrane stiffness for RGP testing in Clearwater grey.

If new calibration data are available, the curves from Figure 3.28 to Figure 3.31 can be further updated using the Bayesian linear regression model. Compared to the deterministic approach used in Sections 3.3 to 3.5, the Bayesian approach is an open system to the new evidence. New evidence can be easily implemented into the Bayesian data structure to update the posterior knowledge without starting from scratch.

3.7.1 Arm displacement correction to membrane thinning and ellipse fitting

Similar to Section 3.5, membrane thinning shall also be considered the last step of data corrections. The radius of the deformed borehole at the azimuth from 0° ~ 360° can be calculated with the addition of the corrected arm displacements and the radius of the RGP probe by performing ellipse fitting in the Bayesian way. With fitted ellipses shown as in Figure 3.17, deformed borehole radii at the azimuth of 0°, 45°, 60° and 90° can be plotted in Figure 3.32 to Figure 3.35. In the Bayesian statistical paradigm, the prediction interval 95% CR in Figure 3.32 to Figure 3.35 can be used to constrain the numerical uncertainty in the inverse analysis and accordingly reduce non-unique solutions.

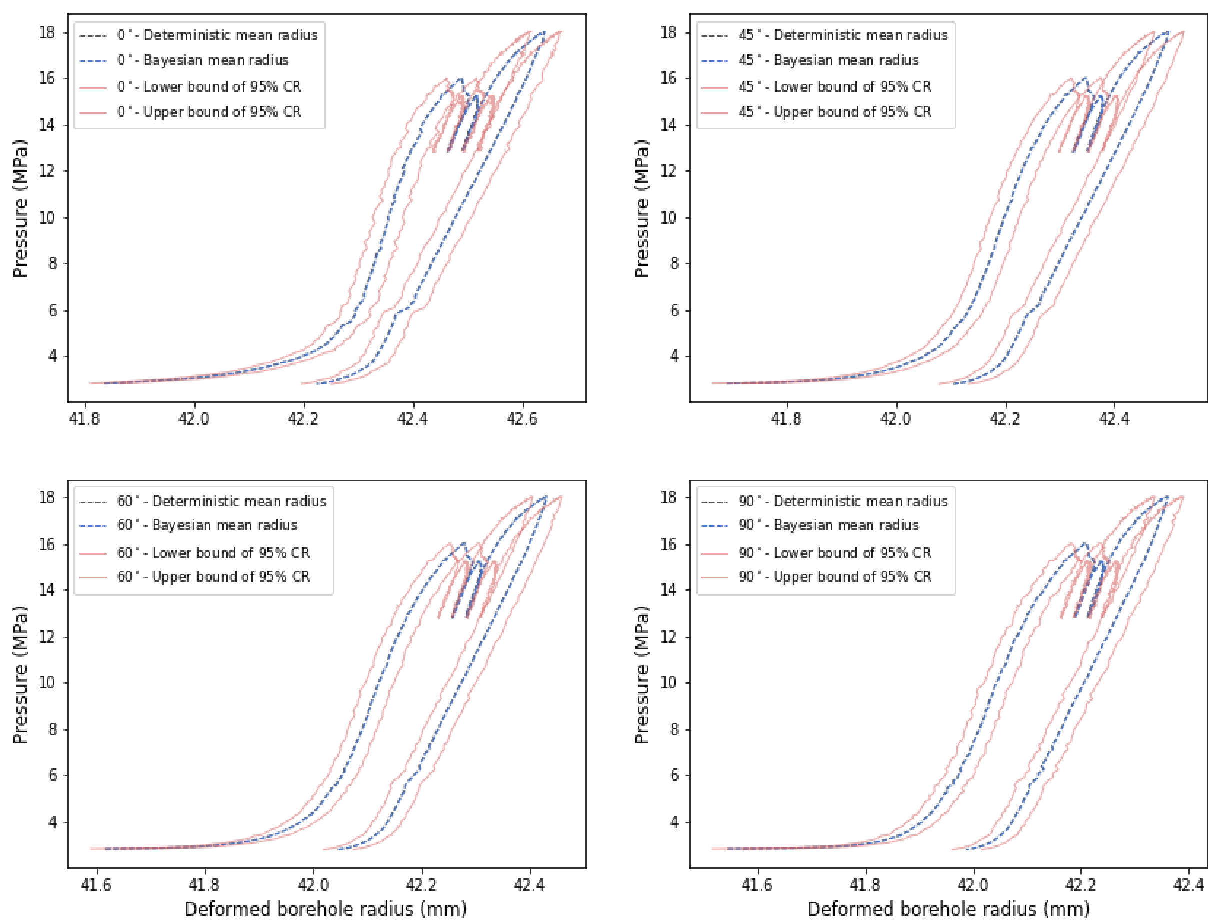

Figure 3.32 Deformed borehole radii corrected to membrane thinning and ellipse fitting in Westgate.

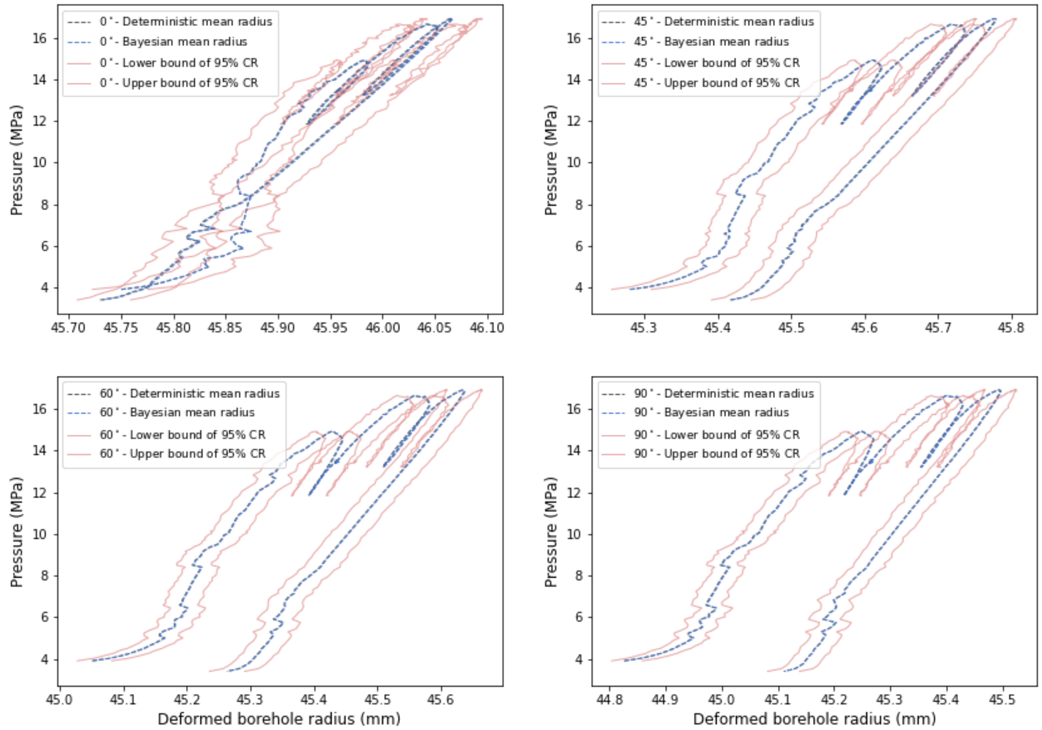

Figure 3.33 Deformed borehole radii corrected to membrane thinning and ellipse fitting in Joli Fou.

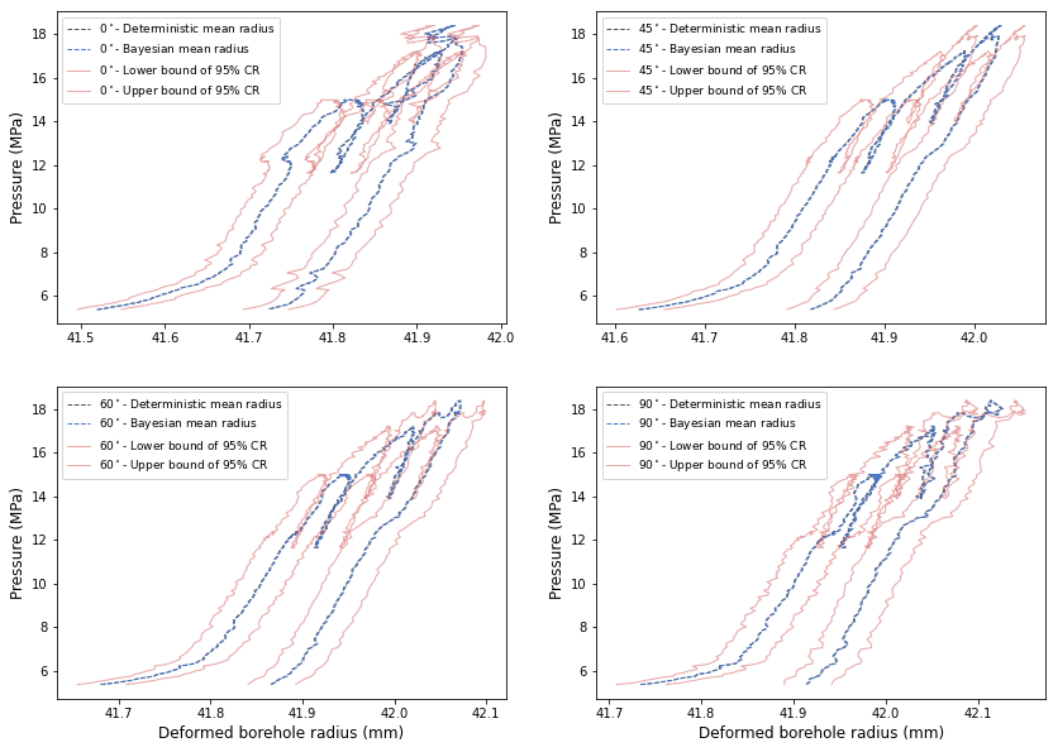

Figure 3.34 Deformed borehole radii corrected to membrane thinning and ellipse fitting in Clearwater

black.

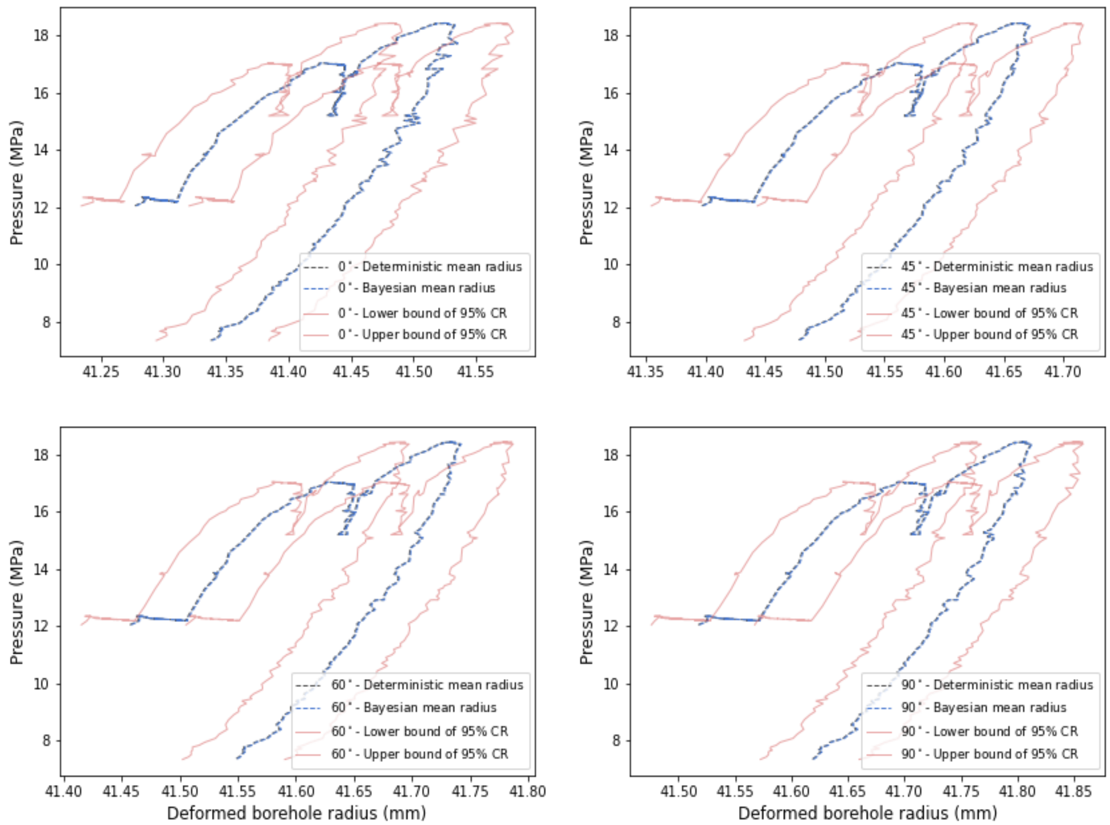

Figure 3.35 Deformed borehole radii corrected to membrane thinning and ellipse fitting in Clearwater grey.

3.8 Summary and Conclusions

Uncertainties in RGP tests were first identified and classified as random errors and systematic errors. Most systematic errors can be reduced or eliminated by following standard procedures, proper training, and maintenance of instruments. The uncertainties due to random errors can be quantified by conducting a statistical regression analysis.

Both deterministic and Bayesian statistical methods were used to analyze raw data. With the deterministic approach, the raw data are converted into arm displacements with the linear regression model. The slope and zero are obtained from micrometre calibration. After the conversion of raw data, the uncorrected testing curves need to be corrected to instrument system compliance, membrane stiffness and thinning. To find the arm displacement at an azimuth of $0° \sim 360°$, ellipse fitting is used to fit the corrected displacements of the six arms.

Thus, the deformed shape of the borehole subjected to applied pressure can be represented by a series of ellipses. The subtraction of the previous ellipse from the current one is the borehole deformation, which can be used in the curve fitting of an RGP test. However, due to the limitation of the deterministic approach, uncertainties propagated from tool calibration, tool deployment, and measurement errors cannot be quantified. As a result, the corrected RGP curve is not unique and may bring forward the problem of non-uniqueness in parameter estimation. To quantify the measurement uncertainties for an RGP test, the Bayesian inference method is adopted in the data corrections to raw data conversion, system compliance, membrane stiffness and thinning.

Raw data from RGP testing can be converted and corrected with a deterministic or statistical approach. The deterministic approach is easy to use but cannot characterize the variability of RGP test curves from errors. In comparison, the statistical method can quantify the uncertainties with a Bayesian linear regression model. The prior information adopted in the Bayesian linear regression model is always open to new data (evidence) and accordingly, the 'belief' continues to be updated with every new dataset. The Bayesian linear regression modelling on the raw data can derive the lower and upper bounds of 95% CR, which can constrain the prediction uncertainty from the parameter estimation. At the same time, the non-unique solutions can be reduced in the inverse analysis workflows, which are described in the following chapter.

4.0 UNCERTAINTY QUANTIFICATION OF IN-SITU HORIZONTAL STRESS WITH PRESSUREMETER USING A STATISTICAL INVERSE ANALYSIS METHOD[1]

4.1 Introduction

Knowledge of the in-situ stress magnitude and orientation plays a very important role in geological/geotechnical engineering and in the development of energy resources, such as caprock integrity, waste fluid disposal, geological storage of CO2, and geothermal energy extraction. The uncertainty of estimated parameters, especially horizontal stress, from in-situ tests, such as pressuremeter tests, is a long-standing challenge owing to the existence of uncertainties from geomaterial spatial variability, measurement errors, limited information, and modelling methods. Therefore, non-unique solutions are often encountered in pressuremeter interpretation. In this study, a statistical inverse analysis method is proposed to solve this issue by combining a closed-form solution, a finite-difference model, and selected optimization algorithms. The objective of statistical inverse analysis is to determine the optimal parameters by minimizing the sum of squared errors while providing the confidence intervals of the inversed parameters. The random variables generated in the optimization process reproduced the potential parameter uncertainties. The Jacobian matrix and confidence intervals were derived from the optimization process to evaluate the variability of the predicted horizontal stress and ground properties. A workflow that demonstrates a statistical inverse method for analyzing pressuremeter results and helps quantify uncertainties of the ground properties and in-situ stress magnitudes and orientations derived from a pressuremeter test is presented.

---

[1] A version of this chapter has been published: Zheng, D., B. Zhang, and R.J. Chalaturnyk, 2021. Uncertainty quantification of in-situ horizontal stress with pressuremeter using a statistical inverse analysis method. Canadian Geotechnical Journal. 59(3): 397-409. https://doi.org/10.1139/cgj-2021-0004

4.2 Background

The pressuremeter was introduced by Louis Menard in 1955 for in-situ testing to estimate ground properties for geotechnical designs (Clarke, 1995; Mair and Wood, 1987; Schnaid, 2009). Generally, there are three types of pressuremeter devices in terms of their installation methods (Mair and Wood, 1987): Menard-type, self-boring (SBP), and push-in pressuremeters. Theoretically, an SBP device can achieve minimal disturbance to adjacent soils by drilling its testing pocket. In the pressuremeter test, the applied pressure, volume, and/or radial displacements are recorded. A typical pressuremeter testing curve includes two components, expansion and contraction, as well as loops, if unloading–loading cycles are performed. Geotechnical properties, such as undrained shear strength and shear modulus, as well as in-situ horizontal stress, can be derived from the pressuremeter testing curves.

Uncertainties in ground properties and in-situ stress fields are associated with aleatory uncertainties (spatial variability) and epistemic uncertainties (measurement errors, limited information, and model uncertainty) in pressuremeter tests (Nadim, 2007). Uncertainty quantification plays a vital role in the assessment of potential natural hazards (Chen and Cui 2017; Cui et al., 2017; Liu et al., 2020). The quantified uncertainty helps to provide a more sophisticated design of hydraulic fracturing, tunnelling, and caprock integrity in subsurface development, considering the spatial variability of geotechnical properties, stress, and pore pressure distributions (Yang et al., 2004; Ghassemi, 2012; Ganesh et al., 2020; Zhang et al., 2021).

In general, pressuremeter tests are interpreted using graphical plotting methods (Gibson and Anderson, 1961; Houlsby and Withers, 1988; Marsland and Randolph, 1977) or curve-fitting methods (Arnold, 1981; Denby and Clough, 1980). Graphical plotting methods involve the construction of a tangent line to the loading or unloading curve, which can determine the geotechnical properties. However, one of the drawbacks of graphical methods is their subjectivity to personal judgments (Clarke, 1995). To fit measured points with predicted ones, a computational model that can be either a closed-form solution or a numerical model is required. Jefferies (1988) proposed a curve-fitting approach to identify the horizontal stress and ground properties by extending the mathematical solution proposed by Gibson and Anderson (1961).

However, the model fit was achieved through visual comparison, which may lead to non-unique solutions (Houlsby, 1989). By extending the hyperbolic model (Duncan and Chang, 1970), Ferreira (1992) numerically fitted the pressuremeter curves using the least-square error curve-fitting technique. Fahey and Carter (1993) performed finite-element analyses to simulate the behavior of pressuremeter tests in sand using a nonlinear elastic–plastic model. Fawaz et al. (2002) conducted pressuremeter chamber tests in sand, and deduced the parameters using the finite element method. Huang et al. (1986) adopted the simplex algorithm in the least-squares error curve-fitting process to solve the problem of repeatability. Levasseur et al. (2008) identified the Mohr–Coulomb parameters using two optimization approaches based on a gradient method and genetic algorithm (GA). In a recent publication, Obrzud et al. (2009) presented the application of a neural network technique for parameter identification based on SBP measurements. Gaone et al. (2019) derived modified Cam clay parameters from SBP testing data by combining traditional interpretation methods, parameter sweeps, and a local minimizer based on the golden section search algorithm and parabolic interpolation. However, the uniqueness of the solution in the parameter estimations discussed above is yet to be addressed in depth.

In general, there are two possible sources of non-uniqueness: (i) the initial parameters are arbitrarily chosen during the numerical curve-fitting process (Arnold, 1981). Houlsby (1989) pointed out that experimental data can be fitted by a wide range of parameter combinations, and (ii) the mathematical minimum is not necessarily the physical minimum. For example, the simplex algorithm (Nelder and Mead, 1965; Huang et al., 1986) is sensitive to the initial values provided at the beginning of the optimization process, leading to different optimal results for each initial dataset. Consequently, the curve-fitting process may produce mathematically optimal values rather than physically optimal values (Papon, 2012).

To address the issue of arbitrarily chosen parameters, the research presented in this paper introduces cut-offs of random parameter variables in inverse analysis to filter unreasonable data points (Clarke, 1995). A priori knowledge of ground properties is essential for defining the physical bounds for a constrained optimization problem. Multiple optimizers were used in the inverse analysis. Notably, the statistical inverse analysis method can accommodate parameter uncertainties during the interpretation of the pressuremeter tests. A statistical assessment of the estimated parameters shows not only the optimal predicted dataset but also the bounds of the predicted values (e.g., 95% confidence intervals (CIs)). Furthermore, correlations between the estimated values were derived from statistical assessments.

To overcome the disadvantages of conventional interpretation techniques for pressuremeter tests, a statistical inverse analysis framework was proposed and applied to the uncertainty quantification of parameter estimation for SBP tests. The results demonstrated its capability to quantify uncertainties in geotechnical design and research.

4.3 Methodology

In geotechnical engineering, inverse analysis has been widely applied for the calibration of constitutive models, the identification of soil parameters, and geotechnical design optimization (Levasseur, 2008; Papon, 2012; Yin et al., 2018). The objective of the proposed statistical inverse analysis of a pressuremeter test is to minimize the errors between the measured and predicted data under a statistical framework, as opposed to the deterministic method adopted by Jefferies (1988) for the parameter estimation of an SBP. The framework of the statistical inverse analysis includes, but is not limited to, the following steps: (i) a priori knowledge of initial values and uncertainty quantification of input variables, (ii) selection of a computational model and coupling with an optimization algorithm, (iii) establishing an objective function, (iv) identification of the optimal dataset based on the optimization criteria, and (v) execution of a statistical assessment of the identified parameters. The workflow for the proposed statistical inverse analysis of pressuremeter tests is shown in Figure 4.1. To begin the statistical inverse analysis, the initial values must be selected for certain optimizers, such as the Levenberg–Marquardt (LMA) and simplex algorithms. For other optimizers, e.g., Monte Carlo simulation (MCS) and subset simulation (SS), independent and identically distributed (IID) parameter samples must be randomly drawn from a proposed probability density function (PDF) (e.g., uniform distribution, Gaussian distribution, and log- normal distribution). The PDFs denote the initial probability distributions of the formation properties and in-situ horizontal stress, which can be defined using a priori knowledge, such as laboratory and field tests, local experience, and literature. A uniform distribution was adopted for the inverse analysis. These IID samples were used as input parameters in the computational model. Solving an objective function involves coupling a computational model with an optimizer.

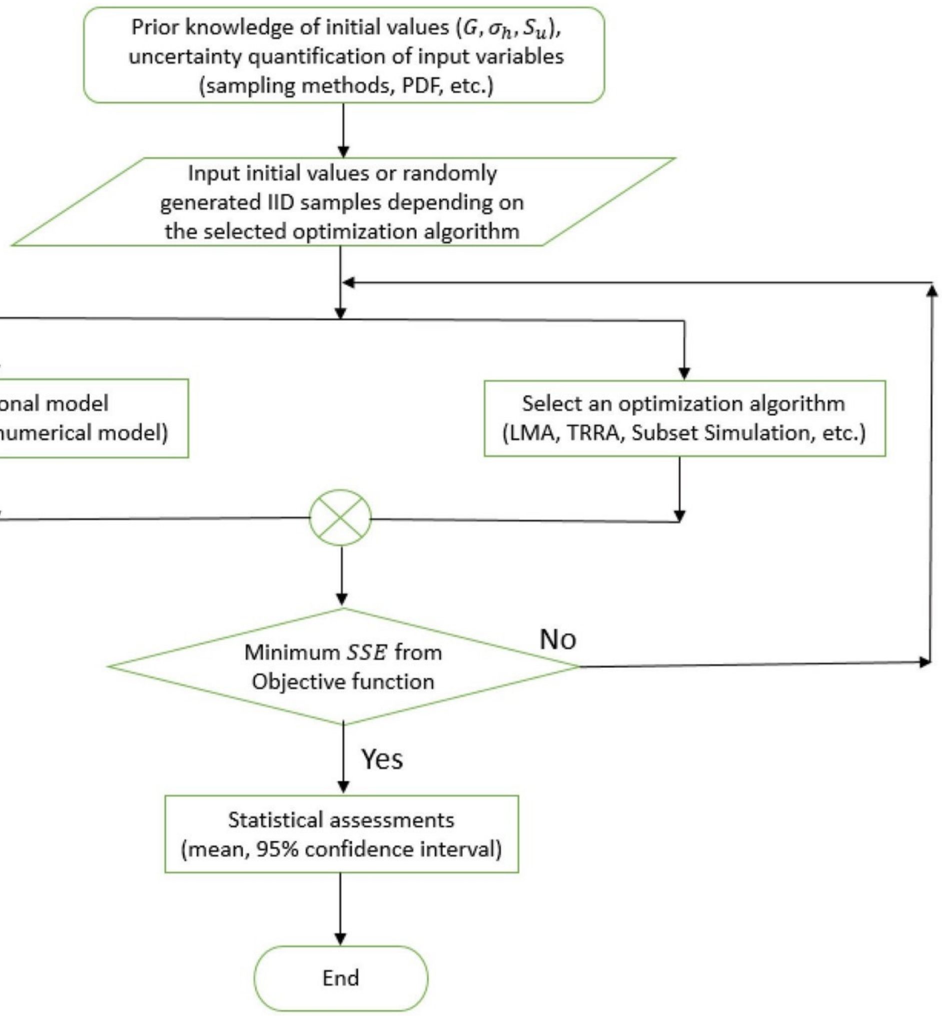

Figure 4.1 Flow chart of statistical inverse analysis of a pressuremeter test. IID, independent and identically distributed; LMA, Levenberg–Marquardt algorithm; PDF, probability density function; TRRA, trust-region reflective algorithm.

4.4 Objective functions

An unweighted nonlinear least-squares (NLLS) performance function (also called the error function) can be formulated to minimize the subjective errors caused by the visual interpretation method proposed by Jefferies (1988). The NLLS performance function is formulated as the objective function in the search process of optimization algorithms (Ahmed and Soubra, 2015; Papon, 2012; Yin et al., 2018). The unweighted NLLS performance function is expressed as

$$SSE = \sum_{i=1}^{n} \left[Y_i - \hat{Y}_i(b_i) \right]^2 \tag{4. 1}$$

where SSE denotes the sum of squared errors, Y_i denotes the observed data, $\hat{Y}_i$ denotes the predicted data, and b_i represents a parameter to be estimated (G, σ_h, S_u). G represents the shear modulus, σ_h is the total horizontal stress, and S_u is the undrained shear strength. $\hat{Y}_i(b_i)$ represents a nonlinear function of b_i for simulating a pressuremeter test. In the inverse analysis, an optimizer must be coupled with a computational model to minimize the SSE, as formulated in Equation 4.1.

4.4.1 Optimization algorithms

The LMA and the trust-region reflective algorithm (TRRA), which are adopted in the statistical inverse analysis, are realized with the nonlinear least-squares solver "lsqnonlin" in Matlab (MathWorks, 2019). To verify the conclusion made by the local optimizers (i.e., LMA and TRRA), a global optimization algorithm, SS, was used in the inverse analysis. The SS code was modified from that of Li and Cao (2016) and implemented to minimize the unweighted NLLS performance function, as described by Equation 4.1. Appendix B briefly introduces the theories of the three optimization algorithms.

4.4.2 Simulation of pressuremeter test

A pressuremeter test can be simulated using either a closed-form solution or numerical model. Based on the solution proposed by Gibson and Anderson (1961), Jefferies (1988) proposed a theoretical relationship between the pressure and ratio of the initial radius to the current radius, a_0/a, at the plastic loading stage:

$$P = \sigma_{h0} + S_u \left[1 + ln \left(\frac{G}{S_u} \right) \right] + S_u ln \left[1 - \left(\frac{a_0}{a} \right)^2 \right] \tag{4.2}$$

To account for the strength softening or hardening effect during unloading in the SBP contraction phase, Jefferies (1988) introduced a fraction β of the undrained shear strength S_u:

$$S_{u_c} = \beta S_u \tag{4.3}$$

Then, the pressure that initiates plastic deformation during the contraction stage becomes $P = P_{max} - (1+\beta)S_u$, and the relationship between P and a can be written as (Jefferies, 1989)

$$P = P_{max} - (1+\beta)S_u - S_u ln\left\{\left[1 - \left(\frac{a}{a_{max}}\right)^2\right]\left[\frac{G}{(1+\beta)S_u}\right]\right\}$$

$$-\beta S_u ln\left\{\left[\left(\frac{a_{max}}{a}\right)^2 - 1\right]\left[\frac{G}{(1+\beta)S_u}\right]\right\} \tag{4.4}$$

where β denotes the softening or hardening coefficient during unloading and a_{max} represents the maximum radius.

The displacements measured in the field can be directly applied to Equations 4.2 and 4.4 after calibration. The proposed inverse analysis of an SBP test in clay can be efficiently conducted using the NLLS curve-fitting inverse analysis technique, as explained previously.

In addition to the closed-form solution introduced above, a two-dimensional numerical model using the finite element method (FEM) or finite difference method (FDM) can be built to simulate pressuremeter tests in clay, sand, and rock (Yeung and Carter, 1990; Yu and Netherton, 2000; Gaone et al., 2019). In the present study, fast Lagrangian analysis of continua (FLAC), a commercial two-dimensional explicit finite-difference program (Itasca, 2011), was applied to model an SBP test in clay. A properly built numerical model can address the sources of inaccuracy from oversimplified assumptions in closed-form solutions regarding pressuremeter geometry, water drainage, and initial disturbance (Yu, 2006). Although the numerical model may encounter convergence issues, it can detect unreasonable initial estimates for an unconstrained optimization problem.

4.4.3 Statistical assessment of identified parameters

To quantify the uncertainty in parameter estimates, statistical assessments should be conducted after the optimization process. The evaluation of uncertainty for inverse analysis requires the definition of mean values, standard deviations (SDs), and confidence intervals (CIs). In the proposed workflow, the covariance for the optimal parameters, b', was calculated as (Knabe et al., 2012):

$$cov(b') = s^2(J^TJ)^{-1} \tag{4.5}$$

where b' represents the estimated optimal parameters, s^2 denotes the calculated error variance, and J denotes the Jacobian matrix, also known as the sensitivity matrix. The error variance, s^2, asymptotically reaches the mean-squared error and is defined as:

$$s^2 = \frac{SSE}{(n-p)} \tag{4.6}$$

where SSE represents the sum-of-squared errors, as calculated using Equation 4.1, n represents the number of observations, p indicates the number of parameters, and $(n-p)$ denotes the degrees of freedom.

The standard deviation (SD) is the square root of diagonal elements of matrix $cov(b')$. With the derived SD, the $100(1-\alpha)\%$ CIs for the optimal parameters are

$$b' \pm t_{(1-\alpha/2,n-p)}\frac{SD(b')}{\sqrt{n}} \tag{4.7}$$

where $SD(b')$ represents the SD of b', and $t_{(1-\alpha/2,n-p)}$ indicates $100(1-\alpha/2)^{th}$ percentile of the t-distribution with ($n-p$) degrees of freedom. The off-diagonal elements of matrix $cov(b')$ are covariance, which can be used to determine the correlation between the optimal parameters. For uncorrelated parameters, the covariance is zero. If parameters are correlated, then their covariance will be nonzero (Weisstein et al. n.d.). Knabe et al. (2012) pointed out that the matrix $cov(b')$ provides the reliability of the estimated parameters in terms of their covariances.

The proposed statistical inverse method can accommodate the parameter uncertainty in the interpretation of pressuremeter tests. With a statistical assessment, the statistics of the estimated parameters provide the confidence bounds together with the optimal values. In addition, correlations between the estimated values can be derived from statistical assessment.

4.5 Case study of an SBP test

The SBP test conducted at the test site Amauligak F-24 (Jefferies, 1988) was reanalyzed using the proposed statistical inverse method. Parameter estimation by Jefferies was based on curve fitting with visual comparison by trial and error. In the case study, a reanalysis of the SBP test was performed using the inverse method under a statistical framework. Model fit was evaluated by coupling the closed-form solution (Jefferies, 1988) or a finite-difference model with the LMA, TRRA, and SS. The results were interpreted using SSE for unweighted residuals and statistics (mean and CIs).

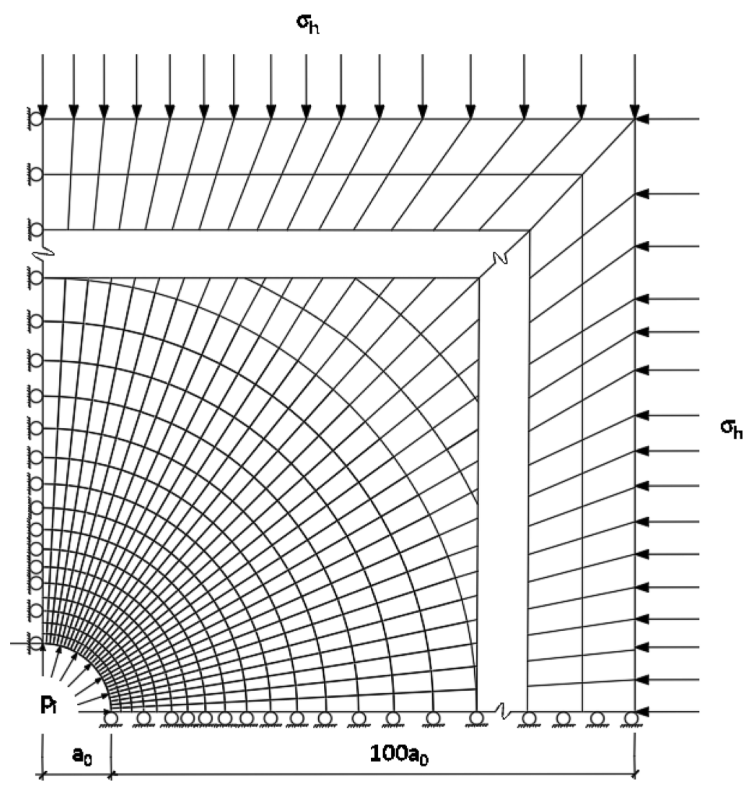

Figure 4.2 Boundary conditions for FLAC model in the inverse analysis.

4.5.1 Project background

The Amauligak F-24 site is located 32 m below sea level. The testing pocket was surrounded by stiff clay (unit D1) approximately 40 m below the mud line. The published SBP testing data (Jefferies, 1988) are utilized for the re-analysis of the SBP testing in clay at this site.

4.5.2 Soil profile

The geotechnical profile below the mudline for the Jefferies et al. (1987) study consists of a 12 m layer of soft clay (units A1 and A2) overlying 24 m of dense to compact sand (unit C). The SBP testing pocket is located in the 15 m massive clay unit (D1) below unit C, which is horizontally bedded silty clay with medium to high plasticity. The water content of unit D1 ranged from 25% to 32%, and the liquid index were close to zero. The a priori information presented by Jefferies et al. (1987) provides the geotechnical constraints for the following inverse analyses of the same SBP testing.

4.5.3 Numerical modelling of an SBP test

In addition to the analytical solution proposed by Jefferies (1988), FLAC modelling was used in the inverse analyses. As the expanding length of the SBP instrument is approximately 0.5 m (Cambridge Insitu Ltd., 2012), the SBP testing in clay was treated as a cylindrical cavity expansion in a homogeneous, isotropic medium to simplify numerical modelling (Wroth, 1984; Jefferies, 1988; Yeung and Carter, 1990; Yu and Netherton, 2000). The studies were conducted using total stresses with the assumption of undrained conditions throughout the test, considering a fast loading rate (Windle and Wroth, 1977; Jefferies, 1988; Liu et al., 2021). Figure 4.2 illustrates the two-dimensional plane–strain discretized domain and boundary conditions. Taking advantage of symmetry, only a quarter of the cylindrical cavity was modelled.

The Mohr–Coulomb model was used to calculate the elastic and plastic responses of the SBP test. Under undrained conditions, the plastic strength of the clay in D1 is represented by the Tresca model with a unique S_u and $\varphi = 0°$.

Random variables, horizontal stress (σ_h), shear modulus (G), and undrained shear strength (S_u), were generated through parameter perturbation in the LMA and TRRA and randomly selected from IID samples in the SS. These random variables were used as the input parameters for the analytical and finite difference FLAC models. The minimization of the objective function formulated using Equation 4.1 was solved by coupling the analytical or the FLAC model with the LMA, TRRA, and SS.

4.6 Criteria applied in determination of best-fit dataset

The goal of the optimization is to determine the optimal dataset in an inverse analysis. The criteria used to determine the best-fit dataset are summarized as follows (the flow chart of the criteria described below is shown in Figure 4.3):

1. Value of SSE: Considered the primary index to determine the optimal dataset with the minimum SSE.

2. SD (Standard Deviation) bar: Length of SD bar shown in Figure 4.4 and Figure 4.5. represents variability of the estimated parameters, which can be treated as a secondary index for determining the optimal dataset.

3. In general, there are three cases in the decision-making process from which the best-fit dataset is selected:

   Case A: A dataset with both the minimal SSE and SD bar is considered the best-fit dataset.

   Case B: For the case of the same minimal SSEs, a dataset with a shorter SD bar is preferred to one with a longer SD bar.

   Case C: If the SSE is minimal, its SD bar is longer, which means an "accurate" fit but larger uncertainty in the curve fitting (or vice versa, the dataset with a greater SSE but a shorter SD bar). In such cases, the assessment should be assisted by other statistical parameters, e.g., coefficient of determination and p-value, and the evidence from other independent tests, such as the field vane test and triaxial test.

4. Knowledge and experience from experts are still important in the final determination of the best-fit dataset.

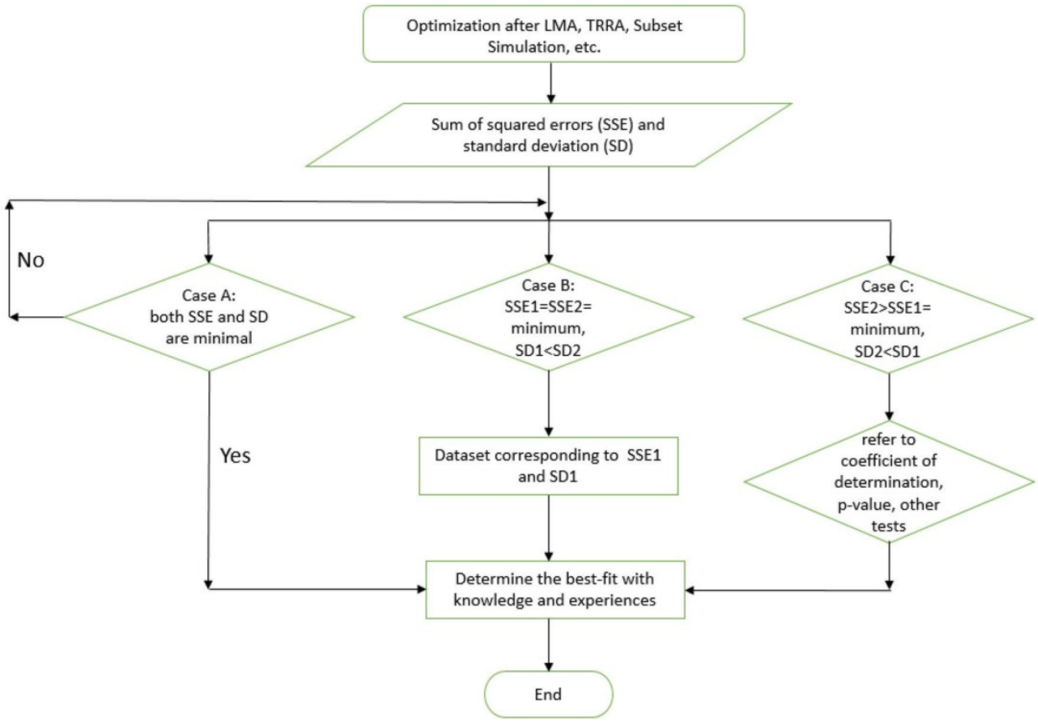

Figure 4.3 Flow chart of criteria applied in the determination of the best-fit dataset.

4.6.1 Statistical inverse analysis of expansion curve

A complete pressuremeter test curve consists of both expansion and contraction parts. To examine the effects of the contraction part on parameter estimation, the inverse analysis presented in this section is performed by considering only the expansion part. The inverse analysis of the complete curve is presented in Section 4.6.2. Two local optimization algorithms (LMA and TRRA), together with a global optimization algorithm (SS), are implemented in the statistical framework.

In the case of the three input parameters, the gradient descent algorithm may be easily confined by local minima. Thus, other optimizers, such as the SS or GA, must be adopted to ensure the global minimum. However, these optimizers often require a large number of iterations to accomplish an optimization task, which becomes computationally costly for inverse analysis using a numerical model. In some cases, a hybrid of local and global optimizers may be an alternative solution.

4.6.1.1 Inverse analysis of expansion curve using local optimizers

The inverse analyses of the SBP test AF85 P06-15 are conducted using the proposed inverse method and compared with the results presented by Jefferies (1988) and from conventional interpretation methods (Appendix B). The expansion part of the SBP test AF85 P06-15 is used. The initial parameters for the inverse analyses of the SBP test are listed in Table 4.1. Three sets of initial parameters are selected to estimate σ_h, G, and S_u. Initial values of dataset A (Initial A) represent the parameters estimated by Jefferies (1988) using the complete expansion and contraction curve, and dataset B (Initial B) considers only the expansion part (refer to Figures. 10 and 12a in Jefferies, 1988). Dataset C (Initial C) was randomly generated to test the robustness of the proposed method in the present study. Initial values of the SSE shown in Table 4.1 have been evaluated using Equation 4.1.

The optimal parameters from the inverse analysis of the expansion curve using the LMA are presented in Table 4.2. In terms of the SSE in Table 4.2, the optimal dataset using the closed-form solution corresponds to the optimal values of datasets A and C, which are virtually identical. In dataset A, G measures 9915 kPa, which is similar to the lower bound reported by Jefferies (1988; see Figure 7a). Similarly, the optimal parameters using the numerical model can be determined as dataset A by examining the SSE in Table 4.2. Figure 4.4 illustrates the σ_h datasets in Table 4.2 with SD bars (one SD below and above the data points). The SDs for Initials A, B, and C were not provided in Jefferies (1988). The lengths of the SD bars shown in Figure 4.4 illustrate that the estimation uncertainty using numerical modelling appears to be higher than that using the closed-form solution, indicating that the numerical model is more sensitive to the variation in input parameters than the closed-form solution while simulating the expansion part owing to the disturbance at the early stage.

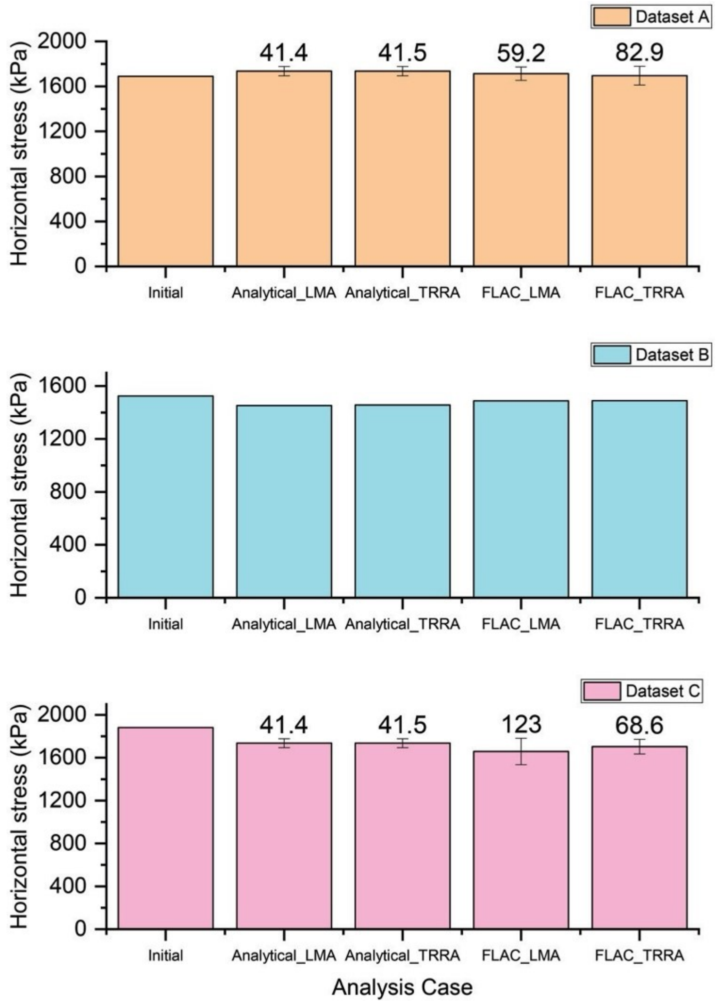

Figure 4.4 Initial and best datasets of horizontal stresses derived from the expansion curve using closed-form solution and numerical model coupled with LMA and TRRA. Note: the number displayed on the top of SD bar is SD, unit: kPa.

Table 4.1 Initial parameters for inverse analysis of expansion curve.

Dataset	Initial values (Initial)			
	σ_{h0} (kPa)	G_0 (kPa)	S_{u0} (kPa)	SSE
A	1690	18 000	160	1.08
B	1525	45 000	165	0.96
C	1882	19 900	178	71.27

Note: Initial values of A (Initial A) and B (Initial B) refer to Figures. 10 and 12a in Jefferies (1988). Initial values of C (Initial C) are random values generated for the inverse analysis.

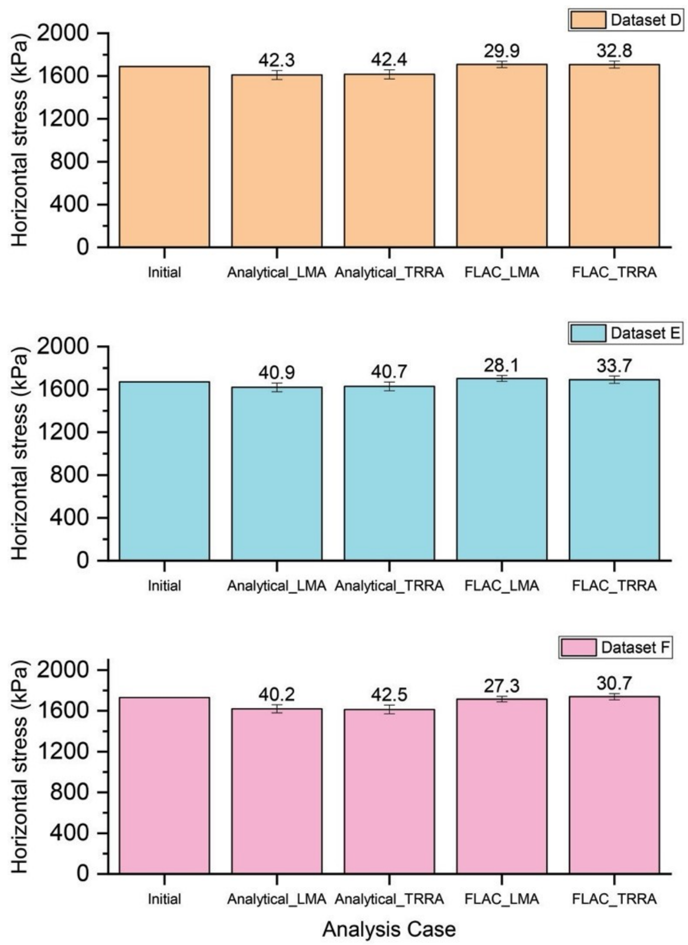

Figure 4.5 Initial and best datasets of horizontal stresses derived from the complete curve using closed-form solution and numerical model coupled with LMA and TRRA. Note: the number displayed on the top of SD bar is SD, unit: kPa.

Table 4.2 Optimal parameters from inverse analysis of expansion curve using LMA

Dataset	Optimal values using the closed-form solution				Optimal values using the numerical model			
	σ_h (kPa)	G (kPa)	S_u (kPa)	SSE	σ_h (kPa)	G (kPa)	S_u (kPa)	SSE
A	1736	9915	190	0.47	1713	15 289	178	0.43
B	1453	44 695	189	0.48	1488	44 997	174	0.45
C	1736	9915	190	0.47	1658	19 975	176	0.44

The SD bars for optimized dataset B in Figure 4.4 are absent because of the ill-conditioned Jacobian matrix caused by the overestimated G. The computational model predicted using dataset B is unstable. A small change in input leads to a significant difference in output. Therefore, dataset B presented in Table 4.2 should be discarded, although the predicted curve fits the measured data quite well.

For a pressuremeter test, σ_h draws the most attention because the soil stiffness and strength can be evaluated by other types of in-situ tests, such as the cone penetration test, standard penetration test, and field vane test. σ_h measures 1713 kPa, as identified from the numerical model in Table 4.2. Compared to the numerical model, the closed-form solution (1736 kPa) seems to overestimate σ_h slightly as well as S_u, and significantly underestimates G by 50%.

The parameters are not constrained when using the LMA. Although the LMA is the most popular algorithm for unconstrained NLLS curve-fitting problems, the TRRA is still necessary to constrain the parameters in the optimization process. Specifically, the limits of the soil stiffness and strength should be well defined to derive a reasonable horizontal stress, σ_h, from inverse analyses.

Table 4.3 Lower and upper bounds for the TRRA

Dataset	Horizontal stress (kPa)	Shear Modulus (kPa)	Undrained shear strength (kPa)
A	(1267; 2113)	(9000; 27 000)	(80; 240)
B	(1267; 2113)	(9000; 50 000) *	(80; 240)
C	(1267; 2113)	(9000; 27 000)	(80; 240)

*To compare with Jefferies (1988), the upper bound of the shear modulus for dataset B was relaxed to 50 000 kPa.

The TRRA was implemented in the minimization of objective functions for the inverse problems, as it can constrain the randomly generated variables within the defined bounds. Table 4.3 defines the initial variabilities of the geotechnical properties and in-situ horizontal stress with lower and upper bounds, which are calculated by assuming 50% deviations from the initial values in Table 4.1. The TRRA conducted a search around the neighbourhood constrained by the bounds defined in Table 4.3. The optimal parameters using the closed-form solution coupled with the TRRA were determined to be datasets A and C in Table 4.4. Although the Initial C (G_0, σ_{h0} , S_{u0}) differs from that of Initial A, only a negligible difference in G was observed between datasets A (9920 kPa) and C (9922 kPa). With bound constraints, the TRRA derived nearly identical optimal values to the LMA.

Table 4.4 Optimal parameters from inverse analysis of expansion curve using TRRA.

Dataset	Optimal values using the closed-form solution				Optimal values using the numerical model			
	σ_h (kPa)	G (kPa)	S_u (kPa)	SSE	σ_h (kPa)	G (kPa)	S_u (kPa)	SSE
A	1736	9920	190	0.47	1695	17 962	173	0.45
B	1456	44 116	189	0.48	1489	42 840	176	0.44
C	1736	9922	190	0.47	1703	16 314	178	0.43

By comparing the SSEs presented in Table 4.4, the optimal horizontal stress derived from the closed-form solution using the TRRA can be determined as 1736 kPa, and from the numerical modelling as 1703 kPa, respectively.

4.6.1.2 Inverse analysis of expansion curve using subset simulation algorithm

As a global optimization algorithm, the SS is implemented to compare the results from the two local optimizers, the LMA and TRRA. Dataset A in Table 4.3 is also used to define the bounds for the SS. With the number of samples N_s = 250, intermediate conditional failure probability $P(F_i)$= 0.1, and maximum number of simulation levels N_l = 5, the SS algorithm can derive the optimal parameters listed in Table 4.5. The global optimizer SS serves as a reliable reference for constraining the solution derived from the two local optimizers.

Table 4.5 Optimal parameters from inverse analysis of expansion curve using SS.

Optimal values using the closed-form solution				Optimal values using the numerical model			
σ_h (kPa)	G (kPa)	S_u (kPa)	SSE	σ_h (kPa)	G (kPa)	S_u (kPa)	SSE
1577	22 930	190	0.49	1680	16 546	166	0.48

4.6.2 Statistical inverse analysis of complete (expansion–contraction) curve

To study the effects of the contraction part on the inverse parameters, the complete expansion–contraction SBP testing curve AF85 P06-15 is utilized in the following inverse analyses.

Table 4.6 Initial parameters for inverse analysis of complete curve.

Dataset	Initial values (Initial)				
	σ_{h0} (kPa)	G_0 (kPa)	S_{u0} (kPa)	β	SSE
D	1690	18 000	160	0.83	1.81
E	1670	20 000	160	0.70	1.29
F	1730	16 000	150	1.30	1.88

Note: Initial values of D (Initial D) refer to Figure 10 in Jefferies (1988).
Initial values of E (Initial E) and F (Initial F) refer to Figures. 8a and 8b in Jefferies (1988).

The initial values of G, σ_h, S_u, and β for datasets D, E, and F in Table 4.6 are adopted from Figures. 8a, 8b, and 10 in Jefferies (1988), and β is defined as the softening or hardening coefficient during unloading in the SBP test. The optimal parameters after inverse analyses using the closed-form solution and the numerical model are presented in Table 4.7. In terms of the SSE in Table 4.7, dataset D is preferred to datasets E and F as the optimal dataset using the closed-form solution and numerical model coupled with the LMA. It can be observed that the SDs (see Figure 4.5) using numerical modelling appear to be lower than those using the closed-form solution, indicating that the prediction made by the numerical model has less uncertainty than the closed-form solution while simulating the entire expansion–contraction curve.

Table 4.7 Optimal parameters from inverse analysis of complete curve using LMA.

Dataset	Optimal values using the closed-form solution					Optimal values using the numerical model				
	σ_h (kPa)	G (kPa)	S_u (kPa)	β	SSE	σ_h (kPa)	G (kPa)	S_u (kPa)	β	SSE
D	1610	23 097	173	0.60	0.99	1709	15 344	180	0.79	0.49

E	1619	22 271	172	0.64	1.02	1702	15 536	183	1.03	0.59
F	1620	21 839	173	0.68	1.04	1715	16 677	170	0.93	0.61

Table 4.8 lists the lower and upper bounds of the TRRA. The optimal datasets using the TRRA are listed in Table 4.9. Similarly, Table 4.10 defines the bounds for the SS and Table 4.11 confirms the global minimum predicted by the two local optimizers.

Table 4.8 Lower and upper bounds for TRRA

Dataset	**Horizontal stress (kPa)**	**Shear Modulus (kPa)**	**Undrained shear strength (kPa)**	$\boldsymbol{\beta}$
D, E, F	(1267; 2113)	(9000; 27 000)	(80; 240)	(0.4; 1.5)

Table 4.9 Optimal datasets from inverse analysis of complete curve using TRRA.

Dataset	**Optimal values using the closed-form solution**					**Optimal values using the numerical model**				
	σ_h (kPa)	G (kPa)	S_u (kPa)	β	**SSE**	σ_h (kPa)	G (kPa)	S_u (kPa)	β	**SSE**
D	1616	23 109	171	0.58	0.99	1707	18 632	167	0.87	0.83
E	1628	22 269	169	0.65	1.03	1691	19 121	172	0.83	0.66
F	1614	22 983	172	0.56	1.00	1739	16 657	156	1.12	0.97

In terms of the derived values G, σ_h, and S_u in Table 4.7 and Table 4.9, different initial values of datasets D, E, and F have similar predictions to the closed-form solution or the numerical model, indicating the robustness of the inverse analysis approach used in this study.

Table 4.10 Lower and upper bounds for SS.

Horizontal stress (kPa)	**Shear Modulus (kPa)**	**Undrained shear strength (kPa)**	$\boldsymbol{\beta}$
(1267; 2113)	(9000; 27 000)	(80; 240)	(0.8; 0.9)

Table 4.11 Optimal parameters from inverse analysis of complete curve using SS.

Optimal values using the closed-form solution					Optimal values using the numerical model				
σ_h (kPa)	G (kPa)	S_u (kPa)	β	SSE	σ_h (kPa)	G (kPa)	S_u (kPa)	β	SSE
1616	24 124	169	0.88	1.04	1725	14 826	174	0.85	0.49

Compared with Figure 4.4, Figure 4.5 indicates that the prediction using the complete curve has lower uncertainty than using only the expansion curve for numerical models. There are two reasons to explain this advantage: (i) the complete curve provides more data points for the inverse analysis, leading to less uncertainty in the prediction, and (ii) the contraction curve is more reliable than the expansion part as the effect of installation disturbance becomes minimal at this stage (Ferreira, 1992; Houlsby and Withers, 1988).

The purpose of using the TRRA is to verify the conclusion made by the LMA and reduce the non-uniqueness caused by arbitrarily chosen parameters and local minimum values. In addition, the uniqueness of the solution can be better addressed through statistical assessments of the derived parameters. Thus, it is more meaningful to derive narrow CIs than "true values" from parameter estimation. The derived narrow CIs are valuable for quantifying the uncertainty of G, σ_h, and S_u for geotechnical design.

4.6.3 Uncertainty quantification of optimal inversed results

With one global optimizer and two local optimizers, the optimal parameters are derived from the initial datasets and their bounds. After the optimization process, the uncertainties from the parameter estimation can be quantified using the statistical assessment methods discussed in Section 4.4.3.

4.6.3.1 Summary of optimal inversed parameters and statistical assessments

Table 4.12 summarizes the derived mean and 95% CIs of G, σ_h, and S_u using the closed-form solution, whereas Table 4.13 shows the numerical model.

In Table 4.12, G appears to be underestimated, while σ_h is overestimated when using the expansion curve only, and vice versa for the complete curve. The closed-form solution tends to be nonconservative in interpreting pressuremeter tests because of oversimplifications in geometry and boundary conditions.

Compared to Table 4.12, the wide distribution in predicted shear modulus (G) values provided in Table 4.13 can be observed within the confidence intervals given for the expansion curve. This indicates that the numerical model is more sensitive to G than the closed-form solution. This is likely due to an apparent Poisson's ratio of 0.49 in the undrained analysis, which causes the clay material to be nearly incompressible in the numerical model. In contrast, static equilibrium, given a Poisson's ratio close to 0.5, does not need to be reached in the closed-form solution as it does in the numerical model.

From Table 4.13 it is interesting to note that the numerical model provides similar mean values of G, σ_h, and S_u for the expansion and complete curves. By contrast, the estimated 95% CI for the expansion curve is much wider than that for the complete curve. Again, the wider CI band for the expansion curve accounts for the uncertainties in the early stage of expansion. Therefore, the complete curve can provide a more reliable prediction than the expansion curve.

Table 4.12 Optimized parameters after inverse analysis of the expansion curve using the closed-form solution

Type	Predicted values	Horizontal stress (σ_h) (kPa)	Shear modulus (G) (kPa)	Undrained strength (S_u) (kPa)	β
Expansion curve	**mean**	1736	9915	190	-
	95% CI	(1652; 1820)	(5412; 14 418)	(180; 199)	-
Complete curve	**mean**	1610	23 097	173	0.60
	95% CI	(1526; 1695)	(13 365; 32 828)	(165; 182)	(0.0; 1.3)

Table 4.13 Optimized parameters after inverse analysis of complete curve using numerical model.

Type	Predicted values	Horizontal stress (σ_h) (kPa)	Shear modulus (G) (kPa)	Undrained strength (S_u) (kPa)	β
Expansion curve	mean	1713	15 289	178	-
	95% CI	(1593; 1832)	(6263; 24 315)	(164; 193)	-
Complete curve	mean	1709	15 344	180	0.79
	95% CI	(1649; 1769)	(11 638; 19 050)	(172; 188)	(0.53; 1.05)

4.6.3.2 Validation of optimized parameters

By examining Table B.1 in Appendix B, the value of σ_h (1690 kPa) deduced from the modified inspection technique (Jefferies, 1988) basically agrees with the corresponding values (1713 kPa and 1709 kPa), as shown in Table 4.13, Table 4.12 shows a slightly higher or lower value of σ_h than that in Table B.1. The mean of S_u (182 kPa) in Table B.1, which was estimated from the SBP curve using the linear regression method, approximately coincides with those in Tables 4.12 and 4.13. The values of G (13 730 kPa and 11 230 kPa) deduced from the triaxial test curve lie roughly within the 95% CI (between 11 638 kPa and 19 050 kPa) predicted by the complete curve (Table 4.13). Simultaneously, the gradient of the unloading–reloading loop in Figure B.3 illustrates a significant increase in stiffness, which may have resulted from the drainage occurring near the probe during this stage (Clarke, 1995). The ratio of shear strength β is identified as 0.79, which approximately coincides with 0.8, as shown in Table B.1. Owing to the advantages of runtime efficiency, it is recommended to conduct a closed-form solution coupled with an optimizer (LMA or TRRA) before performing additional numerical simulations. To determine σ_h, the expansion part of the pressuremeter curve may be sufficient for conducting an appropriate inverse analysis. The complete expansion–contraction curve can be used to investigate the unloading effects on soil properties and provide narrower 95% CIs.

4.6.3.3 Evaluation of model fit with coefficient of determination

Although the statistical values listed in Tables 4.12 and 4.13 provide quantitative assessments of the inversed parameters, visual comparison of the predicted and observed curves adopted by Jefferies (1988) is still meaningful in evaluating the model fit as a final check.

Figure 4.6 and Figure 4.7 illustrate the observed data from test AF85P06-15 (Jefferies, 1988) and the data predicted using analytical and numerical models. The goodness of fit can also be quantified using the coefficient of determination R^2, which is defined as

$$R^2 = 1 - \frac{SSE}{SST} \tag{4.8}$$

where SSE represents the sum of squared errors, as defined in Equation 4.1, and SST indicates the total sum of squares.

$$\mathrm{SST} = \sum_{i=1}^{n}(Y_i - \bar{Y})^2 \tag{4.9}$$

where Y_i denotes observed data, and $\bar{Y}$ represents the mean of observed data.

R^2 can take any value between 0 and 1, with a value equal to 1 indicating the model prediction exactly matches the observed data. Using only visual comparison, it is challenging to make an unbiased judgment of which dataset is the best fit. Therefore, the SSE, SD, and R^2 can evaluate the model fit numerically, which is independent of an observer.

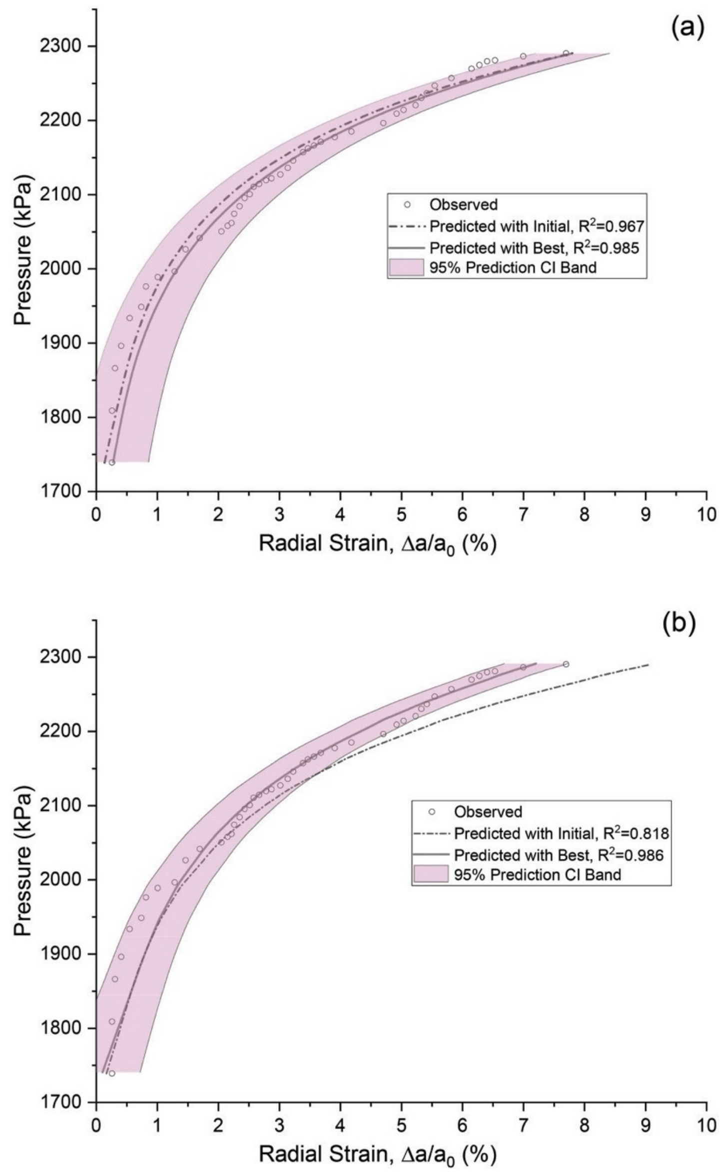

Figure 4.6 Fit of observed data to predicted data using the expansion curve for test AF85P06-15 (Jefferies 1988): (a) predicted with closed-form solution and (b) predicted with numerical model

In terms of R^2 in Figure 4.6a and Figure 4.7a, the best values predicted by the closed-form solution achieve a slightly better fit for the observed data compared to the estimates (initial A in Table 4.1) proposed by Jefferies (1988). Whereas there are significant deviations observed in Figure 4.6b and Figure 4.7b, implying that the best values predicted by the numerical model achieve a significantly better fit than the initial dataset A. The best-fit dataset evaluated with the closed-form solution does not necessarily apply to the numerical model.

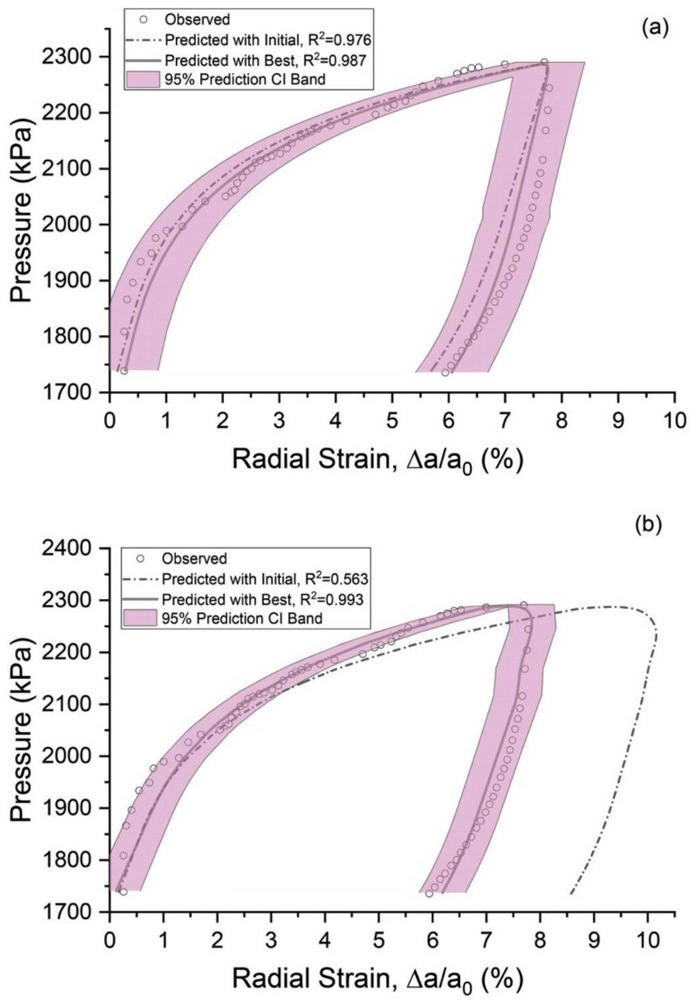

Figure 4.7 Fit of observed data to predicted data using the complete curve for test AF85P06-15 (Jefferies, 1988): (a) predicted with closed-form solution and (b) predicted with numerical model

Jefferies (1988) emphasized the match at the early stage; however, the observed data may be significantly affected by the disturbance of the adjacent soil during SBP installation. The 95% prediction interval (shaded bands in Figure 4.6 and Figure 4.7) provides the lower and upper bounds of the predicted data. The wider band at the early stage of expansion reveals more uncertainties in the curve fitting because of the disturbance caused by tool installation. The narrow band at a later stage verifies the viewpoint proposed by Ferreira (1992) that the latter part of the loading stage is more reliable. Thus, in terms of R^2 and the width of the band, Figure 4.7b shows the best fit for the observed data and corresponding prediction interval.

4.7 Summary and Conclusions

Traditionally, the interpretation of pressuremeter tests has focused on the derivation of soil properties using graphical plotting or curve fitting methods in a deterministic manner. Therefore, the interpreted parameters are usually expressed as the "best" dataset, which may be biased because they fail to account for uncertainty and errors related to soil or rock spatial variability, measurement errors, limited information, and model uncertainty. The proposed statistical approach can employ analytical and numerical models coupled with selected optimization algorithms to quantify the effects of uncertainty and errors on the derived soil properties and horizontal stress. To perform the parameter estimation for an SBP test in clay, both the closed-form solution (Jefferies, 1988) and numerical modelling coupled with three optimization algorithms were adopted in the inverse analyses.

The closed-form solution was used for the initial assessments owing to its computational efficiency. The two-dimensional numerical model can provide more realistic estimates of in-situ parameters. To verify the parameters derived from the inverse analyses, data from the SBP and triaxial tests were also interpreted using graphical plotting and linear-fit regression methods. Finally, the variability of the optimized datasets derived from inverse analysis can be described using the mean, SD, and 95% CIs. The quality of the curve fitting can be quantified using R^2 and prediction intervals.

To minimize non-uniqueness, (i) various optimisation algorithms should be implemented; (ii) the statistical assessment may be unable to improve the accuracy of the predicted mean but can provide precise lower and upper bounds within which the true values may lie; and (iii) other types of laboratory and in-situ tests, such as triaxial and field vane tests, can provide more constraints on the predicted parameters with relatively narrow bounds.

Compared with an analytical solution, a numerical model can simulate an SBP test as a two-dimensional cylindrical cavity expansion, which is similar to a real pressuremeter test. As oversimplification and idealization in the closed-form solution can lead to significant errors in the derived soil properties (Yu, 2006), the numerical model adopted here can identify reasonable combinations of parameters, as presented in this research.

In the future, the statistical inversion code will be extended to consider uncertainties from tool calibrations, installation disturbance, and irregular cavity geometry, as well as a more complex numerical model that considers partial drainage, soil anisotropy, and inhomogeneity using solid and fluid coupling methods (Yin et al., 2021).

Compared with conventional pressuremeter interpretation methods, the proposed statistical inverse analysis can quantify the potential uncertainty and errors from the ground properties and in-situ horizontal stress. Minimization of the objective function with multiple optimizers can reduce the degree of non-uniqueness encountered using conventional methods. Compared with the expansion curve only, the complete curve can predict a more reasonable mean and narrower 95% CIs in the inverse analysis. Statistical assessments of the optimal parameters were used to evaluate the statistics defined by SD and CIs. In addition, the model fitness can be further evaluated using R^2 and prediction intervals. The uncertainties propagated from the ground properties and computational modelling can be quantified statistically.

The statistical methodology described above can be extended to other engineering inverse analysis problems, such as the calibration of constitutive models and inverse analysis of in-situ stress fields for horizontal drilling, tunnelling, and hydraulic fracturing.

5.0 BAYESIAN APPROACH FOR UNCERTAINTY QUANTIFICATION OF IN-SITU HORIZONTAL STRESS AND GEOTECHNICAL PARAMETERS WITH PRESSUREMETER[2]

5.1 Introduction

Knowledge of in-situ horizontal stress for the evaluation of the coefficient of at-rest earth pressure K_0, expressing the ratio between the horizontal and vertical effective geostatic stresses, is indispensable in the design of retaining structures or laboratory-reproduced stress path tests. The pressuremeter has gained increasing attention over the last decades as it could help to determine the anisotropic stress field and soil properties in situ. However, quantification of inversed properties uncertainty remains an outstanding challenge. The frequentist statistical approach was shown to be effective in quantifying the uncertainty from parameter estimation using a self-boring pressuremeter (SBP) test in clay (Zheng et al., 2021). However, a major downside of the frequentist approach is that it is a closed system unable to be continuously updated with new data. On the contrary, a Bayesian approach is an open system with significant advantages in quantifying the parameter uncertainty and utilization of prior knowledge. Prior knowledge of in-situ stress magnitude and geotechnical parameters is obtained from external information sources such as analogue engineering design, geologic environment, and expert judgement. An objective function is formulated to evaluate the logarithm of the probability density function (PDF) by incorporating observed and predicted data. Both the analytical solution and the finite difference numerical model are coupled with sampling algorithms. The Bayesian inference consists of two parts: first, the maximum a posteriori (MAP) method is used to perform a quick point estimation, and then followed by the Markov Chain Monte Carlo (MCMC) simulation to obtain parameter statistics by sampling posterior distributions. Through the Bayesian scheme, prior knowledge is reconciled with the project-specific pressuremeter

---

[2] A version of this chapter has been published: Zheng, D., B. Zhang, and R.J. Chalaturnyk, 2024. Quantifying Uncertainty of In-Situ Horizontal Stress and Geotechnical Parameters Using a Bayesian Inference Approach for Pressuremeter Tests. Canadian Geotechnical Journal. Just-IN https://doi.org/10.1139/cgj-2023-0686

testing data and final posterior distributions of uncertain parameters are summarized from sampling the MCMC chains. In addition, model fit is evaluated with the coefficient of determination R^2, and prediction uncertainty is visualized with the HDI band. Given this new evidence, the posterior distributions can be updated using Bayesian inference. The most outstanding advantage of the proposed Bayesian approach is that it can continuously update one's belief with new data through an open system, which is superior to the frequentist statistical methods so far employed for in-situ horizontal stress studies.

5.2 Background

As an in-situ testing tool, the pressuremeter has gained increasing attention over the past several decades (Clarke, 1995; Gibson and Anderson, 1961; Mair and Wood, 1987; Yu, 2006). With the analysis of the pressuremeter test, soil strength and stiffness, in-situ horizontal stress, and consolidation characteristics of soils can be estimated from the measured data (Jefferies et al., 1987; Elwood et al., 2015; Liu et al., 2017). Conventionally, there are two major ways to estimate the in-situ horizontal stress and geotechnical parameters, which are graphical plotting (Houlsby and Withers, 1988; Marsland and Randolph, 1977) and curve-fitting methods (Jefferies, 1988; Ferreira, 1992). Zheng et al. (2021) discussed these two methods and pointed out that the drawback of graphical plotting is its dependence on individual interpreters (Clark, 1995), and the curve-fitting method may lead to a non-unique solution (Houlsby, 1989). The issue mentioned above can be attributed to soil variability, measurement errors, and uncertainties in a computational model. To solve the problem of non-uniqueness encountered in the analysis of the pressuremeter test, Zheng et al. (2021) proposed a frequentist statistical approach to quantify the uncertainties existing in the parameter estimation for a pressuremeter test.

Uncertainty quantification plays a vital role in the risk assessment of geotechnical structures (Chen and Cui, 2017; Cui et al., 2017; Ganesh et al., 2020; Zhang et al., 2021; Zheng et al., 2022). With the transition from working stress design (WSD) to full probabilistic analysis, uncertainty quantification of geotechnical parameters helps to assess soil variability, measurement errors, and computational models.

In addition to the frequentist statistical framework presented by Zheng et al. (2021) in the geotechnical context, the Bayesian inference method can deal with data in events occurring in a sequence, such as observed data from a monitoring system. Unlike the frequentist approach, whose probability is based on repeatable trials and pooling all the available data together, the Bayesian approach is based on Bayes' theorem by utilizing external prior (expert judgement, experience, and published information) with evidence (observed data) on each stage to conclude a parameter (posterior prediction). The posterior distributions can be obtained with the Bayesian inference on the pressuremeter test, and later, the posterior belief can be updated again with the triaxial tests if they are performed. The belief from Bayesian inference is subject to change with data. Under the Bayesian paradigm, the highest density interval (HDI), analogous to the confidence interval (CI) in frequentist statistics, can be inferred from Markov chain samples to define the lower and upper bounds of the identified parameters. Notably, the mean and its statistics can be continuously updated through Bayesian inference with new data.

Over the past decades, Bayesian inference has been extensively applied in the evaluation of soil and rock properties with laboratory and in-situ tests. Zhang and Liu (1995) analytically inferred posterior probabilistic distribution with conjugate priors based on Bayes' theorem. With the small dataset and little knowledge of prior probability distribution function (PDF), Yan et al. (1997) inferred the posterior distribution of mechanical properties of rock samples based on Bayes' method. By approximating the posterior PDF, Wang et al. (2010) derived the probabilistic characterization of sand friction angles using cone penetration test (CPT) data. Cao and Wang (2014) probabilistically estimated undrained shear strength using a limited number of liquid index test data by selecting the most appropriate likelihood model in Bayesian inference. Wang and Cao (2013) conducted a probabilistic characterization of undrained Young's modulus based on the MCMC simulation. In addition, Cao et al. (2016) proposed a Bayesian sequential updating approach to characterize soil properties based on the over-consolidation ratio (OCR), standard penetration test (SPT), and CPT data. Bozorgzadeh et al. (2019) adopted a non-linear hierarchical Bayesian model to update rock strength by combining data from different sources. Besides the determination of soil or rock properties, the Bayesian approach has been widely used in other areas. Juang et al. (2013) back-analyzed and updated soil parameters for braced excavations using field observation with Bayesian updating methods. Wang et al. (2016) developed a Bayesian inverse model for probabilistic site characterization. Prior information and project-specific observation are combined in this Bayesian approach. Spatial variability of soil properties is addressed to estimate the posterior distribution of the compression modulus at unsampled locations. Zhang et al. (2009) calibrated a Bayesian model using centrifuge tests to study soil slopes under rainfall conditions. Feng et al. (2020) conducted a Bayesian analysis for the uncertainty quantification of in-situ stress magnitude and orientation using overcoring datasets. However, to the best of the author's knowledge, there are few publications about the Bayesian analysis of a pressuremeter test.

With the Bayesian inference methods, the prior knowledge can be reconciled with the project-specific pressuremeter testing data. This solution can overcome the issue of limited testing data in pressuremeter tests by including the previous knowledge and data available in past projects and research. However, previous researchers' (Wang et al., 2010; Juang et al,. 2013; Cao and Wang, 2014) implementation of a simple linear function in the Bayesian analysis may be an oversimplification compared to a more realistic strictly deduced closed-form solution or a well-built numerical model. Consequently, it hurdles the widespread use of the Bayesian inference technique in geotechnical engineering practice and research. Two aspects need to be addressed: (i) a simple linear function usually cannot properly simulate a pressuremeter test due to the complex in-situ testing conditions. It is agreed that only a strictly deduced closed-form solution (Jefferies, 1988) or a robust numerical model (Ferreira, 1992) can adequately simulate a pressuremeter test. Therefore, the critical step in this study is to effectively implement an analytical solution or a numerical model in the Bayesian framework; (ii) Bayesian inference is usually computationally costly compared to traditional deterministic approaches. To accomplish the Bayesian inference task efficiently is another challenge the geotechnical researchers and practitioners must encounter.

To incorporate a strictly deduced closed-form solution or a well-built numerical model into the Bayesian framework, an objective function must be properly formulated. If a numerical simulation is needed, the numerical model should be balanced between efficiency and accuracy. For example, usually a simplified 2D model is used in the pressuremeter numerical analysis (Yeung and Carter, 1990; Liu et al., 2017). The geometry shall be as simple as possible while preserving the key structural elements, and the main features of stress and strain responses can be reproduced at the same time.

Bayesian inference of unknown parameters includes a point estimate with the maximum a posterior (MAP) and a complete Bayesian analysis aiming at the full posterior distributions. Like the frequentist maximum likelihood estimation (MLE), MAP is a point estimator in a Bayesian setting. By default, a local optimization algorithm, such as the Broyden–Fletcher–Goldfarb–Shanno (BFGS) (Kelley, 1999), is used to find the maximum log-posterior in the point estimation. Although the MAP estimator is fast and efficient, only a single parameter can be estimated without the associated parameter uncertainty. Another limitation of a point estimate is the potential solution trapping in the local minimum in high-dimensional posteriors (Salvatier et al., 2016).

Alternatively, the complete Bayesian analysis approach can ensure the global minimum and obtain posterior statistics by summarizing realizations from Markov chains. The MAP tends to estimate the parameters under assumed parametric probability distributions. In contrast, the complete Bayesian analysis aims to report the posterior mean together with the HDI regardless of the target distribution shape.

Compared to frequentist inference, Bayesian inference has the advantage of an open system, whose degrees of belief are subject to changes with new data. In this study, posterior statistics inferred from pressuremeter tests can be continuously updated with new evidence from other laboratory and in-situ tests.

5.3 Methodology

The goal of a pressuremeter test is to record the changes in the applied pressure and radial displacements or cell volume during the expansion and contraction stages. A pressuremeter testing curve analysis is to estimate the values of in-situ horizontal stress and soil parameters for geotechnical design and research. With the observed data from the pressuremeter test, the MAP point estimate approach is first used as a preliminary estimate of in-situ horizontal stress and soil parameters and followed by the complete Bayesian analysis, which summarizes the samples drawn from the posterior distribution after MCMC simulation.

Both MAP optimization and MCMC simulation require a probability distribution for prior input parameters. Prior knowledge of ground properties and in-situ horizontal stress can be taken from analogous case studies, measurements, etc. This study assumes bounded uniform distributions for all prior input parameters in the MAP and MCMC simulation. To simulate a pressuremeter test, an analytical (closed-form solution) or a numerical model shall be adopted in the Bayesian inference. A computational model in Bayesian modelling is implemented in a likelihood function formulated with the observed and predicted data.

For the MAP, the dataset that maximizes the likelihood function corresponds to the optimal point estimates. In MCMC, a sampling algorithm proposes a random move in the model space, which is then passed to the likelihood function. Relative comparison between the likelihoods from the previous and current steps shows which one explains the data better. In the general case, likelihoods and priors at the current proposed and the previous steps are evaluated through the acceptance probability. In case of rejection, the model parameters at the current step retain the values from the previous step and are saved in the chain. Conversely, accepting the new proposed model parameters places them into the chain and sampling proceeds to the next realization.

After drawing from sufficiently large set samples, the convergence of MCMC chains could be evaluated with diagnostics criterion. Once the chain is converged, its elements can be accepted as samples from the target posterior distribution, and statistics can be summarized from those samples, from which the mean and HDIs are the key. The workflow for the proposed Bayesian inference of the pressuremeter test is shown in Figure 5.1. The framework of the Bayesian inference includes, but is not limited to, the following steps: (i) a priori knowledge of initial values and uncertainty quantification of input variables, (ii) selection of a computational model and coupling with an MCMC sampling algorithm, (iii) establishing a likelihood function as the objective function, (iv) identification of the optimal value (the MAP) or the mean and its statistics from posterior distributions (the MCMC) by maximizing the log-likelihood function, and (v) convergence diagnostics.

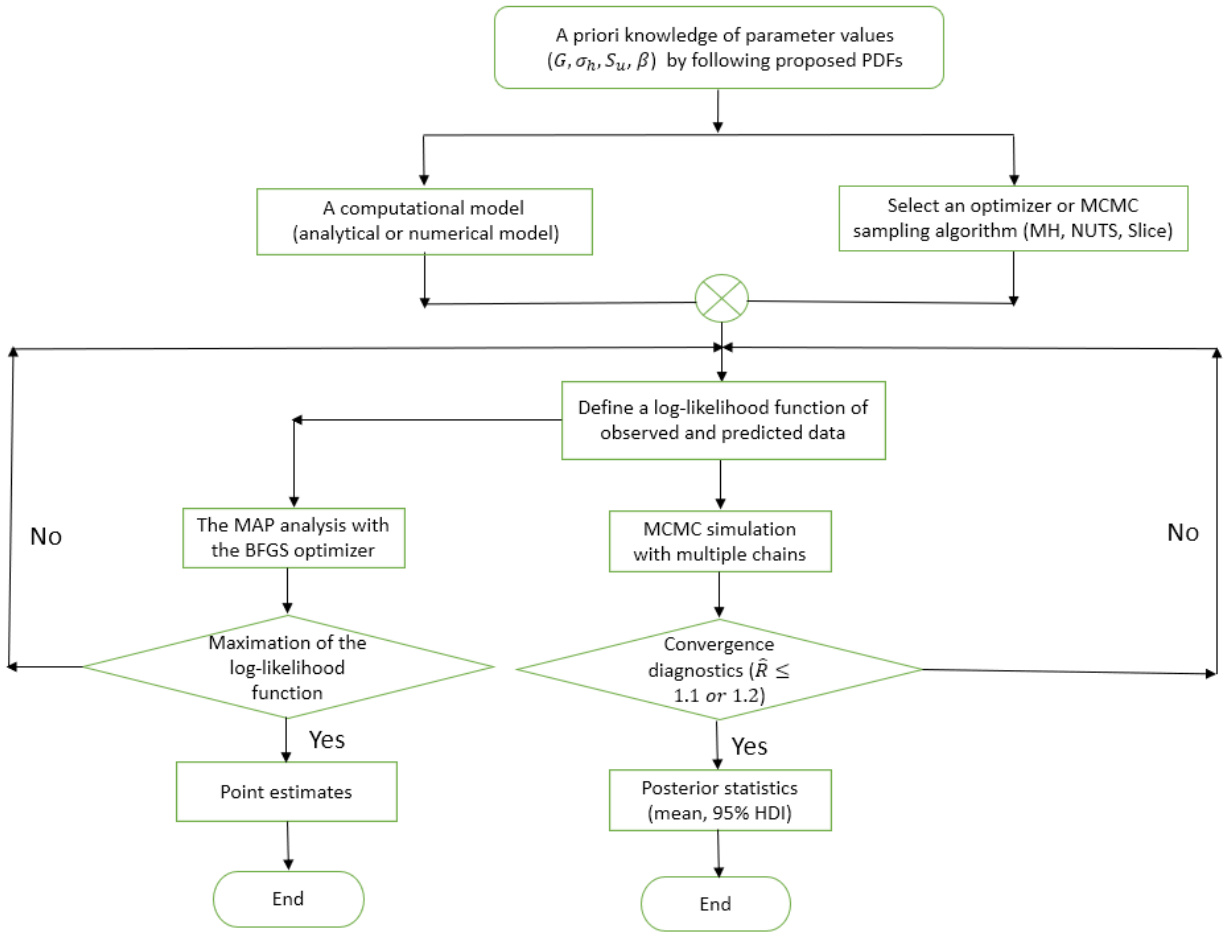

Figure 5.1 Flow chart of Bayesian inference of a pressuremeter test.

5.3.1 Objective function

Both in stochastic sampling and optimization, the maximization of the likelihood function is equivalent to the minimization of an objective function. A log-likelihood function can be formulated as the objective function in the searching process of the BFGS algorithm or the iterative convergence of MCMC chains. Given a normal distribution, the log-likelihood function l can be defined as in Equation 5.1 (Taboga, 2017):

$$l(\mu(\theta),\ \sigma^2;\ y) = -\frac{n}{2}ln(2\pi) - \frac{n}{2}ln(\sigma^2) - \frac{1}{2\sigma^2}\sum_{j=1}^{n}\left(y_j - \mu(\theta)\right)^2 \tag{5.1}$$

where y = $(y_1, y_2, \dots, y_n)$ denotes observed data; μ indicates predicted data; θ denotes unknown parameters, and σ represents the standard deviation. n represents the number of observed data from a pressuremeter test. The parameters $\hat{\theta}$ can be estimated by maximizing the specific log-likelihood function $\hat{l}$ over the parameter space Θ:

$$\hat{\theta} = \arg\max_{\theta\in\Theta} \hat{\ell}(\mu(\theta), \sigma^2; y) \tag{5.2}$$

Similarly, log-likelihood functions for other distributions like Poisson, exponential, and student t distribution can be derived. The log-likelihood function like Equation 5.1 makes the MAP and complete Bayesian analysis easier by implementing an analytical or numerical model in Bayesian inference.

5.3.2 Assumptions and sources of uncertainties

A typical SBP testing curve is composed of the applied pressure and volume changes or radial displacements as illustrated in Figure 5.2. A complete testing curve includes the expansion part, contraction part, and loops if unloading-reloading cycles are performed. Sometimes, hold tests are conducted to investigate the characteristics of hydraulic consolidation.

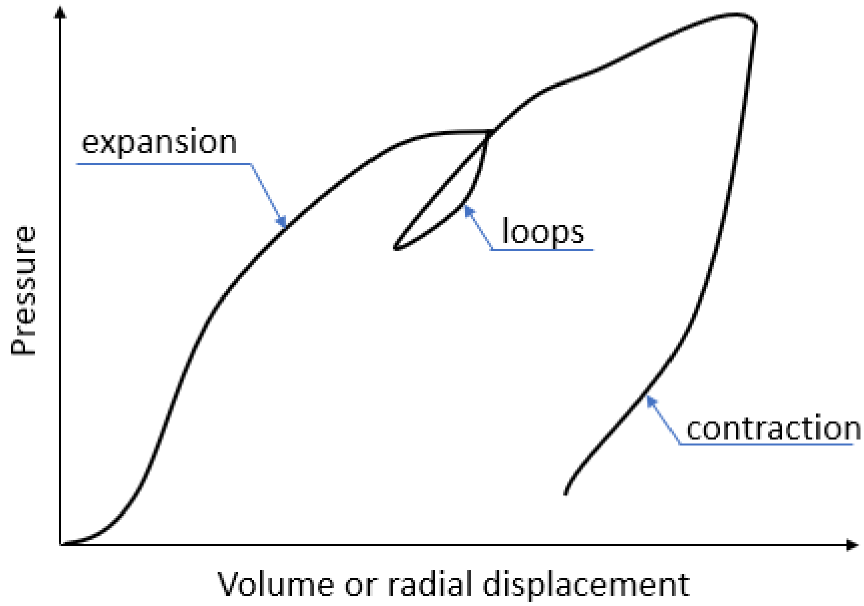

Figure 5.2 A typical SBP testing curve.

The self-boring pressuremeter (SBP) test in Canadian Arctic offshore site investigations (Jefferies et al., 1987) is re-analyzed with the Bayesian inference methods discussed above. To simplify the theoretical analysis and numerical modelling of the SBP test, the effect of the finite pressuremeter length is not considered. The SBP test in the saturated clay is simulated with a cylindrical cavity expansion model in an infinite medium. Owing to the low permeability of clay and impermeability of the pressuremeter membrane, the simulation of stress and pore pressure responses to the expansion of a pressuremeter can be assumed in undrained conditions. Therefore, the Tresca model is adopted to reproduce the constitutive behaviour of the clay around the borehole wall. The isotropic in-situ horizontal stress regime is assumed as Jefferies (1988) only provided the averaged radial displacements. The anisotropy of the in-situ horizontal stress regime can only be derived from the radial displacements measured at multiple azimuthal angles.

The primary sources of uncertainty are measurement errors, soil spatial distribution, and boundary conditions. Here, we focus on variabilities of in-situ horizontal stress, soil stiffness and shear strength in the Bayesian inference analysis.

The analytical solution proposed by Jefferies (1988) is adopted in the current work. However, the numerical model in their study is further simplified due to the extensive computational costs required by the MCMC simulations. The details of the simplified numerical model are explained in Section 5.4.3.

The proposed Bayesian inference method can accommodate parameter uncertainty and aid in pressuremeter test interpretation. The MAP can be performed to obtain a quick preliminary point estimation of the unknown parameters. The complete Bayesian analysis can provide posterior distributions of in-situ horizontal stress and soil parameters with statistics on the estimated parameters summarized as the confidence bounds and the mean values. In addition, the posterior probability can be continuously updated on new data from laboratory and field tests.

5.4 Case Study – Self-Boring Pressuremeter Tests at Amauligak F-24 in Canadian Arctic

5.4.1 Introduction

Jefferies et al. (1987) carried out SBP tests in Canadian Arctic offshore site investigations from 1982 to 1985. Jefferies (1988) presented his analysis of in-situ horizontal stress and soil parameters for the SBP test at Amauligak F-24 using a deterministic curve-fitting method. The SBP testing data was re-analyzed by Zheng et al. (2021) with a frequentist statistical inverse analysis method. This study adopts the Bayesian inference approach to estimate the mean values of in-situ horizontal stress and soil parameters and their statistics from posterior distributions. In addition, data from the interpretation of triaxial and SBP tests presented by Jefferies (1988) and Zheng et al. (2021) are used as new evidence to update the posterior belief after the Bayesian inference.

5.4.2 Project background

The Amauligak F-24 site is located 32 m below sea level. The testing pocket is in a massive stiff clay unit (D1) approximately 40 m below the mud line. The SBP testing data published by (Jefferies, 1988) are utilized for the Bayesian analysis of the SBP testing in clay at this site. The soil profile for the SBP test is briefed by Zheng et al. (2021). The information presented by Jefferies et al. (1987) provides a priori belief for the following Bayesian analyses of this SBP testing.

The geotechnical investigation details can be referred to the relevant documents (Jefferies et al., 1987; Jefferies, 1988).

5.4.3 Numerical simulation of an SBP test

The SBP testing in clay can be treated as a cylindrical cavity expansion and contraction in Tresca material. The closed-form solutions proposed by Jefferies (1988) and a finite-difference model are adopted as computational models in Bayesian inference. Due to the high computational demand for the MCMC simulation, a simple finite-difference model is proposed. Figure 5.3 illustrates the axisymmetric finite-difference discretized domain and plane-strain boundary conditions. The present study applied FLAC, a commercial two-dimensional explicit finite-difference program (Itasca, 2011), to model the SBP test in clay.

The axisymmetric finite-difference model shown in Figure 5.3 is more efficient than the model in Figure 2 (Zheng et al., 2021). The axisymmetric model shown in Figure 5.3 is applied in the case study to simulate the assumed isotropic in-situ horizontal stress as radial strains presented by Jefferies (1988) are calculated from the average radial displacements. The numerical model has fixed top and bottom boundaries, and the effects of vertical stress on parameter estimation are neglected.

The Mohr-Coulomb model is selected as the constitutive model for the clay in the SBP test. Under undrained conditions, the plastic strength of the clay in Unit D1 is represented by the Tresca criterion (e.g., undrained shear strength S_u and friction angle $\varphi = 0°$). In the contraction stage, the effect of unloading on the weakened strength of the clay is evaluated by a softening index β in the numerical model.

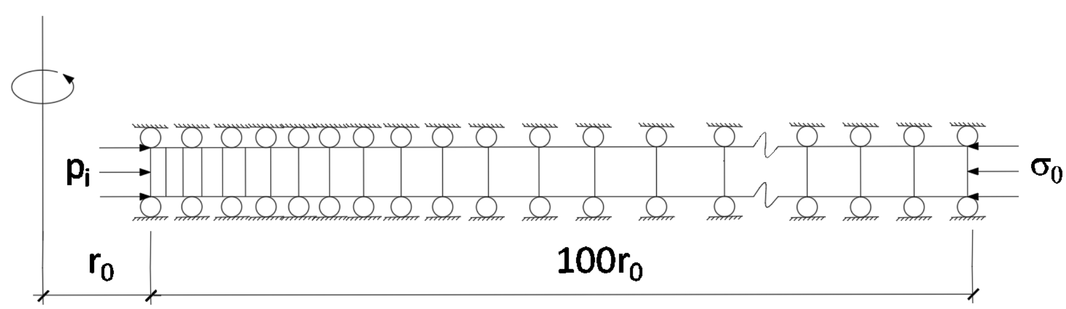

Figure 5.3 Discretized domain and boundary conditions for axisymmetric finite-difference model. Note: r_0 = 41 mm.

Random variables, horizontal stress (σ_h), shear modulus (G), and undrained shear strength (S_u), were generated through a sampling algorithm in the Bayesian inference. These random variables were used as the input parameters for the analytical and finite-difference FLAC models. The maximization of the objective function formulated as Equation 5.1 was solved by coupling the analytical or the FLAC model with an optimizer in the MAP or a sampler in the MCMC simulation.

5.4.4 Bayesian inference analysis of complete curve

A complete pressuremeter test curve consists of expansion and contraction stages. To understand the effects of unloading during the contraction stage upon the parameter estimates from Bayesian inference, the complete expansion-contraction SBP testing curve AF85 P06-15 is utilized in the following Bayesian analyses. Two computational models, the analytical model proposed by Jefferies (1988) and the axisymmetric finite-difference model shown in Figure 5.3, are coupled with the BFGS optimizer in the MAP or the slice sampler in the MCMC simulation. The PDFs of prior parameter values (G, σ_h, S_u and β) for the MAP and MCMC simulations are defined with previous publications and expert experience, as illustrated in Figure 5.4 (analytical) and Figure 5.5 (numerical).

5.4.4.1 Point estimation with MAP for complete curve

As discussed above, MAP is equivalent to MLE when the prior follows a uniform distribution. The local optimizer BFGS in the MAP analysis of the complete curve is used to find the optimal parameter values shown in the Figures. 5.4 and 5.5. By examining the point values predicted by the analytical model in Figure 5.4, we can see the estimate of β is very close to the upper or lower bound. Whereas the numerical model can provide an estimation close to the mean value (see Figure 5.5). In addition, β = 0.85 proves the unloading effects on the shear strength softening during the contraction stage in an SBP test. Usually, the MAP gives a quick point estimation of the analytical and numerical models. However, to verify the results of the MAP using the local optimizer BFGS, the complete Bayesian analysis with MCMC simulations shall be performed. The extreme values predicted by the analytical model are owing to its sensitivity to parameter changes during the optimization.

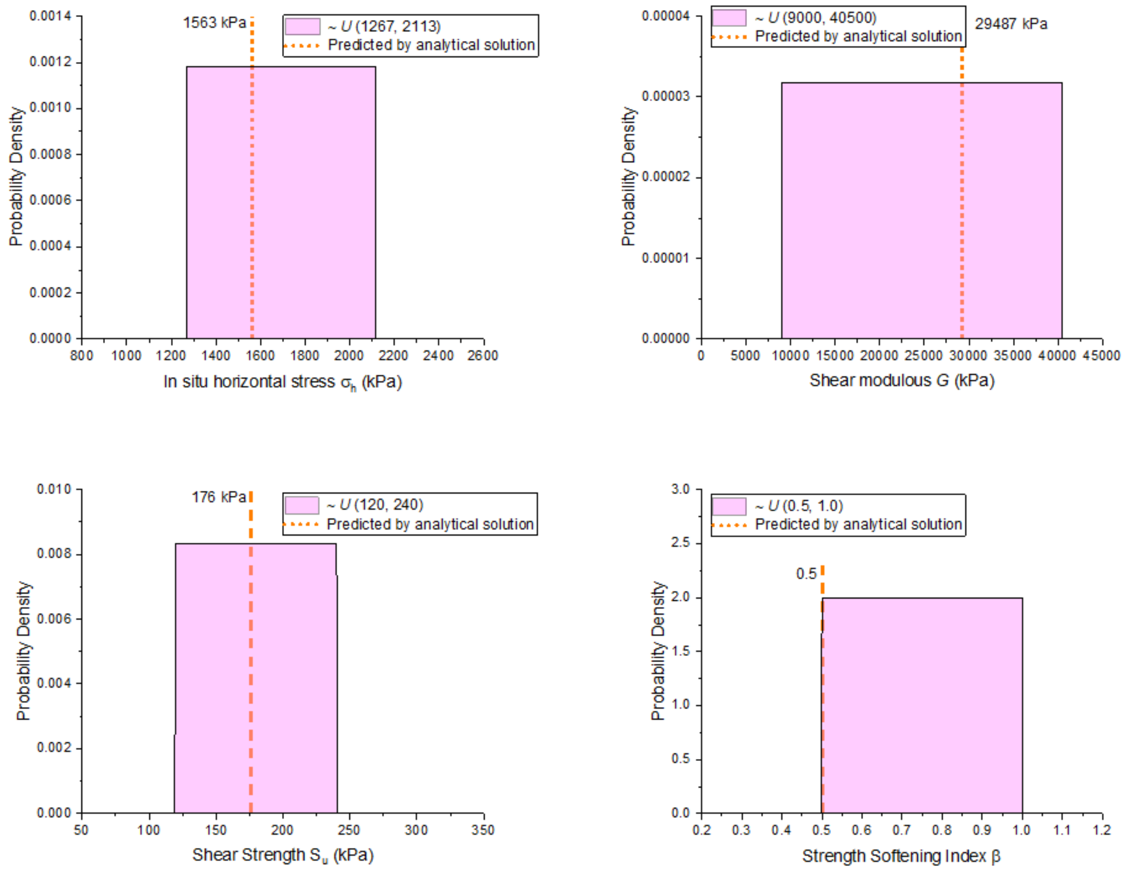

Figure 5.4 PDFs and Point estimates from MAP analysis of the complete curve using an analytical solution. Note: $\sim U(a, b\ )$ denotes uniform distribution.

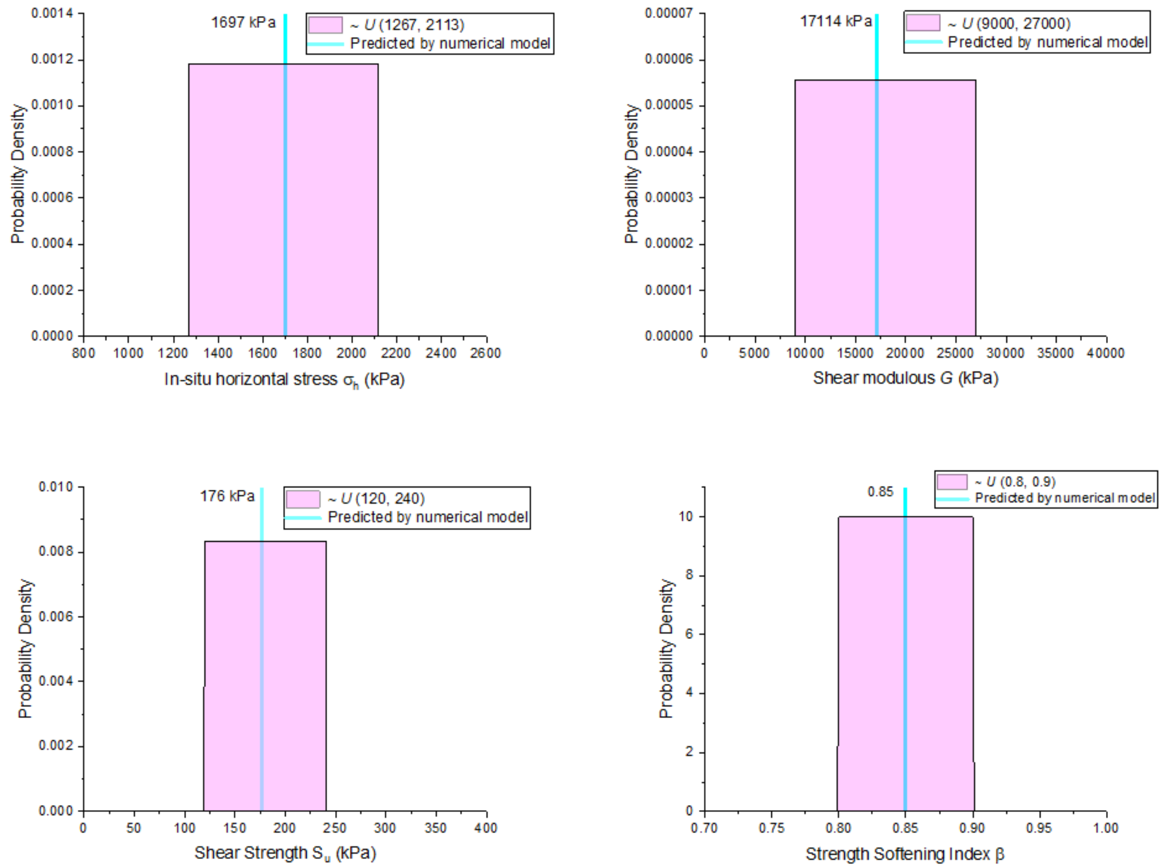

Figure 5.5 PDFs and Point estimates from MAP analysis of the complete curve using a numerical model. Note: $\sim U(a, b\ )$ denotes uniform distribution.

5.4.4.2 MCMC simulation of the complete curve using the analytical model

To carry out the complete Bayesian analysis, MCMC simulation is performed using the slice sampler coupled with the analytical model (Jefferies, 1988). Figure 5.4 illustrates the prior parameter distributions for the MCMC simulations. To account for the strength-softening behaviour of clay at the contraction stage, the additional parameter β proposed by Jefferies (1988) is included in the analytical model. The MCMC sampling is carried out with two MCMC chains: each of them consisting of 2000 draw iterations and 1000 tuning samples.

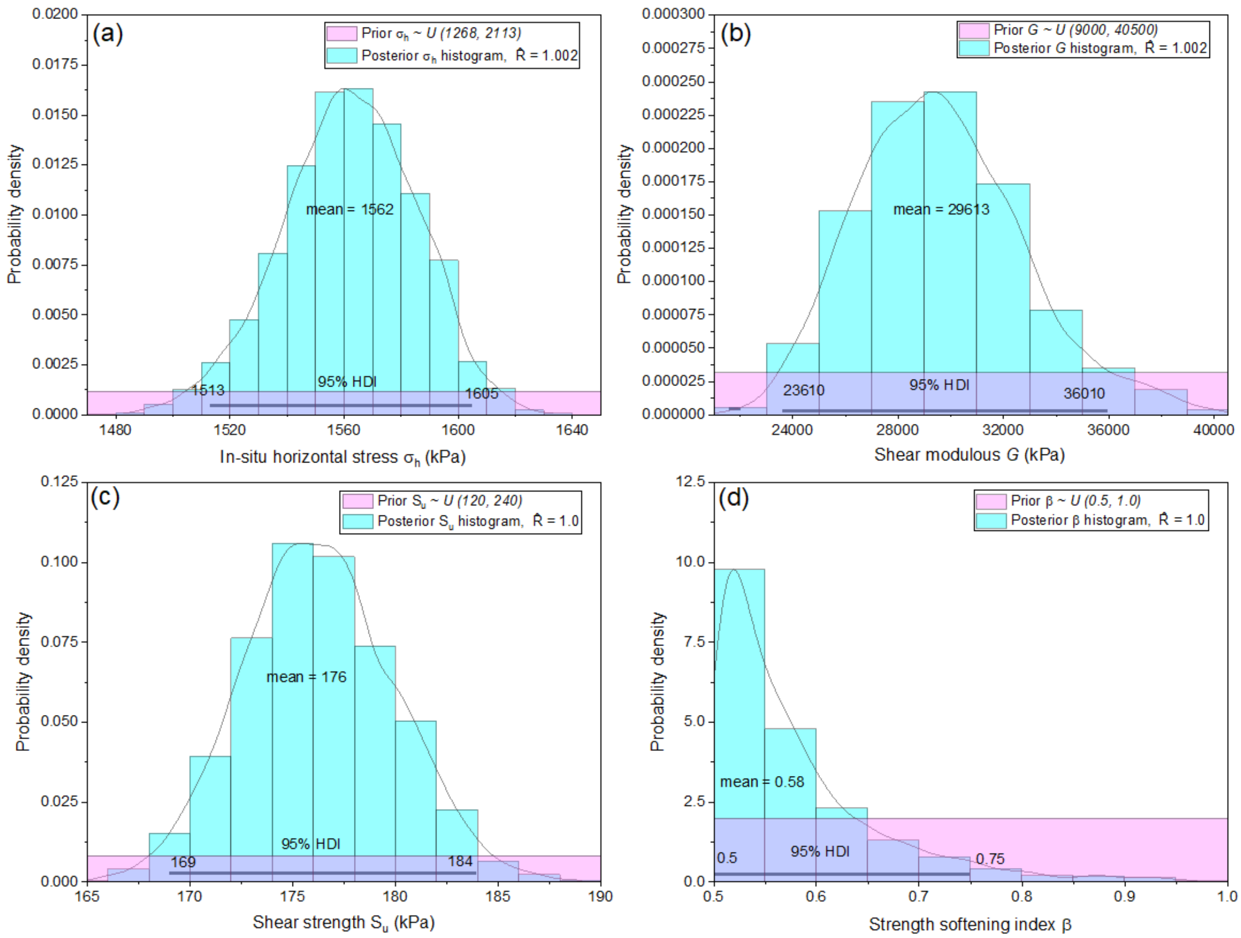

Figure 5.6 Posterior statistics from Bayesian analysis of the complete curve using the analytical model. Note: $\sim U(a, b\ )$ denotes uniform distribution.

Figure 5.6 illustrates the posterior distributions, mean and 95% HDI after MCMC simulations. To quantitatively diagnose convergence for the MCMC simulation, $\hat{R}$ (Gelman and Rubin, 1992; Brooks and Gelman, 1998) shall be examined. As can be seen in Figure 5.6, all the $\hat{R}$ values are less than 1.1 so the chains are deemed to be converged (Gelman and Rubin, 1992; Martin, 2016; Peng, 2021). The narrow normal distribution curves in Figures. 5.6a to 5.6c indicate significantly reduced uncertainties compared to the prior uniform distributions. However, Figure 5.6d shows a half-normal posterior distribution curve. In addition, the outliers of the posterior σ_h samples greater than the 95% HDI fall close to the upper bound of the prior in Figure 5.6d. It indicates that new data is needed to update the posterior belief further.

5.4.4.3 MCMC simulation of the complete curve using the numerical model

To maintain the MCMC computation time acceptable (e.g., about 200 hours for a computer equipped with a 4.5 GHz CPU), two chains with 1000 draw iterations and 500 tune samples per chain are simulated with the slice sampler coupled with the numerical model. The results from the MCMC simulations are plotted in Figure 5.7.

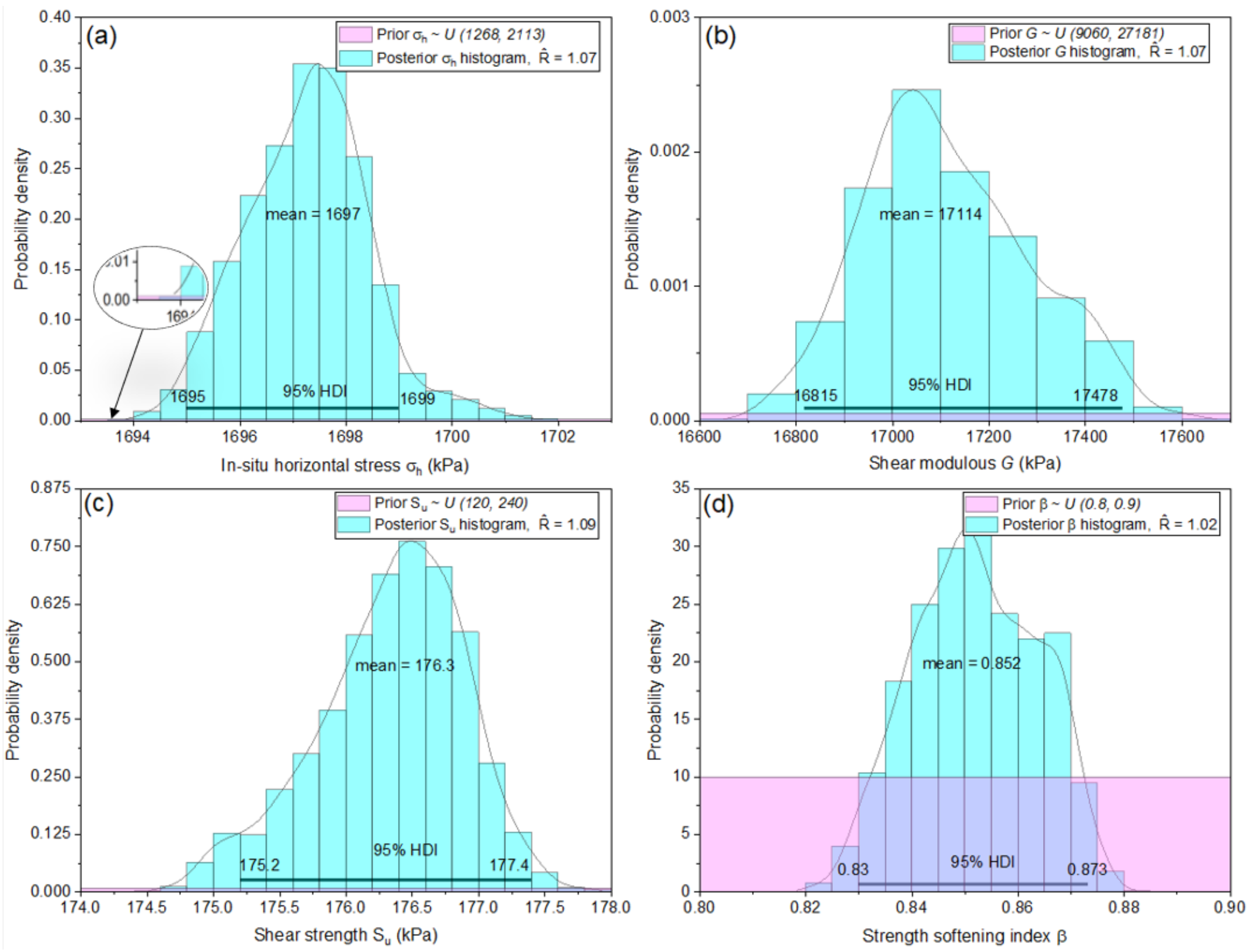

Figure 5.7 Posterior statistics from Bayesian analysis of the complete curve using the numerical model: a) horizontal stress, b) Shear modulus, c) Shear strength and d) Strength softening index. Note: $\sim U(a, b)$ denotes uniform distribution.

In Figure 5.7, all the $\hat{R}$ values for (σ_h, G , S_u β) are less than 1.1, which indicates the chains simulated are converged as well. The posterior distributions in Figure 5.7 are within the prior uniform distributions, implying the numerical model narrowed the uncertainty range compared to the analytical model. The probability density of the prior in Figure 5.7 is much smaller than that of posteriors. Especially the one in Figure 5.7a is too small to be visible, demonstrating the distribution of posterior variables σ_h is highly concentrated around the posterior mean. Compared to Figure 5.6d, Figure 5.7d shows approximately normal distributed posterior samples for the strength softening index β with a much narrower 95% highest density interval (HDI). It indicates that a numerical model can make a more accurate prediction than an analytical model in Bayesian inference.

5.4.5 Visualization of model fit and prediction uncertainty

Although Figures 5.6 and 5.7 illustrate the mean and statistics derived from the Bayesian inference method for the SBP test, the predicted and observed data fit should be visually examined as a final check. At the same time, the coefficient of determination R^2 can show how well the computational model replicates the SBP measurement. In addition, the HDI of posterior distributions can be visualized with shaded bands in the curve-fitting plots. Figure 5.8 illustrates the fit of the observed data to the predicted data, whose uncertainty is characterized by the 95% HDI (shaded band), which is analogous to the frequentist 95% CI band presented by Zheng et al. (2021).

Regarding the coefficient of determination R^2 in Figure 5.8, the numerical model achieves a slightly better fit for the SBP data than the analytical model. In contrast, the prediction band in Figure 5.8a shows more significant uncertainty than Figure 5.8b. For the expansion curve predicted by the analytical model (Figure 5.8a), the width of the 95% HDI band increases with the loading pressure from 1750 kPa to 2100 kPa. Then, the bandwidth decreases from 2100 kPa to 2300 kPa, implying that there exists much less prediction uncertainty at the late stage of expansion predicted with the analytical model (Jefferies, 1988) while using the Bayesian approach.

Besides, Figure 5.8a shows a much wider band at the contraction stage for the complete curve using the analytical model due to the addition of the strength softening index β in the analytical model, which results in higher dimensional posterior distributions. Consequently, the prediction uncertainty increases and the 95% HDI bands widen during the contraction stage.

Similar patterns can be observed in Figure 5.8b for the numerical model. However, the 95% HDI bands are significantly reduced compared to their counterparts in Figure 5.8a, implying the numerical model adopted in this study is less sensitive to the variation in input parameters than the analytical model proposed by Jefferies (1988). Comparing Figure 5.3 with Figure 2 presented by Zheng et al. (2021), the numerical model in this study is simplified owing to the computational efficiency of MCMC simulations. To better simulate the boundary conditions for an SBP test, the 2D plane strain model presented by Zheng et al. (2021) is recommended for this Bayesian inference if the computing power can be significantly increased in the future.

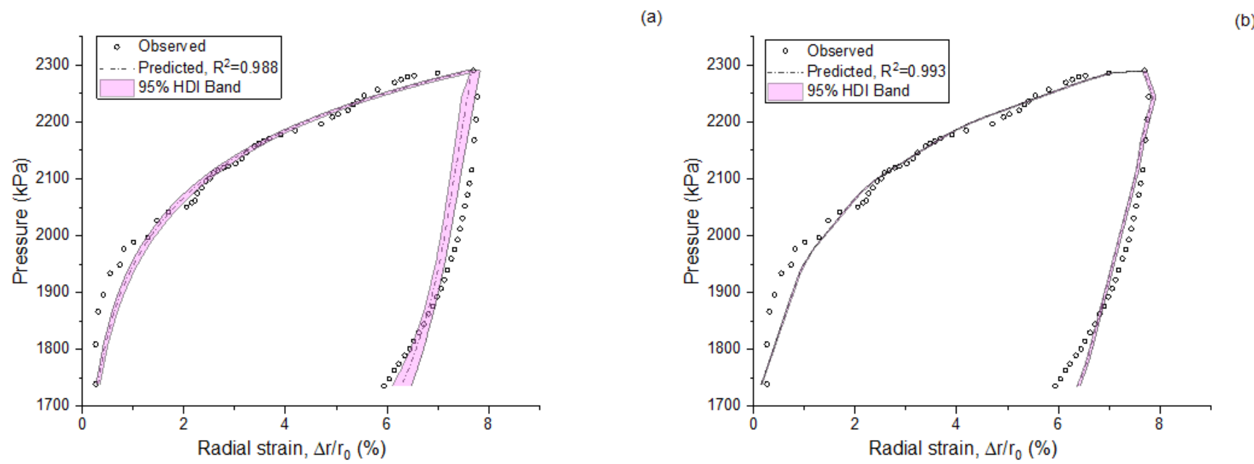

Figure 5.8 Fit of observed data to predicted data for test AF85P06-15 (Jefferies 1988): (a) predicted with the analytical model using the complete curve (b) predicted with the numerical model using the complete curve.

5.4.6 Posterior distribution updated with new evidence

According to Bayesian inference theory (Gelman and Rubin, 1992), posterior knowledge from MCMC simulations can be continuously updated if new evidence is available. In this study, findings presented by other researchers (Jefferies, 1988; Zheng et al., 2021) can be used as new evidence to update posterior distributions derived from the MCMC simulations.

Horizontal stress and soil parameters presented in table B1 (Zheng et al., 2021) and Figures 7, 8, 10, 11, and 12 (Jefferies, 1988) are used as the new data in Bayesian updating. The new evidence is shown in Figure 5.9.

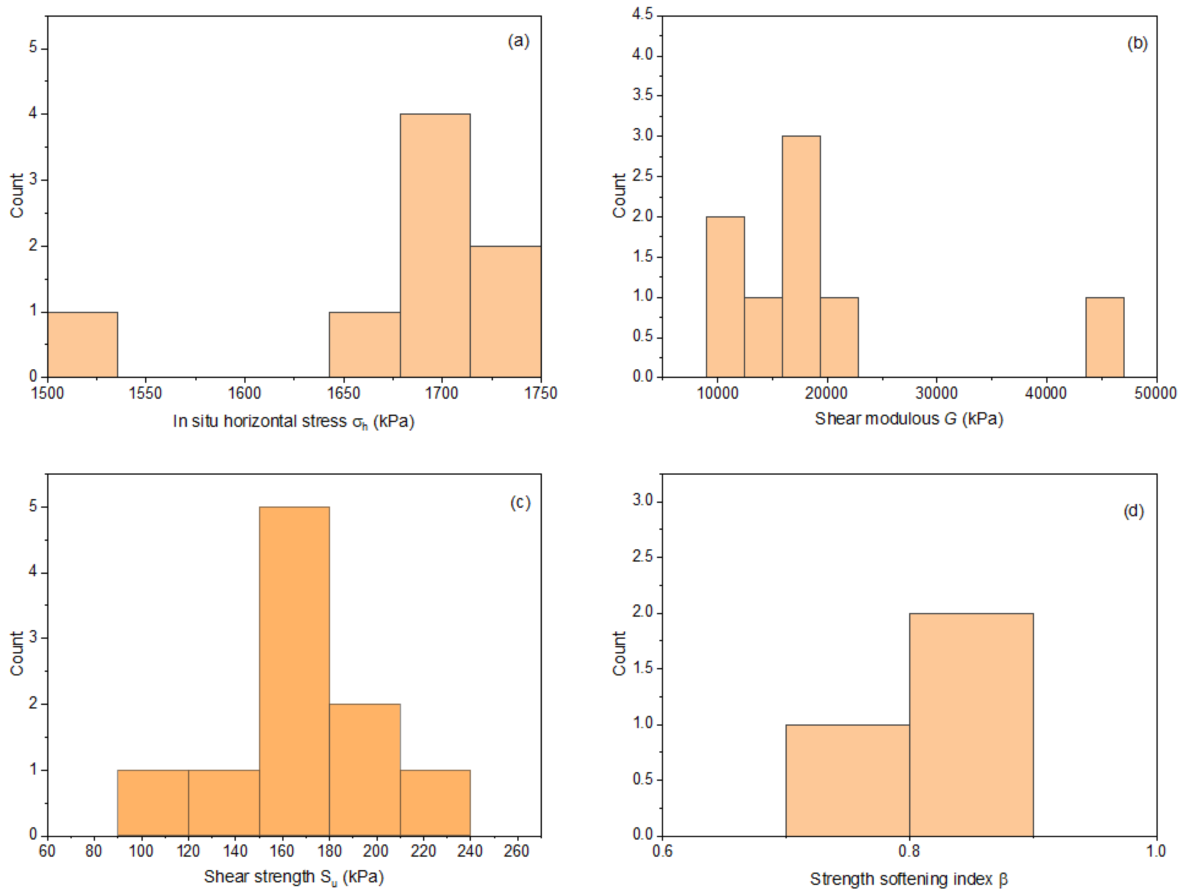

Figure 5.9 New evidence for Bayesian updating the posterior distributions

5.4.6.1 Updated posterior distributions derived from the complete curve using the analytical model

Figure 5.10 demonstrates updated posterior statistics from the MCMC simulations with additional data described in the previous section. The new evidence in Figure 5.9 is used to update the mean and standard deviation of the posterior distribution $(\sigma_h, G, S_u\ and\ \beta)$.

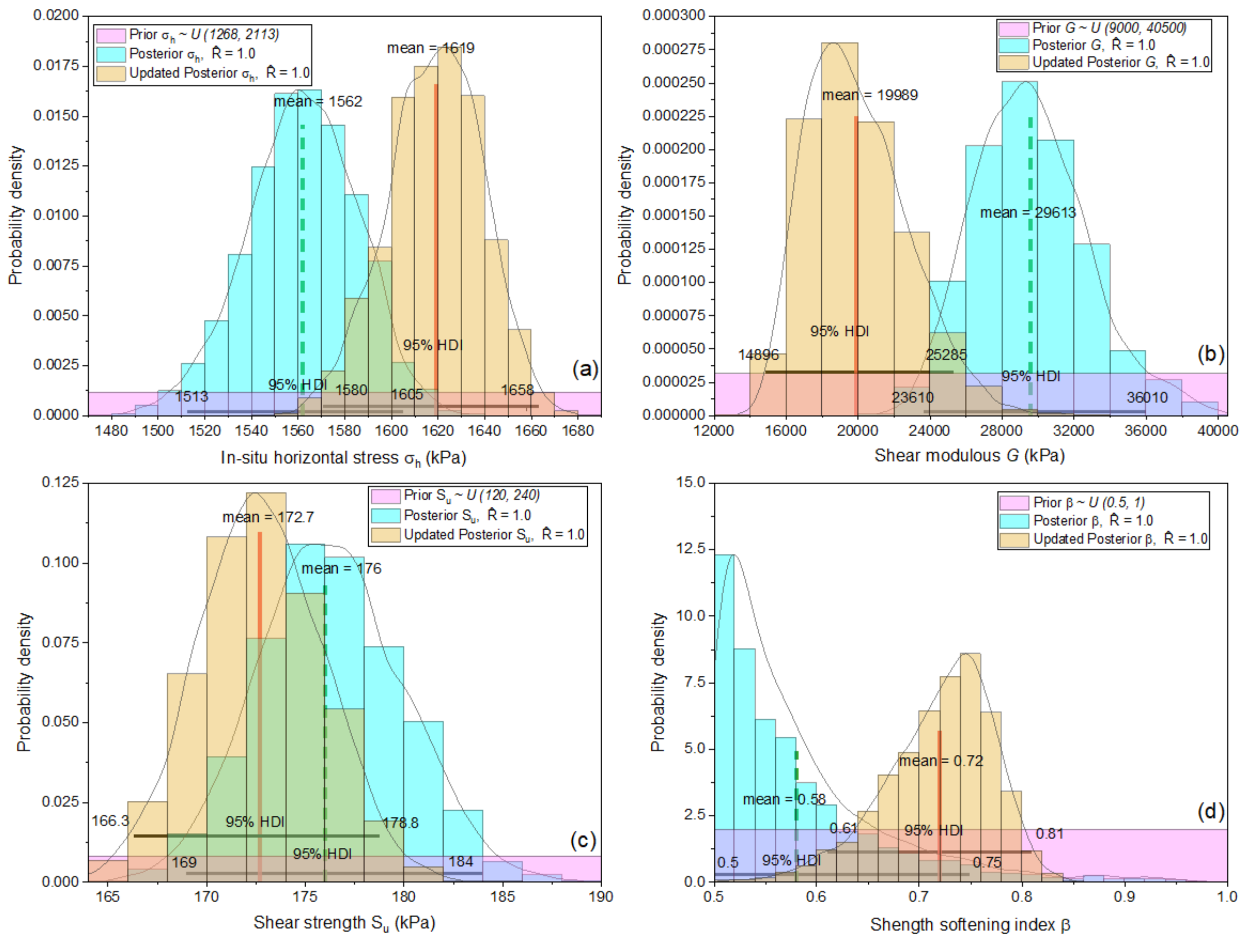

Figure 5.10 Updated posterior distribution of parameters derived from complete curve using analytical model. Note: $\sim U(a, b\ )$ denotes uniform distribution.

Figure 5.10a to Figure 5.10c illustrate similar patterns, where the mean is shifted, and the change of standard deviation is slightly reduced. For in-situ stress and shear strength, the mean value is shifted as the new data deviates from the posterior. The change in standard deviation is negligible because the range of the new feed of data is similar to the posterior before Bayesian updating. In other words, the belief of the mean value might be changed with the new data, but prediction uncertainty is almost unchanged. In the Bayesian paradigm, the degree of belief is a function of observed data, sampling algorithms, computational models, and new evidence. The conclusion is subject to change with new data. Figure 5.10d shows that the mean of the updated posterior β is about 0.72, and 95% HDI is narrower than the posterior. Figure 5.10 shows if the new data deviates from the original posterior, the updated posterior will be subject to considerable changes, even switching from one type of distribution to another.

5.4.6.2 Updated posterior distributions derived from complete curve using numerical model

Updated posterior distributions from the numerical model (Figure 5.11) show similar patterns to the ones from the analytical model (Figure 5.10). The mean of normal distribution curves of (G, σ_h , S_u and β) are shifted to the left after being updated with the new evidence, whereas the spreads are reduced slightly.

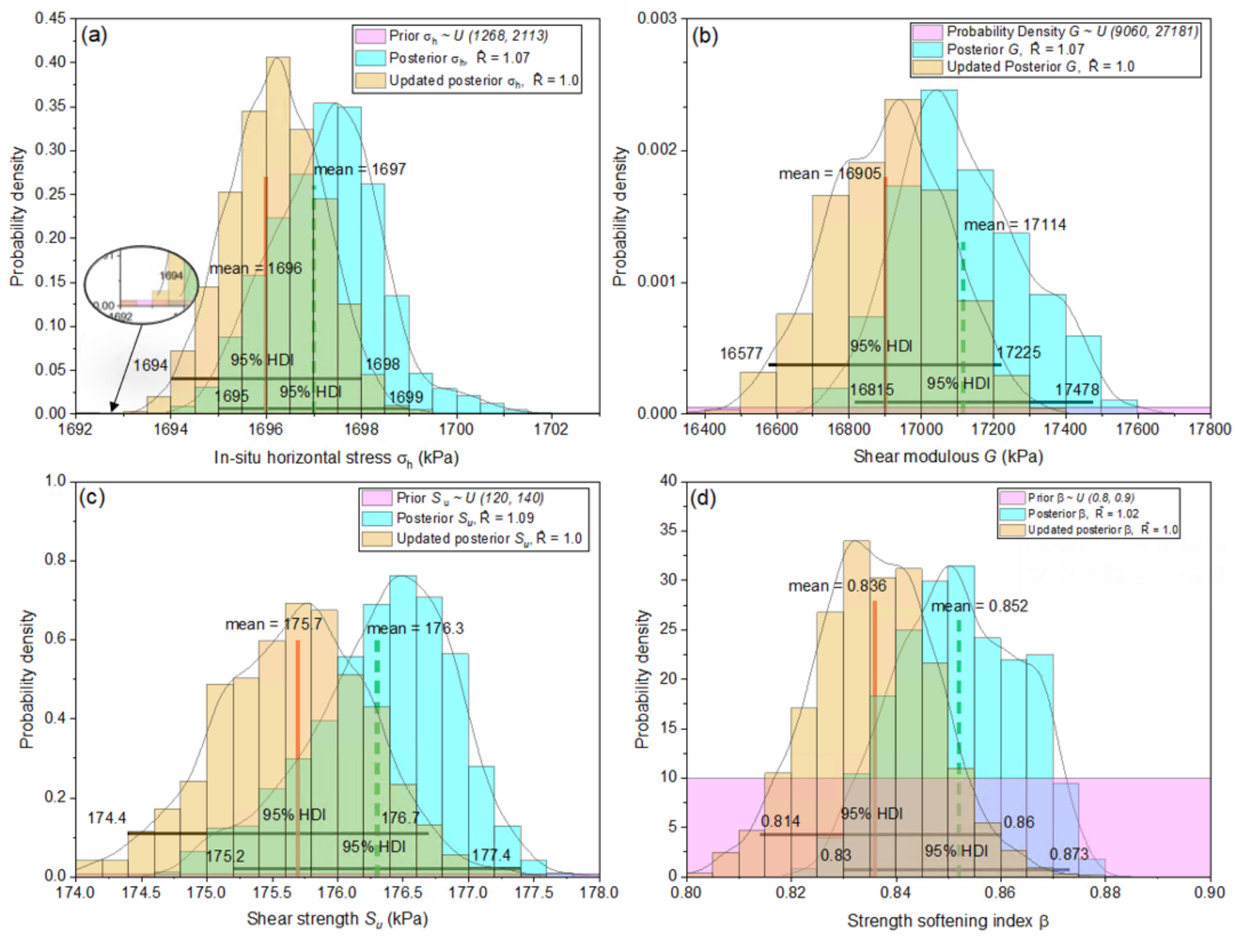

Figure 5.11 Updated posterior distribution of parameters derived from complete curve using numerical model. Note: ~U(a, b) denotes uniform distribution.

The new data updates the predicted mean, but the prediction uncertainty is almost the same. Again, the new evidence shifts the mean of the updated posterior, indicating that our belief is changing with new measurements. With new data in the future, Bayesian updating can be conveniently performed and serve as an open system compared to frequentist inference.

5.5 Summary and Conclusions

This chapter introduces a Bayesian approach for uncertainty quantification of in-situ stress and geotechnical parameters with a pressuremeter test. Uncertainty can be quantified with both frequentist and Bayesian approaches. In Chapter 4, the frequentist approach views parameters as unknown but fixed, whereas the Bayesian approach in Chapter 5 regards them as random variables following prior probability distributions. The standard deviation (SD) in Chapter 4 was calculated from the covariance matrix using perturbed methods. In contrast, this chapter describes the estimation of the SD using MCMC chains. Chapters 4 and 5 provide two options for performing uncertainty quantification for in-situ stress and parameter estimates in pressuremeter tests.

The prior represents external knowledge independent of observations, which may come from previous publications, expert experience, and analogous scientific or engineering experiment settings. A posteriori belief is obtained by reconciling the prior and the observed data through Bayesian inference. The posterior belief can be further updated without starting from scratch if new evidence is available and more data are provided in the future.

Figure 5.10 and Figure 5.11 show that the new data can significantly impact the updated posterior distributions. Therefore, the data shown in Figure 5.9, especially the outliers, may be discarded by other investigators with personal judgement. However, the influence of outliers on the updated posterior distributions would decrease with more new data feeds available. In other words, statistical inferences can be made objectively with sufficient testing data. On the other hand, expert advice, as well as supplementary laboratory and field tests, are helpful in making a decision to accept or discard outliers from new data.

The log-likelihood function in the Bayesian inference is formulated as an objective function with the observed and predicted data. The log-likelihood function can be implemented by following the flow chart shown in Figure 5.1. By maximizing the log-likelihood function, posterior statistics can be obtained from the MCMC simulations. Given the characteristics of an open estimation system, the Bayesian inference approach would not rely on a single SBP test. One's belief in the in-situ stress and soil parameters can always be updated with other SBP tests in the adjacent boreholes, nearby field tests (e.g., CPT, SPT and shear vane test), and laboratory tests. This makes the Bayesian approach distinguishable from the frequentist approach, which cannot be updated without starting from scratch. Therefore, the adoption of the Bayesian inference methods is meaningful in the statistical inference of parameters from in-situ and laboratory tests in geotechnical engineering.

However, because of high computational demands from the MCMC simulation, there is limited usage of numerical models with the Bayesian approach. This issue can be solved or partially solved with a high-performance multi-CPU computer, multi-threaded software, and cloud computing in the future and by designing problem-specific proposal distributions enabling efficient sampling of the solution space.

The Bayesian inference approach can quantify uncertainties from soil variability, measurement error, and computational model. An SBP test presented by Jefferies (1988) was re-analyzed using our proposed MCMC workflow in this chapter. Among the tested algorithms, the slice sampling demonstrates a satisfactory performance with the analytical solution and numerical model. The complete testing curve helps to determine the strength softening parameter β. After MCMC simulations, statistics of parameters (G, σ_h, S_u and β) are summarized from samples drawn from the posterior distribution. Among them, the mean and 95% HDI are used to characterize the uncertainty from parameter estimation. The model fit is evaluated with the coefficient of determination R^2, and the corresponding prediction uncertainty is visualized with the 95% HDI band. The analytical model is very sensitive to parameter changes during the Bayesian inference compared to the numerical model. With the Bayesian approach, this paper introduces a data-driven and open system with potential applications for the events occurring in a sequence, such as a slope stability monitoring system, caprock integrity analysis, and carbon sequestration projects where new data like well test, seismic survey are often provided at different stages of projects.

6.0 STATISTICAL INVERSE ANALYSIS OF THE RGP TESTS AT PRIMROSE-WOLF LAKE OIL SANDS FIELD[3]

6.1 Introduction

Knowledge of the initial in-situ stress plays a vital role in the geomechanical caprock integrity and risk assessment problems experienced in projects of enhanced oil recovery, CO2 sequestration, and underground radioactive waste storage. Traditionally, the minimum in-situ stress is determined from diagnostic fracture injection tests or mini/micro-frac tests. However, measurements of the minimum stress from these tests are deemed inconclusive in the shallow oil sands reservoirs. Consequently, the pursuit of alternative in-situ stress testing techniques results in the development of a reservoir geomechanical pressuremeter, which can be deployed into the borehole using industry-standard wireline technology. In 2016, five borehole intervals in Formations Westgate, Joli Fou and Clearwater were tested with the deployment of the RGP tool at the Primrose-Wolf Lake oil sands field. Inverse analysis of RGP testing data allows for an integrated assessment of the magnitude and orientation of anisotropic in-situ stresses and formation rock stiffness and strength. A statistical method is utilized for the inverse analysis of the RGP tests, from which the mean value and its statistics can be derived. With the statistical method, parameters are first estimated by coupling an analytical, semi-analytical, and numerical model with an optimization algorithm. Then, the non-uniqueness issues in parameter estimation are addressed by uncertainty quantification using statistical assessment methods. With the mean, standard deviations, and confidence intervals, uncertainties from parameter estimation can be quantified. In addition, model fit using the statistical method is examined with the coefficient of determination, R^2, and prediction uncertainty is visualized with the prediction band. Finally, the minimum in-situ horizontal stress measured by the microfrac modular formation dynamics tester is used to compare the findings from the statistical inverse analyses of the RGP tests.

---

[3] A version of this chapter has been published: Zheng, D., N. Deisman, B. Zhang, and R.J. Chalaturnyk, 2023. Statistical inverse analysis of the RGP tests at Primrose-Wolf Lake oil sands field. Proceedings, GeoConvention, Calgary, 6 p.

6.2 Background

With the modification of a conventional high-pressure pressuremeter, a reservoir geomechanical pressuremeter (RGP) was developed by the reservoir geomechanical research group (RG^2) at the University of Alberta in 2016. As an in-situ testing tool, RGP can be deployed into the downhole in the deep geological formation using industry-standard wireline technology. The RGP has seen increasing application in reservoir geomechanics over the past five years (RG^2 , 2016; Liu et al., 2019). With the measurements of cell pressure and radial displacement during the RGP test, the magnitude and orientation of anisotropic in-situ horizontal stresses, as well as rock strength and stiffness, can be derived. Conventionally, parameters such as in-situ horizontal stress and rock properties are estimated with curve-fitting methods (Jefferies, 1988; Ferreira, 1992). However, the curve-fitting methods may lead to non-unique solutions (Houlsby, 1989). The issue of non-unique solutions can be attributed to rock spatial variability, measurement errors, and uncertainties in a computational model. To solve the problem of non-uniqueness encountered in the analysis of a pressuremeter test, Zheng et al. (2021) proposed a statistical method to quantify the uncertainties existing in the parameter estimation for a self-bored pressuremeter (SBP) test. Owing to the deep test depth for an RGP test, some factors, such as deployment techniques, nitrogen gas supply, and borehole disturbance, make an RGP test distinguished from a conventional pressuremeter test. Therefore, the approach proposed by Zheng et al. (2021) for an SBP test in clay can be directly applied here for an RGP test in deep geological formations with minimal modifications.

To perform a statistical inverse analysis of the RGP test, a computational model (analytical, semi-analytical or numerical) needs to be coupled with an optimizer to find the optimal parameters, followed by uncertainty quantification with statistical methods. Zheng et al. (2021) may be referred to for details. Although the inverse techniques presented by Zheng et al. (2021) are utilized in this research, there are some differences from the previous study. For example, the modified strain-softening/hardening constitutive model is proposed to simulate the responses of clay shale to RGP expansion, hold, loading/unloading, and contraction. In addition, the fluid-mechanical coupling technique is used to reproduce the hold test stage. Above all, those changes made in this paper from the previous study are targeted to solve the specific problems encountered in the RGP tests for deep geological formations in Alberta, Canada.

Finally, to verify the findings from the statistical inverse analyses, the minimum in-situ horizontal stress, measured by the microfrac modular formation dynamics tester (MDT), is compared with the predicted horizontal stresses.

6.3 Methodology

The goal of an RGP test is to record the changes in the applied pressure and radial displacements during the expansion, hold, unloading/reloading, and contraction stages. In addition, inverse analysis of an RGP testing curve is performed to estimate the values of in-situ horizontal stress and rock properties for geomechanical investigation. With observed data from the RGP test, point estimation with deterministic methods is usually first carried out and then followed by statistical assessments of estimated parameters.

At the beginning of point estimation, the prior probability distributions for unknown parameters must be assumed. The proposed PDFs, such as uniform, normal, and log-normal distribution, represent a priori knowledge of rock properties and in-situ horizontal stress from previous publications, expert experience, and personal judgment. This study assumes uniform distributions for all unknown parameters. To simulate an RGP test, an analytical solution, a semi-analytical solution, or a numerical model shall be adopted. To conduct the point estimation, an objective function is formulated with the observed and predicted data. In-situ horizontal stress and rock properties can be estimated by minimizing the objective function. Statistics of the estimated parameters are obtained with the statistical assessment methods presented by Zheng et al. (2021).

6.3.1 Objective function

To carry out the inverse analysis of RGP tests, an objective function needs to be defined. In this study, an unweighted nonlinear least squares (NLLS) error function can be formulated to conduct point estimation. The NLLS error function is formulated as the objective function in the search process of optimization algorithms (Ahmed et al., 2015; Papon, 2012; Yin, 2016). The unweighted NLLS performance function is expressed as:

$$MSE = \frac{1}{n}\sum_{i=1}^{n}\left[Y_i - \hat{Y}_i(b_i)\right]^2 \tag{6.1}$$

where MSE denotes the mean squared errors, Y_i denotes observed data, $\hat{Y}_i$ denotes predicted data, n denotes the number of observed data, and b_i represents a parameter to be estimated; $\hat{Y}_i(b_i)$ represents a nonlinear function of b_i for the simulation of an RGP test. In the statistical inverse analysis, an optimizer must be coupled with a computational model to find the minimization of the MSE as formulated in Equation 6.1. In-situ horizontal stresses and rock properties are then estimated through the minimization of Equation 6.1.

6.3.2 Statistical inverse analysis method

The objective of the statistical inverse analysis is to estimate the parameters by minimizing the objective function and their confidence intervals through statistical assessments. In this process, The random variables generated in the optimization process reproduced the potential parameter uncertainties. The Jacobian matrix and CIs are derived from the optimization to evaluate the variability of the predicted horizontal stress and rock properties. A workflow in Figure 6.1 demonstrates the statistical inverse approach for analyzing RGP testing data.

By following the procedures illustrated in Figure 6.1, we can identify the best estimates of geotechnical properties, in-situ stress magnitudes and orientations in deep geological formations from RGP tests. At the same time, estimation uncertainties can be efficiently quantified with mean and statistics after statistical assessments.

Although the methodologies between the analyses of an RGP and SBP (Jefferies, 1988; Zheng et al., 2021) are identical, there are some differences in the selections of optimizers and constitutive models as well as modelling approaches owing to differences in tools and downhole testing conditions. For example, a global optimization algorithm, the SS, is first used to find the optimal parameters at the expansion stage due to high-dimensional inputs. In the following stages, e.g., hold tests, unloading-reloading, and contraction stages, the simplex algorithm is used for runtime efficiency. Also, a semi-analytical solution (Zhou et al., 2015) is implemented in the computational model to simulate a biaxial in-situ stress field. For numerical modelling, a whole instead of a quarter cylindrical cavity geometry is adopted in the finite-difference model. In addition, the modified strain-hardening/softening constitutive model is proposed in this study to reproduce the pore pressure and stress responses of clay shale to the loading and unloading pressures during the RGP test.

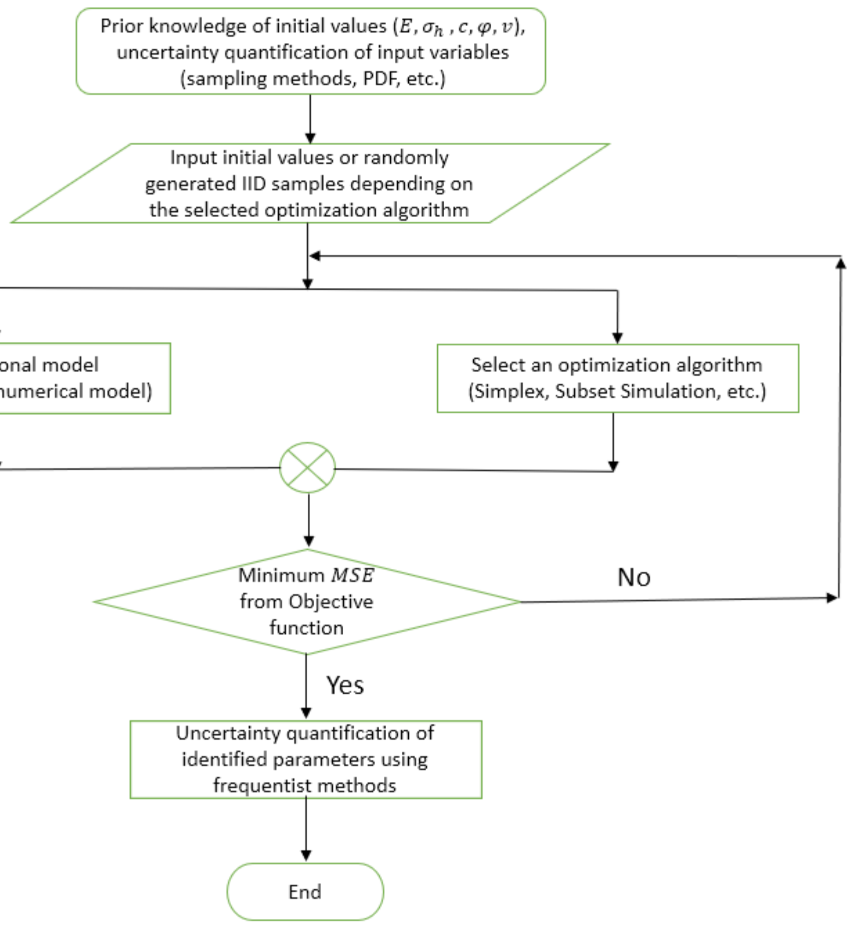

Figure 6.1 Flow chart of statistical inverse analysis of an RGP test

6.3.3 Modelling approaches for the RGP tests in clay shale

The methodology for an SBP analysis presented by Zheng et al. (2021) can be used in the inverse analyses of RGP tests. However, modelling approaches for the RGP tests shall be further studied to accommodate the differences between an SBP and the RGP regarding the test depth, deployment procedure, ground disturbance, and materials (soil and rock) around the borehole wall.

The depths of the RGP tests performed in the Westgate, Joli Fou, and Clearwater formations of the Colorado group vary from 260 m to 450 m (RG^2, 2016). The vertical stress can be integrated with the density log along with other major parameters reported by Schlumberger (2014). According to Zadeh (2016), the Westgate formation consists of a wedge of non-calcareous mudstone and siltstone, which are categorized as hard soils-soft rocks. Given the clay shale permeability measured from laboratory testing (Schlumberger, 2014; Zadeh, 2016) and the loading rate of 5 to 10 kPa/s, the RGP tests are performed under partially drained conditions (Liu, 2015). Undrained cavity expansion conditions are usually assumed in the derivation of analytical and semi-analytical solutions for pressuremeter testing in clay (Gibson and Anderson, 1961; Jefferies, 1988; Zhou et al., 2015). Considering only a minimum loss (0.1% to 10%) of excess pore pressure (RG^2, 2016) during the RGP tests, the undrained condition assumption is still considered to be valid. By examining the RGP testing curves, there is a pressure hold test following the initial expansion. However, the analytical and semi-analytical solutions cannot simulate the hold test and the following stages. Alternatively, the finite-difference modelling can numerically reproduce the complete RGP testing curve by following the same stress paths. Undrained conditions are assumed in all stages except for the hold test, which is under drained deformation and simulated with fluid-mechanical coupling techniques.

Through the discussion above, the clay shale around the borehole wall deforms instantaneously in response to applied pressure changes in the expansion, unload-reload loops, and contraction stages in an RGP test. At the same time, excess pore pressure is generated as a result of mechanical deformations.

In the analytical and semi-analytical solutions, the strength of clay shale around the borehole wall is represented by the Tresca model with a cohesion equal to undrained shear strength S_u and friction angle $\phi=0°$. However, this technique is restricted to a plane-strain problem with a very soft matrix, such as soft clay. According to Zadeh (2016), the geological materials in the Colorado group are clay shales, described as either hard soils or soft rock. Hence, the Tresca model may not properly represent the constitutive behaviour of clay shales around the borehole wall. In this study, the undrained response of materials is simulated in an effective-stress space under a no-flow condition (Itasca, 2011). Under the no-flow condition, the clay shale is treated as porous rock, and the Biot coefficient is applied to account for the stiffness of the material matrix. Drained properties, such as bulk modulus K', cohesion c' and friction angle φ', are used in the undrained analysis. Thus, the modified strain-hardening/softening model (see Section 6.3.5) is used to model the clay shale around the borehole wall. Finally, the fluid flow calculation is turned off to simulate the undrained response while the clay shale undergoes instantaneous deformation. In this case, the fluid around the borehole area reacts to mechanical deformations with changes in pore pressure, which can be simulated using the wet simulation method.

6.3.4 Simulation of the hold tests

Due to the large system volume and unexpected leakage, the nitrogen gas pressure failed to be kept constant during the hold tests (Liu et al., 2019). Therefore, the pressure applied to the contour of the borehole varies with time. Regarding Figure 2.8 (Liu, 2015), the loading rate is small enough to cause the response of clay shale in the borehole vicinity in a drained condition. In such a case, the clay shale consolidates for 10 seconds under each incremental load applied by the RGP membrane. Changes in pore pressure generate volumetric changes, and reversely, volumetric changes lead to the evolution of pore pressure. A closed-form solution (Detournay and Cheng, 1988) is unable to describe the 'unsuccessful' hold tests because the hold pressure is not constant. Hence, a fully fluid-mechanical coupled numerical analysis needs to be performed to simulate the process.

6.3.5 Modified strain-hardening/softening model

Based on the Mohr-Coulomb model, Vermeer and de Borst (1984) proposed a strain-hardening/softening (SS) model, where geotechnical material properties may harden or soften after the onset of plastic yield. Therefore, piecewise-linear functions are used to define softening/hardening bahviors of parameters (cohesion, friction, and dilation) in terms of the plastic shear strain increment Δe^{ps} (Itasca, 2011):

$$\Delta e^{ps} = \frac{1}{\sqrt{2}}\sqrt{(\Delta e_1{}^{ps} - \Delta e_m{}^{ps})^2 + (\Delta e_m{}^{ps})^2 + (\Delta e_3{}^{ps} - \Delta e_m{}^{ps})^2} \tag{6.2}$$

where $\Delta e_m{}^{ps} = \frac{1}{3}(\Delta e_1{}^{ps} + \Delta e_3{}^{ps})$ denotes the volumetric plastic shear strain increment.

Unlike the Mohr-Coulomb model, where properties are assumed to remain constant, the SS model typically defines a piecewise-linear function in the form of a table (Itasca, 2011):

```
table "cohesion" 0, 20e6, 0.01, 10e6
```

where the table defines two line segments:

1). '20e6' denotes that the initial cohesion is 20 MPa at e^{ps} of 0;

2). '10e6' represents that the softened cohesion of 10 MPa when e^{ps} is 0.01. The cohesion remains constant for e^{ps} greater than 0.01.

According to Itasca (2011), the specified values in the Table, e.g., 0.01 and 10e6, need to be determined by back-analysis of the post-failure behavior of a specimen in a triaxial or uniaxial test. However, determining these specified values with acceptable accuracy can be challenging. This is because, in practice, factors like sample scale effects, stress paths, boundary conditions, measurement errors, and the oversimplification of back-analysis modelling can lead to inconsistencies in the specified values between laboratory and in-situ tests.

Another problem is that the SS model assumes a constant Young's modulus, which may not align with the findings of modulus degradation in the degraded zone near the borehole wall in RGP tests, as reported by Liu et al. (2019).

Therefore, based on the SS model, the modified strain-hardening/softening model (modified SS) is proposed for the simulation of the RGP test in this research.

6.3.5.1 Formulation of the modified strain-hardening/softening model

Due to the brittleness of clay shales described as hard soils or soft rocks, damage can be induced by micro-cracks in plastic zones around the borehole during expansion and load-unload loops in an RGP test. Modulus degradation was discussed in the non-linear analysis of concrete by Lubliner et al. (1989). A scalar damage variable d_m between 0 and 1 is introduced to account for the modulus degradation of concrete. Similarly, the modulus degradation of clay shales can also be described in the same way in the modified SS, as shown in Equation 6.3,

$$E = (1 - d_m)E_0 \tag{6.3}$$

where E_0 represents the initial Young's modulus.

To account for the strength softening or hardening effect in unloading during the contraction phase, Jefferies (1988) introduced a simple fraction β of the loading strength:

$$S_{uc} = \beta_{su} S_u \tag{6.4}$$

where S_{uc} denotes the softened or hardened undrained shear strength.

To simulate the clay shale behaviors undergoing undrained deformation, unsuccessful hold test and unloading/loading in the RGP test, softened/hardened variables are introduced in the modified SS model:

1). Stiffness degradation is implemented in the numerical formulation, shown in Equation 6.3.

2). Softened/hardened cohesion c'', friction angle ϕ'' and dilation angle ψ'' are calculated as:

$$c'' = \beta_c c''_0 \tag{6.5}$$

$$\phi'' = \beta_\phi \phi''_0 \tag{6.6}$$

$$\psi'' = \beta_\psi \psi''_0 \tag{6.7}$$

where β_c, β_ϕ , and β_ψ represent softened/hardened variables; c''_0, ϕ''_0 and ψ''_0 represent initial undamaged values.

According to the discussion above, FISH functions corresponding to Equation 6.3 and Equations 6.5 to 6.7 can be written as:

```
zone.prop(zp,'young')= (1.0-d)*E0
zone.prop(zp,'cohesion')=(beta_c)*Su
zone.prop(zp,'friction')=(beta_phi)*Phi
zone.prop(zp,'dilation')=(beta_psi)*Psi
```

where d, beta_c, beta_phi and beta_psi usually range from 0.1 to 1.0 during softening, and greater than 1.0 during hardening. E0, Su, Phi and Psi are initial geotechnical properties. Instead of determining e^{ps} and its corresponding softened/hardened property value in the piecewise-linear function, only the softened/hardened variables (d, beta_c, beta_phi and beta_psi) are needed for each loading increment or several loading increments. The FISH functions above can be easily implemented in FLAC2D/3D.

The difference between the SS and modified SS models lies in the fact that the piecewise-linear function in the SS model updates material properties at each timestep. In contrast, the FISH function in the modified SS model updates material properties at each loading increment or every several loading increments, depending on how we define model properties in the RGP numerical model. For example, the softened undrained shear strength is assumed to be constant throughout the entire unloading stage, as suggested by Jefferies (1988). Another distinction is that model properties in the SS model are updated in each zone, whereas an average value is assigned in the entire degraded zone in the modified SS model (see Figure 6.2). In essence, the modified SS model is an approximation of the SS model. Compared to the SS model, the modified SS model is much easier to implement without the need for back-analysis of laboratory tests to obtain the piecewise function, as is required for the SS model.

6.3.5.2 Implementation of the modified strain-hardening/softening model

Liu et al. (2019) discussed the radial and azimuthal anisotropies of borehole stiffness under a biaxial horizontal stress field. In this study, the presence of anisotropy is extended to borehole shear strength as well. To account for the radial and azimuthal anisotropies of borehole material, the modified SS model for RGP tests can be implemented in terms of radial boundary and azimuthal zoning:

1). The red solid line in Figure 6.2 divides the geometry of the numerical model into two radially distinct zones: a). the degraded zone; and b). the elastic zone. The '`zone.state()`' FISH function can check whether a zone is in an elastic or plastic state. With the '`zone.state()`' FISH function, the geometry of a numerical model can be divided into elastic and plastic zones in the radial direction. The plastic zone exactly coincides with the degraded zone (see Figure 6.2). All hardening and softening behaviours are assumed to occur within the degraded zone. Outside the boundary of the degraded zone, the material properties remain constant at their initial elastic values. The FISH function code that divides the degraded and elastic zones is:

```
fish define modified_SS_Zoning
local zp = zone.head
  loop while zp # null
    local rad = math.sqrt(zone.pos.x(zp)^2 + zone.pos.z(zp)^2)
      if rad>0.041 then
        if zone.state(zp,false)>0 then
            if zone.isgroup(zp,'Zone A')==true then
            zone.prop(zp,'young')= (1.0-d)*E0
            zone.prop(zp,'cohesion')=(beta_c)*Su
            zone.prop(zp,'friction')=(beta_phi)*Phi
            zone.prop(zp,'dilation')=(beta_psi)*Psi
            endif
        endif
      endif
      zp = zone.next(zp)
    endloop
end
```

2). To reproduce the anisotropic borehole response under the biaxial horizontal stress field, the plastic zone is discretized into three subzones in the azimuthal directions (e.g., Zone A, Zone B and Zone C, separated by blue solid lines), as shown in Figure 6.2. The FISH function code for azimuthal subzoning is:

```
fish define subzoning
    local zp = zone.head
    loop while zp # null
        local rad = math.sqrt(zone.pos.x(zp)^2 + zone.pos.z(zp)^2)
        if rad<=2 then
            fi = math.atan2(zone.pos.z(zp),zone.pos.x(zp))
            if fi>=0 & fi<=math.pi/6. then
                zone.group(zp) = 'Zone A'
            else if fi>math.pi/6. & fi<=math.pi/3. then
                zone.group(zp) = 'Zone B'
```

```
            else if fi>math.pi/3. & fi<=math.pi/2. then
                zone.group(zp) = 'Zone C'
            endif
        endif
        zp = zone.next(zp)
    endloop
end
```

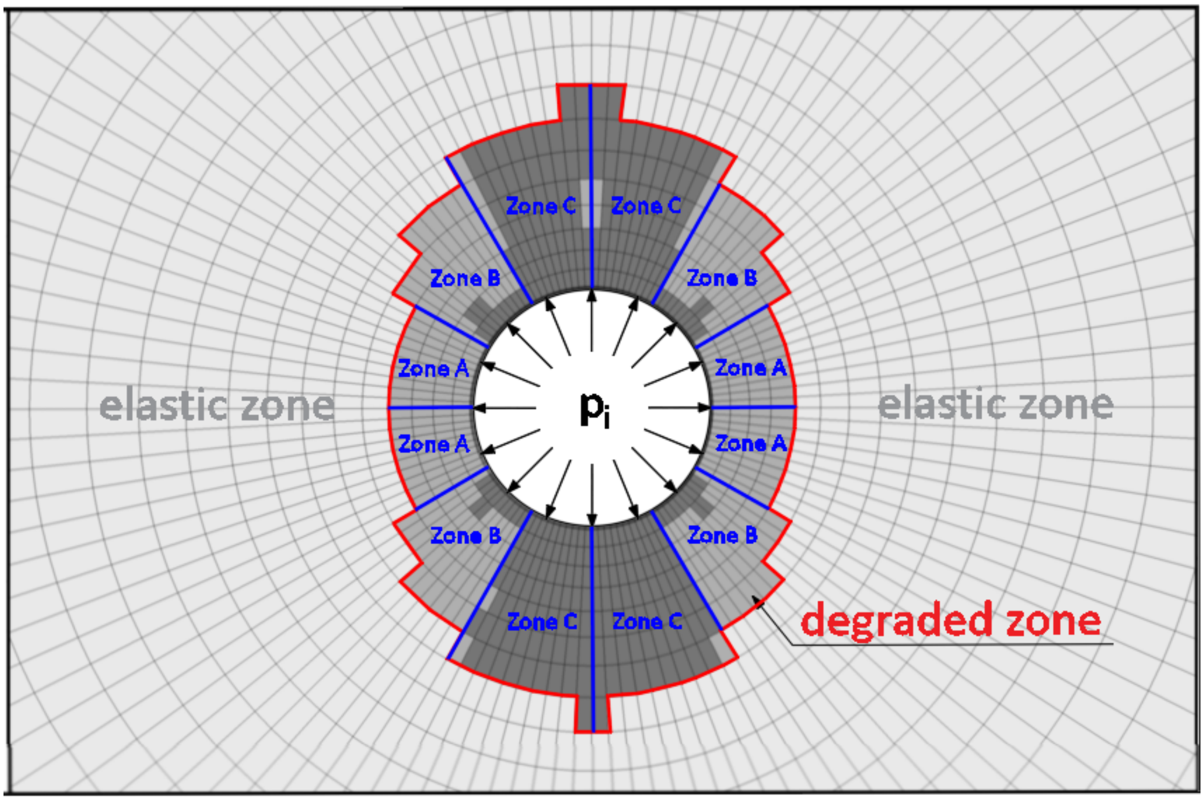

Figure 6.2 Development of degraded zone for the RGP test simulated with the modified SS model

Figure 6.2 illustrates the development of the plastic zone after an incremental loading during the RGP test in the Westgate formation. The boundary of the degraded zone is defined by the elastic-plastic (EP) boundary. Outside of the EP boundary, the material stiffness and shear strength are unchanged or only slightly perturbed, given the stress and boundary conditions. In contrast, the property within each subzone is represented with a localized mean value for each incremental loading/unloading. The EP boundary is supposed to change under different incremental loading/unloading conditions. The task of inverse analysis is to find the optimal softening/hardening variables for each subzone, which can be evaluated with the coupling of an optimizer and the modified SS model. The number of subzones can be divided azimuthally as many as needed. For example, there are three subzones for the Westgate Formation and six subzones for the Clearwater Formation. This method does not require defining the degraded properties in terms of Δe^{ps}. Therefore, the anisotropy of clay shale properties can be evaluated discretely with a simply constitutive model.

However, sudden changes in the material properties may cause disturbances in the model response when using the modified SS model. Sometimes, the numerical simulation fails to converge due to physical instability. Therefore, the choice of softened variables should be made carefully, where the lower and upper bounds of the parameter must be reasonable. Another problem is that only the mean property value is evaluated in each subzone using the modified SS model. If the property distribution in each subzone is of interest, the piecewise function can be used to replace the code line 'zone. prop () = ' in the FISH function 'modified_SS_Zoning' shown in Section 6.3.5.1.

The RGP tests were conducted in an oversized pre-drilled borehole, leading to a full relief of in-situ horizontal stress on the formation of the borehole (Mair and Wood, 1987). As a result, it is challenging to fully compensate for the disturbance caused by borehole drilling and the installation of the RGP tool through inverse analysis. Therefore, uncertainty quantification becomes indispensable to the statistical inverse analysis of the RGP test.

6.4 Statistical analysis of RGP tests in Primrose-Wolf Lake SAGD Project

The methodology discussed in Chapter 4 and the corrected RGP testing data in Chapter 3 is adopted in this case study to carry out point estimation and statistical assessments. The in-situ RGP tests were performed in 2016 at the Primrose-Wolf Lake oil sands field in Alberta, Canada. In total, five test intervals in the Westgate, Joli Fou and Clearwater formations are studied. The objective of this case study is to apply the approaches proposed in Chapters 2 to 5 in the RGP tests in deep geological formations.

6.4.1 Project background

The in-situ test borehole is located at the Primrose south field (legal location: UWI 104/05-36-067-04W4) in the area of thermal oil sands facilities in Cold Lake, Alberta. Figure 6.3 illustrates the approximate location of the observation well B12, in which the RGP tests were performed in 2016 by RG^2 , the University of Alberta.

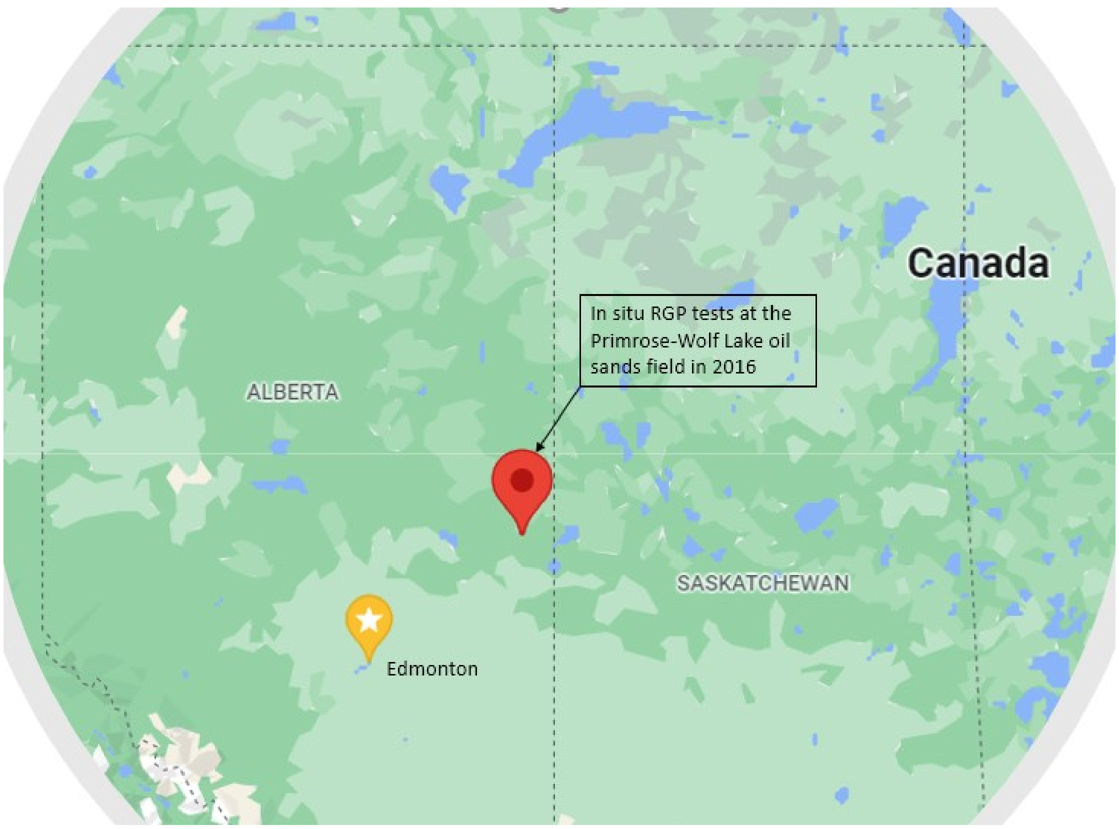

Figure 6.3 Location of the RGP tests (UWI 104/05-36-067-04W4, adopted from Google Map 2022)

6.4.2 RGP field test information

In total, five test intervals in the Formations Westgate, Joli Fou and Clearwater were accomplished. The test depths vary approximately from 259 m to 450 m, which involves the Colorado and Manville geological groups. In the Colorado group, three RGP test intervals are in the Westgate and Joli Fou formations. The other two test pockets at deeper depths are in the Clearwater formation of the Manville group. The RGP test intervals are illustrated in Figure 6.4.

Data retrieved from B0T2 are discarded because the test is deemed unsuccessful (RG^2, 2016). The details of the stratigraphic profile of groups and formations can be referred to in the report presented by Advanced Geotechnology (2001) and Liu et al. (2019).

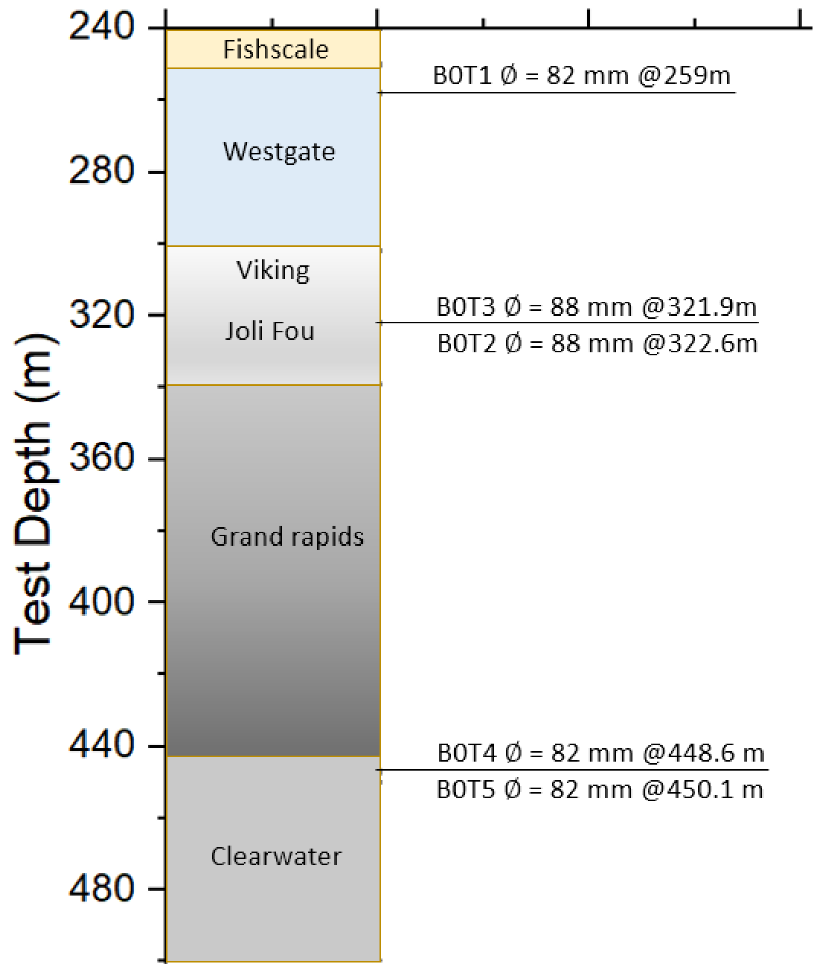

Figure 6.4 RGP tests at the Primrose-Wolf Lake oil sands field in 2016 (note: Ø denotes the diameter of the borehole)

6.4.3 Numerical simulation of an RGP test

Besides the analytical and the semi-analytical solutions (Jefferies, 1988; Zhou et al., 2015), a finite-difference two-dimensional numerical model can simulate stress and strain responses to applied pressure increments during the RGP test. Due to the length-to-diameter ratio L/D = 6.2, the effect of finite pressuremeter length is neglected. Therefore, the RGP test in clay shale can be treated as a cylindrical cavity expansion in a homogeneous, isotropic medium. Figure 6.5 illustrates the two-dimensional plane-strain discretized domain and boundary conditions. To fit the differential radial displacements measured by six strain arms, a whole geometry, rather than a quarter of the borehole cavity plane, is modelled. The numerical model illustrated in Figure 6.5 is adopted in the statistical inverse analysis of the RGP test.

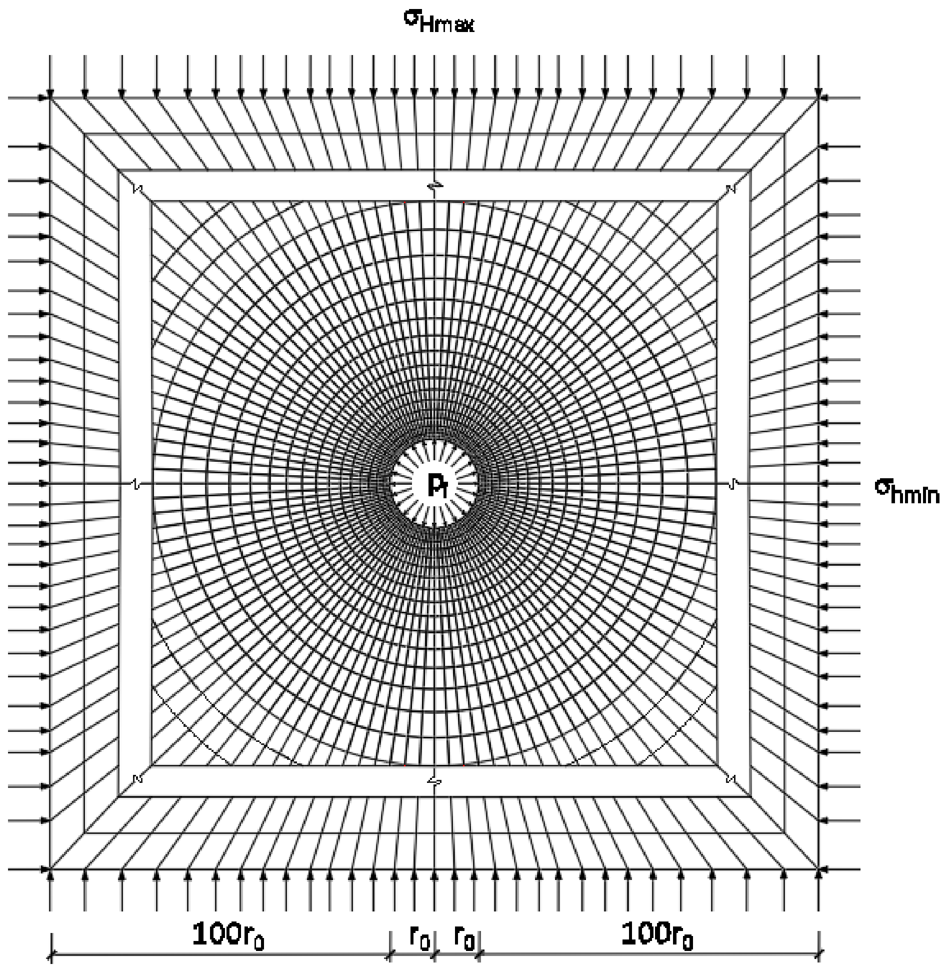

Figure 6.5 Two-dimensional finite-difference grid for the statistical inverse analysis of the RGP test

Random variables, e.g., horizontal stress, shear modulus, and shear strength, are generated through an optimizer during the statistical analysis. These random variables are input parameters for the analytical, semi-analytical solutions, and finite-difference FLAC model. The objective function formulated as Equation 6.1 is solved by coupling the analytical, semi-analytical solutions, and the FLAC model with an optimizer in the inverse analyses.

6.4.4 Statistical inverse analysis of an RGP test

The method discussed by Zheng et al. (2021) is adopted in the statistical inverse analysis of the RGP tests at the Primrose-Wolf Lake oil sands field. Results are presented separately regarding the computational model (analytical, semi-analytical solutions or numerical model) implemented in the analysis. Owing to undrained assumptions, both analytical and semi-analytical solutions are incapable of simulating the hold test. Therefore, only the expansion part of the testing curve can be simulated with analytical and semi-analytical solutions. At the same time, the numerical model can be used in both the expansion part and the whole complete curve, including expansion, hold, unload-reload loops, and contraction parts.

6.4.4.1 Point estimation for expansion curve using analytical solutions assuming isotropic expansion

A complete RGP test curve comprises expansion, hold, unload-reload loops, and contraction stages. To avoid the complexity of analyzing the complete curve, the expansion part can be separated from the complete curve for the point estimation while using the analytical solution. According to Figure 6.4, RGP tests were conducted in the Formations Westgate, Joli Fou, and Clearwater (black shale and grey shale) of the Colorado Group, respectively. The PDFs of initial parameter values (E, σ_0, S_u) for the point estimation are defined with previous publications, expert experience, and personal judgements (Advanced Geotechnology, 2001; Bell and Babcock, 1986; RG^2, 2016; Schlumberger 2014) as illustrated in Figure 6.6 to Figure 6.8, where PDFs follow uniform distributions.

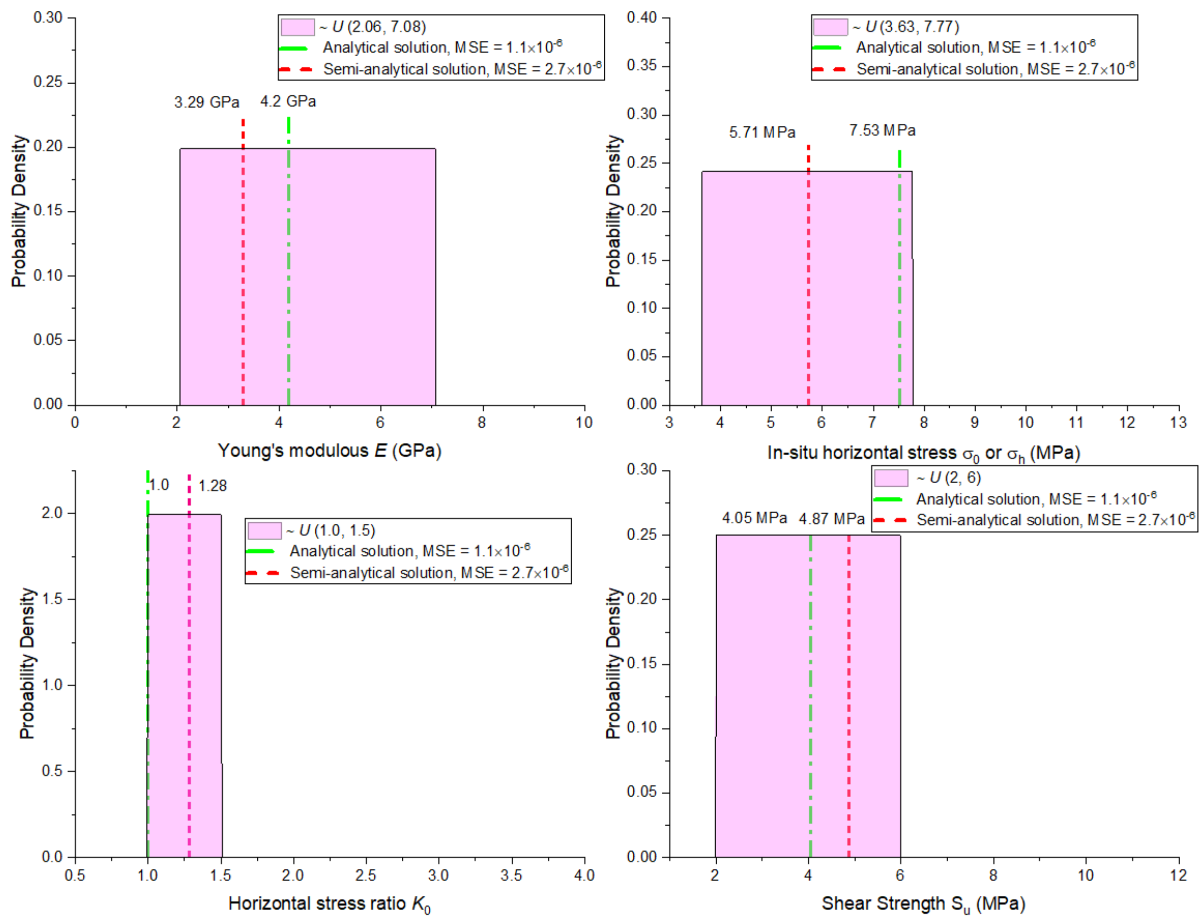

Figure 6.6 Point estimates with expansion curve using analytical and semi-analytical solutions in Westgate

Following the flow chart in Figure 6.1, a global optimization algorithm, the subset simulation (SS) is implemented to minimize the objective function (Equation 6.1). With the number of samples N_s= 1000, intermediate conditional failure probability $P(F_i) = 0.1$, and the maximum number of simulation levels N_l = 10, the average in-situ horizontal stress and rock properties can be estimated with the expansion curve using the analytical solution proposed by Jefferies (1988) (Figure 6.6 to Figure 6.9). Mean squared error (MSE) is used to quantify the goodness of fit to the measured data. The best fit for the tested four formations is the Westgate Formation, corresponding to the minimum value of MSE (1.1×10^{-6}). The reason why the Westgate formation has the smallest MSE is owing to its shallowest test depth corresponding to the least measurement uncertainty during the RGP test.

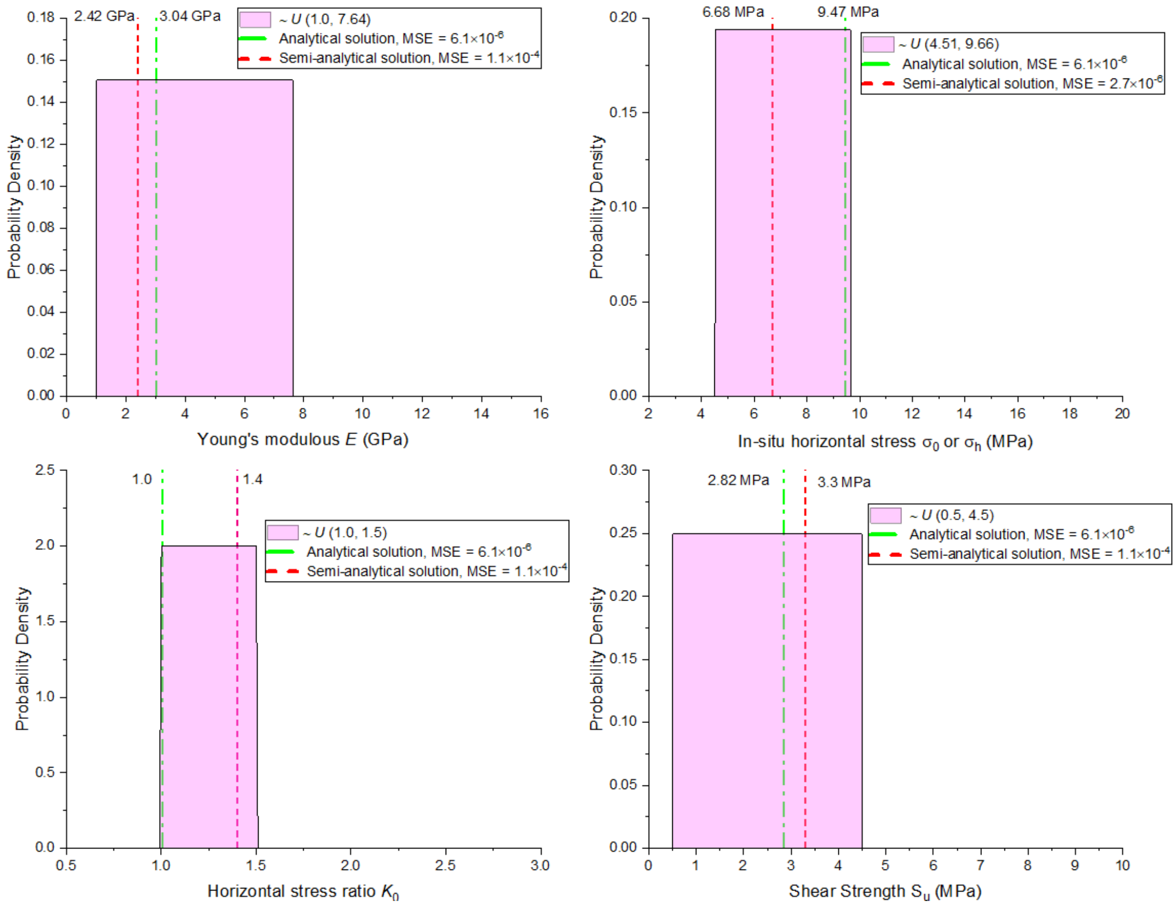

Figure 6.7 Point estimates with expansion curve using analytical and semi-analytical solutions in Joli Fou

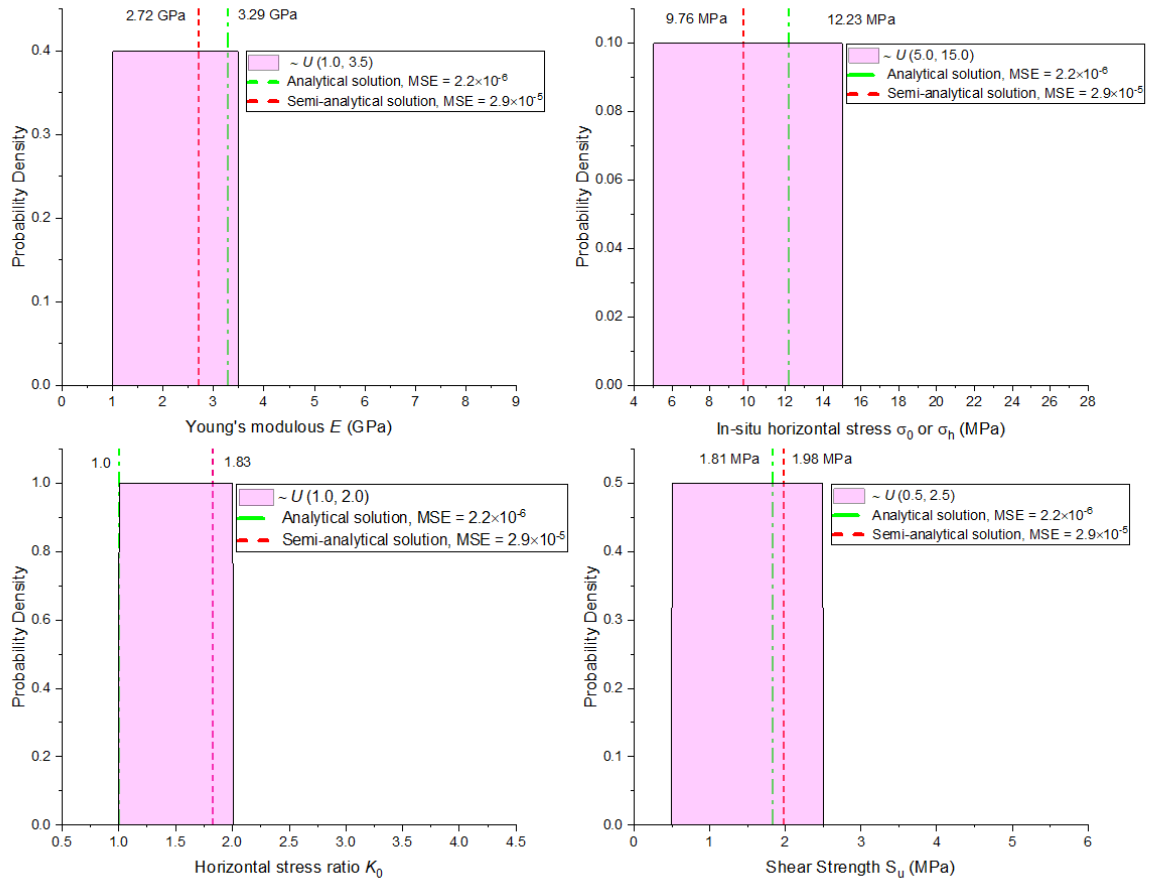

Figure 6.8 Point estimates with expansion curve using analytical and semi-analytical solutions in Clearwater black shale

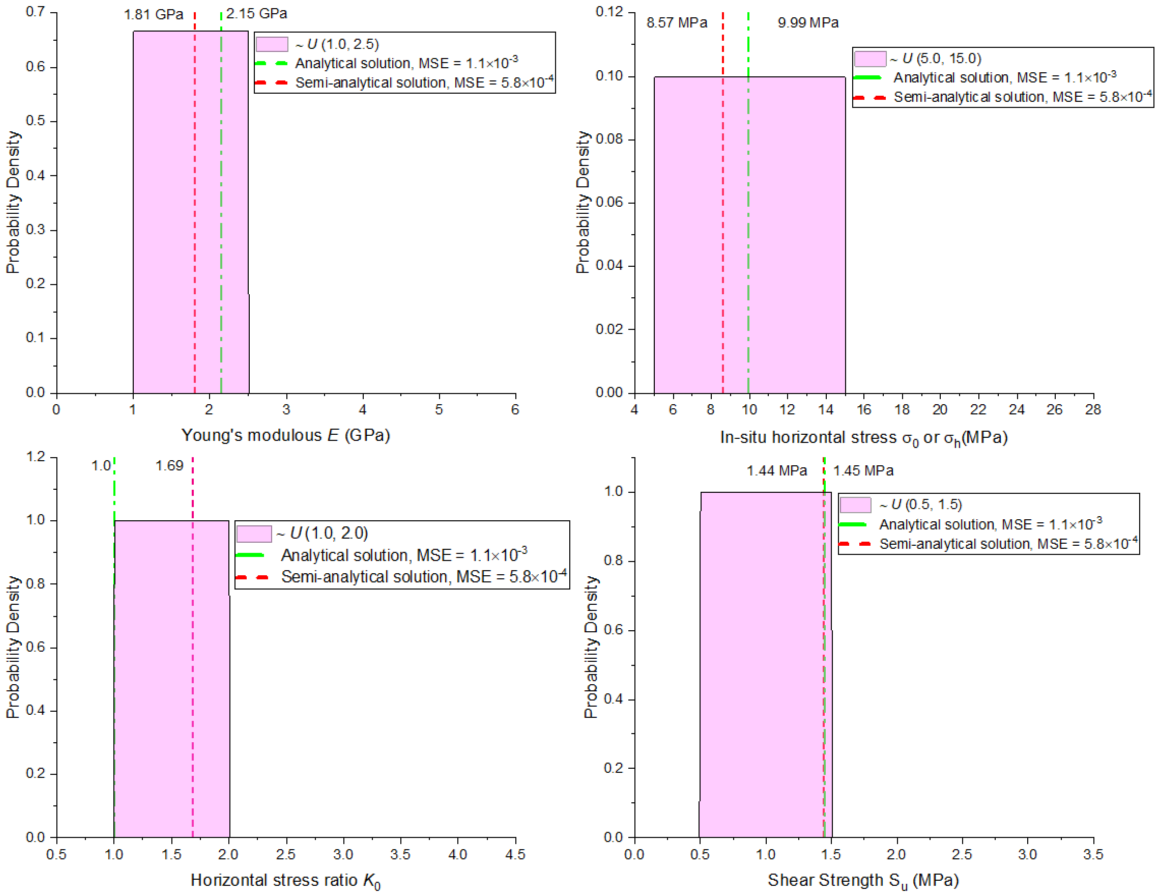

Figure 6.9 Point estimates with expansion curve using analytical and semi-analytical solutions in Clearwater grey shale

6.4.4.2 Point estimation for expansion curve using a semi-analytical solution

To account for the differential radial displacements measured by six strain arms, an anisotropic horizontal stress state should be considered in a computational model. The semi-analytical solution proposed by Zhou et al. (2015) can delineate the anisotropic behaviour of cavity expansion under biaxial boundary stress conditions. Compared to the analytical solution, the semi-analytical solution has four parameters, e.g., (E, σ_h, S_u) and the horizontal stress ratio $K_0 = \sigma_H/\sigma_h$, to be estimated. Initial parameters are assumed to be the random variables following the uniform distributions shown in Figure 6.6 to Figure 6.9. The point estimates of (E, σ_h, S_u, K_0) can be derived from the inverse analysis of RGP tests using the semi-analytical solution coupled with the SS optimizer. With the number of samples N_s = 1000, intermediate conditional failure probability $P(F_i)$ = 0.1, and the maximum number of simulation levels N_l = 10, the results from the inverse analysis are also presented in Figure 6.6 to Figure 6.9.

Although the semi-analytical solution takes 10 to 20 times longer than the analytical solution to accomplish one iteration of the function call, it is still much more efficient than a numerical model in an inverse analysis. A single run for the analytical solution takes approximately 0.01 seconds, whereas the semi-analytical solution takes 10 seconds, and the numerical model takes more than 60 seconds, depending on the loading increments.

According to Figure 6.6 to Figure 6.9, prediction with the semi-analytical solution generally has a greater MSE value than the analytical solution because the biaxial in-situ stress field is considered in the semi-analytical solution. Still, the model fit for the Westgate formation is the best, followed by the Clearwater black shale, Joli Fou, and Clearwater grey shale formations. The goodness of model fit depends on the choices of the computational model, the optimization algorithm, and the quality of the measured data. Noisy data would cause deviations in model fit owing to the uncertainties propagated from rock variability, measurement errors, and modelling.

6.4.4.3 Point estimation for complete curve using the numerical model

A complete RGP test curve comprises expansion, hold, unload-reload loops and contraction parts. To examine the effects of the hold, unload-reload loops and contraction parts on parameter estimation, the complete curve is analyzed in this section. Besides the analytical and semi-analytical solutions, a numerical model shown in Figure 6.5 is used in the point estimates for the expansion curve. The effective stress approach discussed in Section 6.3.3 is performed. The modified SS model (Section 6.3.5) reproduces the stress, strain, and pore pressure responses of clay shale in elastic and degraded zones to applied pressures. The lower and upper bounds of drained properties are illustrated in Figure 6.10 to Figure 6.13 are to constrain the random variables in the parameter optimization.

A hybrid of the simplex and the global optimization algorithm SS is implemented in the point estimation for the complete curve using the numerical model. Other than the isotropic in-situ stress state, the biaxial in-situ horizontal stress is assumed here. In such a case, the anisotropy of in-situ horizontal stress and rock properties are responsible for differential radial displacements measured by individual strain arms. Then, the minimum and maximum horizontal stresses can be estimated with arm displacements at multiple azimuthal directions by fitting an ellipse. At the same time, the orientation of the maximum horizontal stress can be determined by fitting the elliptical shape.

The implementation of the modified SS model could estimate rock properties in both elastic and degraded zones, as shown in Figure 6.2. The estimated in-situ horizontal stresses and clay shale drained properties for the elastic zone (far-field) are illustrated in Figure 6.10 to Figure 6.13. It is shown that the estimated values are considerably different between the assumptions of in-situ stress state (e.g., isotropic and biaxial). The SS optimizer is applied in the expansion phase, and the simplex algorithm is applied in the following stages, including hold test, unload-reload loops, and contraction. To simulate a biaxial horizontal stress field, an elliptical borehole perimeter is assumed. Considering the stress regime in the Western Canadian sedimentary basin (Bell and Babcock, 1986), the deformed elliptical borehole perimeter is a reasonable assumption (Zhou et al., 2015) during an RGP test in the deep clay shale formation in Alberta, Canada. In addition, Figure 6.10 to Figure 6.13 display larger MSE values in the Clearwater formations than in the Westgate and Joli Fou formations, indicating prediction uncertainties increase with the RGP test depth.

In Figure 6.10 to Figure 6.13, the azimuths of horizontal stress σ_H approximately agree with the orientation NE-SW reported by Bell and Babcock (1986), except for Joli Fou and Clearwater grey shale formations. The reason is probably due to the excessive disturbance of the pre-bored borehole during drilling and tool installation (Liu et al., 2019). There are no solutions yet to compensate for the disturbance fully. The future generation of the self-boring RGP tool can significantly reduce the influences and, therefore, the prediction of the azimuth of σ_H is expected to be more consistent with the reported orientation. Figure 6.14 shows the point estimates of hydraulic conductivities for the clay shale in the four test intervals. As there is no measured data for excess pore pressure, the inversed hydraulic conductivities may not represent the true values.

Still, hydraulic conductivity could be predicted more precisely if pore pressure is measured in an RGP test.

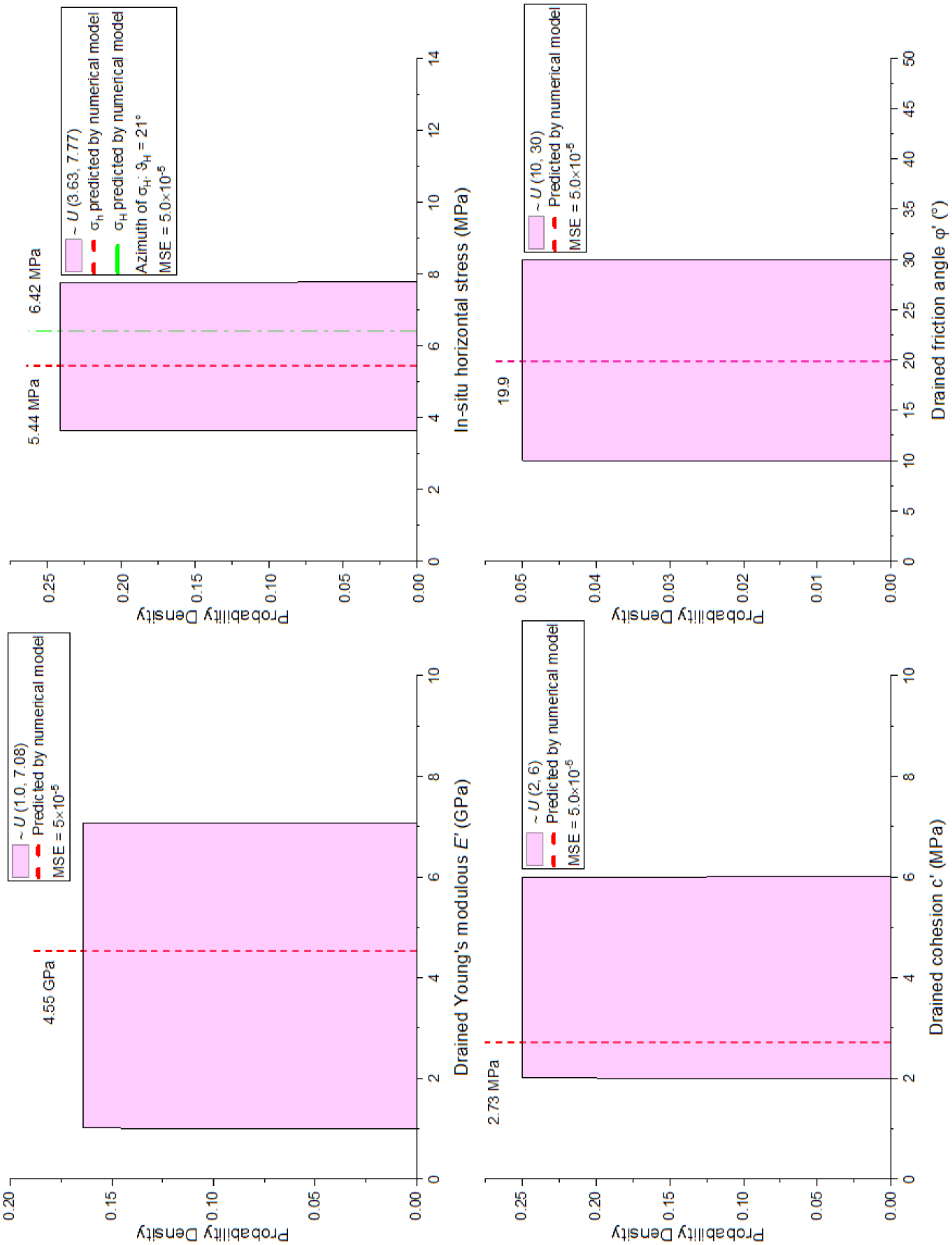

Figure 6.10 Point estimates for the elastic zone with the complete curve using the numerical model in Westgate

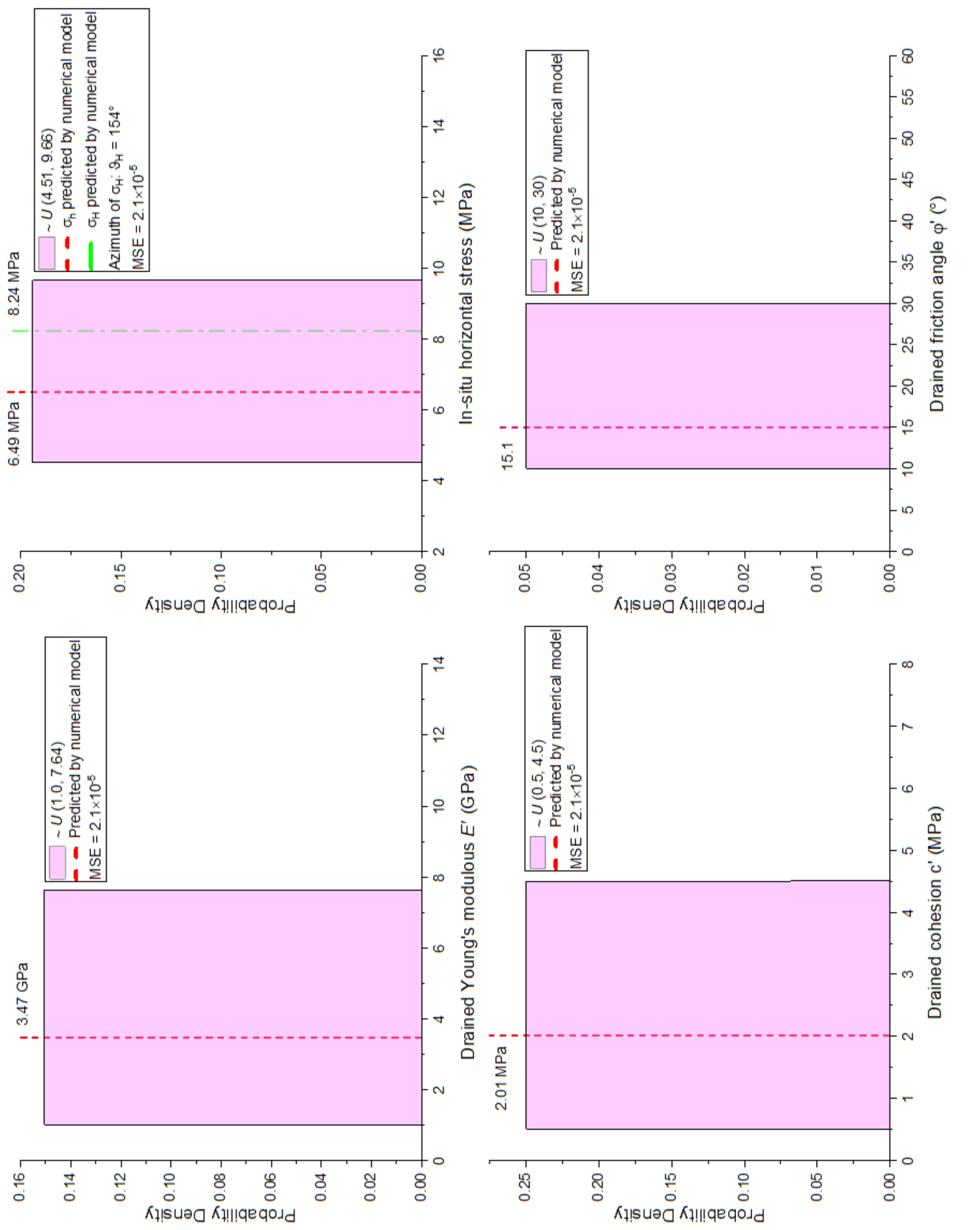

Figure 6.11 Point estimates for the elastic zone with the complete curve using the numerical model in Joli Fou

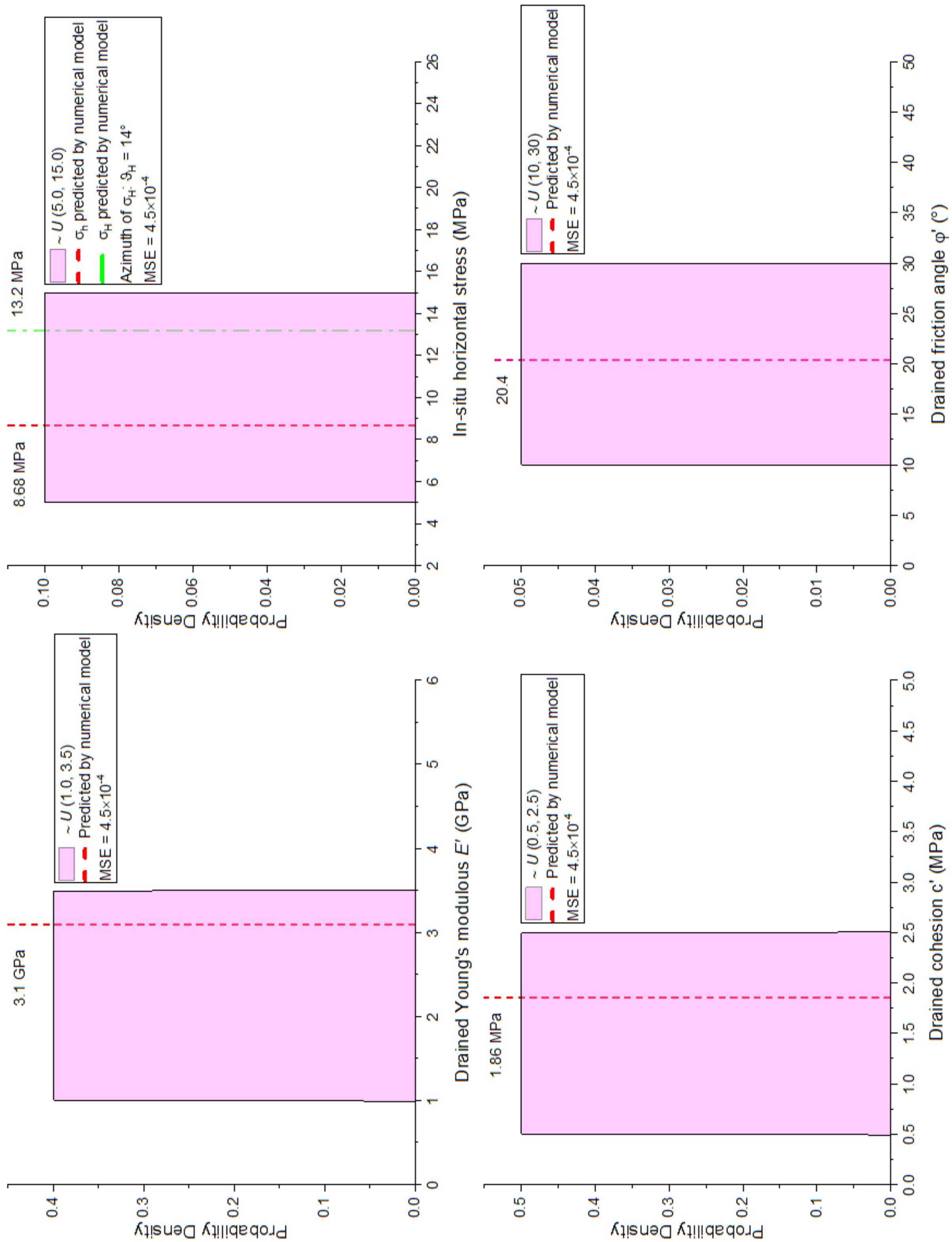

Figure 6.12 Point estimates for the elastic zone with the complete curve using the numerical model in

Clearwater black shale

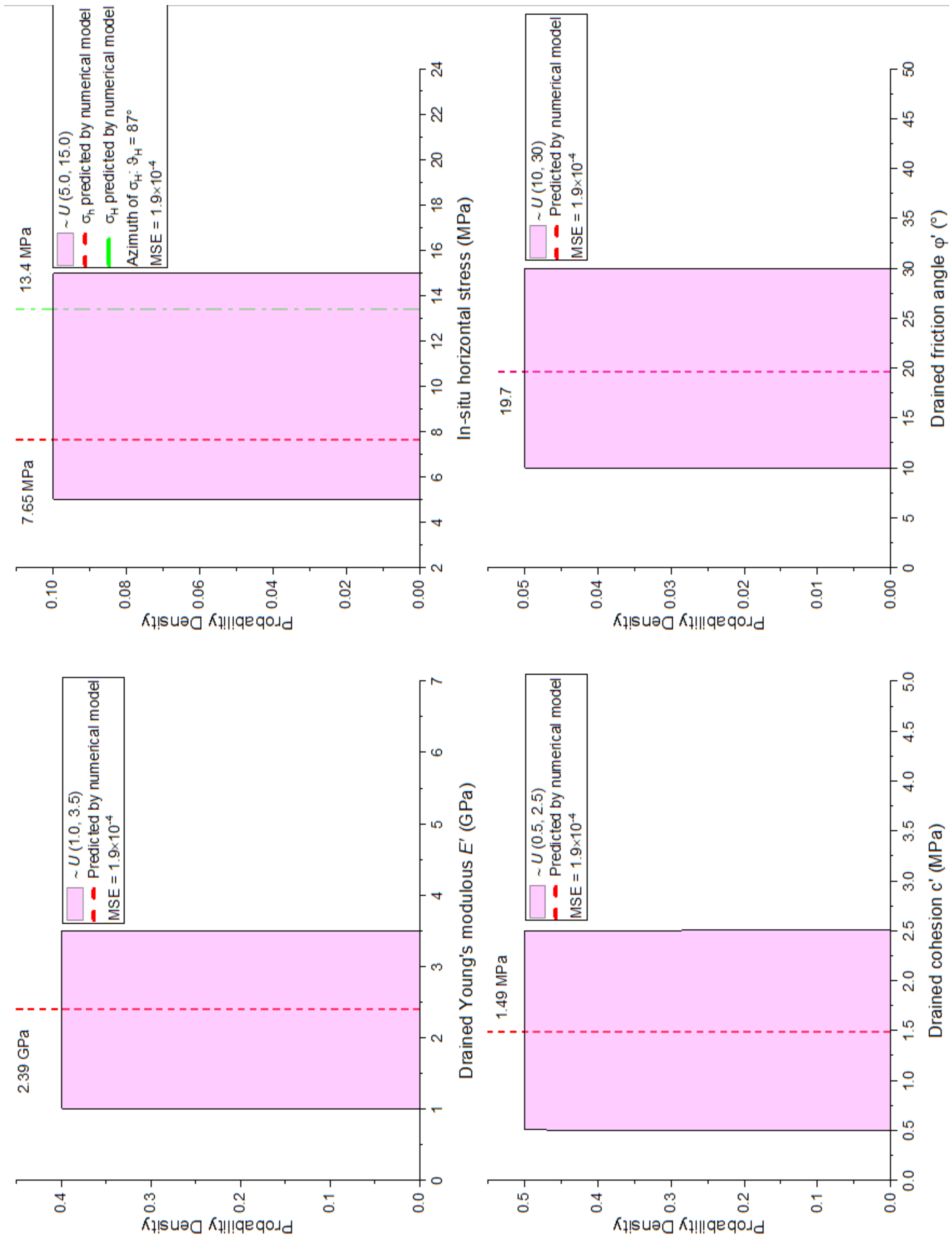

Figure 6.13 Point estimates for the elastic zone with the complete curve using the numerical model in Clearwater grey shale

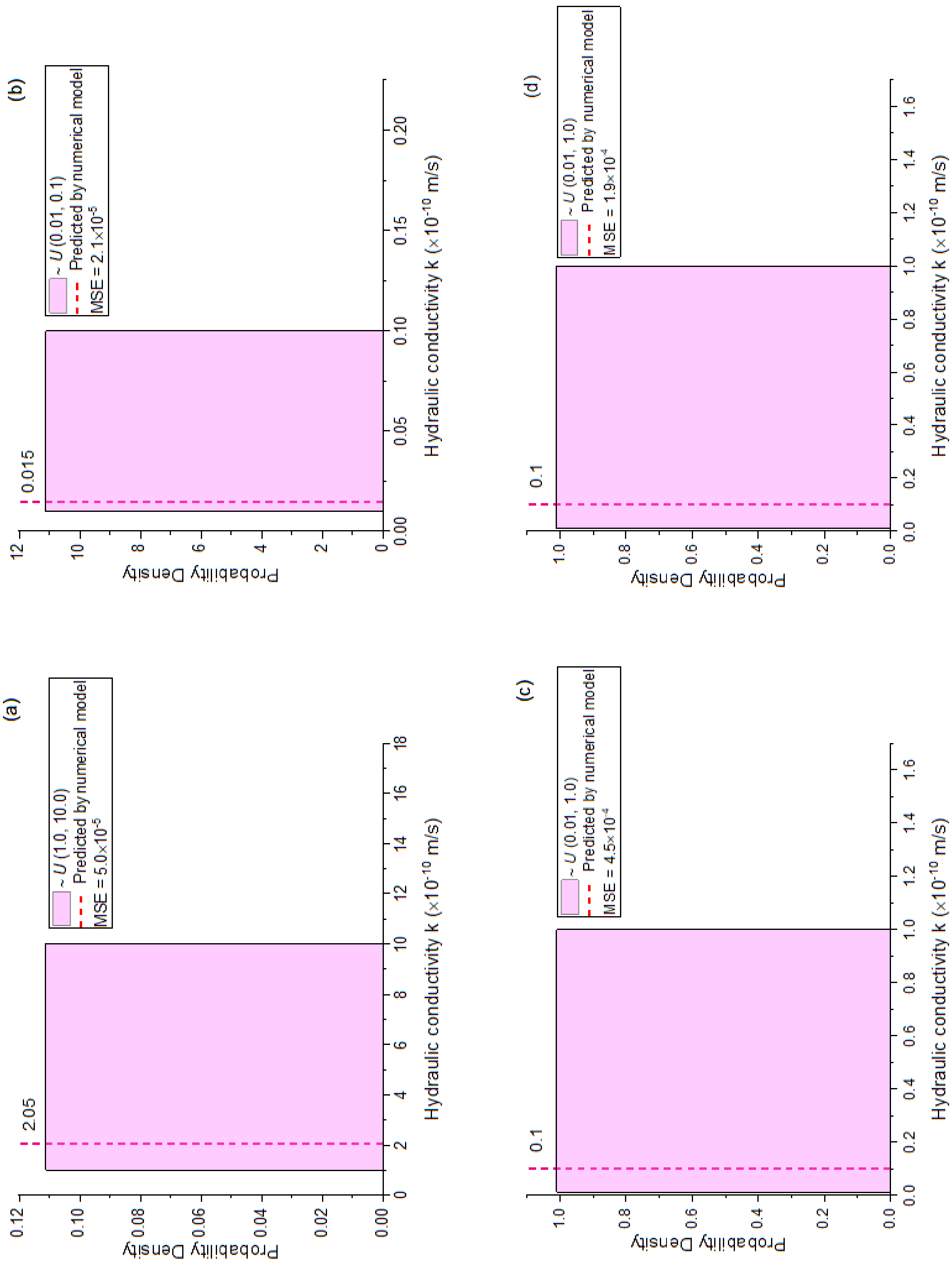

Figure 6.14 PDFs of initial hydraulic conductivity k and point estimates with the complete curve using the numerical model: (a) Westgate, (b) Joli Fou, (c) Clearwater black shale, and (d) Clearwater grey shale

Even with only the expansion part and hold test of the RGP testing curve, the inverse analysis can still satisfactorily predict in-situ parameters in the elastic zone, which are identical to the point estimates shown in Figure 6.9 to Figure 6.14. It indicates that parameters in the elastic zone (Figure 6.2) are almost constant or only slightly perturbed throughout the whole RGP test. However, the inverse analysis of the complete curve helps to understand the constitutive behaviours of clay shale in degraded zones in response to pressure changes, whose results can be referred to in Appendix C.

6.4.4.4 Statistical assessments of the RGP test

Although the minimization of an objective function Equation 6.1 can be used to find the point estimates illustrated in Figures 6.6 to 6.13, the uniqueness of a solution in point estimation is not well addressed (Houlsby, 1989; Zheng et al., 2021). Uncertainties in an RGP test may come from disturbances caused by borehole drilling and tool deployment. Not to mention the errors that resulted from tool calibration, data process and computational modelling. In this section, the statistical assessment method proposed by Zheng et al. (2021) is applied to the uncertainty quantification of point estimation for an RGP test. Results show its capability in quantifying uncertainties for the statistical inverse analysis of the RGP test.

Statistical assessments were carried out for the four RGP tests conducted in the Westgate, Joli Fou, and Clearwater formations. Table 6.1 summarizes the mean values and 95% CIs of $(E', \sigma_h, \sigma_H, c', \varphi')$ derived from the expansion curve using the numerical model.

Mean values in Table 6.1 almost coincide with point estimates illustrated in Figure 6.10 to Figure 6.13, implicating the uniqueness of point estimation using the numerical model is satisfactory. However, the mean values in Table 6.1 do not always agree with point estimates. In other words, there are other combinations of datasets to fit the RGP testing curve using the point estimation approaches discussed above. Alternatively, CIs predicted with the statistical assessment method can quantify the uncertainty of the derived parameters and reduce the solution's non-uniqueness. Thus, the target is to derive narrow CIs rather than "true values" from the parameter point estimation. The predicted CIs of $(E', \sigma_h, \sigma_H, c', \varphi')$ can be used to quantify the uncertainty in the inverse analysis of an RGP test.

Table 6.1 Statistical assessments of parameters derived from expansion curve using the numerical model

Formation	Predicted values	E' (GPa)	σ_h (MPa)	σ_H (MPa)	c' (MPa)	φ'
Westgate	mean	4.55	5.44	6.42	2.73	19.9
	95% CI	(4.49, 4.62)	(5.25, 5.64)	(6.01, 6.90)	(1.99, 3.47)	(16.1, 23.8)
Joli Fou	mean	3.47	6.48	8.21	2.0	15.1
	95% CI	(3.18, 3.77)	(6.40, 6.55)	(8.08, 8.35)	(1.60, 2.40)	(12.2, 17.9)
Clearwater black shale	mean	3.10	8.68	13.2	1.86	20.4
	95% CI	(2.97, 3.23)	(8.05, 9.31)	(12.1, 14.2)	(1.68, 2.03)	(18.9, 22.0)
Clearwater grey shale	mean	2.39	7.73	13.4	1.49	19.7
	95% CI	(2.06, 2.71)	(6.89, 8.56)	(11.9, 15.0)	(1.22, 1.76)	(17.1, 22.3)

The complete expansion-contraction RGP testing curve is utilized in the following statistical assessment to study the effects of the unload-reload loops and the contraction part on the derived parameters. Table 6.2 summarizes the mean values and 95% CIs of $(E', \sigma_h, \sigma_H, c', \varphi')$ of the parameters derived from the complete curve using the numerical model.

Table 6.2 Statistical assessments of parameters derived from complete curve using the numerical model

Formation	Predicted values	E' (GPa)	σ_h (MPa)	σ_H (MPa)	c' (MPa)	φ'
Westgate	mean	4.56	5.44	6.44	2.74	20.0
	95% CI	(4.55, 4.56)	(5.41, 5.47)	(6.38, 6.51)	(2.68, 2.80)	(19.6, 20.3)
Joli Fou	mean	3.47	6.49	8.25	2.01	15.1
	95% CI	(3.41, 3.53)	(6.47, 6.50)	(8.23, 8.28)	(1.99, 2.04)	(14.8, 15.3)
Clearwater Black Shale	mean	3.10	8.68	13.2	1.86	20.4
	95% CI	(3.06, 3.14)	(8.56, 8.79)	(13.0, 13.3)	(1.78, 1.93)	(19.7, 21.2)
Clearwater Grey Shale	mean	2.39	7.73	13.4	1.49	19.7
	95% CI	(2.37, 2.41)	(7.70, 7.76)	(13.4, 13.5)	(1.47, 1.51)	(19.4, 20.0)

Mean values in Table 6.2 are approximately identical to Table 6.1, but 95% CIs are much narrower. This can be explained by the fact that more data points are included in the inverse analysis and mathematically reduce prediction uncertainties. However, due to the complexity of the RGP testing curves, data points in unload-reload loops may not be able to reduce the estimation uncertainties identified in Table 6.2, which is explained in detail in Section 6.4.4.5.

6.4.4.5 Evaluation of the model fit with the coefficient of determination

Although the statistics listed in Table 6.1 and Table 6.2 provide quantitative assessments of the inversed parameters, a visual comparison of predicted and observed curves is still meaningful in evaluating the model fit. The prediction bands calculated with the 95% CIs are plotted in Figure 6.15 and Figure 6.16. The coefficient of determination (CoD), R^2 is also calculated.

The numerical modelling can reproduce the test curves with satisfactory accuracy ($R^2 > 0.97$). Prediction uncertainties quantified in Table 6.1 can be illustrated in Figure 6.15 with prediction bands. The change of the prediction band represents the variability of uncertainty, which is the narrower the band is, the less the uncertainty is, and vice versa.

Figure 6.15 illustrates the 95% CI prediction band for the expansion curve at the azimuthal orientation of 45°, representing those at any other direction. There is a very narrow prediction band at the early stage of the expansion curve, as shown in Figure 6.15a, showing that the uncertainty of predicted data is minimal at the beginning of the expansion and then gradually increases to the maximum at the end of the expansion for the RGP test in the Westgate formation. A similar trend wasn't observed in other formations, implying that the RGP test in Westgate is more reliable than the others.

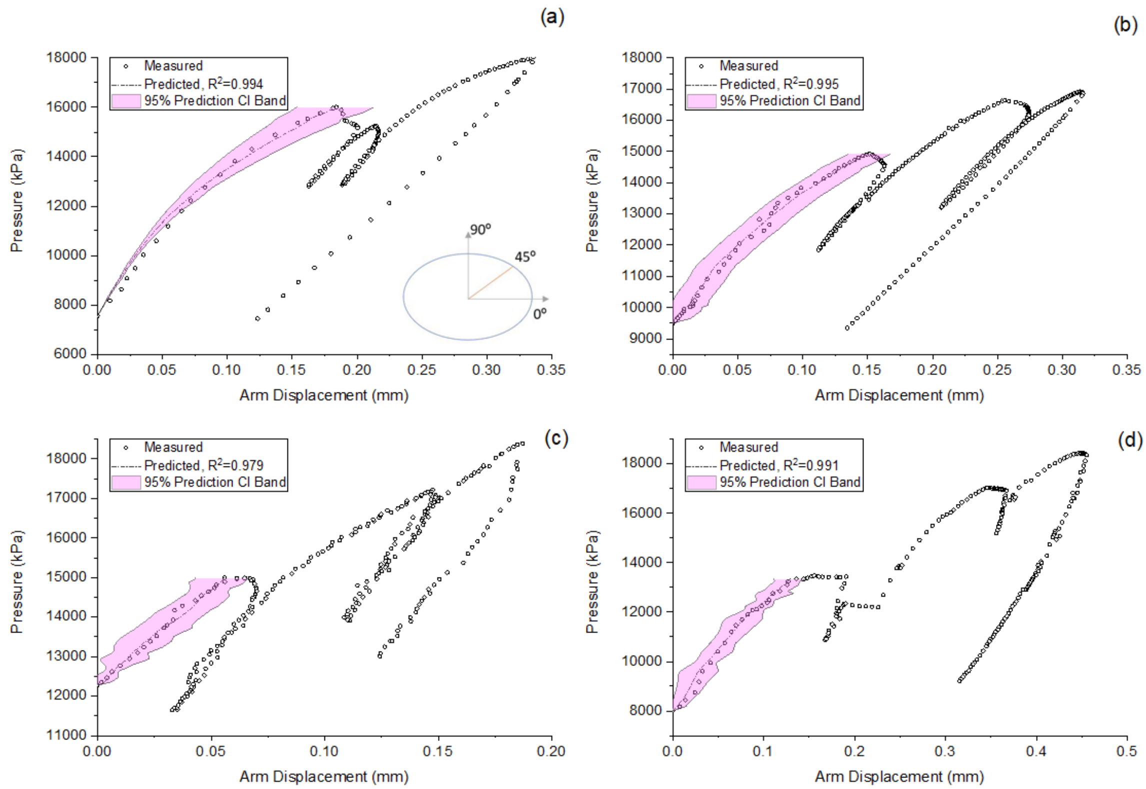

Note: (a) Westgate, (b) Joli Fou, (c) Clearwater black shale, and (d) Clearwater grey shale.

Figure 6.15 Fit of observed to predicted data using the numerical modelling for the expansion curve at 45°

Figure 6.16 illustrates the 95% CI prediction bands of the complete curves. Interestingly, the prediction bands are relatively narrow at the expansion stage, especially in Figure 6.16a (Westgate) and Figure 6.16d (Clearwater grey shale). It can be explained that the observed data at the expansion stage are more reliable than those at the following stages. Figure 6.16 shows several unload-reload loops and hold tests between the expansion curve and the contraction curve. As Liu et al. (2019) pointed out, these hold tests were deemed unsuccessful due to nitrogen gas leakage and the large system volume. Still, more uncertainties could be generated in the following unload-reload loops because of the unstable supply of gas. As a result, it is suggested that an RGP test in deep formation should be conducted as simply as possible by including expansion and contraction parts only if the horizontal stress is most concerned.

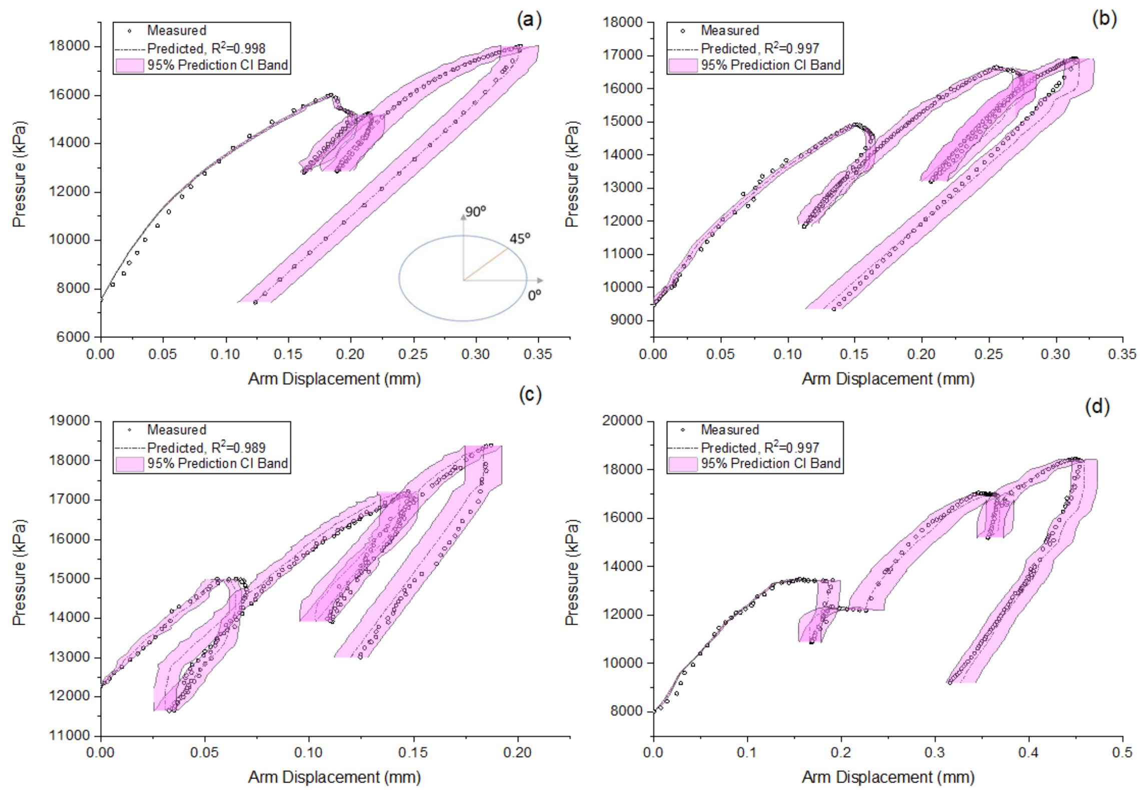

Note: (a) Westgate, (b) Joli Fou, (c) Clearwater black shale, and (d) Clearwater grey shale.

Figure 6.16 Fit of observed to predicted data using the numerical modelling for the complete curve at 45°

In general, narrower prediction bands can be observed from the expansion part in Figure 6.16 than in Figure 6.15. As more data points are involved in the statistical assessments, and mathematically, the uncertainties in the whole curve fitting are dramatically reduced. However, data points in unload-reload loops cannot reduce the prediction uncertainties. Consequently, prediction bands at the expansion stage in Figure 6.16 are mathematically narrow only rather than physically more certain. The prediction bands in Figure 6.15 are better than those in Figure 6.16 to represent the true prediction intervals. The CIs should refer to Table 6.1 rather than Table 6.2.

If there are no unload-reload loops and hold tests in Figure 6.16, the contraction curve should be more reliable than the expansion part, as the effect of installation disturbance becomes minimal at this stage (Ferreira, 1992; Houlsby and Withers, 1988).

6.4.4.6 Profile of horizontal stress derived from statistical assessment method

For an RGP test, the in-situ horizontal stress draws the most attention as the rock stiffness and strength can be evaluated by other types of in-situ tests. Schlumberger performed microfrac tests (CNRL, 2011) in Wells 11-11 and 11-12 at Primrose East, near this RGP testing site. The microfrac modular formation dynamics tester (MDT) was used to measure the minimum in-situ horizontal stress σ_h at various depths in the Colorado Group shales. The values of σ_h estimated with the MDT are plotted in Figure 6.17, together with the horizontal stress data points listed in Table 6.1.

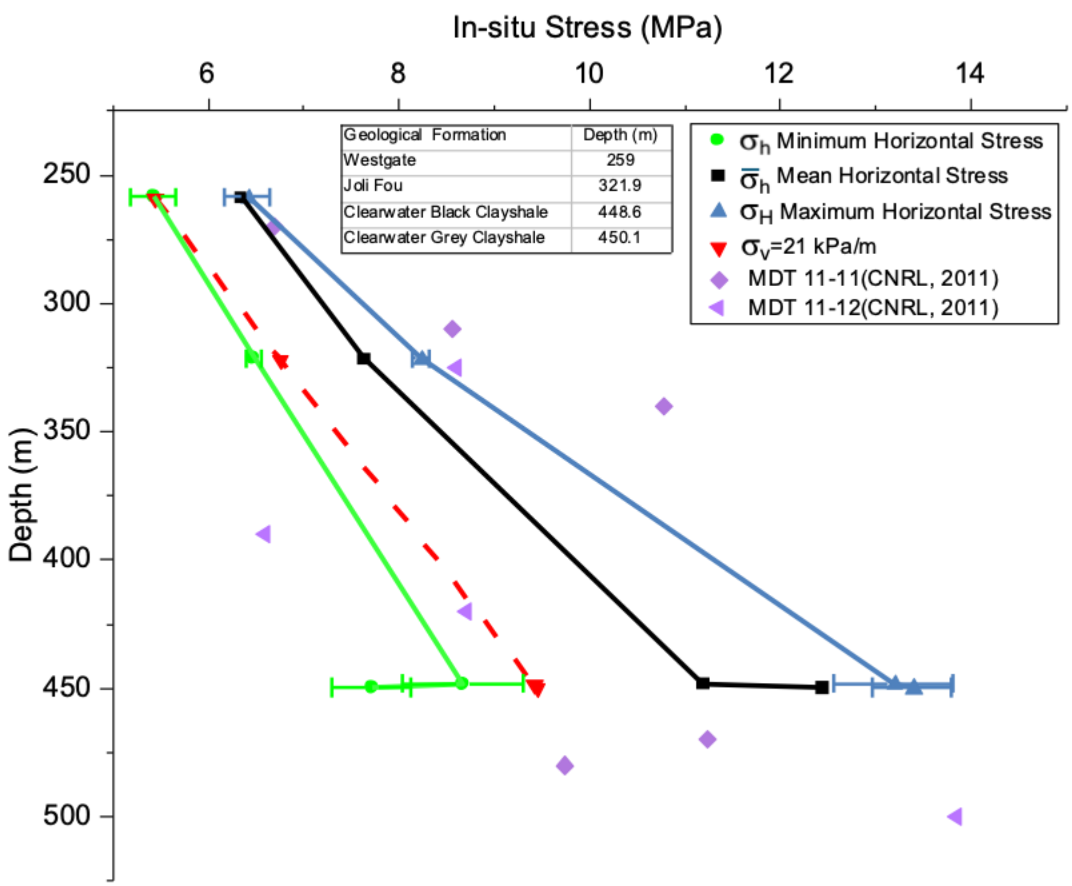

Figure 6.17 Profile of in-situ stresses derived from statistical assessment methods using the numerical model

The mean values of (σ_h, σ_H) measure the magnitudes of the horizontal stresses at the test interval in each formation. Figure 6.17 illustrates the profile of the mean values of horizontal stresses derived from inverse analyses using numerical modelling. Through the discussion above, uncertainties from the horizontal stresses are evaluated using the expansion curve. By conducting the proposed statistical assessment on the expansion curve, the variabilities of (σ_h, σ_H) are illustrated with the SD bars, which represent the 95% CIs of the predicted (σ_h, σ_H). By examining the length of SD bars, Joli Fou has the least uncertainty than other formations in terms of the derived horizontal stresses. Clearwater formations account for the most significant uncertainty in the evaluation of horizontal stresses. It can be easily seen that both the measured (MDT) and predicted data points lie within the ranges defined by the SD bars, showing that the proposed statistical assessment method can constrain the horizontal stresses estimated by the MDT and RGP tools.

6.5 Summary and Conclusions

This section explains using the inverse analysis of the RGP field test in the Primrose site through the analytical solution, semi-analytical solution, and numerical modelling coupled with the SS and Simplex optimization methods. To estimate in-situ parameter values, random variables are generated and passed into a computational model. After thousands of iterations, the minimum value of the objective function can be determined, which corresponds to the best in-situ parameter estimates. A case study presents the results of the inverse analysis of RGP tests at the Primrose-Wolf Lake oil sands field near Bonnyville, Alberta.

Due to the assumption and limitations, only the expansion part of an RGP test curve was simulated in the inverse analysis using analytical and semi-analytical solutions. To fit the complete testing curve, a fluid-mechanical coupling technique using the effective stress approach in the finite-difference models was adopted in the numerical model. Drained material properties instead of undrained ones were used in numerical modelling.

The analytical solution (Jefferies, 1988) is runtime efficient but unsuitable for simulating a complete RGP testing curve, including hold and unload-reload loops. Furthermore, the analytical solution can not simulate the in-situ stress anisotropy. Nevertheless, the semi-analytical solution can satisfactorily predict the minimum horizontal stress and probably overestimate the maximum horizontal stress. The semi-analytical solution is preferred to a numerical model in an inverse analysis regarding the computing cost.

Consolidation in a pressure hold test following the expansion stage cannot be solved with Jefferies' and Zhou's solutions because of their undrained assumption. The pressure variation during the 'unsuccessful' hold tests at the Primrose-Wolf Lake site prevented it from being solved analytically. Only a fluid-mechanical coupling technique can reproduce the process numerically. Without pore pressure measurement, the hydraulic conductivity derived from inverse analysis cannot be calibrated. Therefore, the k values listed in Figure 6.14 might not be predicted accurately.

The modified SS model has advantages over the SS model while simulating the borehole wall responses to applied pressure. The material strain-hardening/softening behaviours can be quantified with hardened/softened variables, which can simplify the inverse analysis of the RGP test.

Due to the existence of non-unique solutions, uncertainties from the RGP test and the inverse analysis should be quantified with statistics (mean and 95% CIs) using the proposed statistical assessment method. The predicted CIs constrain the variability of clay shale properties and horizontal stresses. Thus, the non-uniqueness of the solution can be partially reduced if it cannot be eliminated. Alternatively, the prediction bands in Figures 6.15 and 6.16 illustrate the variabilities of predicted arm displacements in response to the pressure increment in an RGP test. The width of the prediction band is the function of 95% CIs in Table 6.1 and Table 6.2. Due to the unsuccessful hold tests, there are more uncertainties generated in unload-reload loops. Data points measured in unload-reload loops cannot physically reduce the solution's non-uniqueness. In such cases, statistics from the expansion curve (Table 6.1) are preferred to the ones from the complete curve (Table 6.2).

Curve-fittings in upper Formations (Westgate and Joli Fou) are better than in lower Formations (Clearwater) due to the quality of measured data points. With the increase in testing depth, more uncertainties are expected to be encountered in the RGP test. Due to nitrogen gas leakage and the large system volume in the RGP tests in deep formations, more uncertainties were encountered in the hold tests and the following unload-reload loops. In such a case, data points measured in unload-reload loops cannot physically reduce the non-uniqueness of the solution. Therefore, the expansion curve predicts a more reasonable mean and narrower 95% CIs in the inverse analysis than the complete curve does. It is advised to conduct a simple test comprising the expansion and contraction parts only if the horizontal stress is paid interest.

The statistical method described above can be extended to other engineering inverse analysis problems, such as pile load tests, landslide monitoring, and deep excavation open pits.

In addition to the statistical inverse methods applied in this chapter, a Bayesian inverse analysis of the RGP tests at the Primrose – Wolf Lake oil sands field is discussed in Chapter 7.

7.0 BAYESIAN INVERSE ANALYSIS OF THE RGP TESTS AT PRIMROSE-WOLF LAKE OIL SANDS FIELD

A reservoir geomechanical pressuremeter (RGP) was developed by the reservoir geomechanical research group (RG^2) at the University of Alberta in 2016. As an in-situ testing tool, RGP was deployed into the downhole in three geological formations (Westgate, Joli Fou, and Clearwater) using industry-standard wireline technology (RG^2, 2016; Liu et al., 2019). Bayesian inverse analysis of the RGP test comprises two parts: i) point estimation by the maximum a posteriori (MAP) method, and ii) statistical inference using Markov Chain Monte Carlo (MCMC) simulation. With the cell pressure and radial displacements measured during the RGP tests, in-situ horizontal stress and rock properties can be derived from the point estimation using the MAP method. However, Like deterministic methods, MAP may find non-unique solutions (Houlsby, 1989) due to a local optimizer used. To solve the problem of non-uniqueness encountered in the MAP analysis of the RGP test, Bayesian inference is introduced to estimate parameter mean and their statistics. Under the Bayesian paradigm, the highest density interval (HDI) can be inferred from Markov chain samples. To perform the Bayesian inference, a computational model (analytical) needs to be coupled with a sampling algorithm in MCMC simulations. The mean and its statistics can be summarized with samples drawn from MCMC chains that distinguish from the frequentist perturbation method. After MCMC simulations, posterior belief from Bayesian inference can be continuously updated if new evidence is available, which makes the Bayesian inference superior to the traditional frequentist statistical methods.

Finally, the goodness of curve fit is evaluated with the coefficient of determination R^2. in addition, the highest density interval (HDI) of posterior distributions can also be obtained from the MCMC chains.

7.1.1 Methodology

The goal of an RGP test is to record the changes in the applied pressure and radial displacements during the expansion, contraction, hold, and loading/reloading stages. In addition, an RGP testing curve analysis is performed to estimate the values of in-situ horizontal stress and rock properties for geomechanical investigation. With observed data from the RGP test, point estimation with the MAP method is usually first carried out and then followed by MCMC analysis.

At the beginning of the point estimation, the prior probability distribution for unknown parameters must be assumed. The proposed PDFs, such as uniform, normal, and log-normal distribution, represent a priori knowledge of rock properties and in-situ horizontal stress from previous publications, expert experience, and personal judgment. This study assumes uniform distributions for all unknown parameters. To simulate an RGP test, an analytical (closed-form) solution shall be adopted. To conduct the point estimation, an objective function shall be formulated with the observed and predicted data. In-situ horizontal stress and rock properties can be estimated by minimizing or maximizing the objective function.

Statistics of the estimated parameters can be performed with the frequentist assessment methods presented by Zheng et al. (2021). Alternatively, Bayesian inference analysis can find the mean and its statistics by summarizing the posterior samples after MCMC simulations. As a result, a sampling algorithm, such as the Metropolis-Hastings (MH), No-U-Turn (NUTS) and slice sampler, needs to be coupled with a computational model in the MCMC simulation. The convergence of an MCMC chain often depends on the efficiency of a computational model and the selection of a sampler.

7.1.2 Objective function

To carry out the inverse analysis of RGP tests, an objective function needs to be defined. In the Bayesian method, a log-likelihood function can be formulated as the objective function in the searching process of a local optimization algorithm using MAP or the iterative convergence of MCMC chains. Given a normal distribution, the log-likelihood function ℓ can be defined as in Equation 7.1 (Taboga, 2017):

$$\ell(\mu(\theta),\ \sigma^2;\ y) = -\frac{n}{2} ln(2\pi) - \frac{n}{2} ln(\sigma^2) - \frac{1}{2\sigma^2} \sum_{j=1}^{n} \left(y_j - \mu(\theta)\right)^2 \tag{7.1}$$

where $y = (y_1, y_2, \ldots, y_n)$ denotes observed data; μ indicates predicted data; θ denotes unknown parameters, and σ represents the standard deviation. n represents the number of observed data from a pressuremeter test. The parameters $\widehat{\theta}$ can be estimated by maximizing the specific log-likelihood function $\widehat{\ell}$ over the parameter space Θ:

$$\hat{\theta} = \arg\max_{\theta \in \Theta} \hat{\ell}(\mu(\theta), \sigma^2; y) \tag{7.2}$$

Similarly, log-likelihood functions for other distributions like Poisson, exponential, and student t distribution can be derived. The log-likelihood function like Equations 7.1 and 7.2 makes the MAP and MCMC analysis easier by implementing an analytical or numerical model in the Bayesian inference framework.

7.1.3 Workflow of the Bayesian inverse analysis

For the Bayesian methods, the dataset that maximizes the likelihood function with the BFGS optimizer in the MAP corresponds to the optimal point estimates; In MCMC sampling, a sampling algorithm, such as the NUTS and slice sampler, generates random variables defined by the prior PDFs. Those random variables are passed into the objective function formulated as a likelihood function. After many iterations, the convergence of MCMC chains could be evaluated with diagnostics criterion. Once the chain is converged, its elements can be accepted as samples from the target posterior distribution. As a result, posterior statistics can be summarized from those samples, from which the mean and 95% HDIs are statistically obtained. The workflow for the proposed Bayesian inference of the pressuremeter test is shown in Figure 7.1.

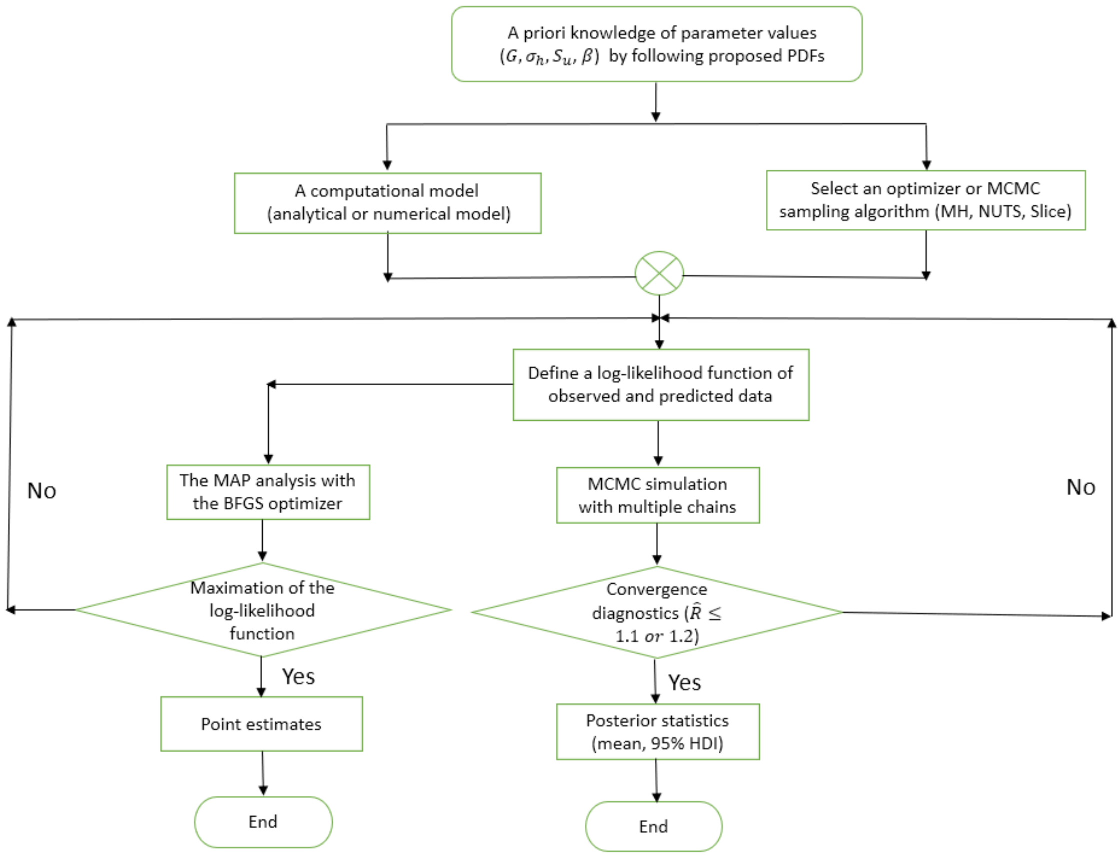

Figure 7.1 Flow chart of Bayesian Statistical inference of an RGP test.

The framework of the Bayesian inference includes, but is not limited to, the following steps: (i) a priori knowledge of initial values and uncertainty quantification of input variables, (ii) selection of a computational model and coupling with an MCMC sampling algorithm, (iii) establishing a likelihood function as the objective function, (iv) identification of the optimal value (MAP) or the mean and its statistics from posterior distributions (MCMC) by maximizing the log-likelihood function, and (v) convergence diagnostics.

7.1.4 Bayesian model building of RGP field tests

Project background and RGP test information can be referred to in Sections 6.1 and 6.2. Because of the extremely high computational cost, it is impractical to adopt a numerical model in the Bayesian analysis. Therefore, only the analytical solution (Jefferies, 1988) is used in the Bayesian analysis. Random variables, e.g., horizontal stress, shear modulus, and shear strength, are generated through a sampling algorithm in the Bayesian inference. These random variables were used as the input parameters for the analytical solution. The objective function formulated as Equation 7.1 is solved by coupling the analytical solution in Bayesian analyses.

7.1.5 Results from Bayesian inverse analysis of RGP field tests

The maximum a posterior (MAP) and the Bayesian inference with MCMC simulations can be performed for the RGP tests in the Primrose-Wolf oil sands project. Due to the limitation of the analytical solution, only the expansion part of an RGP test curve is simulated with the analytical solution.

7.1.5.1 Point estimation with MAP using the analytical solution

MAP is a point estimator in a Bayesian setting. The Broyden–Fletcher–Goldfarb–Shanno (BFGS) optimization algorithm can find the maximum of the log-likelihood function ℓ defined in Equation 7.1. Compared to the Bayesian inference with MCMC simulations, the MAP estimator is fast and efficient. However, only point values can be estimated without associated statistics.

MAP is equivalent to maximum likelihood estimation (MLE), while prior follows a uniform distribution. However, as a local optimizer, BFGS in the MAP analysis can only find the local optimal parameter values, which are shown in Figure 7.2 to Figure 7.4.

By examining Figure 7.2 to Figure 7.4, the MAP method can make essentially identical predictions to the results in Section 6.4.4 using the SS optimizer. However, although the MAP method is efficient, a point estimate can be biased in local regions. For example, MAP does not entirely coincide with the SS optimizer in terms of the parameter estimates for the Clearwater grey shale formation. Alternatively, the Bayesian inference with MCMC simulations can ensure the global minimum by sampling data from the posterior distribution.

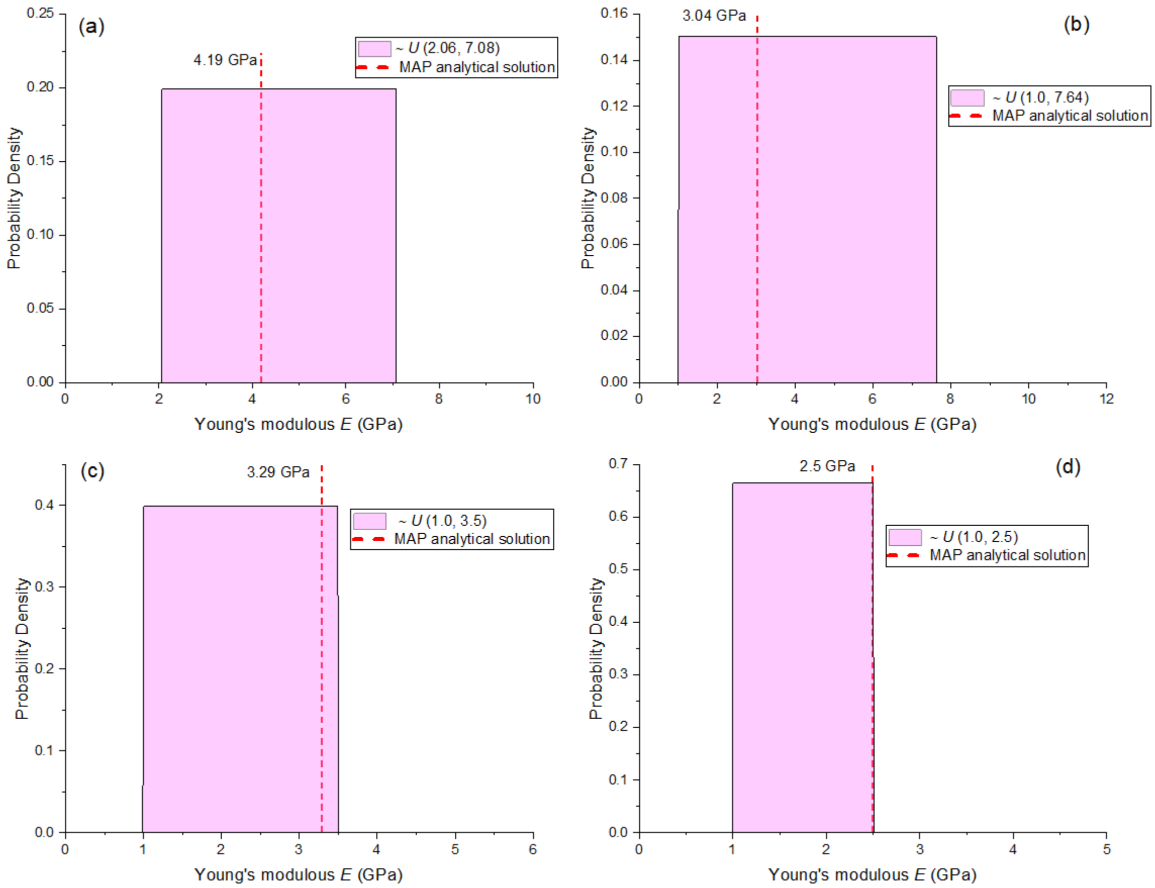

Figure 7.2 PDFs of initial Young's modulus E and point estimates with MAP using the analytical solution: (a) Westgate (b) Joli Fou (c) Clearwater black shale and (d) Clearwater grey shale.

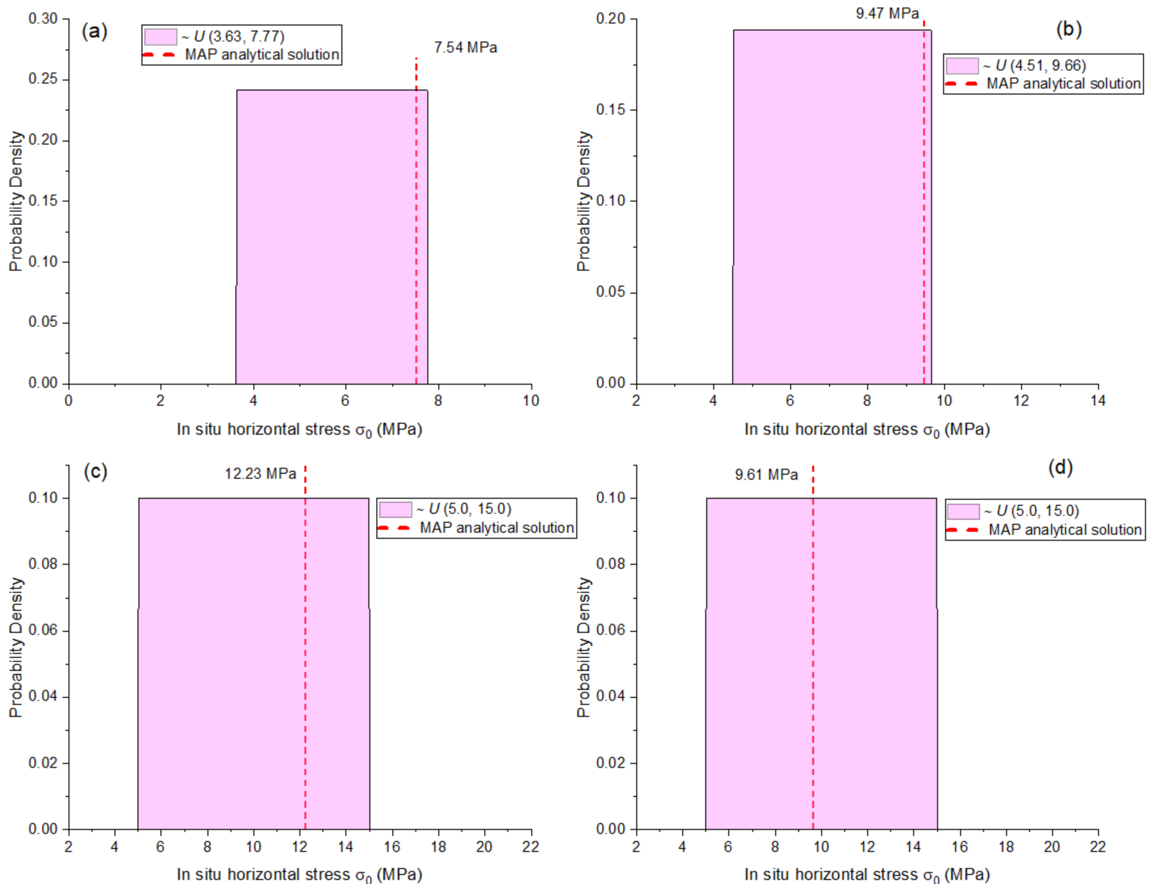

Figure 7.3 PDFs of initial horizontal stress σ_0 and point estimates with MAP using the analytical solution: (a) Westgate (b) Joli Fou (c) Clearwater black shale and (d) Clearwater grey shale

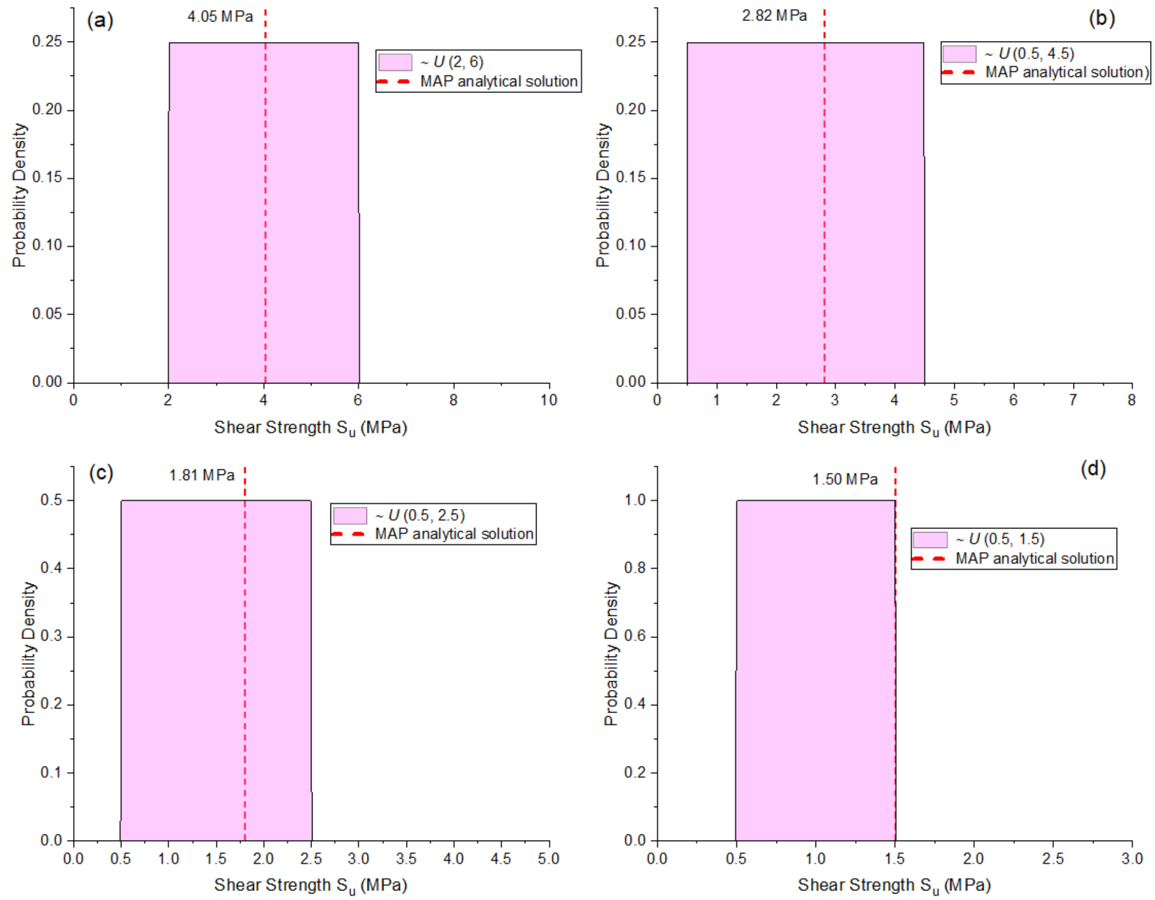

Figure 7.4 PDFs of initial shear strength S_u and point estimates with MAP using the analytical solution: (a) Westgate, (b) Joli Fou, (c) Clearwater black shale and (d) Clearwater grey shale

7.1.5.2 Bayesian inference with MCMC using the analytical solution

Besides the point estimation with the MAP method, a complete Bayesian inference can obtain mean and posterior statistics through MCMC simulations. The No-U-Turn (NUTS) sampling algorithm is selected for the MCMC simulations using the analytical solution (Jefferies, 1988) for the expansion parts of RGP tests.

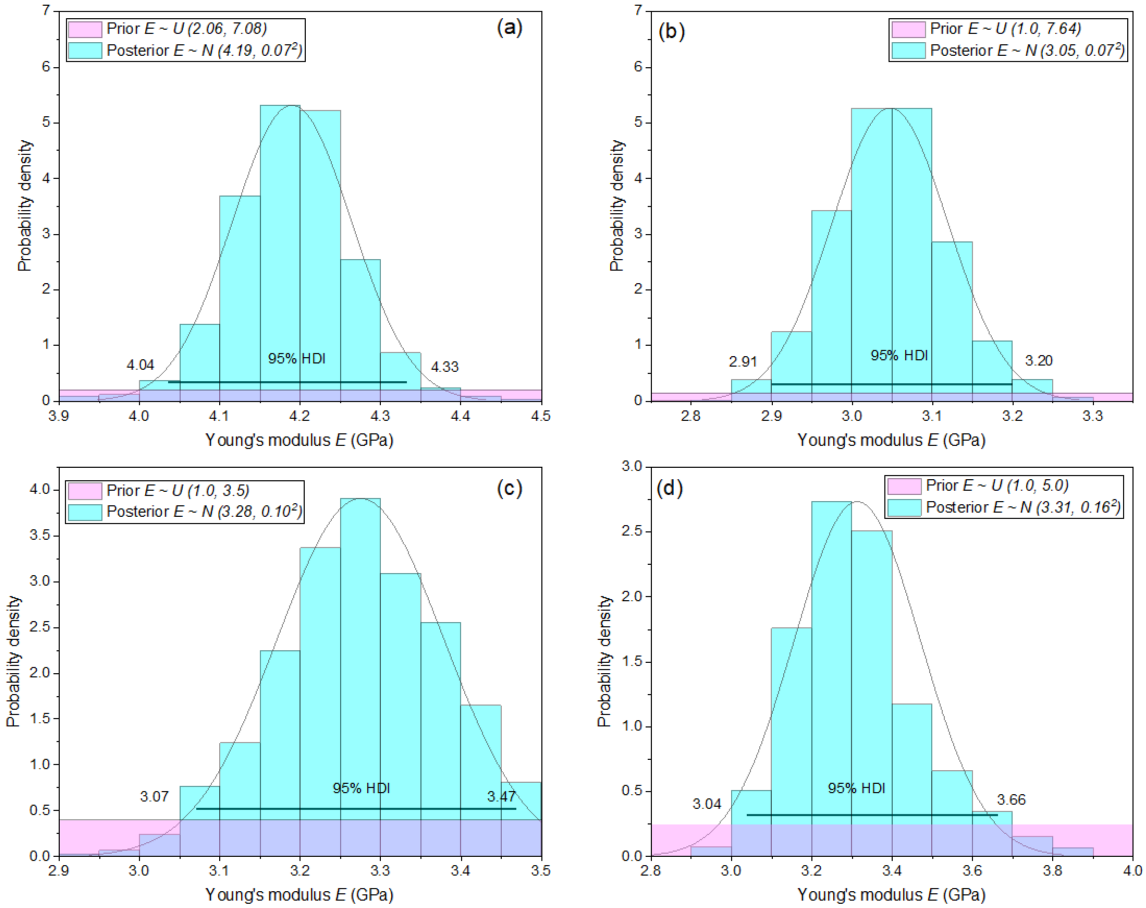

Figure 7.5 Probability density distributions of prior and posterior Young's modulus E estimated with MCMC using the analytical solution: (a) Westgate, (b) Joli Fou, (c) Clearwater black shale, and (d) Clearwater gray shale. Note: $\sim U(a, b)$ denotes uniform distribution; $\sim N(\mu, \sigma^2)$ denotes normal distribution.

Based on the gradient of the log posterior density, NUTS can achieve faster convergence than other samplers on high-dimensional problems. On the other side, NUTS may become slow in leapfrog if a scaling matrix parameter is not set as a reasonable value. Therefore, proper initial values can accelerate sampling in NUTS. Two chains, with 1000 draw iterations and 1000 tune samples for each chain, are simulated in the MCMC using the NUTS sampler coupled with the analytical solution (Jefferies 1988). Figure 7.5 to Figure 7.7 illustrate the histograms of posterior parameter samples, the PDFs of prior and posterior, and their statistics after Bayesian inference using MCMC simulation.

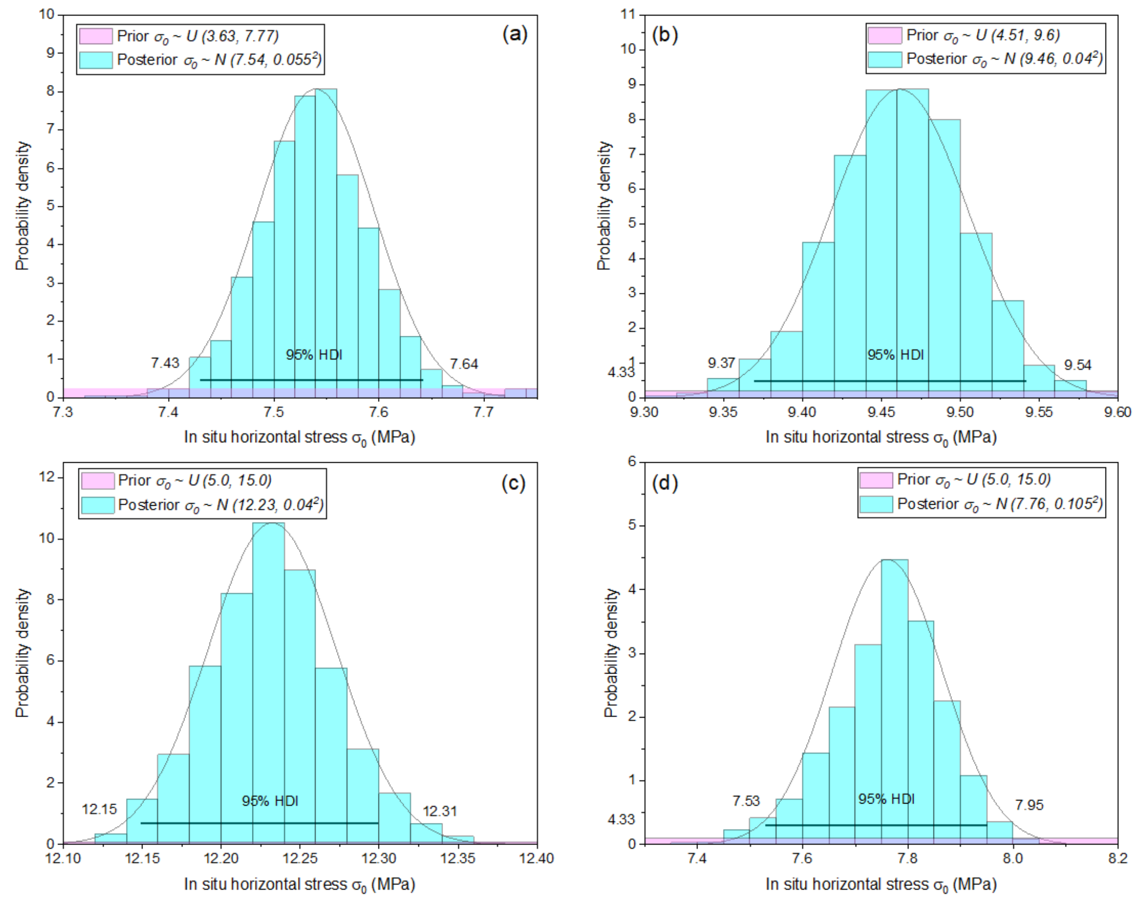

Figure 7.6 Probability density distributions of prior and posterior in-situ horizontal stress σ_{h0} estimated with MCMC using the analytical solution: (a) Westgate, (b) Joli Fou, (c) Clearwater black shale and (d) Clearwater grey shale.

The mean values of posterior samples coincide with the point estimates by the SS optimizer and MAP method, except for the Clearwater grey shale formation owing to the existence of non-unique solutions. The Bayesian inference approach provides not only the mean values but also their statistics summarized from the posterior samples after MCMC simulation. Therefore, uncertainty from the parameter estimation can be quantified with 95% HDI, which can partially solve the non-uniqueness problem while using a deterministic method. To quantitively diagnose convergence for MCMC simulation using a sampler, $\hat{R}$ (Gelman and Rubin, 1992; Brooks and Gelman, 1998) shall be examined. In Figure 7.5 to Figure 7.7, all the $\hat{R}$ values are less than 1.1, which is deemed convergent for an MCMC simulation (Martin, 2016).

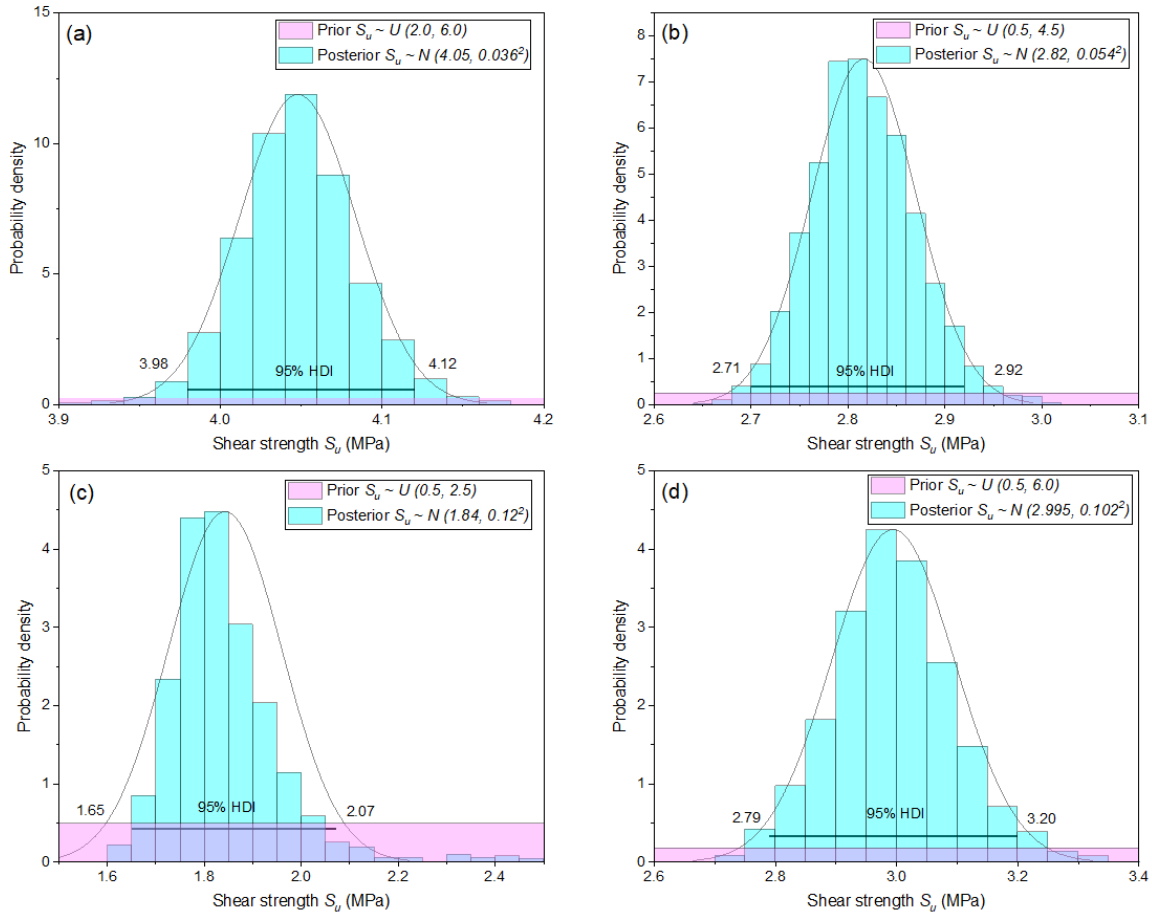

Figure 7.7 Probability density distributions of prior and posterior shear strength S_u estimated with MCMC using the analytical solution: (a) Westgate, (b) Joli Fou, (c) Clearwater black shale and (d) Clearwater grey shale.

7.1.5.3 Visualization of model fit and prediction uncertainty

Although Figure 7.5 to Figure 7.7 illustrate the mean and statistics derived from the Bayesian inference method for the RGP tests, the match between the predicted and observed data should be visually examined as a final check. The goodness of curve fit shall be evaluated with the coefficient of determination R^2. The highest density interval (HDI) of posterior distributions can also be obtained from the MCMC chains. Figure 7.8 displays the curve fit between the observed data and the predicted data. The 95% HDI (shaded bands in Figure 7.8), which is equivalent to the frequentist 95% CI, provides the lower and upper bounds of the predicted data.

The coefficients of determination R^2 in Figure 7.8 are all greater than 0.99, indicating the analytical solution achieves an excellent fit for the RGP data.

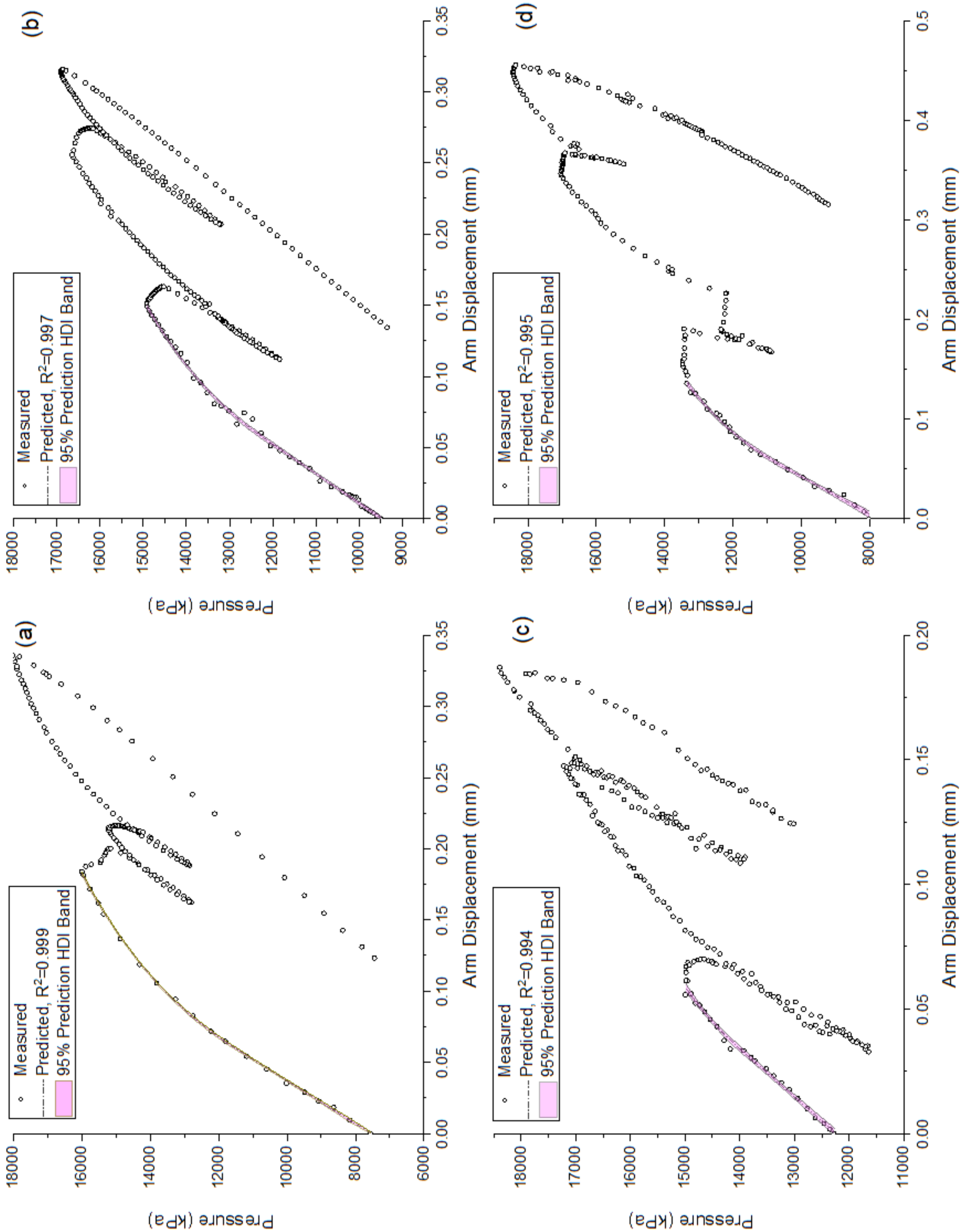

Figure 7.8 Fit of observed data to predicted data using analytical solution after MCMC simulations: (a)

Westgate, (b) Joli Fou, (c) Clearwater black shale and (d) Clearwater grey shale.

As the width of the 95% HDI bands in Figure 7.8 is narrow, the prediction uncertainty of the analytical solution can be neglected. Therefore, the analytical solution (Jefferies, 1988) applies to the Bayesian inference of RGP tests.

7.1.5.4 Posterior distribution updated with other testing data

According to Gelman and Rubin (1992), posterior belief from Bayesian inference can be continuously updated if new evidence is available, such as laboratory testing data. In this study, only triaxial compression tests on the specimens retrieved from the Westgate formation (Schlumberger, 2014) can be used as new evidence to update the posterior distributions of Young's modulus E. Because of the lack of testing data, posterior distributions of in-situ horizontal stress and shear strength cannot be updated. Also, new evidence from the Joli Fou and Clearwater formations is either insufficient or not provided. Therefore, posterior distributions for such parameters in the two geological formations are not updated either. The values of Young's modulus E presented in table R3 (Schlumberger, 2014) are used as the new evidence in Bayesian updating. The histogram of the triaxial testing data is shown in Figure 7.9.

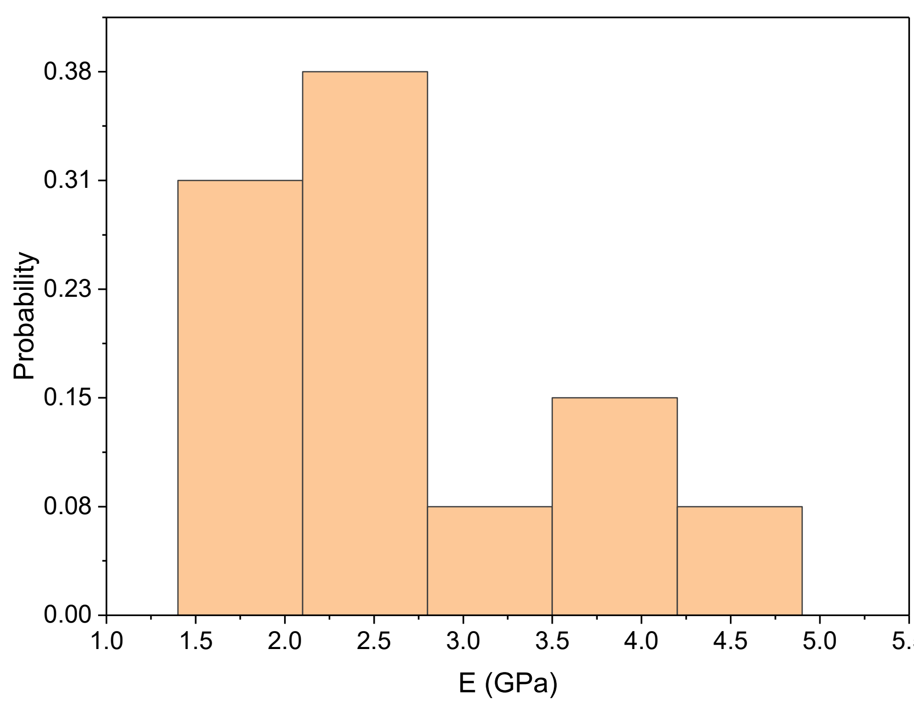

Figure 7.9 New evidence for Bayesian updating the posterior distributions of Young's modulus E

Figure 7.10 shows the posterior distribution and updated belief of Young's modulus E using the analytical solution. The mean and the lower and upper bounds of the updated 95% HDI are also illustrated.

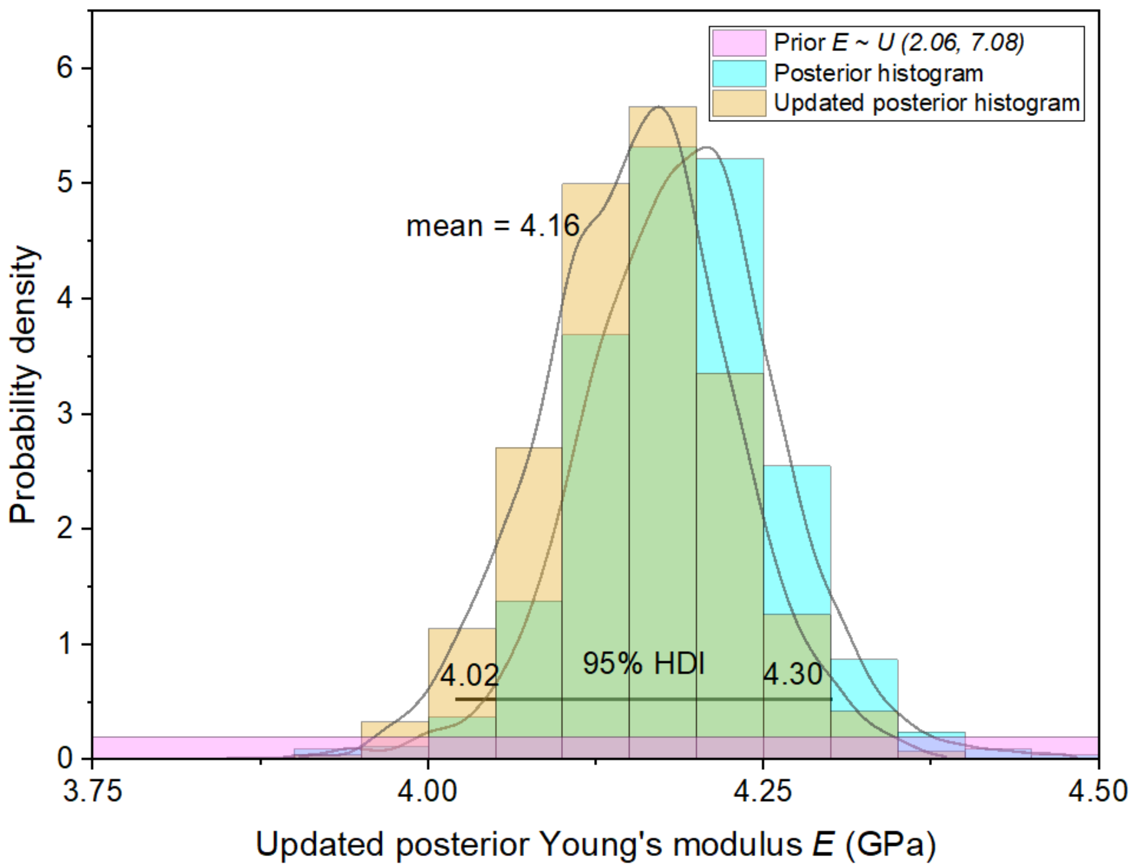

Figure 7.10 Updated posterior distribution and histogram of Young's modulus using the new evidence

The new evidence (triaxial data) updates the mean by moving the posterior distribution E to the left in Figure 7.10 with a slightly higher probability density. Also, the updated normal curve has a narrower spread, implicating fewer uncertainties in the updated belief.

If the new evidence includes in-situ horizontal stress and shear strength, the updates for these parameters can also be performed in the same way. In the Bayesian paradigm, the degree of belief is a function of observed data, sampling algorithms, computational models, and new evidence. The conclusion is subject to change with new data. Again, the new evidence shifts the mean of the updated posterior, indicating that our belief is changing with new measurements. With new data in the future, Bayesian updating can be conveniently performed and serve as an open system compared to frequentist inference.

7.2 Summary and Conclusions

As an alternative to the deterministic and frequentist methods, Bayesian inference methods are adopted in the inverse analysis of RGP tests in the clay shale formations. The log-likelihood function in the Bayesian inference is formulated as an objective function with random variables following prior distributions, the observed and predicted data. The log-likelihood function can be implemented by following the flow chart shown in Figure 7.1. Point estimates can be obtained from MAP or mean value from the MCMC simulations by maximising the log-likelihood function. Point estimation and statistical assessments under the Bayesian paradigm are carried out using the MAP and MCMC simulations with the analytical solution (Jefferies, 1988). Parameter estimates from MAP with the analytical solution approximately agree with those from inverse analyses using the frequentist methods in Section 6.4.4.

MAP is a fast and straightforward approach for obtaining point estimates. However, as the BFGS optimization algorithm in the MAP method is a local optimizer, the estimated parameters may be trapped in local minimums while in high dimensional posteriors. MCMC simulations using NUTS coupled with the analytical solution achieve the best performance.

As the Bayesian inference approach is an open estimation system. One’s belief on the in-situ horizontal stress and rock properties is not fixed. Therefore, the Bayesian belief is subjected to changes upon new data available in the future. New evidence from field and laboratory tests makes the Bayesian approach distinguishable from the frequentist approach, whose belief cannot be updated without starting from scratch.

Compared to the conventional pressuremeter interpretation methods, the proposed statistical inverse analysis can quantify the potential uncertainty and errors from ground properties and in-situ horizontal stress.

The statistical assessments of the optimal parameters can evaluate the statistics defined by the SD and CIs. Also, the model fitness can be further evaluated with the coefficients of determination R^2 and prediction intervals. The uncertainties propagated from rock properties and computational modelling can be quantified statistically.

The Bayesian approach is an alternative method to conduct the inverse analysis of the RGP test. The MAP method can quickly find point estimates by maximizing the log-likelihood function ℓ defined in Equation 7.1. In comparison, the complete Bayesian inference can summarize mean parameter values and their statistics from the posterior samples after MCMC simulations. Bayesian inference is an open system, which is deemed an advantage over the frequentist statistical method. Posterior distributions can be continuously updated with new data (evidence) without starting from scratch. Therefore, parameter estimates using the present testing data are subject to changes with new observations from other laboratory and in-situ tests in the future. Due to the limitation of computing power, only the analytical solution in tandem with NUTS achieves satisfactory outcomes from the Bayesian inferences. More powerful computers and cloud computing techniques are expected to improve the performance of Bayesian inference using a numerical model in the foreseeable future.

The Bayesian approach discussed in this paper has potential applications for other geotechnical projects, such as pile load tests, slope stability assessment, caprock integrity evaluation, and the mining industry, where data are continuously updated throughout a project's life span.

8.0 CONCLUSIONS AND RECOMMENDATION FOR FUTURE RESEARCH

8.1 Conclusions

1. Analysis of raw data can be done using deterministic or statistical methods. The deterministic method converts electrical signals into arm displacements, which are subsequently corrected to account for system compliance and membrane stiffness. However, this method doesn't adequately handle variability in RGP test curves, which results from measurement errors. In contrast, the statistical method, such as Bayesian linear regression, quantifies these uncertainties effectively. This model establishes the lower and upper bounds of arm displacements with a 95% confidence range, thereby quantifying uncertainty due to measurement errors. The study shows that the proposed Bayesian linear regression model can robustly address both random and systematic errors.

2. The proposed statistical inverse analysis approach outperforms conventional pressuremeter interpretation methods by quantifying potential uncertainty and errors from ground properties and in-situ horizontal stress. The use of multiple optimizers to minimize the objective function reduces the degree of non-uniqueness. The complete curve, as opposed to just the expansion curve, predicts a more reasonable mean and narrower 95% confidence intervals in the inverse analysis. Non-unique solutions can be addressed using statistical assessment methods that evaluate statistics defined by standard deviation and confidence intervals. Additionally, model fitness can be further evaluated using R^2 and prediction intervals. The study demonstrates that uncertainties propagated from ground properties and computational modelling can be statistically quantified using the proposed methodology.

3. The Bayesian inference approach, using MCMC simulations, quantifies uncertainties arising from soil variability, measurement errors, and computational models. It integrates an analytical solution and a numerical model into the log-likelihood function to optimize the log-posterior. Among the tested algorithms, the slice sampling algorithm performs satisfactorily. Unlike frequentist methods, this approach directly summarizes

parameter statistics from posterior distribution samples, using the mean and 95% HDI to characterize uncertainty in parameter estimation. The model fit uncertainty can be visualized with a 95% HDI band. This Bayesian approach proves especially beneficial in projects involving time-series data.

4. The proposed statistical inverse analysis surpasses traditional deterministic methods by quantifying potential uncertainties and errors from deep ground properties and anisotropic in-situ horizontal stresses using RGP tests. The modified strain-hardening/softening model, which can be easily implemented with FISH functions in FLAC/FLAC3D, effectively characterizes rock softening/hardening behaviors in degraded zones. The Bayesian approach provides an alternative for RGP test inverse analysis. The MAP method can quickly find point estimates by maximizing the log-likelihood function. In contrast, complete Bayesian inference summarizes mean parameter values and their statistics from posterior samples after MCMC simulations. As an open system, Bayesian inference can continuously update posterior distributions with new data, offering an advantage over the frequentist method.

8.2 Limitations of research

This research's uncertainty quantification of the RGP testing curve has several limitations:

1. Homogeneous geology: the research assumes a homogeneous geological setting, which may not accurately represent the natural variability and complexity of geological formations.

2. Isotropy consideration: the study does not account for anisotropy, which refers to the directional dependence of rock properties. This could lead to oversimplified models that do not capture the true behavior of the subsurface materials.

3. Fracture development and rock heterogeneities: the study does not consider the development of fractures and the heterogeneity of rocks in deep testing pockets, which can significantly impact the results.

4. Downhole temperatures and nearby production operations: the effects of varying downhole temperatures and nearby SAGD processes are not included, which could influence the testing outcomes.

5. Validation of the modified SS model: more laboratory tests are needed to validate the modified SS model.

6. Bayesian inference limitations:

- Works well with a simplified numerical model or an analytical solution only. High computational resources are required for a complex numerical model.
- MCMC simulation is time-consuming and practical only for a simple testing curve like the SBP test in Chapter 5 or the expansion part of RGP tests in Chapter 7.
- The quality of new data (evidence) was not taken into consideration in Bayesian updating in Chapter 7.

8.3 Future work

Future uncertainty quantification of the RGP testing curve will consider additional factors, such as fractures and rock heterogeneities. The proposed modified SS model requires further mathematical deduction and validation with more field and laboratory data. Integration with other finite element analysis software like TEMP/W in GeoStudio, on platforms like Matlab or Python, will expand the applicability of the proposed uncertainty quantification approaches to various research fields, including thermal analysis.

In addition to Bayesian inference methods, future studies could apply other machine learning methods, such as deep neural networks.

In conclusion, the methodology and techniques used in this research can be further developed and easily implemented for other engineering uncertainty quantification practices and research.

- Improvements to the hardware such as digital twins, sonic device, would help to acquire additional test data to constrain estimates of in-situ stress.

- This research was conducted with pre-bored pressuremeter procedures, but significant improvements in in-situ stress estimates would result from the development of a self-boring RGP.
- A new Bayesian updating method with new data quality assessment should be developed.

8.4 Contributions

- Addressed the non-uniqueness issues in pressuremeter parameter estimation using a frequentist statistical assessment method.
- Applied Bayesian inference methods in parameter estimation with pressuremeter testing data, implementing an analytical or numerical model in the Bayesian framework. The advantage of the proposed Bayesian approach over frequentist statistical methods for in-situ horizontal stress studies is its ability to continuously update beliefs with new data.
- Proposed a modified SS model for simulating the constitutive behavior of borehole walls under pressure, eliminating the need for a user-defined piecewise-linear table.
- Constructed a Python and Matlab platform using both frequentist and Bayesian modelling techniques to carry out parameter estimation and quantify the uncertainties of the estimated parameters utilzing the data from RGP tests in deep underground projects.

REFERENCES

Advanced Geotechnology. 2001. Geological and geomechanical characterization of the Lea Park Formation, Colorado Group, and Upper Mannville Group Caprocks. Advanced Geotechnology Inc., Calgary, Alberta.

Ahmed, A., and Soubra, A.H. 2015. Application of the subset simulation approach to spatially varying soils. In Risk and reliability in geotechnical engineering. Edited by Phoon, K.K., and Ching, J. CRC Press, Taylor and Francis Group, London. pp. 561–577.

Alberta Energy Regulator. 2014. Development of the maximum operating pressure formula for steam-assisted gravity drainage schemes in the shallow thermal area. RC-03

Alberta Energy Regulator. 2024. Directive 023: Oil sands project applications.

Arnold, M. 1981. Empirical evaluation of pressuremeter test data. Canadian Geotechnical Journal. 18(3): 455-459. doi.org/10.1139/t81-050

Au, S.K., and Wang, Y. 2014. Engineering risk assessment with subset simulation. John Wiley and Sons, Singapore.

Baguelin, F. 1972. Expansion of cylindrical probe in cohesive soils. J. Soil Mech. Found. Div. ASCE, 98(11).

Bandyopadhyay, P. S., and Malcolm R. F. 2011. Philosophy of statistics. Oxford: North-Holland.

Bard, J. 1974. Nonlinear parameter estimation. Academic Press, New York.

Bassett, R. and Deride, J. 2019. Maximum a posteriori estimator as a limit of Bayes estimators. Mathematical Programming. 174, 129–144 (2019). doi.org/10.1007/s10107-018-1241-0

Bell, J. S. and Babcock, E. A. 1986. The stress regime of the Western Canadian Basin and implications for hydrocarbon production. Bulletin of Canadian Petroleum Geology, v. 34, p. 364-378.

Bell, J. S., and Gough, D. I. 1981, Intraplate stress orientation from Alberta oil-wells, Evolution of the Earth, Geodynamics series Vol. 5

Betancourt, M. 2017. A Conceptual Introduction to Hamiltonian Monte Carlo. arXiv: Methodology (2017): n. pag.

Bolton, M., and Whittle, R. 1999. A non-linear elastic/perfectly plastic analysis for plane strain undrained expansion tests. Géotechnique 49, 133–141.

Bozorgzadeh, N., Harrison,J., and Escobar, M. 2019. Hierarchical Bayesian modelling of geotechnical data: application to rock strength. Géotechnique. 69:12:1056-1070. doi.org/10.1680/jgeot.17.P.282

Brooks, S. and Gelman, A. 1998. General Methods for Monitoring Convergence of Iterative Simulations, Journal of Computational and Graphical Statistics, 7:4, 434-455, DOI: 10.1080/10618600.1998.10474787

Cambridge In-situ Ltd. 2012. Working instructions for Cambridge 73mm high pressure dilatometer, serial number 111011. Cambridge, England.

Cao, J., 2017. Deep learning and its application in deep gas reservoir prediction, Vol. 39, No.6, Computing Techniques for Geophysical and Geotechnical Exploration (in Chinese).

Cao, L., Teh, C., and Chang, M. 2001. Undrained cavity expansion in modified Cam-clay I: Theoretical analysis. Géotechnique 51, 323–334.

Cao, Z., and Wang, Y. 2014. Bayesian Model Comparison and Characterization of Undrained Shear Strength Journal of Geotechnical and Geoenvironmental Engineering. 140 (6), 04014018. DOI: 10.1061/(ASCE)GT.1943-5606.0001108.

Cao, Z., Wang, Y., and Li, D. 2016. Site-specific characterization of soil properties using multiple measurements from different test procedures at different locations – A Bayesian sequential updating approach. Engineering Geology. 211:150-161. doi.org/10.1016/j.enggeo.2016.06.021.

Carter, J., Booker, J., and Yeung, S. 1986. Cavity expansion in cohesive-frictional soils. Géotechnique 2, 349–358.

Chen, X. Z., and Cui, Y. 2017. The formation of the Wulipo landslide and the resulting debris flow in Dujiangyan City, China. Journal of Mountain Science. 14(6), 1100-1112. doi.org/10.1007/s11629-017-4392-1

Clarke, B.G. 1995. Pressuremeters in geotechnical design. Blackie academic and professional, Glasgow.

Clarke, B.G., and Allan, P.G. 1990. Self-boring pressuremeter tests from a gallery at 220 m below ground. In Proceedings of Pressuremeters – A British Geotechnical Society Symposium, London.

CNRL. 2011. Pad 74 Final Investigation Report, Primrose east expansion in-situ oil sands project. Calgary, Alberta.

Coleman, T., and Li, Y. 1994. On the convergence of interior-reflective Newton methods for nonlinear minimization subject to bounds. Mathematical Programming 67, 189-224. doi.org/10.1007/BF01582221

Collins, I. F., and Yu, H. S. 1996. Undrained cavity expansions in critical state soils. International Journal for numerical and analytical methods in geomechanics. Vol. 20, 489-516

Conn, A., Gould, N., and Toint, P. 2000. Trust region methods. MOS-SIAM series on optimization. doi.org/10.1137/1.9780898719857

Cooley, R.L., and Naff, R.L. 1990. Regression modeling of ground-water flow: Techniques in Water-Resources Investigations, 03-B4, U.S. Geological Survey. doi.org/10.3133/twri03B4

Cui, Y., Zhou, X. J., and Guo, C. X. 2017. Experimental study on the moving characteristics of fine grains in wide grading unconsolidated soil under heavy rainfall. Journal of Mountain Science. 14(3), 417-431. doi.org/10.1007/s11629-016-4303-x

DeGroot, D.J., and Baecher, G. 1993. Estimating autocovariance of in-situ soil properties, ASCE, Journal of Geotechnical Engineering, 119(1): 147-167. doi.org/10.1061/(ASCE)0733-9410(1993)119:1(147)

Denby, G. M., and Clough, G. W. 1980. Self-boring pressuremeter tests in clay, ASCE, Journal of Geotechnical Engineering Division. 106(12), 1369-1387.

Detournay, E., and Cheng, A.H-D. 1988. Poroelastic response of a borehole in a non-hydrostatic stress field. International Journal of Rock Mechanics and Mining Sciences & Geomechanics Abstracts. 25(3): 171-182. doi.org/10.1016/0148-9062(88)92299-1.

Duncan, J.M., and Chang, C.Y. 1970. Nonlinear analysis of stress and strain in soils. J. SMFE Div. ASCE, 96(5), 755-757

Elwood, D.E., Martin, C.D., Fredlund, D.G., and Ward Wilson, G. 2015. Volumetric changes and point of saturation around a pressuremeter probe used in unsaturated soils. Journal of Geotechnical and Geoenvironmental Engineering, 141(11). doi:10.1061/(ASCE)GT.1943-5606.0001352.

Fahey, M., 1988. Self-boring pressuremeter testing in calcareous soil. In Proceedings of the International Conference on Calcareous Sediments. Edited by Jewell, R.J., and Andrews. D.C Balkema, Perth, Australia. pp. 165–173.

Fahey, M., and Carter, J.P., 1986. Some effects of rate of loading and drainage on pressuremeter tests in clay. In Proceedings of the Specialty Geomechanics Symposium: Interpretation of Field Testing For Design Parameters. pp. 50–55.

Fahey, M., and Carter, J.P., 1993. A finite element study of the pressuremeter test in sand using a nonlinear elastic-plastic model. Canadian Geotechnical Journal. 30(2): 348-362. doi.org/10.1139/t93-029

Fawaz, A., Boulon, M., and Flavigny. E., 2002. Parameters deduced from the pressuremeter test. Canadian Geotechnical Journal. 39(6): 1333-1340. doi.org/10.1139/t02-099

Feng, Y., Bozorgzadeh, N., Harrison, J., 2020. Bayesian analysis for uncertainty quantification of in-situ stress data. International Journal of Rock Mechanics and Mining Sciences. 134:104381. doi.org/10.1016/j.ijrmms.2020.104381.

Ferguson, T. 1982. An Inconsistent Maximum Likelihood Estimate. Journal of the American Statistical Association. 77:380, 831-834. doi:10.1080/01621459.1982.10477894.

Ferreira, R.S. 1992. Interpretation of pressuremeter tests using a curve fitting technique. PhD thesis, Department of Civil and Environmental Engineering, The University of Alberta, Edmonton, A.B.

FLAC Fast Lagrangian Analysis of Continua User's Guide. 2011. Itasca Consulting Group Inc., Minneapolis, Minnesota.

Ganesh, A., Zhang B., Chalaturnyk R., and Prasad V. 2019. Uncertainty quantification of the factor of safety in a steam-assisted gravity drainage process through polynomial chaos expansion. Computers and Chemical Engineering,133. doi.org/10.1016/j.compchemeng.2019.106663

Gaone, F.M., Doherty, J.P., and Gourvenec, S. 2019. An optimization strategy for evaluating modified Cam clay parameters using self-boring pressuremeter test data. Year. Canadian Geotechnical Journal. 56(11): 1668-1679. doi.org/10.1139/cgj-2018-0385

Gelman, A., and Rubin D.B. 1992. Inference from iterative simulation using multiple sequences. Statist. Sci. 7(4):457-472. doi.org/10.1214/ss/1177011136

Gelman, A., Carlin, J.B., Stern, H.S., Dunson, D.B., Vehtari, A. and Rubin, D.B. 2014, Bayesian data analysis, Third edition., Chapman & Hall/CRC texts in statistical science, CRC Press

Ghassemi, A. 2012. A review of some rock mechanics issues in geothermal reservoir development. Geotech Geol Eng 30, 647–664. doi.org/10.1007/s10706-012-9508-3

Gibson, R., and Anderson, W. 1961. In-situ measurement of soil properties with the pressuremeter. Civil Engineering Public Works Review 56: 615–618.

Hastings, W. K. 1970. Monte Carlo sampling methods using Markov chains and their applications. Biometrika, 57(1), 97–109.

Houlsby, G. 1989. Determination of horizontal geostatic stress in clay with self-bored pressuremeter: Discussion. Canadian Geotechnical Journal, 26(4): 758-759. doi.org/10.1139/t89-092

Houlsby, G., and Withers, N. 1988. Analysis of the cone pressuremeter test in clay. Géotechnique. 38: 575–587. doi.org/10.1680/geot.1988.38.4.575

Huang, A.B., Chameau, J.L., and Holtz, R.D. 1986. Interpretation of pressuremeter data in cohesive soils by simple algorithm. Géotechnique, 36(4): 599–603. doi.org/10.1680/geot.1986.36.4.599

Hughes, J., Wroth, C., and Windle, D. 1977. Pressuremeter tests in sands. Géotechnique 27, 455–477.

Itasca. 2011. Fast Lagrangian Analysis of Continua User's Guide. Itasca Consulting Group Inc., Minneapolis, Minnesota.

J. Lubliner, J. Oliver, S. Oller, E. Oñate. 1989. A plastic-damage model for concrete. International Journal of Solids and Structures. 25(3):299-326. doi.org/10.1016/0020-7683(89)90050-4.

Jacobi, L., Joshi, M., and Zhu, D. 2018. Automated Sensitivity Analysis for Bayesian Inference via Markov Chain Monte Carlo: Applications to Gibbs Sampling. http://dx.doi.org/10.2139/ssrn.2984054

Jang, I.S., Chung, C.-K., Kim, M.M., and Cho, S.M. 2003. Numerical assessment on the consolidation characteristics of clays from strain holding, self-boring pressuremeter test. Computers and Geotechnics, 30: 121–140. doi:10.1016/S0266-352X(02)00031-9.

Jefferies, M. 1988. Determination of horizontal geostatic stress in clay with self-bored pressuremeter. Canadian Geotechnical Journal, 25(3): 559–573. doi.org/10.1139/t88-061

Jefferies, M. 1989. Determination of horizontal geostatic stress in clay with self-bored pressuremeter: Reply. Canadian Geotechnical Journal. 26(4): 760-763. doi.org/10.1139/t89-093

Jefferies, M., Crooks, J., Becker, D., and Hill, P. 1987. Independence of geostatic stress from overconsolidation in some Beaufort Sea clays. Canadian Geotechnical Journal, 24(3): 342-356. doi.org/10.1139/t87-045

Juang, C., Luo, Z., Atamturktur, S., and Huang, H. 2013. Bayesian updating of soil parameters for braced excavations using field observations. Journal of Geotechnical and Geoenvironmental Engineering. 139(3): 395-406

Kelley, C. 1999. Iterative Methods for Optimization, Philadelphia: Society for Industrial and Applied Mathematics, 71–86. doi.org/10.1137/1.9781611970920

Knabe, T., Schweiger, H., and Schanz, T. 2012. Calibration of constitutive parameters by inverse analysis for a geotechnical boundary problem. Canadian Geotechnical Journal. 49(2): 170–183. doi:10.1139/T11-091

Krige, D. G. 1951. A statistical approach to some mine valuation and allied problems on

Kulhaway, F. H., and Phoon, K. K. 1996. Engineering judgement in the evolution from deterministic to reliability-based foundation design. In Proceedings of Uncertainty '96, Uncertainty in the Geologic Environment: From Theory to Practice, American Society of Civil Engineers, New York, Vol. 1, pp. 29-48.

Lacasse, S., and Nadim, F. 1996. Uncertainties in characterizing soil properties. In Proceedings of Uncertainty '96, Uncertainty in the Geologic Environment: From Theory to Practice, American Society of Civil Engineers, New York, Vol. 1, pp. 49-74.

Ladanyi, B. 1972. In-situ determination of undrained stress-strain behavior of sensitive clays with the pressuremeter. Canadian Geotechnical Journal. 9(3): 313-319. https://doi.org/10.1139/t72-034

Lataniotis, C., Wicaksono, D., Marelli, S., and Sudret, B. 2021. UQLab user manual – Kriging (Gaussian process modeling), Report # UQLab-V1.4-105, Chair of Risk, Safety and Uncertainty Quantification, ETH Zurich, Switzerland

Ledesma, A., Gens, A., and Alonso, E.E. 1996. Estimation of parameters in geotechnical backanalysis. I. Maximum likelihood approach. Computers and Geotechnics. 18(1): 1–27. doi:10.1016/0266-352X(95)00021-2

Levasseur, S., Malecot, Y., Boulon, M., and Flavigny, E. 2008. Soil parameter identification using a genetic algorithm. International Journal for Numerical and Analytical Methods in Geomechanics. 32(2):189-213. doi.org/10.1002/nag.614

Levenberg, K. 1944. A method for the solution of certain nonlinear problems in least squares. Quarterly of Applied Mathematics, 2 (2): 164–168.

Li, H.S., and Cao, Z.J. 2016. Matlab codes of Subset Simulation for reliability analysis and structural optimization. Struct Multidisciplinary Optimization 54:391-410. doi.org/10.1007/s00158-016-1414-5

Liu, D., Cui, Y., Guo, J., Yu, Z., Chan, D., and Lei, M. 2020. Investigating the effects of clay/sand content on depositional mechanisms of submarine debris flows through physical and numerical modeling. Landslides. 17: 1863-1880. doi.org/10.1007/s10346-020-01387-6

Liu, L. 2015. Numerical study of reservoir geomechanical pressuremeter testing under anisotropic in-situ stresses. MSc. thesis, University of Alberta

Liu, L. 2017. Data analysis for RGP test at CNRL Primrose site. Internal report, University of Alberta. 26 p.

Liu, L., Chalaturnyk, R., Deisman, N., and Zambrano-Narvaez, G., 2019. Anisotropic borehole response from pressuremeter testing in deep clay shale formations. Canadian Geotechnical Journal. Just-IN doi.org/10.1139/cgj-2019-0801

Liu, L., Elwood, D., Martin, D. and Chalaturnyk, R. 2017. Determination of permeability of overconsolidated clay from pressuremeter pressure hold tests. Canadian Geotechnical Journal. 55(4): 514-527. https://doi.org/10.1139/cgj-2017-0279

Lubliner, J., Oliver, J., Oller, S., and Oñate, E. 1989. A plastic-damage model for concrete. International Journal of Solids and Structures, 25(3), 299-326. doi.org/10.1016/0020-7683(89)90050-4.

Mair, R., and Wood, D. 1987. Pressuremeter testing: methods and interpretation (CIRIA Ground Engineering Report: In-situ testing). CIRIA and Butterworths, London.

Marquardt, D. 1963. An algorithm for least-squares estimation on nonlinear parameters. SIAM J. Appl. Math. 11, 431–441. doi.org/10.1137/0111030

Marsland, A., and Randolph, M. 1977. Comparisons of the results from pressuremeter tests and large in-situ plate tests in London Clay. Géotechnique. 27(2):217–243. doi.org/10.1680/geot.1977.27.2.217

Martin, O. 2016. Bayesian analysis with Python, first edition, Birmingham, UK: Packt Publishing.

MATLAB and Statistics Toolbox Release 2019b. 2019. The MathWorks, Inc., Natick, Massachusetts, United States.

Metropolis, N. 1953. Equations of state calculations by fast computing machines. J. Chem. Phys., 21(6), 1087–1092.

Moré, J.J. 1978. The Levenberg-Marquardt algorithm: Implementation and theory. Numerical Analysis. In Proceedings of the Biennial conference held at Dundee, 28 June 28-1 July 1977. Springer, Berlin, Heidelberg, pp. 105-116.

Morrison, D. 1960. Methods for nonlinear least squares problems and convergence proofs. In Proceedings of the Seminar on Tracking Programs and Orbit Determination, Jet Propulsion Laboratory, Pasadena, pp. 1–9.

Nadim, F. 2007. Tools and strategies for dealing with uncertainty in geotechnics. In Probabilistic methods in geotechnical engineering, SpringerWienNewYork, pp. 71–95.

Neal, R. M. 2011. MCMC using Hamiltonian dynamics. In Handbook of Markov Chain Monte Carlo, Chapter 5, pp. 113–162. Boca Raton, Florida, USA: Chapman & Hall/CRC.

Nelder, J.A., and Mead, R. 1965. A simplex method for function minimization. The Computer Journal. 7(4):308-313. doi.org/10.1093/comjnl/7.4.308

Obrzud, R.F., Vulliet, L., and Truty, A. 2009. A combined neural network/gradient-based approach for the identification of constitutive model parameters using self-boring pressuremeter tests, International Journal for Numerical and Analytical Methods in Geomechanics, 33:817-849. doi.org/10.1002/nag.750

Origin (Pro), Version 2020. 2020. OriginLab Corporation, Northampton, MA, USA.

Palmer, A.C. 1972, Undrained plane-strain expansion of a cylindrical cavity in clay: a simple interpretation of the pressuremeter test. Géotechnique. 22(3): 451-457. https://doi.org/10.1680/geot.1972.22.3.451

Papon, A., Riou, Y., Dano, C., and Hicher, P.Y. 2012. Single- and multi- objective genetic algorithm optimization for identifying soil parameters. International Journal for Numerical and Analytical Methods in Geomechanics. 36(5):597-618. doi.org/10.1002/nag.1019

Peng, R.D. 2021. Advanced Statistical Computing. https://bookdown.org/rdpeng/advstatcomp/

Prevost, J. H., and Höeg, K. 1975. Analysis of pressuremeter in strain softening soil. Journal of the Geotechnical Engineering Division. ASCE, 101(8). https://doi.org/10.1061/AJGEB6.0000181

RG^2 . 2016. Data analysis of RGP tests conducted at CNRL Primrose/Wolf Lake CSS site. University of Alberta

Salvatier J, Wiecki TV, and Fonnesbeck C. 2016. Probabilistic programming in Python using PyMC3. PeerJ Computer Science 2:e55. doi.org/10.7717/peerj-cs.55

Sánchez, F.E., Aguado, M.B., and Lavín, J.R.S. 2014. Interpretation of the pressuremeter test using numerical models based on deformation tensor equations. Bull Eng Geol Environ 73, 141–146. doi.org/10.1007/s10064-013-0528-x

Santner, T., Williams, B., and Notz, W. 2003. The design and analysis of computer experiments. Springer series in Statistics. Springer.

Sawilowsky, S., and Fahoome, G. 2003. Statistics through Monte Carlo Simulation with Fortran. Journal of Modern Applied Statistical Methods Inc., Michigan.

Schlumberger. 2014. Geomechanics characterization of selected core material from Westgate Formation, Colorado Group. Schlumberger Ltd., Salt Lake City, Utah.

Schnaid, F. 2009. In-situ testing in geomechanics: The main tests, first edition, Abington, Oxon. Taylor and Francis Group, New York.

Schueller, G. I. 2009. Efficient Monte Carlo simulation procedures in structural uncertainty and reliability analysis - recent advances. Journal of Structural Engineering and Mechanics. 32(1):1–20. doi.org/10.12989/sem.2009.32.1.001

Schwerzmann, A., Funk, M., and Blatter, H. 2006. Borehole logging with an eight-arm caliper-inclinometer probe. Journal of Glaciology, 52(178): 381–388.doi:10.3189/172756506781828520.

Shuttle, D. 2007. Cylindrical cavity expansion and contraction in Tresca soil. Géotechnique. 57(3): 305–308. doi.org/10.1680/geot.2007.57.3.305

Snedecor, G.W., and Cochran, W.G. 1964. Statistical methods. University of Iowa Press. Ames, Iowa.

Spendley, W., Hext G., Himsworth, F. 1962. Sequential Application of Simplex Designs in Optimisation and Evolutionary Operation, Technometrics, 4: 441-461

Straub, D., and Papaioannou, I. 2015. Bayesian updating with structural reliability methods. Journal of Engineering Mechanics. 141(3): 04014134. DOI:10.1061/(ASCE)EM.1943-7889.0000839

Taboga, M. 2017. "Normal distribution - Maximum Likelihood Estimation", Lectures on probability theory and mathematical statistics, Third edition. Kindle Direct Publishing. Online appendix. https://www.statlect.com/fundamentals-of-statistics/normal-distribution-maximum-likelihood. [cited 7 April 2022]

Taylor, J. 1997. An introduction to error analysis: The study of uncertainties in physical measurements, second edition. Sausalito, California.

Upton, G., and Cook, I. 2008. A Dictionary of Statistics (2 rev. ed.). Oxford University Press. DOI: 10.1093/acref/9780199541454.001.0001

Vermeer, P. A., and De Borst, R. 1984. Non-Associated Plasticity for Soils, Concrete and Rock, Heron,29(3), 3-64 https://repository.tudelft.nl/islandora/object/uuid:4ee188ab-8ce0-4df3-adf5-9010ebfaabf0?collection=research

Wagner, P.R., Nagel, J., Marelli, S., Sudret, B. 2021. UQLab user manual – Bayesian inference for model calibration and inverse problems, Report # UQLab-V1.4-113, Chair of Risk, Safety and Uncertainty Quantification, ETH Zurich, Switzerland

Wang, C.H., Harken, B., Osorio-Murillo, C.A., Zhu, H.H., Rubin, Y. 2016. Bayesian approach for probabilistic site characterization assimilating borehole experiments and Cone

Penetration Tests, Engineering Geology, Volume 207, Pages 1-13, doi.org/10.1016/j.enggeo.2016.04.002.

Wang, K., and Sun, W. 2018. A multiscale multi-permeability poroplasticity model linked by recursive homogenizations and deep learning. Computer Methods in Applied Mechanics and Engineering. 334: 337–380. doi.org/10.1016/j.cma.2018.01.036.

Wang, Y., and Cao Z. 2013. Probabilistic characterization of Young's modulus of soil using equivalent samples. Engineering Geology. 159: 106–118. doi.org/10.1016/j.enggeo.2013.03.017

Wang, Y., Au, S. K., Cao, Z. 2010. Bayesian approach for probabilistic characterization of sand friction angles, Engineering Geology, 114: 354-363. doi.org/10.1016/j.enggeo.2010.05.013.

Weisstein, E.W. "Covariance." From MathWorld-A Wolfram web resource. Available from https://mathworld.wolfram.com/Covariance.html [cited 5 January 2021]

Windle, D., and Wroth, C.P. 1977. The use of a self-boring pressuremeter to determine the undrained properties of clays, Ground Engineering. Available from https://www.cambridge-insitu.com/resources/references/use-self-boring-pressuremeter-determine-undrained-properties-clays [cited 5 January 2021]

Witowski, K., Feucht, M., and Stander, N. 2011. An effective curve matching metric for parameter identification using partial mapping. In Proceedings 8th European LS-DYNA® Users Conference, Strasbourg

Wroth, C. P. 1984. The interpretation of in-situ soil tests. Géotechnique. 34:4, 449-489. doi.org/10.1680/geot.1984.34.4.449

Yan, C.F., Chen, H., and Zhang, J. 1997. The use of Bayes' method to infer distribution of mechanical parameters. Journal of Chongqing Jianzhu University (in Chinese), 19(2):65-69

Yang, T., Tham L., Tang C., Liang Z., and Tsui Y. 2004. Influence of heterogeneity of mechanical properties on hydraulic fracturing in permeable rocks. Rock Mechanics and Rock Engineering, 37(4): 251-275. doi:10.1007/s00603-003-0022-z

Yang, T., Tham L., Tang C., Liang Z., and Tsui Y. 2004. Influence of heterogeneity of mechanical properties on hydraulic fracturing in permeable rocks. Rock Mechanics and Rock Engineering, 37(4): 251-275. https://doi:10.1007/s00603-003-0022-z

Yeh, W. 1986. Review of parameter identification procedures in ground-water hydrology: The inverse problem: Water Resources Research. Vol. 22, No.2, p.95-108. doi.org/10.1029/WR022i002p00095

Yeung, S., and Carter, J. 1990. Interpretation of the pressuremeter test in clay allowing for membrane end effects and material non-homogeneity. In Proceeding of the Third International Symposium on Pressuremeters, 2-6 April 1990. British Geotechnical Society, Oxford University, London, pp. 199-208.

Yin, Y., Cui, Y., Tang, Y., Liu, D., Lei, M., and Chan, D. 2021. Solid–fluid sequentially coupled simulation of internal erosion of soils due to seepage. Granular Matter. 23(20). doi.org/10.1007/s10035-020-01076-0

Yin, Z.Y., Jin, Y.F., Shen, J.S., and Hicher, P.Y. 2016. Optimization techniques for identifying soil parameters in geotechnical engineering: comparative study and enhancement. International Journal for Numerical and Analytical Methods in Geomechanics, 42(1):70-94. doi.org/10.1002/nag.2714

Yu, H.S. 1993. A new procedure for obtaining design parameters from pressuremeter tests. Aust. Civil Eng. Trans., Vol. CE35(4), 353-359

Yu, H. S., and Netherton, M. 2000. Performance of displacement finite elements for modelling incompressible materials. International Journal for Numerical and Analytical Methods in Geomechanics. 24(7):627-653. doi.org/10.1002/(SICI)1096-9853(200006)24:7<627:: AID-NAG86>3.0. C.O.;2-L

Yu, H. S., Charles, M, and Khong, C. 2005. Analysis of pressuremeter geometry effects using critical state models. International Journal for numerical and analytical methods in geomechanics. 29(8): 845-859. doi.org/10.1002/nag.448

Yu, H. S. 2006. The First James K. Mitchell Lecture in-situ soil testing: from mechanics to interpretation. Geomechanics and Geoengineering. 1(3): 165-195. doi:10.1080/17486020600986884

Yuan, Y. 2015. Recent advances in trust region algorithms. Math. Program., 151:249–281. doi: 10.1007/s10107-015-0893-2

Yuan, Y., Xu, B., and Claes P. 2013. Design of caprock integrity in thermal stimulation of shallow oil-sands reservoirs. J Can Pet Technol 52: 266–278. doi: doi.org/10.2118/149371-PA

Zadeh, N. 2016. Multiple packer techniques for in-situ stress measurement in hard soils-soft rocks. Ph.D. thesis, University of Alberta

Zhang, B., Chalaturnyk R., and Boisvert J. 2020. A numerical characterization workflow for assessing the strength and failure modes of heterogeneous oil sands. Canadian Geotechnical Journal. e-First doi.org/10.1139/cgj-2020-0137.

Zhang, G.W. and Liu, L.Y. 1995. Determination of distribution of random variable parameters using Bayesian method. Chinese J. of Geotechnical Engineering (in Chinese). 17(3): 91-94

Zhang, J., Zhang, L. M., and Tang, W. 2009. Bayesian Framework for Characterizing Geotechnical Model Uncertainty. Journal of Geotechnical and Geoenvironmental Engineering. 135(7): 932-940

Zheng, D., Zhang, B., and Chalaturnyk, R. 2021. Uncertainty quantification of in-situ horizontal stress with pressuremeter using a statistical inverse analysis method. Canadian Geotechnical Journal. https://doi.org/10.1139/cgj-2021-0004

Zheng, D., Dreger, C., Zhang, B., and Chalaturnyk, R. 2022. Reliability analysis of a compacted fill slope reinforced with geogrids. In Proceedings of the 20th International Conference on Soil Mechanics and Geotechnical Engineering, Sydney, Australia.

Zheng, D., Deisman, N., Zhang, B., and Chalaturnyk, R. 2023. Statistical inverse analysis of the RGP tests at Primrose-Wolf Lake oil sands field. GeoConvention 2023, Calgary, Canada.

Zheng, D., Zhang, B., and Chalaturnyk, R. 2024 Quantifying uncertainty of in-situ horizontal stress and geotechnical parameters using a Bayesian inference approach for pressuremeter tests. Canadian Geotechnical Journal. Just-IN https://doi.org/10.1139/cgj-2023-0686

Zhou, H., Kong, G. Liu, H. 2015. A semi-analytical solution for cylindrical cavity expansion in elastic-perfectly plastic soil under biaxial in-situ stress field, Géotechnique. doi.org/10.1680/jgeot.15.P.115

Zoback, M. D. 2007. Reservoir Geomechanics. Cambridge University Press

Appendix A Verification of the modified strain-hardening /softening model through THE interpretation of triaxial testing data

In Chapter 6, the modified strain-hardening/softening (SS) model was utilized in numerical modelling to quantify the clay shale constitutive response to applied pressure in the RGP test. Although the goodness of fit to the RGP testing curve was satisfied, the validity of the modified SS model still needs to be verified with the data from other types of measurements, such as the triaxial compression test. Schlumberger (2014) reported triaxial compression tests on sample cores retrieved from the Westgate Formation. Therefore, data measured from the triaxial compression test on sample WG1-4(H) were chosen to validate the proposed modified SS model.

A.1 Summary of the triaxial compression test on WG1-4(H)

The sample core WG1-4(H) was collected at a depth of 287.03 m, with a dimension of 19 mm × 38 mm (D×L) and the horizontal sample orientation. The standard consolidated-drained triaxial test was conducted at a controlled axial strain rate of 5×10^{-6} in/in/s. The results of the triaxial test on sample WG1-4(H) are summarized in Table A.1.

Table A.1 Summary of the triaxial compression test on WG1-4(H)

Sample	Bulk density (g/cm^3)	σ'_3 (MPa)	σ'_1 (MPa)	c′ (MPa)	φ' (°)	ν'_1	ν'_2	E′ (GPa)
WG 1-4(H)	2.09	14	46	6	20	0.35	0.39	4.26

Note: υ'_1 is the Poisson's ratio normal to the bedding plane; υ'_2 is the Poisson's ratio parallel to the bedding plane.

Figure A.1 shows the specimen WG1-4(H) testing curve during the consolidated-drained triaxial test. The triaxial testing curve demonstrates a typical strain-softening behaviour after peak strength with a residual strength of 20 MPa. The workflow to fit the stress-strain curve numerically with a proper constitutive model is discussed below. As in previous chapters, the inverse analysis of the triaxial test can find the best-fit curve and derive the mechanical properties of specimen WG1-4(H).

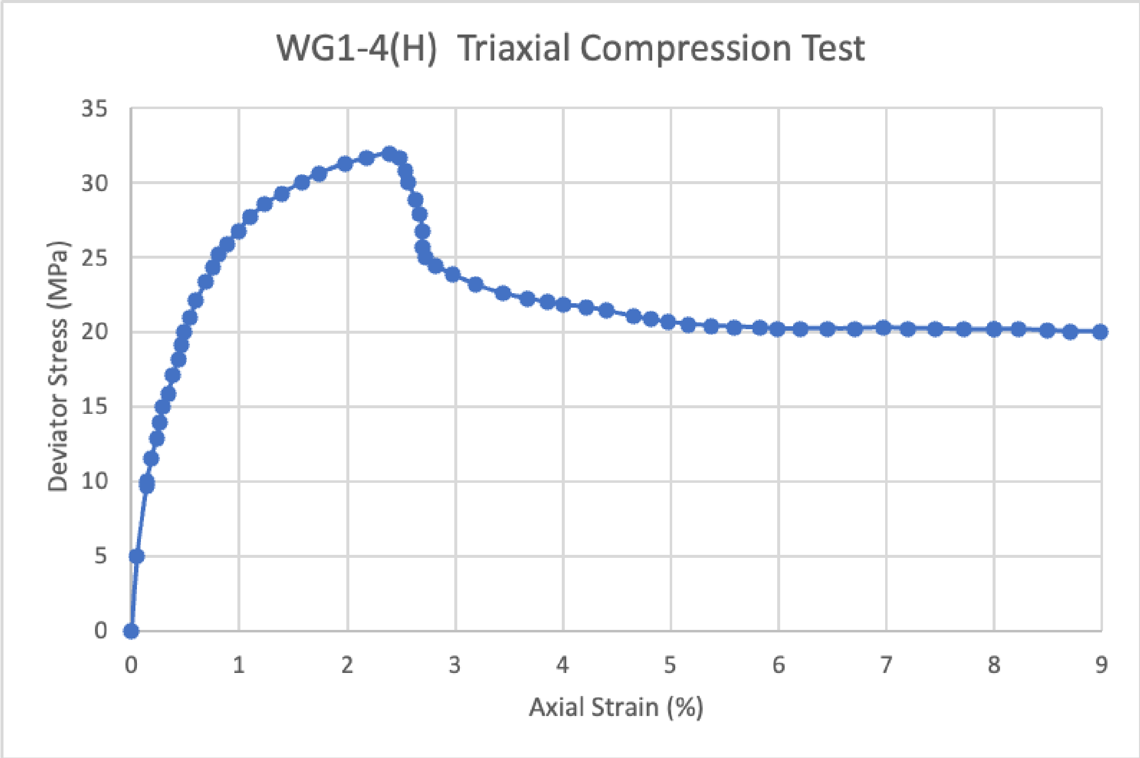

Figure A.1 Specimen WG1-4(H) triaxial consolidated-drained testing curve

A.2 Numerical modelling of the triaxial compression test on WG1-4(H)

For the numerical simulation, the drained triaxial compression test on sample core WG1-4(H) is modelled with a FLAC3D (Itasca, 2011) cylindrical model shown in Figure A.2 . The dimensions of the cylinder are 19 mm in diameter and 38 mm in height, respectively.

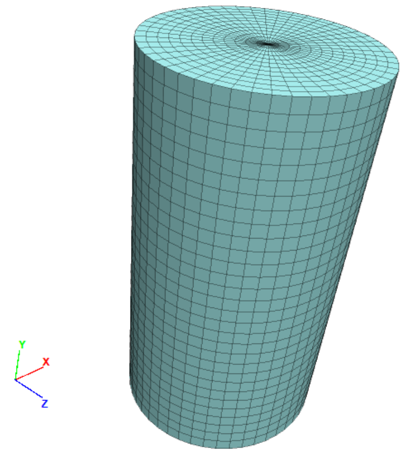

Figure A.2 FLAC3D model simulating the WG1-4(H) triaxial consolidated-drained test

The grid is fixed at the bottom of the cylinder. A uniform velocity boundary condition with a magnitude of 1×10^{-6} m/sec is applied in the y-direction at the top of the cylinder to induce axial compression. A constant lateral confining pressure $\sigma_3' = 14$ MPa is imposed on the perimeter of the cylinder. As the triaxial cell is vented to the atmosphere, no extra pore pressure should be generated during the drained triaxial test.

A.3 Curve fitting of the triaxial compression test on WG1-4(H)

To fit the testing curve shown in Figure A.1 , the numerical tests using the Mohr-Coulomb model, the SS model and the modified SS model are performed in the inverse analyses of the triaxial test. However, there are some differences from the previous inverse analyses of RGP tests. First, as the mechanical properties of the specimen are already presented in the report (Schlumberger, 2014), it seems redundant to estimate all the parameter values again through inverse analysis. However, the anisotropy of Poisson's ratio (e.g., ν_1' and ν_2' in Table A.1) cannot be simulated with the Mohr-Coulomb model in FLAC3D. Therefore, an equivalent isotropic Poisson's ratio must be determined using the inverse analysis approach. Second, the softening ratios of the stiffness and strength for the degraded material in the SS model and the modified SS model need to be estimated using inverse techniques. Third, due to the velocity boundary condition applied on the top of the cylinder, the objective function defined as in Equation 6.1 shall be modified accordingly.

A.3.1 The objective function for the triaxial compression test

In general, SSE, as defined in Equation 6.1, works well in the case of ordinate-based curve matching problems. However, while encountering the test curves simulated with uniform velocity boundary conditions in a triaxial test, the measured and predicted data points often do not coincide horizontally, which causes some data points to be ignored. Witowski (2011) introduced the partial curve mapping method to compute the area between measured and predicted curves. The objective function defined in Equation 6.1 should be reformulated by mapping the measured data points onto the predicted curve. The unweighted nonlinear least squares (NLLS) objective function can be modified as:

$$MSE = \frac{1}{n_t}\sum_{i=1}^{n_t}\left[P_i - \hat{P}_i(b_i)\right]^2 \quad \text{(A.1)}$$

where P_i denotes the measured pressure after mapping, $\hat{P}_i$ denotes the predicted pressure and b_j represents a parameter to be estimated, such as (E', c', φ'). $\hat{P}_i(b_i)$ represents a nonlinear function of b_j for the simulation of a triaxial test. E' represents the drained Young's modulus, c' indicates the drained cohesion and φ' denotes the drained friction angle. n_t represents the total loading increments in the numerical simulation. The displacement variables in Equation 6.1 are substituted with the pressure variables in Equation A.1 owing to the displacement-controlled numerical simulation for the triaxial test. This study implements the SS optimiser to minimise the MSE formulated in Equation A.1.

A.3.2 Inverse analysis of the triaxial test using the Mohr-Coulomb model

With the geometry and boundary conditions described above, the Mohr-Coulomb model is coupled with the SS optimizer in the inverse analysis of the triaxial test. Thus, the isotropic Poisson's ratio is the only parameter to be estimated. Given the normal and parallel Poisson's ratios listed in Table A.1, the lower and upper bound of the equivalent isotropic Poisson's ratio v' is between 0.1 and 0.4 in the inverse analysis.

With the number of samples $N_s = 250$, intermediate conditional failure probability $P(F_i) = 0.1$, and the maximum number of simulation levels $N_l = 5$, the value of v' is estimated to be 0.21, with an MSE of 16.1. Figure A.3 illustrates the predicted and measured curves for WG1-4(H). Since the Mohr-Coulomb model is an ideal elastic-plastic model, the softening behaviour after peak strength can not be simulated. Therefore, the simulated stress-displacement curve shows a plateau after the peak.

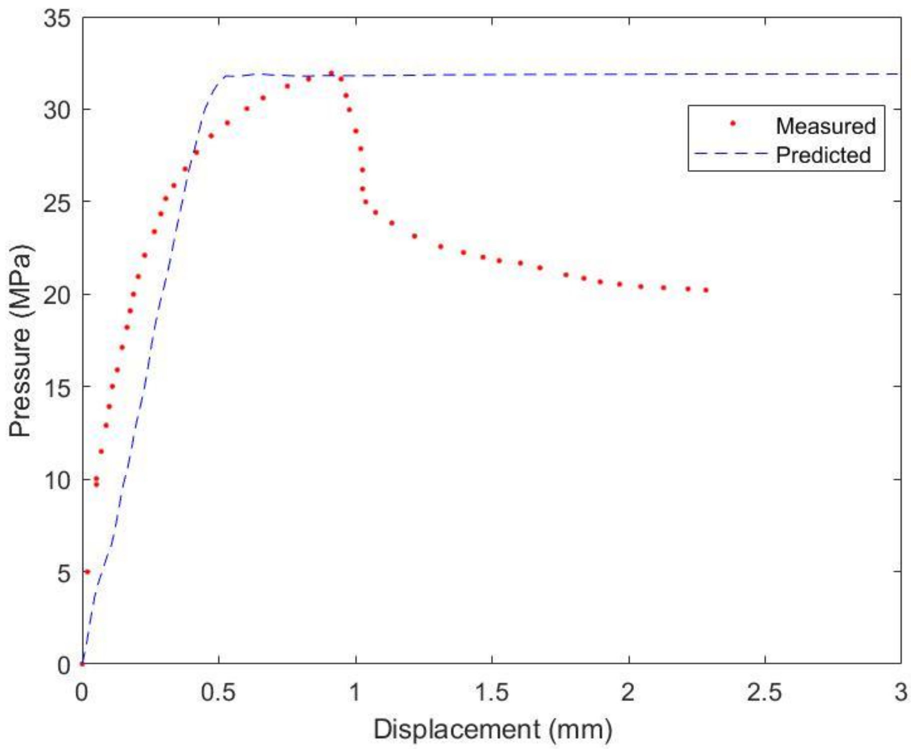

Figure A.3 Predicted and measured curves for WG1-4(H) using the Mohr-Coulomb model

A.3.3 Inverse analysis of the triaxial test using strain-hardening/softening model

To simulate the softening phase after the peak (Figure A.3), the strain—hardening/softening (SS) model (Itasca, 2011) is implemented in the inverse analysis of the triaxial test. According to the manual (Itasca, 2011), the material hardening/softening properties in the SS model are user-defined piecewise-linear functions of plastic strain increments Δe^{ps}. However, as discussed in Section 6.3.5, the hardening and softening variables (Equations 6.4 to 6.7) are difficult to be defined with a trial-and-error method.

The material properties hardened or softened with Δe^{ps} are cohesion, friction angle, dilation angle and tensile strength (Itasca, 2011). Due to the potential development of fissures in the clay shale specimen during the triaxial test, cohesion is most susceptible to change. Thus, the user-defined piecewise-linear table is defined below.

Table A.2 Piecewise-linear strain hardening/softening property in WG1-4(H)

Δe^{ps}	0	0.05	0.1	1
Cohesion (MPa)	6	$\mathbf{6} \times \boldsymbol{\beta}_{\boldsymbol{c1}}$	$\mathbf{6} \times \boldsymbol{\beta}_{\boldsymbol{c2}}$	$\mathbf{6} \times \boldsymbol{\beta}_{\boldsymbol{c2}}$

Note: β_{c1} and β_{c2} are the coefficients of hardened or softened property

The lower and upper bounds of β_{c1}, β_{c2} and v' for the inverse analysis are defined in Table A.3.

Table A.3 Lower and upper bounds for the inverse analysis of triaxial test WG1-4(H) using the SS model

Parameter	v'	β_{c1}	β_{c2}
Lower bound	0.1	0.75	0.2
Upper bound	0.4	1.25	0.4

With the number of samples $N_s = 250$, intermediate conditional failure probability $P(F_i) = 0.1$, and the maximum number of simulation levels $N_l = 10$, the inverse analysis was performed using the SS optimizer coupled with the SS model. Table A.4 lists the estimated values with an MSE of 3.92. Figure A.4 illustrates the predicted and measured curves for WG1-4(H).

Table A.4 Results from the inverse analysis of triaxial test WG1-4(H) using the SS model

Parameter	v'	β_{c1}	β_{c2}	MSE
Estimated value	0.14	0.90	0.30	3.92

The Poisson's ratio v' estimated from the SS model equals 0.14, compared to 0.21 from the Mohr-Coulomb model. The non-uniqueness of the solution is caused by the deterministic approach used in the inverse analysis. Statistical assessments can be used to address this problem.

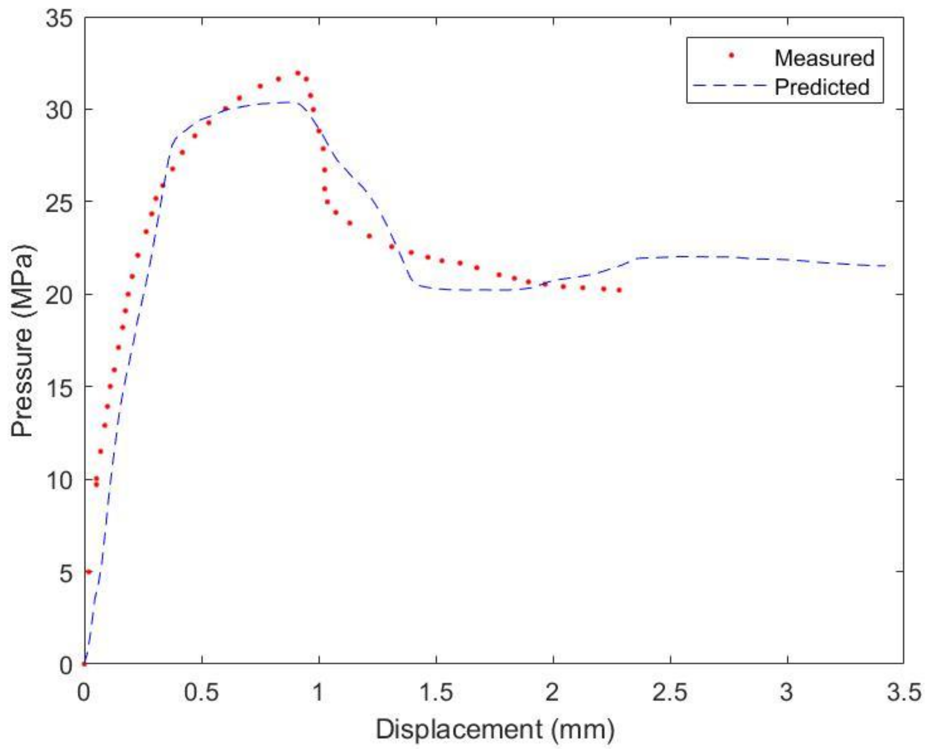

Figure A.4 Predicted and measured curves for WG1-4(H) using the SS model

The curve fit in Figure A.4 is substantially improved by visual comparison than Figure A.3 . Also, the MSE values (e.g., 3.92 vs. 16.1) can confirm the improvement of model fit by the SS model than the Mohr-Coulomb model. However, because the accuracy of hardened/softened properties defined by Δe^{ps} is highly dependent upon the user-defined piecewise-linear functions, the non-unique piecewise-linear functions defined in the SS model may cause more problems if not properly defined.

A.3.4 Inverse analysis of the triaxial test using the modified strain-hardening/softening model

The modified SS model is explained in Section 6.3.5 in Chapter 6. For a modified SS model, user-defined piecewise-linear functions are not required. Instead, the material strain-hardening/softening behaviours in the modified SS model are described with strain-hardened/softened variables, which are functions of plastic indicators (e.g., 0, 1 and 2 in FLAC3D) rather than plastic strain increments Δe^{ps}. With the implementation of plastic indicators in a numerical model, the difficulties in defining the hardened/softened variables are overcome. In essence, the zones in the modified SS model are discretized with elastic and plastic areas, which can approximate the material hardening/softening properties defined by Δe^{ps}. Therefore, the modified SS model can significantly simplify the inverse analysis without losing accuracy.

As mentioned above, only cohesion is most susceptible to softening with the increase of axial strain for specimen WG1-4(H). The degraded variable of cohesion defined by Equation 6.5 is β_c. The lower and upper bounds of v' and β_c for the inverse analysis are defined in Table A.5.

Table A.5 Lower and upper bounds for the inverse analysis of triaxial test WG1-4(H) using the modified SS model

Parameter	v'	β_c
Lower bound	0.1	0.1
Upper bound	0.4	0.5

With the number of samples $N_s = 250$, intermediate conditional failure probability $P(F_i) = 0.1$, and the maximum number of simulation levels $N_l = 10$, the inverse analysis was performed using the SS optimizer coupled with the modified SS model. Table A.6 lists the estimated values after the inverse analysis.

Table A.6 Results from the inverse analysis of triaxial test WG1-4(H) using the modified SS model

Parameter	v'	β_c	MSE
Estimated value	0.13	0.36	3.23

The degraded variable β_c is 0.36, which means the cohesion of this specimen has been softened more than 60% after the peak. Figure A.5 illustrates the predicted and measured curves for WG1-4(H), indicating a better model fit than Figure A.4 . Besides visual comparisons, the MSE of 3.2 can also justify the best curve fit by the modified SS model in the inverse analyses.

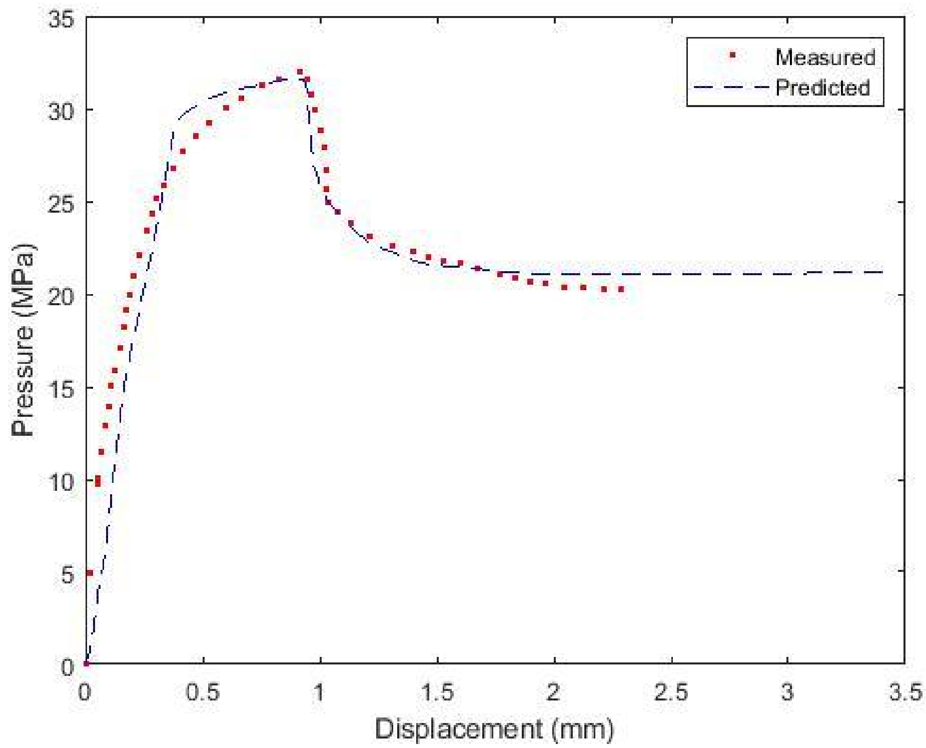

Figure A.5 Predicted and measured curves for WG1-4(H) using the modified SS model

The Poisson's ratio v' estimated from the modified SS model equals 0.13, the SS model 0.14, and the Mohr-Coulomb model 0.21, respectively. Non-uniqueness cannot be eliminated with the deterministic optimization approach used in the inverse analysis. Statistical assessments are expected to address this non-uniqueness problem. However, the objective of Appendix A is to verify the advantages of the modified SS model over the other two constitutive models in the model fit for a triaxial test. Uncertainty quantification of the inverse analysis for the triaxial test shall be further studied in the future.

A.4 Summary and Conclusion

The SS optimizer performs inverse analyses of the triaxial test on specimen WG1-4(H). The Poisson's ratio v' and the softening variables are derived from the inverse analyses. Due to the velocity boundary conditions, the measured and predicted data points often do not coincide horizontally. Then, the curve mapping method is used to compare the measured curve with the predicted curves. As a result, the objective function (Equation A.1) is formulated with the MSE in terms of pressure. Through the inverse analyses, the advantages of the modified SS model over the SS model and the Mohr-Coulomb model in the curve fitting are verified with the values of MSE and visual comparisons. In addition, the modified SS model is validated by its convenience and applicability.

Appendix B Optimization algorithms for inverse analysis and interpretation of SBP tests using conventional deterministic method

B.1 Optimization algorithms for inverse analysis

To solve the objective functions, the Gauss–Newton algorithm (GNA) can be used as a modified Newton's method for determining the minimum of a function. Here, the LMA is used to find the local minimum for the objective function (Levenberg, 1944; Morrison, 1960; Marquardt, 1963):

$$(J^T J + I\lambda)\delta = J^T[y - f(b)] \tag{B.1}$$

where I represents the identity matrix. The LMA can converge to a local minimum (Conn, 2000) but not necessarily the global minimum. With the Jacobian matrix calculated in the iterative procedure, statistical assessment upon the identified parameter values can be efficiently conducted.

Rather than searching along a line in one direction in the LMA, the trust-region algorithm (TRA) explores the vicinity of the trust region. TRAs are a class of iterative methods for nonlinear optimization problems which have been extensively studied for decades (Yuan, 2015; Conn, 2000). To minimize the objective function, $f(x), x \in X$, a trial step can be computed by solving the following trust-region subproblem:

$$\min_{d}[q(d), d \in N] \tag{B.2}$$

where q represents an approximation of the objective function f(x), d indicates a trial step, and N denotes a region of trust.

Usually, q is approximated by a quadratic function, and the trust-region neighbourhood is generally spherical or ellipsoidal (Moré, 1978). Due to the constraint of the trust region, the TRA can be applied in cases of negative curvature of an objective function and ill-conditioned problems (Yuan, 2015). To accelerate the quadratic convergence, Coleman and Li (1994) proposed a piecewise reflective line search at each iteration to modify the TRA. The modified TRA is called the trust-region reflective algorithm (TRRA).

SS was initially developed for seismic risk analysis of building structures subjected to stochastic earthquake motions (Au and Wang, 2014). As an alternative to the MCS, SS is a Monte Carlo methodology that takes advantage of the Markov Chain Monte Carlo (MCMC) method and a simple evolutionary strategy (Schueller, 2009). Like other optimization algorithms using heuristic techniques, the SS algorithm is based on a stochastic search algorithm for global optimization problems. SS is more efficient than MCS, particularly when using a computationally costly numerical model. In the SS algorithm, the failure probability of a rare event can be estimated by multiplication of a sequence of conditional failure probabilities of intermediate events, which can be evaluated as follows:

Given a failure event F, let $F_1 \supset F_2 \supset \cdots \supset F_m = F$ be a decreasing sequence of failure events,

$$P_F = P(F_m) = P(\cap_{i=1}^{m} F_i) = P(F_1) \prod_{i=1}^{m-1} P(F_{i+1}|F_i) \qquad \text{(B.3)}$$

where P_F denotes the probability of failure; $P(F_i\ )$ represents the failure probability of an intermediate event; and $\{P(F_{i+1}|F_i): i = 1,2, \dots m-1\}$ denotes the conditional probabilities (Au and Wang, 2014).

B.2 Interpretation of SBP tests using conventional deterministic methods

Conventional methods are first applied to interpret the SBP tests, which can verify the effectiveness of the results from the inverse analysis. Geotechnical data from triaxial tests (Jefferies, 1987) are also deduced to constrain the range of estimated parameters.

B.2.1 Interpretation of SBP tests using graphical plotting and linear fit regression methods

With the assistance of constructing lines, σ_h, G, and S_u can be deduced by examining a pressuremeter testing curve (Gibson and Anderson, 1961; Houlsby and Withers, 1988; Marsland and Randolph, 1977).

The lift-off method is usually applicable to identify the horizontal stress, σ_h, for SBP tests, although it is criticized for its subjectivity (Clarke, 1995; Mair and Wood, 1987). To reduce the subjectivity, Jefferies (1987) improved the lift-off method by introducing a modified inspection technique. It is believed that σ_h lies at a stress lower than the yield stress, σ_{hy}. Therefore, the method needs to identify σ_{hy} by the first observation of excess pore pressure change or inspection of the pressuremeter-displacement curve. Thus, σ_{h0} can be located from the intersection of the constructed instrument stiffness line and the gradient line determined by the unloading–reloading cycle. From Figure B.1, σ_{h0} is evaluated as 1690 kPa using the modified inspection technique, which lies in the range of 1670 ± 30 kPa reported by Jefferies (1987).

According to Mair and Wood (1987), S_u can be deduced from the slope of a straight line by plotting the SBP data as $p : \ln(\Delta V/V)$. Alternatively, the slope of a straight line can be determined through the linear fit regression by use of Origin 2020 (OriginLab, 2020). The benefit of using this approach is to reduce subjectivity, and therefore, results become repeatable. The undrained shear strength S_u is identified in Figure B.2 as 182 ± 7.6 kPa. Similarly, the shear modulus, G, can be determined as 49 540 ± 1378 kPa, which is one-half of the fitted slope value in Figure B.3 (Mair and Wood, 1987).

B.2.3 Interpretation of triaxial tests using graphical plotting methods

Jefferies (1988) reported an anisotropically consolidated undrained triaxial test with shear stress reversal. The initial Young's modulus, E_i, and the secant modulus at 50% strength, E_{50}, can be inferred from the line construction on the triaxial testing curve. Figure B.4 indicates that E_i and E_{50} is 41 200 kPa and 33 700 kPa, corresponding to G_i = 13 730 kPa and G_{50} = 11 230 kPa, respectively.

At the same time, the shear strength, S_u, in loading and unloading is identified as 238 kPa and 191 kPa from the peak positive and negative deviatoric stresses. In addition, the softening coefficient, β, defined in Equation 4.3 is 0.8 by calculating the ratio of shear strength in loading to unloading.

Table B.1 summarizes the results from the interpretation of both SBP and triaxial tests. Compared to the triaxial test, G deduced from the unloading–reloading loop seems to be overestimated. This may be due to the drainage taking place near the probe during this stage (Clarke, 1995), which could exaggerate the deduced value of G. The undrained shear strength, S_u, can refer to Table B.1.

Table B.1 Results from the conventional interpretation of SBP and triaxial tests

Method	σ_{h0} (kPa)	G (kPa)	S_u (kPa)
Modified inspection on the SBP test curve	1690	-	-
Linear fit regression of the SBP test curve	-	49 540 ± 1378	182 ± 7.6
Line construction on the triaxial test curve	-	13 730 (G_i) 11 230 (G_{50})	238 (loading)* 191 (unloading)

***Note:** The ratio of shear strength in loading to unloading β is calculated as 191/238 = 0.8

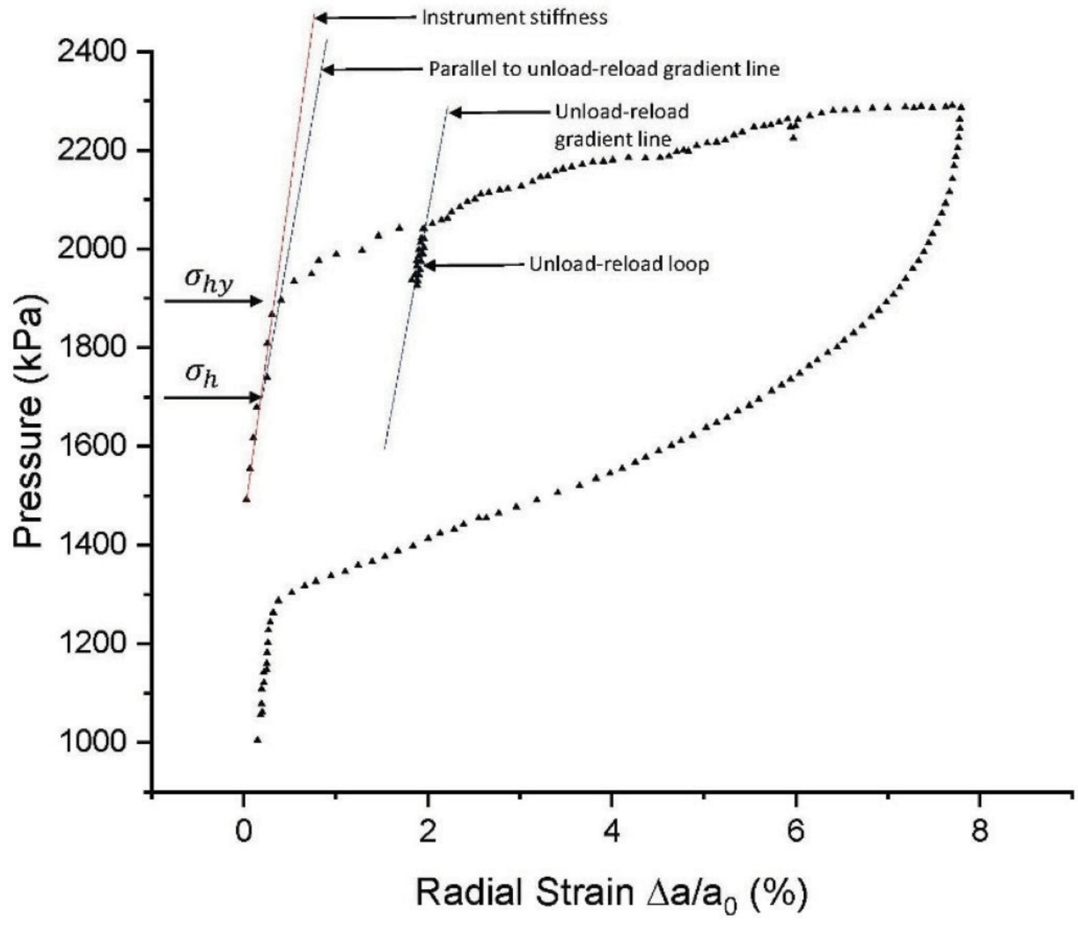

Figure B.1 Identification of the horizontal stress σ_{h0} using graphical plotting method (reproduced from Jefferies, 1987)

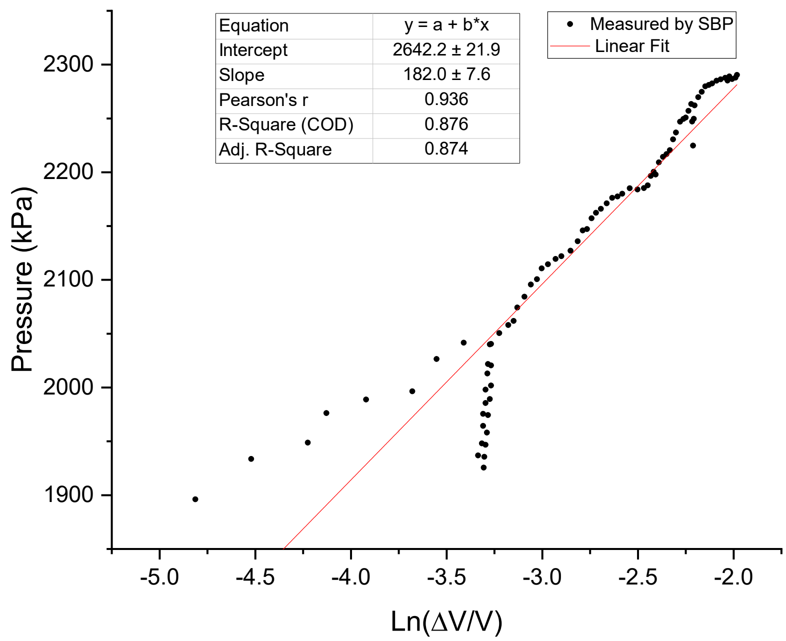

Figure B.2 Identification of the undrained shear strength S_u using the linear fitting method

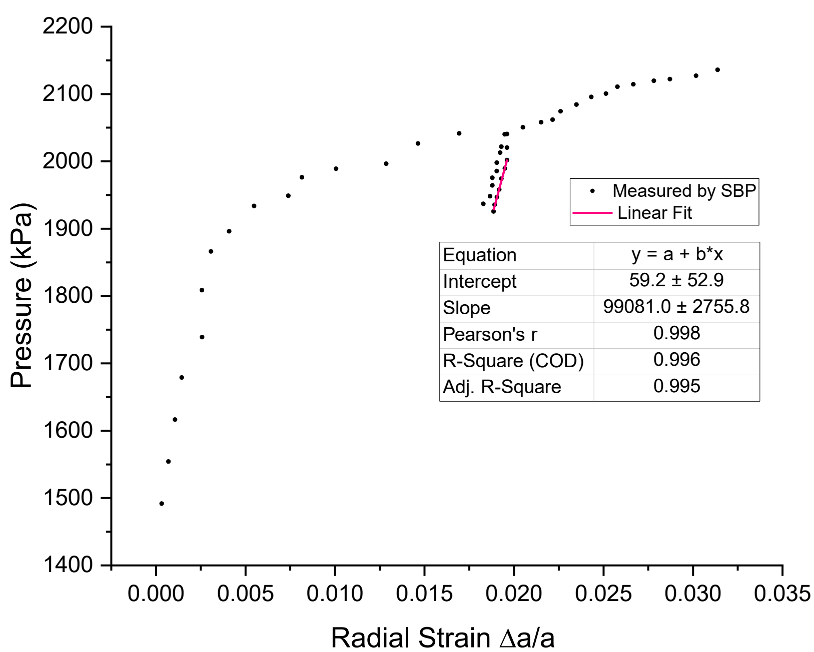

Figure B.3 Identification of the shear modulus G using the linear fitting regression method

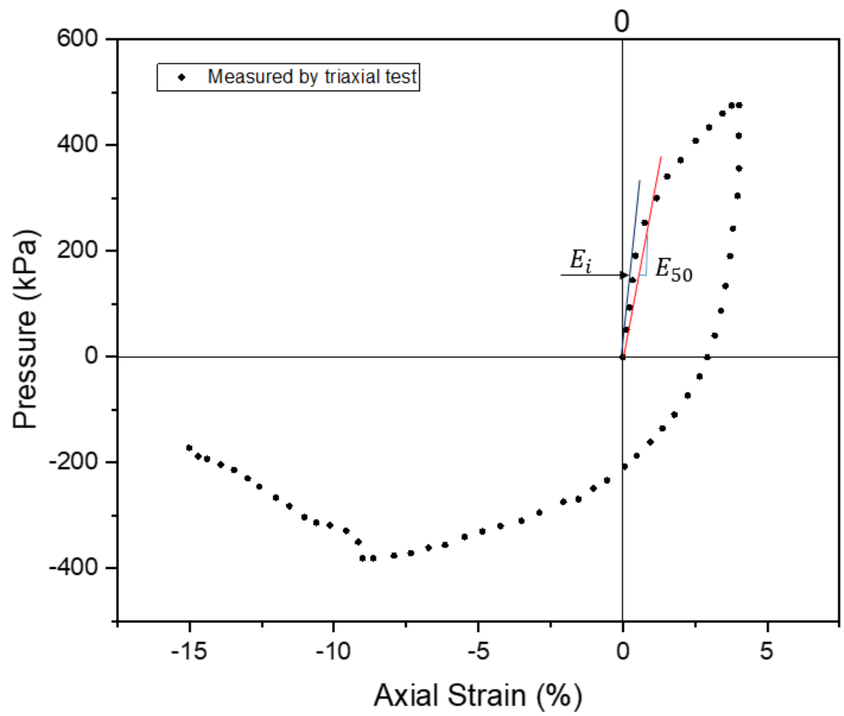

Figure B.4 Identification of the Young's modulus $\boldsymbol{E}$ using the line construction method

Appendix C Stiffness and strength of clay shale in the plastic zones

Figure C.1 to Figure C.12 illustrate the variations of stiffness and shear strength of clay shale in the plastic zones (degraded zone defined in Figure 6.2) at all stages during RGP testing, e.g., expansion, hold, unload-reload loops and contraction. Before the installation of the RGP tool, stress relief occurs in the oversized pre-drilled borehole. Therefore, borehole breakouts can occur if the stress concentration around the borehole exceeds the strength of the rock (Zoback, 2010). During an RGP test, the rubber membrane is expanded against the borehole wall at the expansion stage, followed by a hold test, unload-reload loops, and contraction. As a result, strain-softening or strain-hardening of clay shale can occur around the borehole wall.

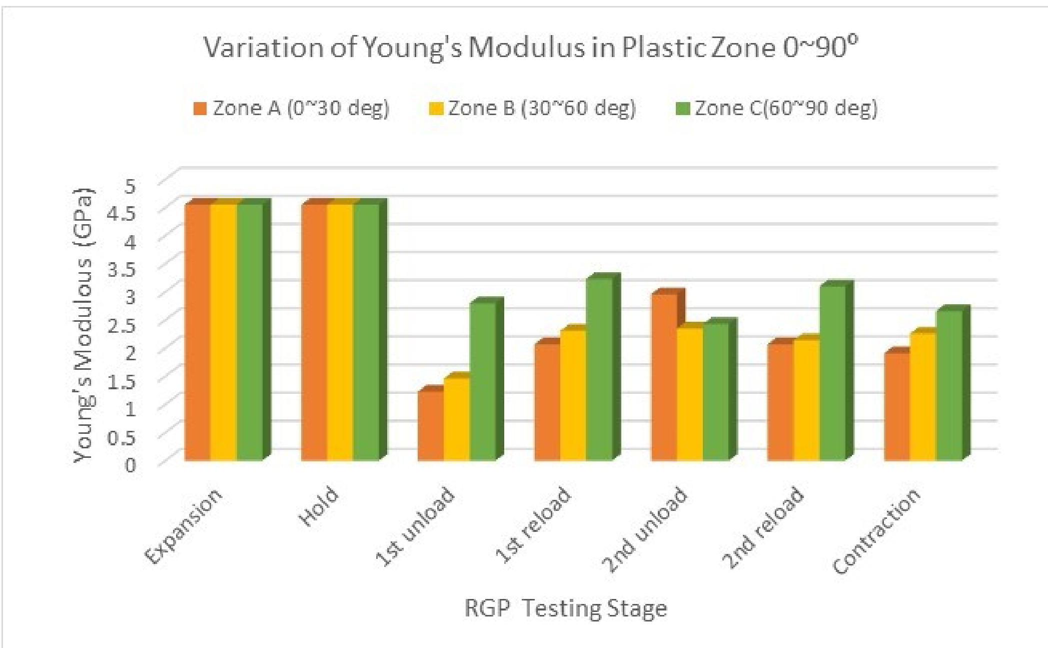

Figure C.1 Variation of Young's modulus in degraded zone estimated from the complete curve in Westgate formation

In the Westgate formation, Young's modulus remains constant in the expansion and hold test stages until the 1st unload-reload loop. The two unload-reload loops cause Young's modulus to degrade azimuthally from Zone A to Zone C, which is in response to biaxial in-situ stresses and borehole stiffness anisotropy (Liu et al., 2020). Young's modulus fluctuates more than 50% between 1st unload and contraction, indicating drastic variations of material stiffness around the borehole during the RGP test. The degraded stiffness implicates a strain-softening behaviour of clay shale in the Westgate formation. Figure C.2 and Figure C.3 demonstrate the variations of shear strength in RGP testing, which are caused by the same reasons mentioned above. The reduction of cohesion can be observed in the hold test and reload. And recovery of cohesion in unloads and contraction, which might be explained by the closure of cracks and fissures in the vicinity of the borehole during unloading and contraction. Compared to cohesion, friction angles vary much less in all the stages. Consequently, there exists uncertainty in the modelling of an RGP test.

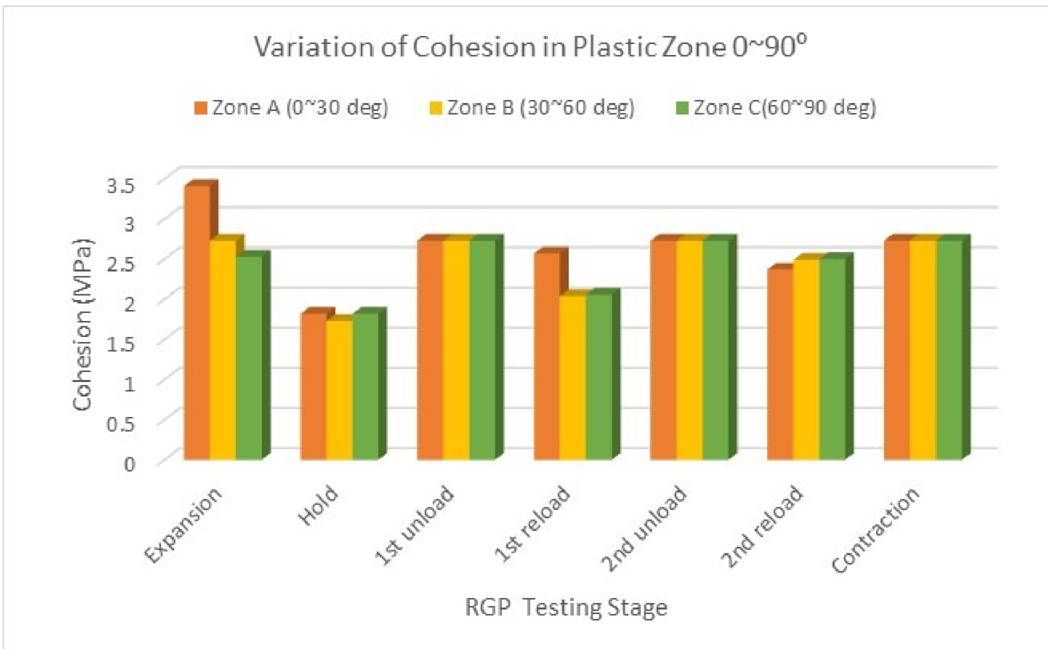

Figure C.2 Variation of cohesion in degraded zone estimated from the complete curve in Westgate

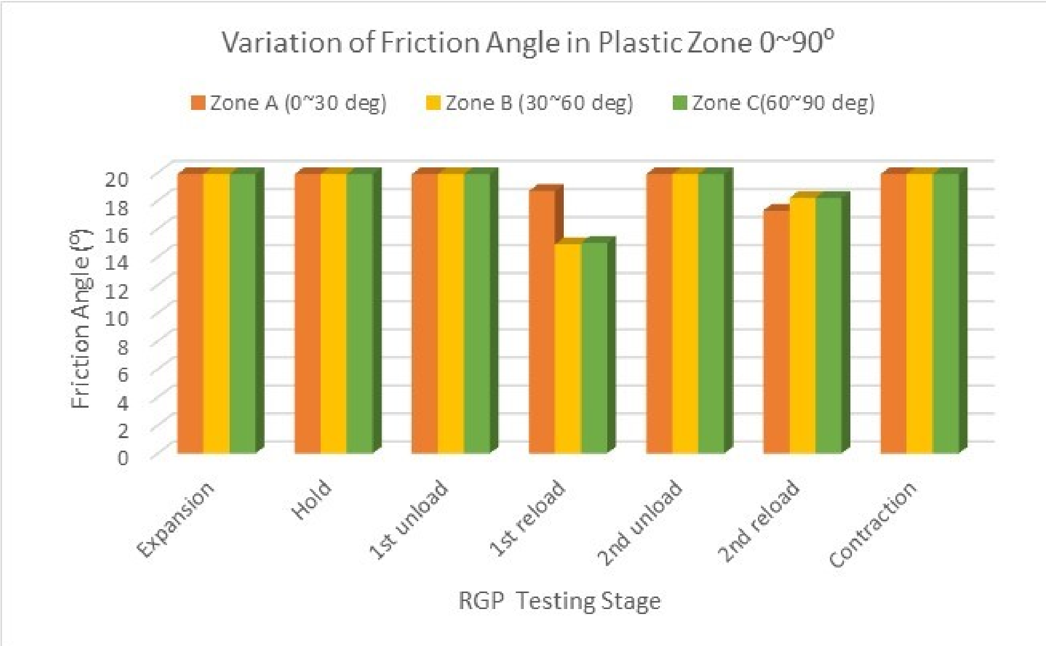

Figure C.3 Variation of friction angle in degraded zone estimated from the complete curve in Westgate

In Figure C.4, there are drastic azimuthal variations of Young's moduli in Zone A in expansion, hold test, and 1st reload, which can be explained by a flat oval-shaped borehole in the Joli Fou formation. This flatness of the deformed borehole may result from local heterogeneity, and the inversed Young's moduli may not represent the true value for Zone A in expansion, hold test and 1st reload.

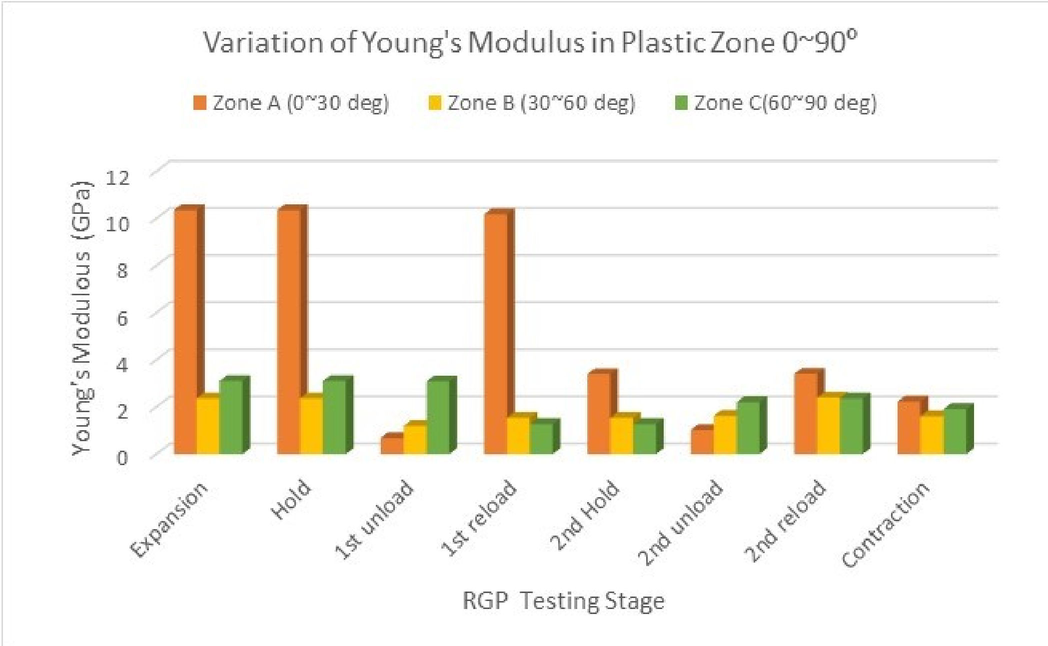

Figure C.4 Variation of Young's moduli in degraded zone estimated from the complete curve in Joli Fou

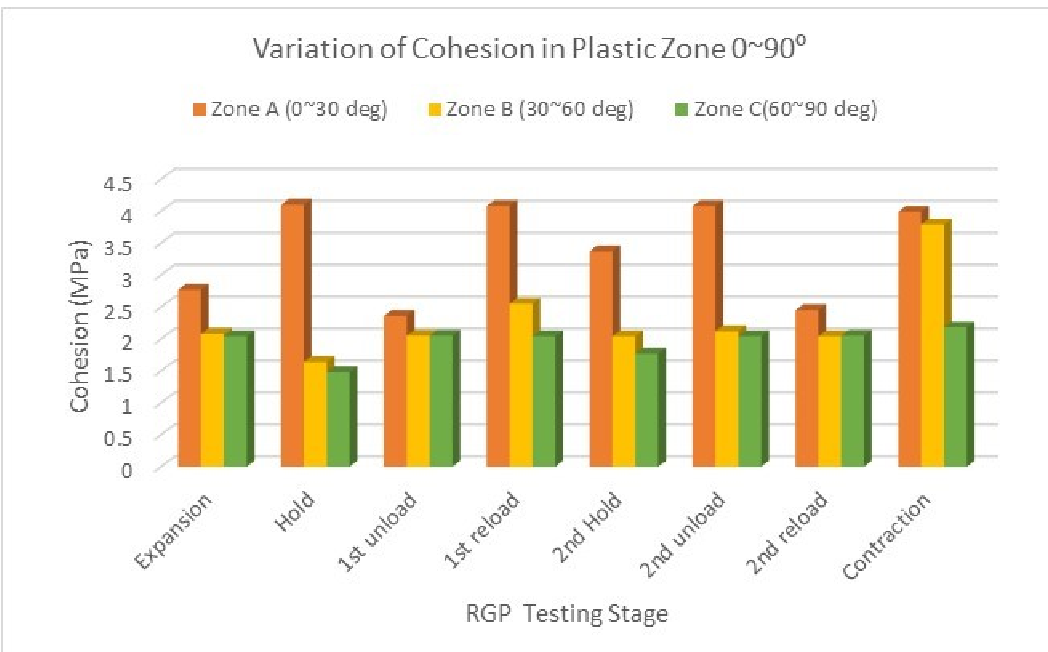

Figure C.5 Variation of cohesion in degraded zone estimated from the complete curve in Joli Fou

Figure C.5 shows no clear trend of variations with reference to the distributions of inversed cohesion values. At the same time, Figure C.6 shows a uniform pattern of friction angle variation.

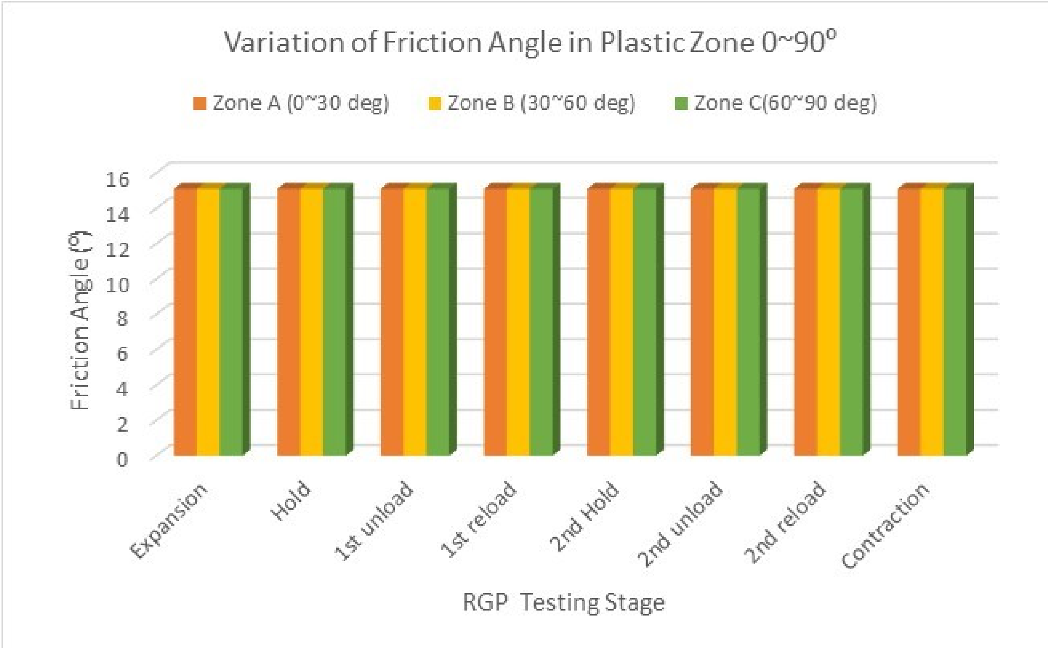

Figure C.6 Variation of friction angle in degraded zone estimated from the complete curve in Joli Fou

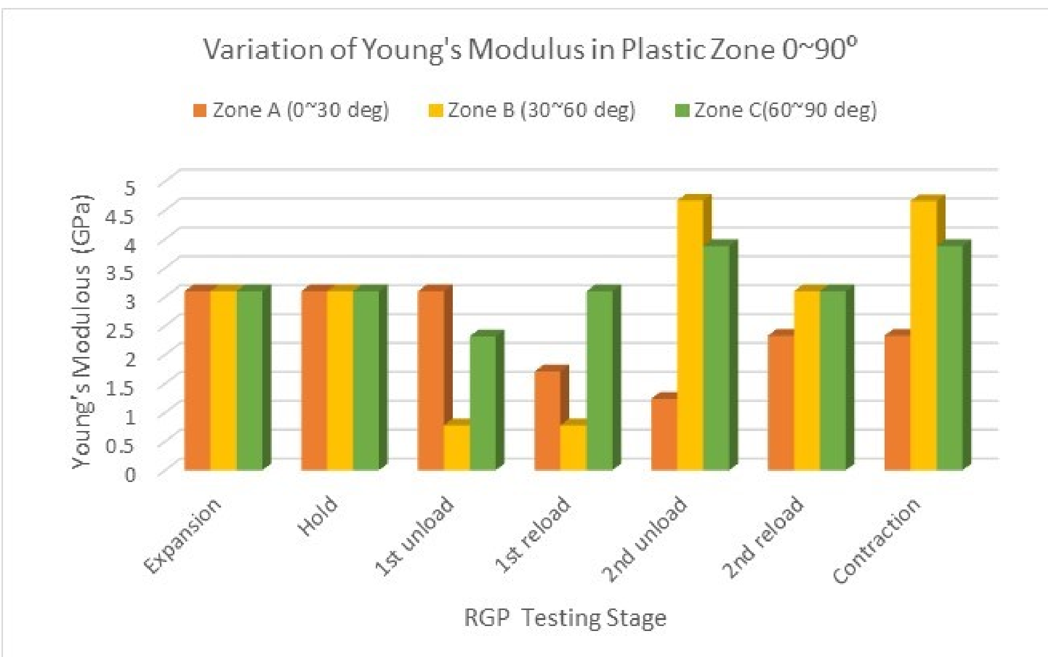

Figure C.7 Variation of Young's moduli in degraded zone estimated from the complete curve in Clearwater black

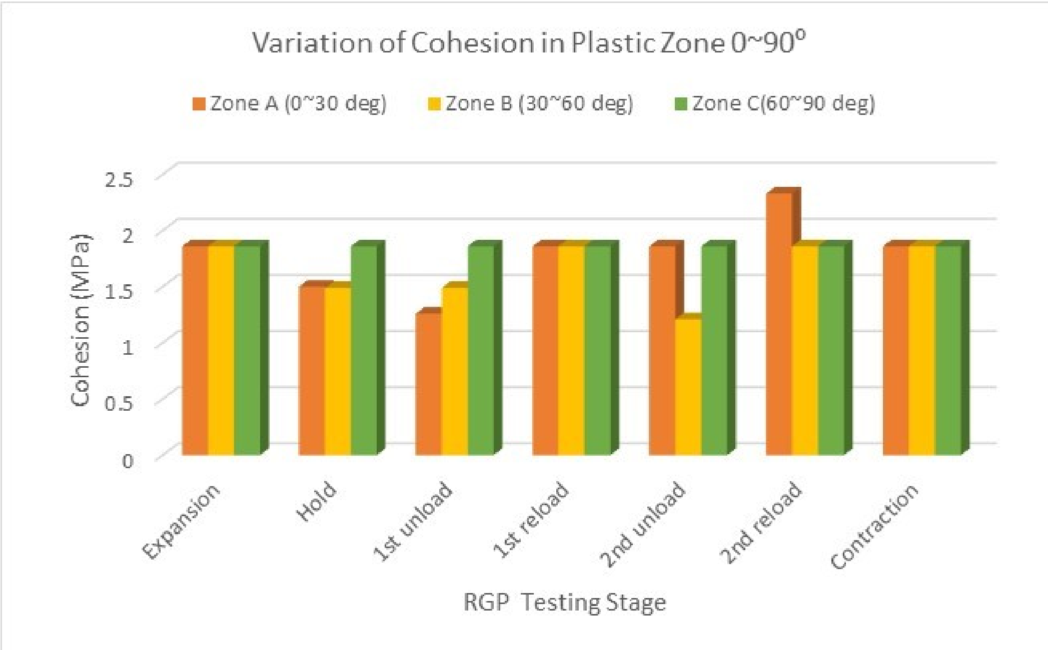

Figure C.8 Variation of cohesion in degraded zone estimated from the complete curve in Clearwater black

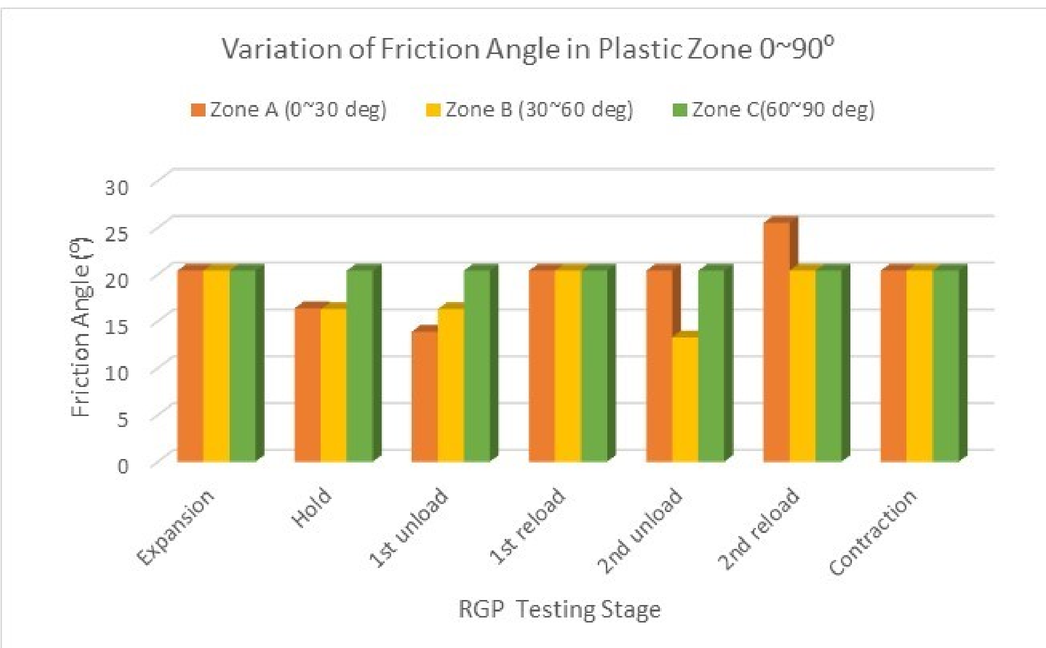

Figure C.9 Variation of friction angle in degraded zone estimated from the complete curve in Clearwater black

Contrary to the Westgate formation, clay shale in the Clearwater black shale formation implicates a strain-hardening behaviour for Young's moduli, according to Figure C.7, except for Zone A.

However, at the end of RGP testing, both cohesion and friction angle recover from softening (Figures C.8 and C.9).

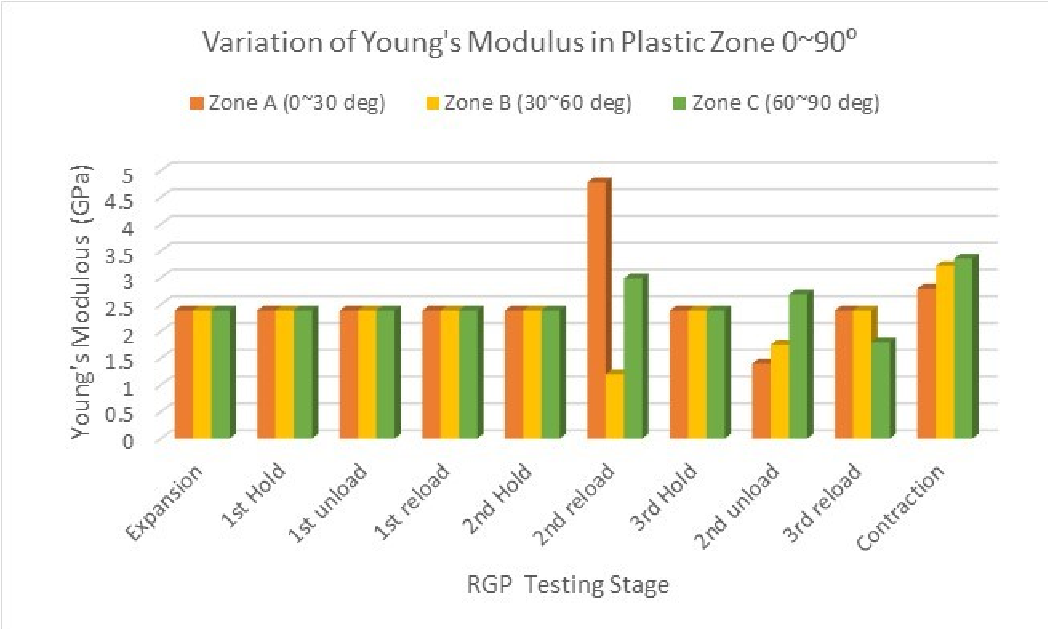

Figure C.10 Variation of Young's modulus in degraded zone estimated from the complete curve in Clearwater grey

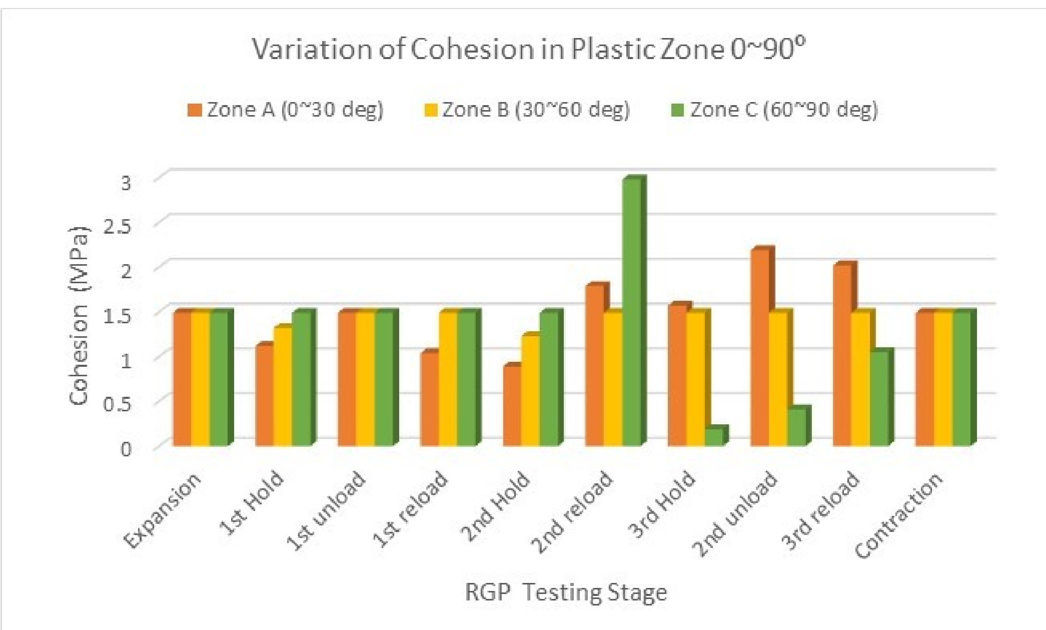

Figure C.11 Variation of cohesion in degraded zone estimated from the complete curve in Clearwater grey

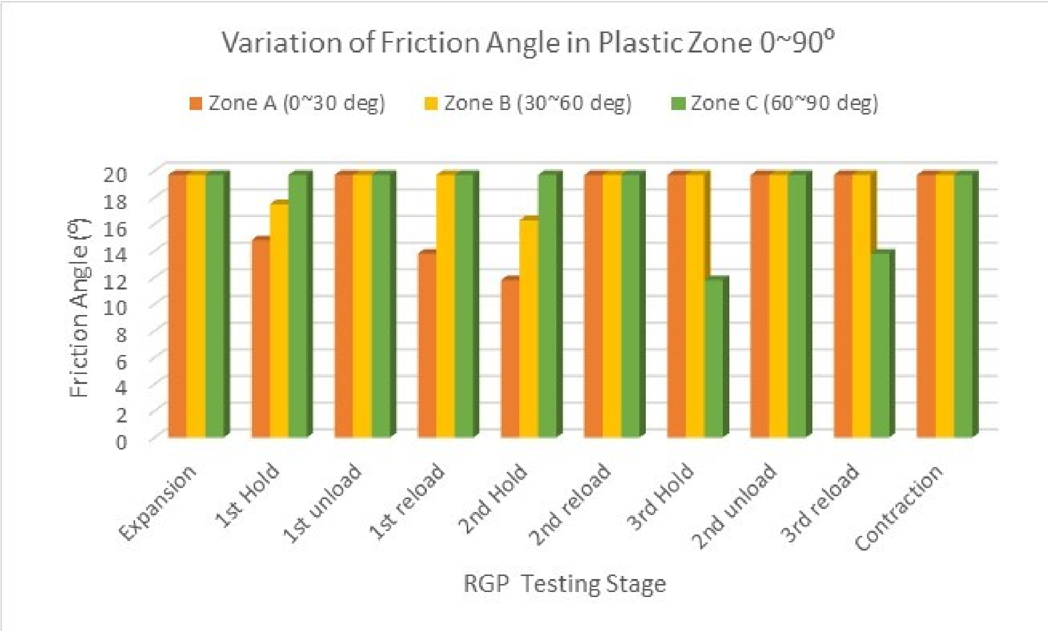

Figure C.12 Variation of friction angle in degraded zone estimated from the complete curve in Clearwater grey

A similar conclusion can be made for the Clearwater grey shale formation. This observation can be explained as being due to the high clay content in the Clearwater clay shale (Liu et al., 2020).

Although dramatic changes in material properties are observed in the degraded zones in all RGP testing stages, there are no significant variations of stiffness and shear strength in the elastic zone, which can be understood owing to the far field. In other words, the expansion of the rubber membrane can only result in the variation of material properties in the degraded zone, as shown in Figure 6.2. Beyond the EP boundary, the in-situ properties would not be affected by the pressure applied by the RGP.